THESE

Pour obtenir le diplôme de doctorat

Spécialité : Chimie

Préparée au sein de l'Université de Rouen Normandie

En partenariat international avec Nicolaus Copernicus University in Toruń, Poland

Ionic liquid-based hybrid electrolyte membranes for proton conducting fuel cells

Présentée et soutenue par

Mohammad EBRAHIMI

Soutenance prevue le 3 Juin 2024 devant le jury composé de		
Mme Murielle RABILLER-BAUDRY	Professeur / Professeur / Rennes University, Institute of Chemical Sciences	Rapporteur
Mr Wojciech FABIANOWSKI	dr hab. inż. prof. Uczelni / Wojskowy Instytut Chemii i Radiometrii	Rapporteur
Mme Beata POŚPIECH	dr hab., prof. uczelni / Politechnika w Częstochowie	Rapporteur
Mme Isabelle DEZ	dr HDR / Laboratory of Molecular and Thioorganique Chemistry / ENSICAEN / University of Caen	Examinateur
Mr Stanislaw KOTER	Professeur / Professeur / Nicolaus Copernicus University in Toruń	Examinateur
Mr Andrzej WOJTCZAK	Professeur / Professeur / Nicolaus Copernicus University in Toruń	Examinateur
Mme Kateryna FATYEYEVA	Dr HDR / McF / Université de Rouen Normandie	Codirectrice de thèse
Mr Wojciech KUJAWSKI	Professeur / Professeur / Nicolaus Copernicus University in Toruń	Codirecteur de thèse

Thèse dirigée par Prof. Wojciech KUJAWSKI du Faculté de Chimie, Université Nicolaus Copernicus à Toruń (Pologne) et Dr. Kateryna FATYEYEVA du laboratoire Polymères, Biopolymères et Surfaces, UMR CNRS 6270 (France)

Uniwersytet Mikołaja Kopernika w Toruniu
Wydział Chemii
Katedra Chemii Fizycznej i Fizykochemii Polimerów
we współpracy z
Université de Rouen Normandie (France)
Laboratoire Polymères, Biopolymères et Surfaces, UMR CNRS 6270

Mohammad Ebrahimi

doktorat realizowany w trybie podwójnego dyplomu
na kierunku chemia

Ionic liquid-based hybrid electrolyte membranes for proton conducting fuel cells

Promotorzy

Prof. dr hab. Wojciech Kujawski
Wydział Chemii UMK w Toruniu

dr hab. Kateryna Fatyeyeva
Université de Rouen Normandie

Toruń 2024

Contents

Acknowledgements

"I am among those who think that science has great beauty"

– Maria Skłodowska-Curie –

Yes! Science is very beautiful as Madam Curie mentioned and I am so happy to live and work in her country. Living for three years and half in Poland and France was a great opportunity for me to have a lot of precious experiences. It was very difficult, but I knew that diamond is valuable because of its resistance to pressure. That is why I did not give up when I encountered with difficult problems. Now, I am here and thinking about the sweet and bitter memories that I had which I really miss those days. During this way several people helped and gave me positive pulses that I would like to express my deepest gratitude to them.

First of all I would like to appreciate Polish and French people who gave this opportunity to live among them. All the time I wished to visit these two beautiful countries with amazing history and my wish exchanged to the truth and I had this chance to get familiar with friendly and amiable Polish and French people. I deeply feel that Torun and Rouen are my second homes. You are all the time in my heart.

I would like to express my profound gratitude to dr. Kateryna FATYEYEVA and prof. Wojciech KUJAWSKI as the co-director and director of my PhD thesis, respectively, for providing me this opportunity to work in two international scientific environments, namely at Department of Physical Chemistry and Physical Chemistry of Polymers, Faculty of Chemistry, Nicolaus Copernicus University in Torun (NCU, Poland) and Polymers, Biopolymers, and Surfaces (PBS) research unit, the University of Rouen Normandy (URN, France). Thank you for your priceless and invaluable advices and assistance during this time. I do not forget that when I had problem, you did guide me and gave me positive pulses to continue and overcome problems. I never forget our meetings which they took hours (even till evening) to find the way for removing the obstacles in front of my work. To dr. Kateryna FATYEYEVA (Katya) for her great contribution, constant help, advice, and encouragement not only in my PhD study but also in my personal life. For her remarks and guidance especially in organic chemistry (ionic liquid synthesis) and electrochemistry which determined the scientific direction of the work and allowed me to develop my scientific skills as a young researcher. I also deeply appreciate her kindness and assistance (e.g. opening bank account, immigration office, and dormitory) which as a foreigner such helps had great influences on my work progress. To prof. Wojciech KUJAWSKI who did trust and accept me as his PhD student. For his remarks and guidance especially in physical chemistry and polymer science. I do not forget that I did learn the basis of membrane and membrane technology from you. Moreover, I do appreciate your great editorial comments for writing the article and dissertation.

Acknowledgements

To dr. Yaroslav KOBZAR who was the closest colleague of mine and collaborated a lot on my work. I would like to truly appreciate your advice and guidance in the ionic liquid synthesis, electrochemistry, and preparation of composite membrane. Your words always made me motivated to overcome the problems of my work.

To dr. Amelié MARTIN, Sara RABIA, and Solene de MEZERAC, we were not only colleagues but also you were my best friends in France. To dr. Amelié MARTIN as my first colleague in PBS research unit who helped me to adapt myself with new scientific environment. To Sarah RABIA who all the time helped me with French bureaucracy. To Solene de MEZERAC who was all the time patient and kind with my French bad pronunciations. I learned a lot of beautiful French words from you. Having such friends like three of you made my life in France much more pleasant.

To Waldemar JANKOWSKI and Guoqiang (Grant) LI who were my first colleagues at NCU. I would like deeply thank for your help and kindness at the beginning of my Ph.D thesis. I cannot forget those amazing memories that we had during the conference in Zakopane.

I would also like to record my sincere thanks to prof. Stéphane MARAIS who gave me several key comments regarding the ion conductive composite membranes. To prof. Stéphane MARAIS for your enjoyable talks, work suggestions, and good mood.

To dr hab. Joanna KUJAWA NCU prof. and dr hab. Ewa OLEWNIK-KRUSZKOWSKA NCU prof. for your positive moods, advices, and sharing your visions. I enjoyed all the time for having fruitful discussions with you and having your guidance for my future carrier. Thank you very much.

To my teammates at PBS: Guillaume, Sebastien, Etienne, Di, Huu Van, Juan, Morgane, Koceila, Olive, Delphine, Klara, Nicolas, Maiwenn, Alina, and Katia. I am sure that the most unforgettable memories that we had together were “gouter” parties every Friday afternoon.

To all members of chair at PBS including dr. Corinne CHAPPEY, dr. Virginie DULONG, dr. Nadege FOLLAIN, dr. Louise HESPEL, dr. Pascal THEBAULT, prof. Laurent LEBRUN, prof. Didier LE CERF, it was my pleasure to work with you in the same research unit. To dr. Corinne CHAPPEY for all the talks that we had about history and food recipes during the lunch time and “gouter”.

To the members of Department of Physical Chemistry and Physiochemistry of Polymers at the NCU in Toruń: dr. Piotr ADAMCZAK, dr. Magdalena GIERSZEWSKA, dr. Katarzyna KNOZOWSKA, dr. Marta GLODEK, prof. Stanisław KOTER, dr. Izabela KOTER, dr hab. Jacek NOWACZYK NCU prof., dr hab. Piotr SZCZEPAŃSKI NCU prof. for all the comments, suggestions, and fruitful discussions.

Acknowledgements

To all my friends: Arash, Saeed, Babak, Jaber, Parastoo, Zufa, Omid, Nazila, Masood, Frahnaz, Mostafa, Mahzad, Hossam, Steve, Mehrdad, Spozhmai, Marvan, Anis, Soleiman, Jahangir, Guillaume, Kevin, Ansoor, Gibi, Geo, Sonia, Mansura, Ahmad, Zahra, Domenika, Natalia, Sarah, Irem, Vipol, Dhiraj, Simran, Samaneh, Ebru, Min Sung, Yassin, Delaram, Saman, Elize, Hassan, Zinat, Mahboubeh, Lisa, Alireza, and Mohammad reza. For your moral support, sharing happiness and sadness together, and friendly discussions and activities (shopping, traveling, volleyball, basketball). It was my pleasure to meet you in my life.

This PhD thesis (HERMES project) was a joint project between NCU and URN and it was financially supported by NCU and Normandy region.

The last but not the least is to my family: my mother, father, sister, brother in law, and my wife. I know that words are not able to explain my feelings to you, but I like to say that I am truly grateful for having you in my life. Thank you for everything.

List of Figures

List of Figures

List of Tables

Abbreviations

[Ac]	acetate
[Ala]	alaninate
[APMIM][Br]-GO	1-(3-aminopropyl)-3-methylimidazolium bromide functionalized graphene oxide
[BAIM][TFSI]	2-butylaminoimidazolinium bis(trifluoromethylsulfonyl)imide
[BIM]	1-(*n*-butyl)imidazolium
[BIM][TFSI]	1-butylimidazolium bis(trifluoromethylsulfonyl)imide
[BUPH]	di-*n*-butyl phosphate
[DCA]	dicyanamide
[DEPA]	3-hydroxy-N, N-dimethylpropan-1-aminium
[DETA]	2-hydroxy-N, N-dimethylethanaminium
[EHPH]	bis(2-ethylhexyl)phosphate
[EIM][TFSI]	1-ethylimidazolium bis(trifluoromethylsulfonyl)imide
[Gly]	glycinate
[H_2PO_4]	dihydrogen phosphate
[HMIM][Cl]	1-hexyl-3-methylimidazolium chloride
[HS]	hydrogen sulfate
[MBuIM][H_2PO_4]	2,3-dimethyl-1-butyl imidazolium dihydrogen phosphate
[MIM]	1-methylimidazolium
[MIM][TFS]	1-methylimidazolium trifluoromethanesulfonate
[MIM][TFSI]	1-methylimidazolium bis(trifluoromethylsulfonyl)imide
[MTIM][Cl]	1-methyl-3-(3-trimethoxysilylpropyl)imidazolium chloride
[MTOA][Cl]	methyltrioctil ammonium chloride
[OMIM][PF_6]	1-octyl-3-methylimidazolium hexafluorophosphate

[PIM][TFSI]	1-propylimidazolium bis(trifluoromethylsulfonyl)imide
[Pro]	prolinate
[Ser]	serinate
[SMIM]	1-(4-sulfobutyl)-3-methylimidazolium
[SMIM][HS]	1-(4-sulfobutyl)-3-methylimidazolium hydrogen sulfate
[SMIM][TFS]	1-(4-sulfobutyl)-3-methylimidazolium trifluoromethanesulfonate
[SMIM][TFSI]	1-(4-sulfobutyl)-3-methylimidazolium bis(trifluoromethanesulfonyl)imide)
[TFA]	trifluoroacetate
[TFS]	trifluoromethanesulfonate
[TFSI]	bis(trifluoromethylsulfonyl)imide
[TS]	tosylate
[VBIM][Br]	1-vinyl-3-butylimidazolium bromide
[VBIM][NTf_2]	1-vinyl-3-butylimidazolium bis(trifluoromethylsulfonyl)imide
[VMIM][I]	1-vinyl-3-methylimidazolium iodide
AFC	alkaline fuel cell
AFM	atomic force microscopy
A-IL	aprotic ionic liquid
ATR	attenuated total reflection
B-IL	basic ionic liquid
Bio-IL	bio-ionic liquid
BrPAEK	brominated poly(arylene ether ketone)
CA	contact angle
CAB	cellulose acetate butyrate
CAP	cellulose acetate propionate

CCM	catalyst coated membrane
C-IL	chiral ionic liquid
COD_R	chemical organic demand removal
DMAc	dimethylacetamide
DMF	dimethylformamide
DMFC	direct methanol fuel cell
DMSO	dimethyl sulfoxide
DSC	differential scanning calorimetry
EDX	energy-dispersive X-ray spectroscopy
E-IL	energetic ionic liquid
EIS	electrochemical impedance spectroscope
FD	freeze drying
FFC	field flow channel
F-IL	functionalized IL
FTIR	Fourier transform infrared spectroscopy
GDL	gas diffusion layer
GO	graphene oxide
HT-PEMFC	high temperature polymer electrolyte membrane fuel cell
IEC	ion exchange capacity
IL	ionic liquid
LbLSA	layer by layer self-assembly
MCFC	molten carbonate fuel cell
MEA	membrane electrode assembly
MFC	microbial fuel cell

M-IL	metallic ionic liquid
NF	nanofiltration
N-IL	neutral ionic liquid
NMP	*N, N*-methylpyrrolidone
NMR	nuclear magnetic resonance spectroscopy
NP	nanoparticle
OCP	open circuit potential
OSW	office of saline water
PA	phosphoric acid
PA6	polyamide-6
PAFC	phosphoric acid fuel cell
PEG	polyethylene glycol
PEM	polymer electrolyte membrane
PEMFC	polymer electrolyte membrane fuel cell
PFSP	perfluoro-sulfonated polymers
P-IL	poly (ionic) liquid
Pr-IL	protic ionic liquid
PSAN	poly(styrene/acrylonitrile)
PSSA	poly(styrenesulfonic acid)
PU	polyurethane
PVC	poly(vinyl chloride)
PVP	poly(vinyl pyrrolidone)
QAPSU	quaternary ammonium functionalized polysulfone
QPSU	quaternary polysulfone

RH	relative humidity
RT-IL	room temperature ionic liquid
SBA-15	Santa Barbara amorphous-15
SC	spin-coating
SEM	scanning electron microscopy
S-IL	supported ionic liquid
SILM	supported ionic liquid membrane
SOFC	solid oxide fuel cell
SPEEK	sulfonated poly(ether ether ketone)
SPEK	sulfonated poly(ether ketone)
SPI	sulfonated polyimide
SPM	scanning probe microscopy
SPS	sulfonated polysulfone
SPS-IL	switchable polarity solvent ionic liquid
TGA	thermogravimetric analysis
TMSCl	chlorotrimethylsilane
TNT	titanate nanotube
TS-IL	task specific ionic liquid
VAF	vacuum-assisted flocculation
WU	water uptake

Symbols

A	membrane surface area [cm^2]
A_w	surface area in wet state [cm^2]
A_0	surface area in dry state [cm^2]

C_f	feed concentration [mol·L^{-1}]
C_p	permeate concentration [mol·L^{-1}]
d	density [g·mL^{-1}]
E_a	activation energy [J·mol^{-1}]
L	membrane thickness [µm]
L_p	hydrodynamic permeability [L·m^{-2}·h^{-1}·bar^{-1}]
Mw	molecular weight [g·mol^{-1}]
N_p	number of points in a given area [-]
r	roughness factor [-]
R	retention [-]
R	universal gas constant [8.314 J·mol^{-1}·K^{-1}]
R_a	average roughness [nm]
r_p	pore radius [µm]
R_q	root mean square [nm]
t	thickness in wet state [µm]
T	absolute temperature [K]
t_0	thickness in dry state [µm]
$T_{5\%}$	temperature of 5% weight loss [°C]
$T_{10\%}$	temperature of 10% weight loss [°C]
T_{deg}	degradation temperature [°C]
T_g	glass transition temperature [°C]
V	volume of membrane in wet state [cm^3]
V_0	volume of membrane in dry state [cm^3]
W_{dry}	membrane weight at dry state [mg]

W_{wet}	membrane weight at wet state [mg]
Z_{ave}	average height value [nm]
Z_i	current height value [nm]

Greek symbols

γ^{lg}	interface tension of liquid/gas interface [$mN \cdot m^{-1}$]
γ^{sg}	interface tension of solid/gas interface [$mN \cdot m^{-1}$]
γ^{sl}	interface tension of solid/liquid interface [$mN \cdot m^{-1}$]
Δp	applied pressure [Pa]
Δt	time of filtration [h]
ΔV	volume of permeate [L]
θ_Y	contact angle [°]
ρ_{water}	water density [$g \cdot mL^{-1}$]
σ	ionic conductivity [$S \cdot cm^{-1}$]
σ	surface tension of air/liquid interface [$N \cdot m^{-1}$]
σ_0	pre-exponential factor [$S \cdot cm^{-1}$]
φ	horizontal projection area fraction of the solid/liquid interface [-]

Introduction

Introduction

Energy generation is one of the most serious challenges for mankind. Indeed, energy is the fuel of life and human daily routine is entirely dependent on it as the life without energy is almost impossible. For this reason, governments all over the world started to search stable resources of energy for the survival and development of humanity. Wood, coal, oil, natural gas, and nuclear energy are the major classical or nonrenewable sources of energy. Nonrenewable sources help mankind to develop its life, however, they cause countless adverse environmental and health problems [1,2]. Air contamination, water pollution, water scarcity, acid rains, and ozone depletion are some of the most serious environmental problems caused by using classical resources of energy. Moreover, health problems (such as cardiovascular diseases, various types of cancers, and respiratory problems) should not be ignored. However, the most dangerous problem for human and our future generations is the global warming owing to the emission of greenhouse gasses including carbon monoxide (CO), carbon dioxide (CO_2), and methane [3,4]. As a result, efforts for finding new alternatives for sustainable energy sources increase continuously. Up to now, a wide range of renewable energy sources have been developed and already utilized, such as solar, wind, tidal, hydropower, geothermal, and fuel cell technology [5,6]. Among them fuel cells attract a lot of attention of researchers and governors as the sustainable source of energy production [7-10].

Fuel cell is an electrochemical device which is able to generate electrical energy from the chemical reaction. There are several types of fuel cells, namely alkaline fuel cell, direct methanol fuel cell, phosphoric acid fuel cell, molten carbonate fuel cell, solid oxide fuel cell, and polymer electrolyte membrane fuel cell (PEMFC). Each mentioned fuel cell type has its own characteristics depending on the electrolyte type, operation conditions, and technological elements. PEMFC is the most common type of fuel cell due to its remarkable properties, including quick start up, acceptable efficiency, and good power density. Hydrogen and oxygen are consumed in PEMFC as the fuel and oxidizer, respectively, and water, heat, and electricity are the only products of the reaction. Consequently, PEMFC is considered as a source of green energy. Each PEMFC consists of different parts, such as polymer electrolyte membrane (PEM), gas diffusion layer, catalyst, field flow channel, current collector, catalyst, end plate, and bolts. The most vital part is PEM [7,11-13].

In fact, PEM has the responsibility of the conduction of protons from anode to cathode to ensure a desirable proton conductivity. Nafion® is the most commonly used polymer. This polymer has some remarkable features, including great proton conductivity, tunable mechanical, thermal and chemical stability. Nonetheless, the use of Nafion® is not possible in wide range of temperatures as at the temperatures higher than 80 °C, the proton conductivity is significantly reduced because of the water evaporation. Therefore, protons are unable to be transported from anodic compartment to the cathodic one. Moreover, for the PEMFC operation at low temperature (< 80 °C), the use of very high purity hydrogen is

essential, otherwise, the catalyst will be poisoned by CO [14]. Besides, by rising the operating temperature, the rate of reaction kinetic increases. Thus, PEMFC operating at high temperature (≥ 80 °C) is favorable. The PEMFC able to be used at elevated temperature is called high temperature PEMFC (HT-PEMFC). In HT-PEMFC the presence of water for proton conducting is not necessary and, thus, its performance is independent on humidity and allows using less pure hydrogen as the fuel that is more economically interesting. Besides, some other fuels (such as biogas, natural gas, and methanol) can be also used. In addition, higher temperature will promote the reaction between hydrogen and oxygen [7,12,15-18].

Currently, ionic liquids (ILs) are widely used in different applications (e.g. metal extraction, membrane separation process, greenhouse gas recovery, industrial waste recycling, and hydrogen purification) [19,20]. These organic salts are usually liquid at the temperature lower than 100 °C owing to the fact that they contain organic cations and organic or inorganic anions without no strong interactions between them. Nowadays, a number of ILs (i.e. protic ionic liquids, task specific ionic liquids, basic ionic liquids, neutral ionic liquids, switchable polarity solvent ILs, energetic ionic liquids, bio ionic liquids, supported ionic liquids, metallic ionic liquids, chiral ionic liquids, and poly ionic liquids) is synthesized owing to the excellent features, including good thermal and chemical stability, high proton conductivity, non-flammability, low vapor pressure, low toxicity, and great electrochemical stability. Thus, ILs can be used as a conductive medium in PEM. Generally, owing to the presence of a mobile hydrogen ion in structure of protic ionic liquids, their use in HT-PEMFC is more common as they are able to transport easily protons through the polymer film at high temperature. Therefore, the use of such PEM at low hydration level is possible. However, IL-based PEM still suffers from the IL leaching during the process. Actually, the proton conductivity and efficiency of modified PEM decreases over the time because of the IL leaching. Some methods were proposed to overcome the IL leaching, namely crosslinking, the addition of nanoparticles (NPs), and the use of inorganic or organic fillers [7,12,21-24].

The aim of this PhD thesis was the synthesis of the thermally stable and conductive ILs and use them as an additive to prepare proton conductive membranes for PEMFC application at elevated temperature. Various ILs containing different cations and anions were synthesized and characterized. Moreover, three polymers (i.e. cellulose acetate propionate, cellulose acetate butyrate, and polyamide-6) were utilized as the polymer matrix. The physical, chemical, electrochemical, transport, morphological, and thermal properties of fabricated membranes were investigated.

This PhD thesis is a joint project between Nicolaus Copernicus University in Toruń (NCU) (Poland) and University of Rouen Normandie (URN) (France). As a result, some parts of this project were done at the Faculty of Chemistry of NCU (from 01.10.2020 to 06.04.2022 and from 07.10.2023 to 06.04.2024) and some of them were carried out in the Polymers, Biopolymers, Surfaces (PBS) research

unit (UMR CNRS 6270) at URN (from 07.04.2022 to 06.10.2023). Furthermore, the financial support for this project was provided by NCU, Normandy region (HERMES project, 2020–2023), and the Graduate School of research XL-Chem (ANR-18-EURE-0020 XL-Chem).

The present manuscript is divided into five chapters. The first chapter is “State of the Art” part presenting the energy generation, fuel cell, and the use of IL-based composite membrane for PEMFC application.

The “Materials and Characterization Methods” chapter is devoted to the used chemical materials (e.g. polymers, solvents, ILs, and other chemical reagents), the techniques used for the membrane preparation, and IL synthesis. Also, the analyses and characterization methods are described.

The third chapter “Ionic Liquids: Synthesis and Characterization” gives information about synthesis of novel protic ionic liquids by acid-base neutralization reaction. Several new imidazolium- and hydroxylammonium-based ionic liquids were synthesized and the influence of anion and cation nature on their thermal stability and ionic conductivity was investigated and correlated with the IL structure.

The fourth chapter “Polyamide 6-based Membrane” focuses on the preparation of porous polyamide-6 membrane by nonsolvent-induced phase separation technique. In this chapter, the physical, morphological, and transport properties of polyamide-6 membranes with different gelation time are evaluated.

The fifth chapter “Ionic Liquid-based Membranes” is dedicated to fabrication of IL-based membranes by a phase inversion method. In this chapter, the chemical, physical, thermal, and mechanical properties of fabricated composite membrane are presented and discussed. Also, the ionic conductivity of IL-based membranes at elevated temperature and under anhydrous conditions is analyzed.

The “General Conclusion and Prospects” section is devoted to the summary of the obtained results and provides some suggestions for the future study.

Chapter 1. State of the Art

1.1. Fuel Cells

Nowadays, the energy generation is one of the most vital concerns of human life [25-27]. The energy is considered as the fuel of the life. Thus, governors and politicians have already invested huge budget to find a source of sustainable energy production [8,28]. Up to now, the majority of energy all over the world has been generated from nonrenewable sources, including wood, coal, oil, natural gas, and nuclear energy. However, their use has negative influence on our ecosystem, namely air contamination, water pollution, water scarcity, acid rain, and ozone depletion [8,9,11,28]. Equally important is the fact that they can cause major health problems, including cardiovascular diseases, various types of cancers, and respiratory problems [9-11,29,30]. In addition, global warming owing to the emission of greenhouse gases (such as CO, CO_2, and methane), thus accelerating all these negative effects [8,11,28,29]. Therefore, the necessity of renewable alternative sources of energy generation becomes urgent. Generally, there are different ways to generate green energy (for example, solar, wind, tidal, biomass, and hydropower) [10,28,29]. One of the promising ways to generate green energy is fuel cells technology as the only by-product is water [7,9,11,31].

Fuel cell technology attracts attention owing to the possibility to convert chemical energy of reaction into electricity. In 1839, a Welsh scientist William Robert Grove could accidentally prepare the first fuel cell by reversing the electrolysis of water [32,33]. His fuel cell, also known as the "Grove cell", contained two platinum electrodes immersed into the dilute sulfuric acid electrolyte and sealed by two tubes containing oxygen and hydrogen and electrodes. He observed that water was produced and its level rose [32,33]. Moreover, Grove cell was able to generate small electrical current (12 A and 1.8 V). He could also combine several sets of cells (he named such a system as “gas battery”) and increase the electrical current [32-34].

The basic principles of the chemistry and electricity of the fuel cell were discussed [32]. Different theories were proposed (e.g. contact and chemical theories) for explaining the process and over the years the understanding of fuel cell technology was improved and various types of fuel cells were discovered [32-35]. Today, there are various types of fuel cells with different electrolytes, operating conditions, design and technology parameters, namely molten carbonate fuel cell (MCFC), solid oxide fuel cell (SOFC), phosphoric acid fuel cell (PAFC), direct methanol fuel cell (DMFC), alkaline fuel cell (AFC), and PEMFC (Fig. 1.1).

1.1.1. Polymer Electrolyte Membrane Fuel Cells

Among the different types of fuel cells, the widespread use of PEMFCs in both laboratory and industry scales can be explained by their remarkable features, such as great power density, good efficiency, and quick and easy startup [12,36,37]. Furthermore, PEMFCs are utilized in different fields including

automotive industry, portable electronic devices, and power generation (backup source) [13,38]. There are some car companies (such as Honda, Hyundai, and Toyota) which are introduced PEMFCs on the commercial scale [39]. These cars are also known as hydrogen-based cars or zero emission cars [39,40]. The interest of the production of such cars increases as they are safe and environmentally friendly. Indeed, PEMFC has high potential to be employed in drones, military, and space science since it is able to work at the wide temperature range (low, moderate, and high) and it has also quick dynamic response [41]. By providing pure hydrogen as the fuel and oxygen as the oxidizer agent, electricity, water, and heat are generated (Fig. 1.2).

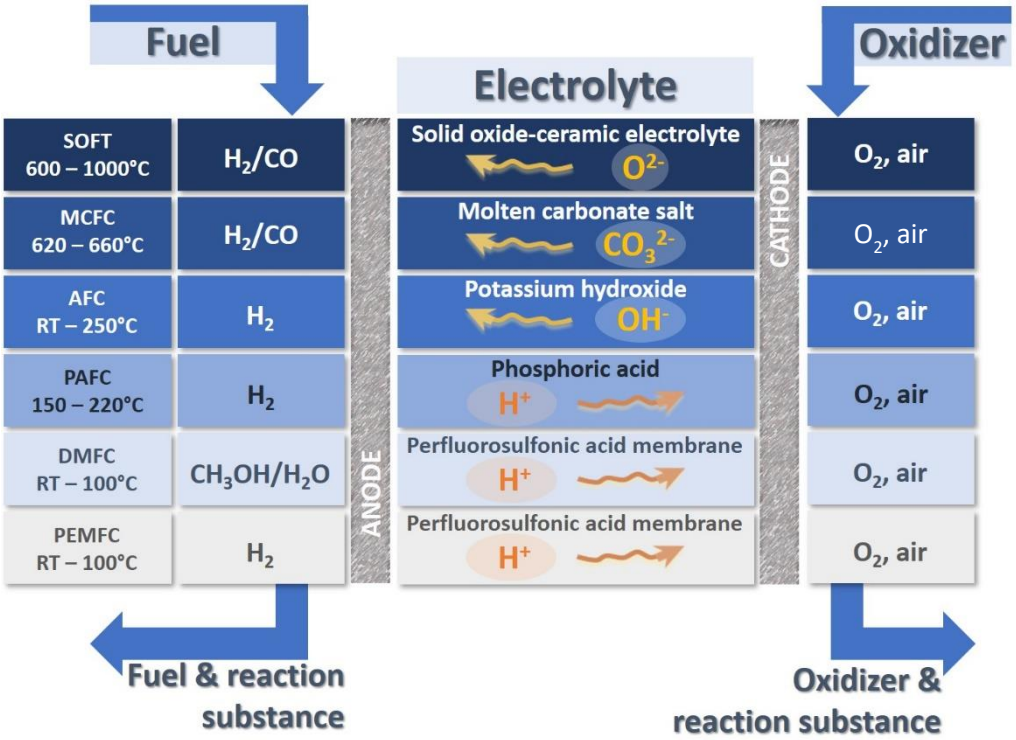

Figure 1.1. Schematic demonstration of different types of fuel cells (From "A Review on Ionic Liquids-Based Membranes for Middle and High Temperature Polymer Electrolyte Membrane Fuel Cells (PEM FCs)" by Ebrahimi, M.; Kujawski, W.; Fatyeyeva, K.; Kujawa, J., 2021, International journal of molecular sciences, 22, 5430, under the license CC BY 4.0) [7].

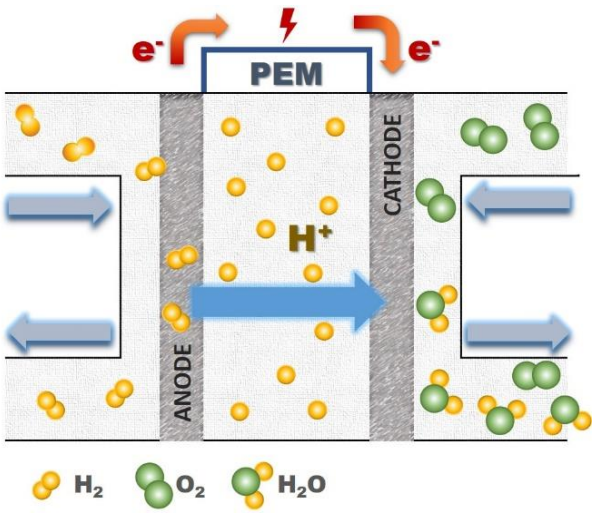

Figure 1.2. Schematic representation of PEMFC (From "A Review on Ionic Liquids-Based Membranes for Middle and High Temperature Polymer Electrolyte Membrane Fuel Cells (PEM FCs)" by Ebrahimi, M.; Kujawski, W.; Fatyeyeva, K.; Kujawa, J., 2021, International journal of molecular sciences, 22, 5430, under the license CC BY 4.0) [7].

Each hydrogen molecule at anode splits into two hydrogen ions (protons) and electrons owing to the presence of catalyst which is typically platinum (Pt) since it has better catalytic performance, high stability to work in different operating conditions, and also great resistance against corrosion [7,13,42]. The hydrogen ions pass through the membrane to participate in oxygen reduction reaction and electrons enter to electrical cycle to generate electricity and arrive to cathode [7,12]. The hydrogen oxidation reaction (i.e. $H_2 \rightarrow 2H^+ + 2e^-$) does not need to absorb or release energy [43]:

$$H_2 \rightarrow 2H^+ + 2e^- \quad (1.1)$$

During the oxygen reduction reaction at the cathode (i.e. $0.5O_2 + 2H^+ + 2e^- \rightarrow H_2O$), water is produced. This reduction reaction is producing heat and is considered as the exothermic reaction [43]:

$$0.5O_2 + 2H^+ + 2e^- \rightarrow H_2O \quad (1.2)$$

By combining these two reactions, the overall reaction (i.e. $H_2 + 0.5O_2 \rightarrow H_2O$) is noted to be an exothermic reaction [43]:

$$H_2 + 0.5O_2 \rightarrow H_2O \quad (1.3)$$

Unlike internal combustion engines, PEMFC is a very promising candidate to generate energy as the sustainable energy production source [7,44]. Usually, each PEMFC has various parts, such as PEM, gas diffusion layer (GDL), field flow channel (FFC), catalyst, current collector, gasket, end plate, and fittings (Fig. 1.3). Each component has its own requirements [45]. Membrane electrode assembly (MEA) (PEM with electrodes and catalyst layers) is known to be the main body of PEMFC [46]. Three-layer, five-layer, and seven-layer MEA can be used [12,46]. In three-layer MEA, PEM (which is also called catalyst coated membrane (CCM)) is sandwiched between anodic and cathodic catalyst layers. For preparing five-layer MEA, CCM should be inserted between two GDLs [12]. In case of seven-layer MEA, five-layers MEA should be placed between two gaskets.

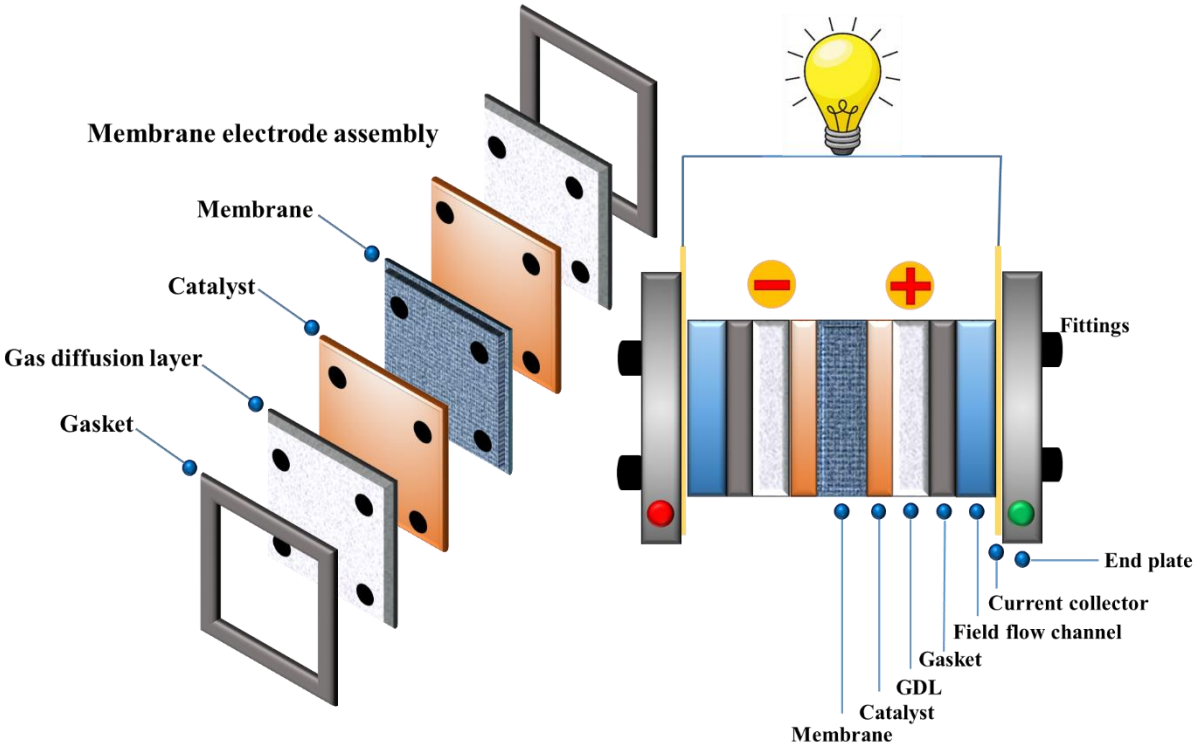

Figure 1.3. Schematic illustration of MEA in a single cell PEMFC.

1.2. Polymer Electrolyte Membrane

The most vital part of each PEMFC is PEM (Fig. 1.2). A high ion conduction of PEM is an essential matter. In general, there are two main mechanisms of proton conduction through the PEM − vehicle and Grotthuss mechanisms [47-49]. Humidity and operating temperature are two criteria parameters influencing the proton conduction mechanism. In case of vehicle mechanism, the proton conduction takes place at low and moderate temperature range under fully hydrated conditions [50]. The presence of water molecules is necessary as they are responsible for protons transporting through the membrane (Fig. 1.4a). However, by

rising the operating temperature, the water molecules begin to evaporate, provoking a significant decrease of proton conductivity [18]. The dominant mechanism of proton conduction at high operating temperature and non-humid conditions is the Grotthuss mechanism (Fig. 1.4b) [18,51,52]. In fact, in this case water is not responsible for ions transporting because the protons are jumping from one to another reactive center. This mechanism is also known as the proton hopping mechanism [51,52].

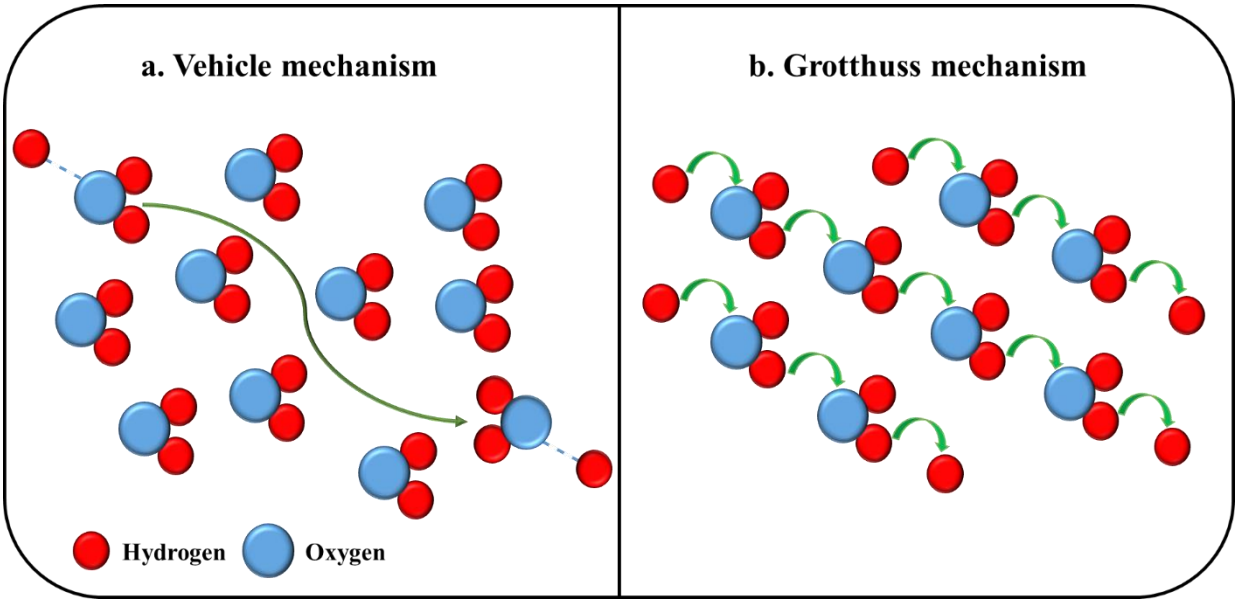

Figure 1.4. Schematic illustration of different proton transport mechanisms.

Up to now, perfluoro-sulfonated polymers (PFSP) (such as Nafion®, Flemion®, and Hyflon®) are the most common polymers used for the PEM fabrication since they possess good mechanical resistance, high proton conductivity, and excellent chemical and electrochemical stability [53]. Despite the fact that PFSPs, particularly Nafion®, show good proton conductivity at low temperature, their performance is extremely dependent on humidity (hydration level) as the proton conduction is carried out due to the vehicle mechanism (Fig. 1.4a) [53,54]. Therefore, at elevated temperature (over 80 °C), the proton conductivity of Nafion® membrane decreases noticeably owing to the water evaporation. Indeed, Nafion® as PEM has a good performance in the temperature range between 60 and 80 °C [53,54]. Moreover, owing to the low glass transition temperature of Nafion® (T_{g1} ~ 130 °C and T_{g2} ~ 240 °C), the mechanical stability of this polymer is reduced at elevated temperature [54,55].

It is noted that working at high temperature under a non-humid condition has several advantages – the fast kinetics of the chemical reactions, the possibility to use hydrogen with lower purity, and utilization of other gases (that makes PEMFC operation cheaper) [12]. Furthermore, high temperature utilization allows avoiding the catalyst poisoning by CO gas [7,12].

The PEMFC used at high temperature is called high temperature PEMFC (HT-PEMFC) and its performance does not depend on the humidity level [7]. In fact, HT-PEMFC can be used in a wide range of temperature and relative humidity (RH). A numerous research studies were performed to find possible alternatives for Nafion® [17]. Several ways were proposed to improve the proton conductivity of PEM at high temperatures, namely modifying the Nafion® membrane by addition of different fillers, the use of sulfonated polymers (e.g. sulfonated poly (ether ketone) (SPEK), sulfonated poly (ether ether ketone) (SPEEK), sulfonated polyimide (SPI), and sulfonated poly sulfone (SPS)) [7,12,17,56-65]. Even if such membranes showed acceptable improvement regarding proton conductivity, they still need humidity for proton transporting through PEM. Therefore, to prepare membranes with high proton conductivity at elevated temperature under aqueous free environment and good mechanical, thermal, chemical, and electrochemical stabilities, the use of inorganic compounds, NPs, phosphoric acid (PA), and ILs can be proposed [7,12]. A comparative summary of the mentioned methods to improve PEM performance for HT-PEMFC application is presented in Table 1.1.

1.2.1. Nanoparticles-based Nafion® Membranes

One of the approaches to improve the proton conductivity of Nafion®-based membranes is an addition of NPs because they can provide a number of channels and networks for the proton transferring through the membrane [60,66]. It is worth noting that introducing NPs into the Nafion® matrix can also improve the membrane thermal stability [60]. Research findings reveal that the addition of NPs can diminish the water evaporation at the temperature higher than 80 °C [66]. A wide range of NPs has been used to prepare PEM, including titanium dioxide (TiO_2), graphene oxide (GO), silicon dioxide (SiO_2), and zirconium dioxide (ZrO_2) [59-61,66]. Amjadi and coworkers [60] introduced TiO_2 nanoparticles into Nafion® in order to preparing composite membrane for HT-PEMFC application. They fabricated TiO_2/Nafion® composite membrane *via in-situ* sol–gel and casting techniques. The results showed that the water uptake (WU) of TiO_2/Nafion® composite membrane with 3 wt.% of TiO_2 was almost 50% higher than that of unmodified membrane. Differential scanning calorimetry (DSC) results also demonstrated that the addition of TiO_2 particles led to the T_g rising – in case of the composite membrane with 10 wt.% of TiO_2 it was 25 °C higher than that of the pure Nafion® membrane. Despite the fact that the pure Nafion® membrane showed a higher current density (500 $mA \cdot cm^{-2}$) than the current density of composite samples (300 $mA \cdot cm^{-2}$) at 70 °C and 0.4 V, the TiO_2/Nafion® composite revealed higher current density at 110 °C. In another research, Cozzy et al. [67] incorporated TiO_2 particles functionalized by propylsulfonic acid into the Nafion® membrane. The membrane proton conductivity was evaluated from 40 to 140 °C. The results revealed that the composite membrane containing 10 wt.% of propylsulfonic-functionalized TiO_2 showed a better proton conductivity of 0.08 $S \cdot cm^{-1}$ at 140 °C than that of the pure Nafion® membrane (0.039 $S \cdot cm^{-1}$). Besides, the

pure Nafion® membrane showed the current density of 202 $mA \cdot cm^{-2}$ at 110 °C and 0.2 V while the functionalized TiO_2/Nafion® membrane demonstrated a higher current density of 316 $mA \cdot cm^{-2}$ at the same operating condition. Amjadi and coworkers [61] incorporated SiO_2 particles into commercial Nafion® 117 *via* sol–gel method in order to use this composite membrane in HT-PEMFC. It was found that WU of the modified SiO_2/Nafion® 117 membrane containing 7 wt.% SiO_2 was 30% higher than that of unmodified Nafion® 117. Besides, the addition of SiO_2 particles to the Nafion® 117 membrane enhanced the T_g value of composite membranes in comparison with the pure membrane. It was observed that the proton conductivity of pristine membrane at 23 °C and 30 ± 5% RH (11.21 $mS \cdot cm^{-1}$) was higher than that of composite membranes with different doping levels. However, the fuel cell performance of SiO_2/Nafion® 117 composite membranes was improved as compared with the pristine membrane by increasing the temperature up to 110 °C. In another research, Ibrahim et al. [66] prepared composite membrane based on GO and Nafion® with different thicknesses (30, 40, and 50 μm) by solution casting method. It was found that the GO/Nafion® composite membrane showed better mechanical stability than the stability of pure Nafion® membrane (higher stress at the same strain). Moreover, the composite membranes demonstrated higher WU than that of pure membranes and the highest value was noted for GO/Nafion® membrane with the thickness of 30 μm (32.86 ± 3.62 %). Furthermore, the composite membrane showed better fuel cell performance as compared with unmodified Nafion® membranes – the maximum value of power density and current density (0.7 $W \cdot cm^{-2}$ and 1.6 $A \cdot cm^{-2}$, respectively) was observed for GO/Nafion® composite membrane with the thickness of 30 μm.

It can be seen that the addition of NPs to the Nafion® membrane is a promising method to prepare the composite PEM for HT-PEMFC because NPs can enhance WU of composite membranes owing to the filler hydrophilic character and possible physical and chemical interactions between NPs and Nafion® [12,60,61]. Moreover, NPs can improve the proton conductivity of composite membranes since they can introduce new conductive networks in the membrane [59-61,67]. Also, such modified membranes show good fuel cell performance and proton conductivity under the humid condition [12,59,66]. However, owing to the presence of humidity, the water evaporation is the main drawback causing ionic conductivity reduction at elevated temperatures [12,59].

1.2.2. Membranes Containing Phosphoric Acid (PA)

Another approach to fabricate a thermally stable PEM for HT-PEMFC with high conductivity is introducing of PA [12,68]. PA can transport protons through the membrane at the temperature higher than 80 °C since it has low volatility and is stable at elevated temperatures [68,69]. However, the addition of PA may decrease the PEM mechanical stability [69]. Hence, the balance between proton conductivity and mechanical stability should be adjusted. The PA possible leaching from PEM should be also taken into

account because it reduces the proton conductivity [12]. Li and coworkers [70] prepared new composite membranes containing nitrogen heterocycle (NH)/PA/brominated poly(arylene ether ketone) (BrPAEK). At the beginning, NH/BrPAEK membrane was first prepared by phase inversion technique and then the membrane sample was immersed into the PA solution. The conductivity measurement performed in the temperature range from 100 to 170 °C revealed that the modified NH/PA/BrPAEK membrane showed a conductivity value of 0.091 $S \cdot cm^{-1}$ at 170 °C. Moreover, the composite membrane demonstrated high value of PA uptake (53 – 339%). Moreover, it was observed that the PA leaching decreased by an addition of nitrogen heterocyclic compound. In another work, Bai et al. [71] prepared composite membrane containing poly(1-vinylimidazole)/PA/polysulfone (PS) by phase inversion method. Initially, poly(1-vinylimidazole) was grafted onto PS and the membrane was soaked into the PA solution. It was found that the grafted poly(1-vinylimidazole) provided a number of sites for PA adsorption. The resultant poly(1-vinylimidazole)/PA/PS composite film is characterized by acceptable proton conductivity of 127 $mS \cdot cm^{-1}$ at 160 °C. Furthermore, this membrane showed good mechanical tensile strength of 7.94 MPa. Che et al. [72] fabricated composite membrane based on SPEEK/PA/polyurethane (PU) by phase inversion method. Pure PU was charged by SPEEK and then the membrane was prepared. The obtained SPEEK/PU membrane was submerged in PA solution. The resultant SPEEK/PA/PU composite membrane showed better thermal stability (180 °C) than PA/PU membrane (110 °C). The SPEEK/PA/PU composite membrane revealed acceptable tensile strength of 2.7 MPa even though pure PU, SPEEK, SPEEK/PU membranes showed better mechanical properties. Moreover, the resultant composite polymer membrane demonstrated a proton conductivity of 0.3 $mS \cdot cm^{-1}$ at 160 °C under dry conditions.

It was shown that the PA addition can improve the performance of non-fluorinated-based membranes at high temperature and non-humid condition, but this type of membrane suffers from mechanical stability reduction [12,73]. Furthermore, the PA leaching is the main drawback of this method. In order to overcome these limitations, it was proposed to mix the polymers or to add fillers or to prepare a cross-linked membrane [12].

1.2.3. Inorganic Compounds/Non-fluorinated-based Membrane

Another way to improve the physical and chemical properties of non-fluorinated-based PEM at elevated temperatures is utilizing of inorganic particles [7]. Such method increases the number of functional networks resulting in the proton conductivity rising [12,74]. Furthermore, such functional networks can also increase the PA retention ability owing to the chemical interactions between PA and inorganic particles [12,75]. Kuo and Lin investigated the influence of the presence of two different mesoporous silicates (i.e. MCM-41 and SBA-15) in polybenzimidazole (PBI) membranes [74]. The modified MCM-4/PBI and SBA-15/PBI membranes demonstrated better mechanical properties and PA retention ability than those of the

pristine PBI membrane. The highest stress at break was found for MCM-41/PBI membrane with 20 wt.% of MCM-41 (45.55 ± 2.12 MPa) while the highest Young's modulus was noted for SBA-15/PBI membrane containing 10 wt.% SBA-15 (13.73 ± 0.68 MPa). It was also found that the PA doping level increased by introducing the fillers as compared with pure PBI membrane – the maximum value (2.9 ± 0.1 g PA/g membrane) was observed for MCM-41/PBI composite membrane with 10 wt.% of MCM-41. Moreover, the best fuel cell performance was noted for MCM-41(10 wt.%)/PBI composite film with the power density of 310 $mW \cdot cm^{-2}$. In another research, Moradi and coworkers [76] prepared a new composite Fe_2TiO_5/PA/PBI membrane. The influence of Fe_2TiO_5 content on the physicochemical properties of composite membrane was evaluated. The mechanical properties of Fe_2TiO_5/PBI composite membranes before and after the PA doping were higher than those of pure PBI membrane. The highest tensile strength and Young's modulus were measured for undoped composite membrane with 4 wt.% of filler (120 MPa and 1.8 GPa, respectively). The Fe_2TiO_5/PA/PBI composite film containing 4 wt.% of nanoparticle showed the maximum proton conductivity of 78 $mS \cdot cm^{-1}$ at 180 °C. Also, this membrane revealed the best fuel cell performance with power and current density of 0.43 $W \cdot cm^2$ and 0.85 $A \cdot cm^2$ at 180 °C, respectively. Bai et al. [77] fabricated new conductive and mechanical stable membrane based on graphitic carbon nitride (CN)/PA/polyethersulfone (PES)-poly(vinyl pyrrolidone) (PVP) by phase inversion method. CN was added to the composite polymer solution *via* facile blending technique. The proton conductivity was measured for membrane samples in the temperature range from 120 to 180 °C. The results showed that introducing CN enhanced the PA doping level, thus leading to rising of the membrane proton conductivity around 36% (104 $mS \cdot cm^{-1}$ at 160 °C). The highest value of proton conductivity was observed for CN/PA/PES-PVP composite membrane containing 0.5 wt.% of CN at 180 °C. Mechanical stability of composite membrane was also improved by CN adding. The tensile strength of the composite membrane increased by approximately 60% in comparison with unmodified PES-PVP membrane owing to strengthening of interactions between CN and polymers. Moreover, the composite membrane showed a great power density of 512 $mW \cdot cm^{-2}$ at 160 °C.

The incorporation of inorganic compounds allows increasing the acid retention ability owing to the physical interactions between filler and acid [74,77]. Also, inorganic particles ensure a number of networks, thus, improving the proton conductivity. Nonetheless, the addition of large amount of inorganic particles can provoke the appearance of some aggregations [76,77]. These formed clusters have negative effect on transferring the protons through the PEM and, as the consequence, a decrease of proton conductivity is noted [12,76,77].

Table 1.1. Summary information related to the performance of composite membranes elaborated by different techniques.

Modification method	Membrane composition	Max. proton conductivity ($mS \cdot cm^{-1}$)	Operating temperature (°C)	Observations	Ref.
Modification of Nafion® membranes with NPs	TiO_2/Nafion®	2.11	25, 70, and 110	Composite membranes were fabricated by *in-situ* sol–gel and casting methods. The WU value of composite membrane was 50% higher than that of pure Nafion® membrane. Addition of TiO_2 resulted in increasing thermal stability of composite membrane as compared with the pure one. Although pure membrane showed higher current density at 70 °C as compared to composite samples, at 110 °C an opposite behavior was observed.	[60]
	TiO_2-propylsulfonic acid/Nafion®	80	40 to 140	The composite membrane showed higher proton conductivity than the conductivity of pure Nafion® membrane at 140 °C. The composite membrane demonstrated higher current density (316 $mA \cdot cm^{-2}$ at 110 °C and 0.2 V) in comparison with the current density measured for pure membrane (202 $mA \cdot cm^{-2}$).	[67]
	SiO_2/Nafion® 117	7.11	23, 70, and 110	It was found that the WU of composite membrane was 50% higher than the WU value of the pristine membrane.	[61]

				The proton conductivity of pristine membrane at RT was higher than the conductivity of composite samples. The composite membrane showed better fuel cell performance at 110 °C as compared with the pristine membrane.	
	GO/Nafion®	–	80 to 120	Membranes with different thickness (30, 40, and 50 μm) were prepared. The composite membrane with the thickness of 30 μm showed the highest WU of 32.86 ± 3.62 % and the highest power density and current density at 100 °C and 0.25 V (0.7 $W \cdot cm^{-2}$and 1.6 $A \cdot cm^{-2}$, respectively).	[66]
The use of PA-based membranes	NH/PA/BrPAEK	91	100 to 170	The increase of the NH amount led to rising the proton conductivity. There was a linear relationship between temperature and proton conductivity. The introduction of NH led to the increasing PA retention ability. The PA uptake increased up to 339.9% by enhancing the content of NH.	[70]
	poly(1-vinylimidazole)/PA/PS	141	120 to 180	The composite membranes were prepared by a phase inversion technique.	[71]

				The presence of poly(1-vinylimidazole) increased the membrane capacity to the PA adsorption. The composite membrane demonstrated high tensile strength of 7.94 MPa.	
	SPEEK/PA/PU	0.3	80 to 160	SPEEK/PA/PU composite films showed better thermal stability as compared with PA/PU membrane. The addition of PA led to decreasing mechanical stability of resultant composite membranes.	[72]
Introduction of inorganic compounds in non-fluorinated membrane	MCM-4/PBI SBA-15/PBI	–	160	The MCM-4/PBI composite membrane showed the highest stress at break of 45.55 ± 2.12 MPa. The SBA-15/PBI membrane demonstrated the maximum value of Young's modulus (13.73 ± 0.68 MPa). The MCM-4/PBI composite membrane showed the highest power density of 310 $mW \cdot cm^{-2}$.	[74]
	Fe_2TiO_5/PBI	78	25 to 180	The Fe_2TiO_5/PBI composite membrane with 4 wt.% of filler showed the highest tensile strength and Young's modulus of 120 MPa and 1.8 GPa, respectively.	[76]

	CN/PA/PES-PVP	104	120 to 180	CN/PA/PES-PVP composite membrane containing 0.5 wt.% of CN showed the best proton conductivity at 180 °C. The mechanical stability of composite membranes was higher than that of pristine PES-PVP membrane. The composite membrane demonstrated high power density of 512 $mW \cdot cm^{-2}$ at 160 °C. [77]

1.3. Ionic Liquids: Structure and Properties

Nowadays, ILs attract great attention of researchers and industrial companies, therefore, the number of published articles and books increases [78-81]. ILs refer to salts which consist of organic cations and inorganic or organic anions [82,83]. These salts are usually in a liquid state at the temperature lower than 100 °C. The word "IL" was originally applied for molten salts, however, now is also used for salts with the melting temperature below 100 °C [22,24,83]. The main reason why ILs are usually liquid is the different size of cations (Fig. 1.5) and anions (Fig. 1.6). As a result, the physical and chemical interactions between them are usually weak [21,22,83]. ILs possess features that make them unique, such as negligible volatility, great ionic conductivity, excellent thermal resistance, low melting and glass transition temperature, non-flammability, and good chemical stability [22,24,83,84]. Hence, ILs can be considered as an excellent alternative for solvents that cause numerous environmental problems [21,83,85].

ILs are considered as "green solvents" [22]. However, their toxicity should not be ignored – it was found that ILs with different natures (such as sulphonium, phosphonium, benzimidazolium, pyrrolidinium, and pyridinium) have negative environmental influence [22,24]. Due to all these characteristics, ILs are used in various fields including gas separation, metal extraction, drug delivery, and wastewater treatment [7,22,24,86]. However, the main application of ILs is in electrochemical systems (fuel cells and batteries) owing to their high proton conductivity and thermal stability [87]. Due to these properties, they can serve as proton conductive medium instead of water in order to prevent conductivity decrease at high temperatures [7].

Various types of ILs are identified, namely task specific ionic liquids (TS-ILs), room temperature ionic liquids (RT-ILs), neutral ionic liquids (N-ILs), supported ionic liquids (S-ILs), bio-ionic liquids (bio-ILs), basic ionic liquids (B-ILs), chiral ionic liquids (C-ILs), energetic ionic liquids (E-ILs), switchable polarity solvent ILs (SPS-ILs), protic ionic liquids (Pr-ILs), aprotic ionic liquids (A-ILs), metallic ionic liquids (M-ILs), and poly ionic liquids (P-ILs) [7,22,24,88-97]. Indeed, such variety of ILs (around 10^8) is due to numerous possible combination of cation and anion. Among all types of ILs, TS-ILs are the most popular, since they may contain different functional groups in their structure which make them desirable for different applications [22,24]. These ILs are also called functionalized ILs (F-ILs) [7]. However, their synthesis can have several steps and is rather time-consuming process [7,22]. Some general information concerning various types of ILs is gathered in Table 1.2

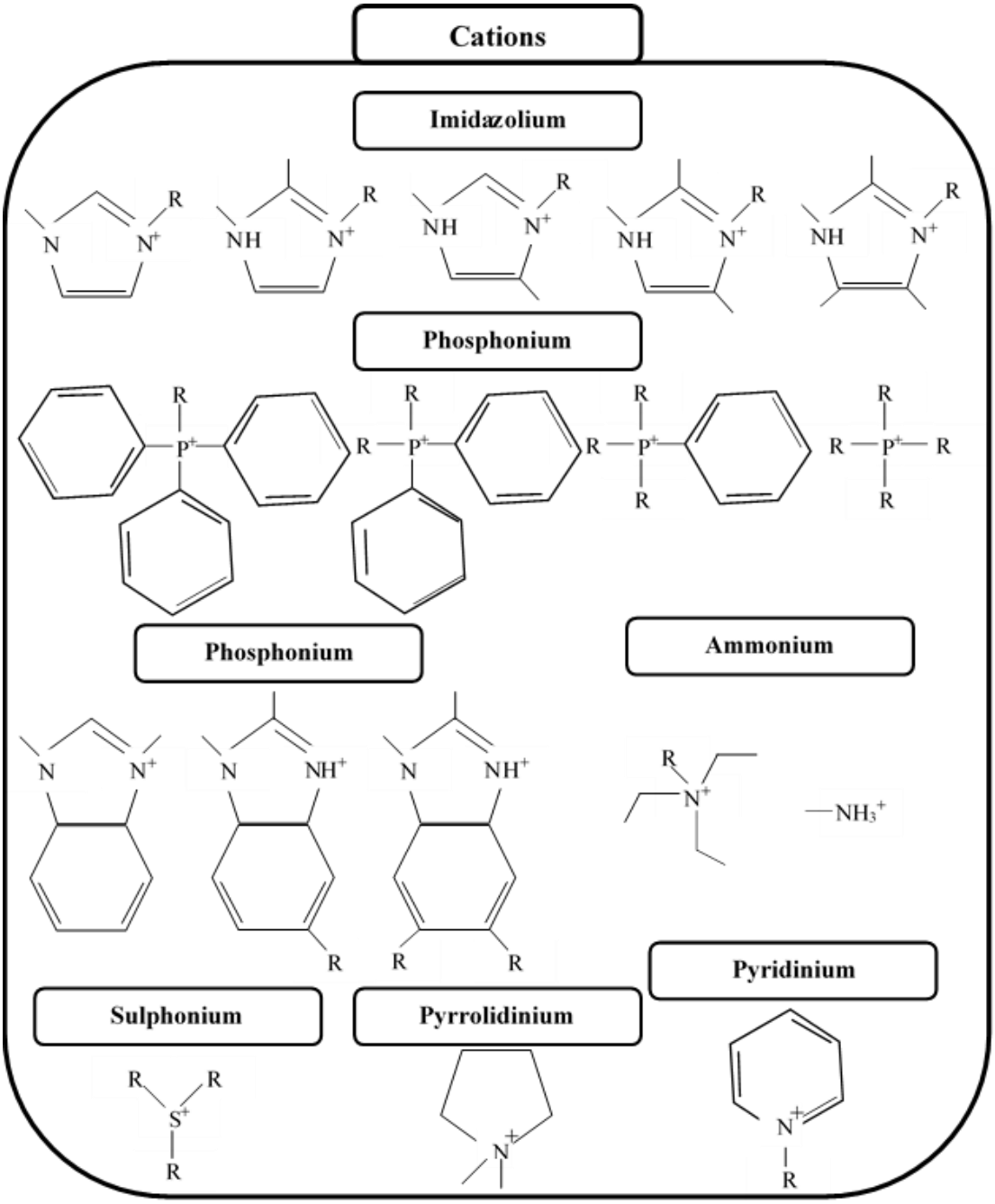

Figure 1.5. Chemical structure of cations commonly used in ILs.

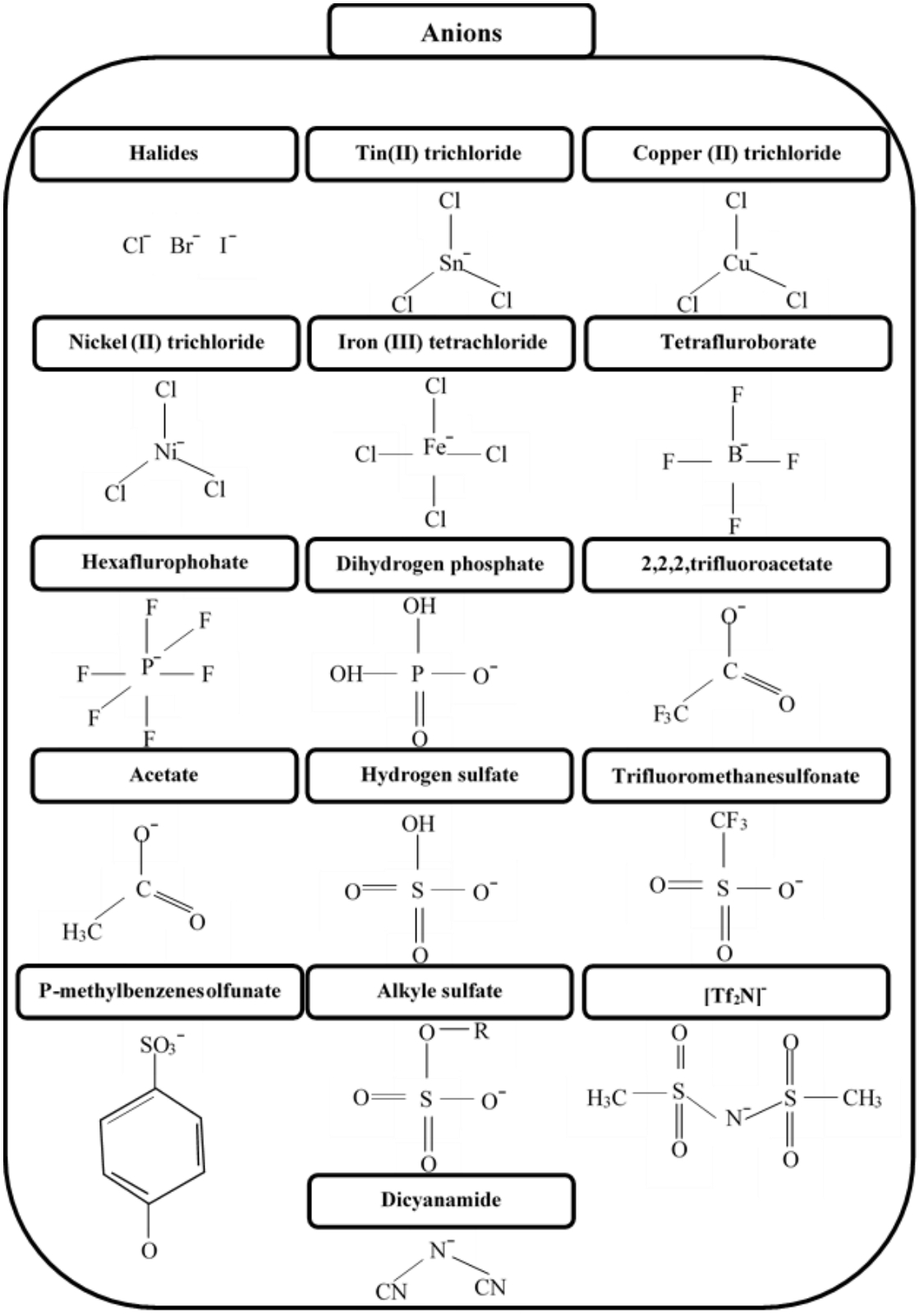

Figure 1.6. Chemical structure of anions commonly used in ILs.

Table 1.2. General information about different kinds of ILs and their properties.

Type of ionic liquid	Abbreviation	Summary and property	Possible application	Ref.
Chiral ionic liquids	C-ILs	This kind of ILs is usually synthesized by asymmetric synthesis or chiral pool and they can contain polar, axial or central chirality. Owing to their nature, the process of their synthesis is difficult and expensive.	Liquid chiral chromatography, stereo selective polymerization, synthesis of potential active chiral compounds, liquids crystal, NMR chiral discrimination, solvent, electrolyte, and catalyst.	[22]
Switchable polarity solvent ionic liquids	SPS-ILs	SPS-ILs are usually synthesized by proton transfer reaction. They have acceptable resistance against wet condition for synthesis and operation.	Solvent recovery and solute separation.	[91]
Protic ionic liquids	Pr-ILs	Pr-ILs can be quickly synthesized by transferring hydrogen ion (H^+) from a Brønsted acid to a Brønsted base. The process of proton-transfer is boosted by using strong bases or acids or both of them. These ILs have good proton conductivity, fluidity, and low melting point.	Alkaline batteries, fuel cells, dehydration, choromatogeraphy (both liquid and gas), and hydrolysis.	[88]
Bio-ionic liquids	Bio-ILs	Bio-ILs are often produced by sustainable bio-precursors; therefore, they are environmentally friendly, bio-degradable, biocompatible, and non-toxic. They have high thermal stability and viscosity. Besides, their solubility in other liquids (water and organic solvents) is strictly depended on the cation nature.	Biodiesel production, renewable diesel and jet fuel, chemical compounds production (like herbicides).	[94]
Poly ionic liquids	P-ILs	P-ILs are also known as polymerized ionic liquids. In spite of the high charge density of P-ILs, they usually have wide glass transition temperature range.	Polymer electrolytes for batteries, fuel cells, carbon electrodes, sensors, organic transistors, super capacitors, catalysts, photoresists, and corrosion inhibitors.	[96]

Energetic ionic liquids	E-ILs	E-ILs have low melting point, high thermal stability and density, and they are considered as environmentally friendly materials.	Explosives (e.g. trinitrotoluene), pyrotechnics, and propellants.	[97]
Neutral ionic liquids	N-ILs	The electrostatic interactions between anions and cations are typically very weak. As a result, N-ILs have low melting point and viscosity.	Solvent, and organic transformation.	[22]
Metallic ionic liquids	M-ILs	This type of IL contains metal halides (e.g., $[AlCl_3^-]$, $[CuCl_3^-]$, $[SnCl_3^-]$, and $[Al_2Br_7^-]$). M-ILs are highly viscous in comparison with other types of ILs. M-ILs are typically stable under moisture and ambient conditions.	Catalyst, solvent, organometallic chemistry hydration process, and recycling of nuclear waste.	[90]
Basic ionic liquids	B-ILs	B-ILs are considered as eco-friendly, flexible, non-volatile, active and selective catalysts; thus, B-ILs are good alternative for conventional bases (e.g., KOH, NaOH, and $NaHCO_3$). Unlike traditional bases, B-ILs do not suffer from environmental issue, waste production, and corrosion.	Organic transformation (e.g., Michael addition, aldol condensation, Knoevenagel condensation, Henry reaction, oximation, and Michael reaction), catalyst, and solvent.	[89]
Supported ionic liquids	S-ILs	The use of S-ILs increases because of high cost of pure ILs. These ILs are usually used on silica support, thus, requiring lower IL amount. The application of S-ILs can accelerate ILs use on industrial and commercial scale.	Solvent, catalyst, reactor systems, and separation process.	[92]

1.3.1. Synthesis of ILs

There are different methods used to synthesize ILs (i.e. acid-base neutralization, metathesis, and alkylation reactions), which are based on the IL type and application requirements [22,95,98]. ILs are usually classified into two categories: primary ILs and secondary ILs [7,95].

The primary ILs are typically synthesized by protonation or alkylation of a base by an acid or a haloalkane [7,99]. Primary ILs usually contain halide-based anions (i.e. Cl^-, Br^-, I^-, and F^-) (Fig. 1.7). The alkylation reaction possesses some benefits such as the moderate operating temperature and the reasonable cost of reagents [99]. However, the synthesis difficulties are more pronounced owing to the reactivity of halide-based anions ($Cl^- < Br^- < I^-$) [7,99]. For instance, performing the alkylation reaction with 1-chloropropane (haloalkane) requires more time as compared with 1-bromopropane under the similar operating conditions as chloride is less reactive than bromide [99,100]. Moreover, haloalkane containing bromide and iodide requires lower reaction temperature owing to their high reactivity [7]. For example, the required temperature for 1-bromobutane and iodomethane is 35 and 0 °C, respectively [99]. In case of haloalkanes with iodide, the temperature should be precisely controlled in order to avoid secondary reactions [7,99]. In general, the reaction is performed in ice bath and the reaction mixture is protected from sunlight since these reagents are photoactive. The use of fluorine-based haloalkanes for synthesis of primary ILs is not practical owing to the fact that the covalent bond between fluorine and carbon is very strong [7,99]. Bao and coworkers synthesized a primary ILs (1-hexyl-3-methylimidazolium chloride ([HMIM][Cl]) by alkylation reaction [101]. 1-methylimidazole and 1-chlorohexane were utilized as the base and haloalkane, respectively. The alkylation reaction was carried out in the presence of cyclohexane as the solvent in a round-bottom flask at 60 °C for 72 h. Then, the resultant IL was washed with ethyl acetate for removing solvent and unreacted compounds. Finally, the pure IL was dried in the oven at 70 °C for 24 h. Fang et al. [102] synthesized two primary ILs (i.e. 1-vinyl-3-butylimidazolium bromide [VBIM][Br] and 1-vinyl-3-methylimidazolium iodide [VMIM][I]) by alkylation reaction between 1-vinylimidazole (base) and 1-bromobutane and methyl iodide (haloalkanes). The operating temperature and required time for synthesizing [VMIM][I] (0 °C and 6 h) were less than those for [VBIM][Br] (35 °C and 12 h). [VBIM][Br] and [VMIM][I] were washed by ethyl ether and dried at RT for a day in the final synthesis step. Besides, the synthesized primary ILs can be further used for the synthesis of secondary ILs with more complex chemical structure. There are two main ways to synthesize secondary ILs: metathesis reaction and acid-base neutralization [7].

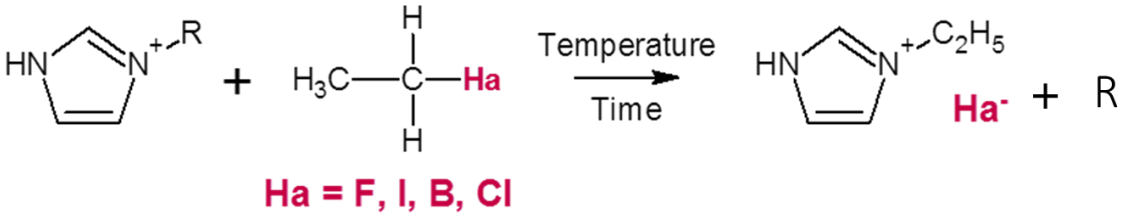

Figure 1.7. Example of alkylation for obtaining primary ILs (Adopted from "Ionic liquids synthesis–methodologies" by Ferraz, R.; Prudencio, C.; Vieira, M.; Fernandes, R.; Noronha, J.P.; Petrovski, Z., 2015, Organic Chemistry Current Research, 4, under the license CCBYNCND 3.0. Copyright 2015 Longdom) [100].

In order to synthesize secondary ILs metathesis reaction is usually used (Fig. 1.8). Indeed, this method is one of the most common and practical ways [99,100]. In general, to prepare halide free ILs, the reaction is carried out between a metallic salt and primary ILs (Fig. 1.8). In this method, phase transfer process allows obtaining pure ILs without any impurities [99].

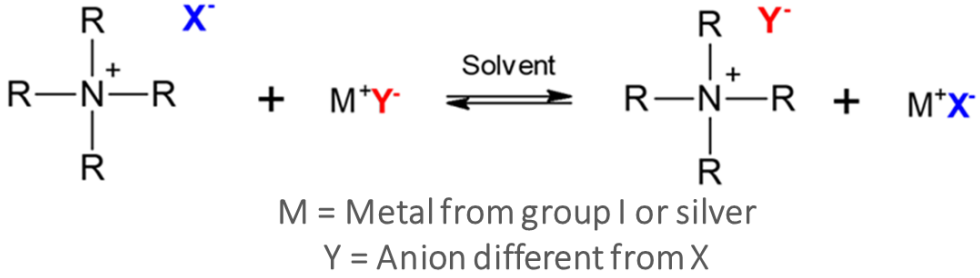

Figure 1.8. Metathesis reaction of the synthesis of secondary ILs (Adopted from "Ionic liquids synthesis–methodologies" by Ferraz, R.; Prudencio, C.; Vieira, M.; Fernandes, R.; Noronha, J.P.; Petrovski, Z., 2015, Organic Chemistry Current Research, 4, under the license CCBYNCND 3.0. Copyright 2015 Longdom) [100].

Hooshyari and coworkers [103] synthesized a primary IL (1,6-di(3-methylimidazolium)hexane bis bromide) by alkylation reaction between a base (1-methylimidazole) and haloalkane (1,6-dibromopropane). Subsequently, a secondary IL (1,6-di(3-methylimidazolium)hexane bis(hexafluorophosphate)) was obtained by a metathesis reaction between synthesized primary IL and a salt (potassium hexafluorophosphate). In another research, Lin et al. [104] synthesized a secondary IL (1-vinyl-3-butylimidazolium bis(trifluoromethylsulfonyl)imide [VBIM][NTf_2]) by two steps synthesis. At the begining, an alkylation reaction was conducted between *n*-vinylimidazole and 1-bromobutane (haloalkane) to synthesize a primary IL (1-vinyl-3-butylimidazolium bromide [VBIM][Br]). Then, the metathesis

reaction was carried out between bistrifluoromethanesulfonimide lithium (salt) and the synthesized primary IL ([VBIM][Br]) to synthesis [VBIM][NTf_2].

The acid-base neutralization is also used to obtain secondary ILs (Fig. 1.9) [95]. In this case, a simple neutralization between a Brønsted acid and a Brønsted base allows obtaining IL. The reaction is conducted between an acid and a base in the presence of solvent or it can be also performed after alkylation reaction between a primary ILs and an acid [99,100].

Figure 1.9. Acid-base neutralization reaction for the synthesis of secondary ILs (Adopted from "Ionic liquids synthesis–methodologies" by Ferraz, R.; Prudencio, C.; Vieira, M.; Fernandes, R.; Noronha, J.P.; Petrovski, Z., 2015, Organic Chemistry Current Research, 4, under the license CCBYNCND 3.0. Copyright 2015 Longdom) [100].

Maiti et al. [105] synthesized a secondary IL (2,3-dimethyl-1-butyl imidazolium dihydrogen phosphate [MBuIM][H_2PO_4]) in two steps. In the first step, an alkylation reaction was conducted between 1,2-dimethyl imidazole and 1-bromobutane (haloalkane) to synthesize a primary IL (2,3-dimethyl-1-butyl imidazolium bromide). In the second stage, the acid-base neutralization reaction was carried out between phosphoric acid and the synthesized 2,3-dimethyl-1-butyl imidazolium bromide (primary IL) to obtain [MBuIM][H_2PO_4]. Lin and coworkers [23] synthesized a secondary IL (1-methylimidazolium trifluoromethanesulfonate [MIM][TFS]) by neutralization technique. For this purpose, 1-methylimidazole (as the Brønsted base) was added to the vessel with solvent (ethyl acetate) under stirring. Then, the trifluoromethanesulfonic acid (as the Brønsted acid) was added drop by drop (the temperature should be maintained at 0 °C). Finally, the obtained IL was washed with solvent and then was dried in the oven.

Although both reactions (i.e. acid-base neutralization and metathesis reaction) are used, their drawbacks should be taken into consideration. In metathesis reaction, the halides are very reactive during metathesis reaction, therefore, they can react with other components and produce non desirable products [100]. Furthermore, the number of available commercial metal salts is not sufficient [100]. Moreover, the temperature sensitivity of the acid-base neutralization reaction is rather high as temperature increase provokes appearance of different impurities [7,100].

1.3.2. ILs Application

Nowadays, ILs are used for both academic and industrial purposes (including metal extraction, electrochemistry, engineering chemistry, gas separation, solvent, physical chemistry, analytical chemistry, biological aid, engineering, and fuel cells) owing to their remarkable properties [12,22,24]. Here, only their application in fuel cells will be discussed.

Elumalai and Dharmalingam [106] used 1-methyl-3-(3-trimethoxysilylpropyl)imidazolium chloride ([MTIM][Cl])-titanate nanotubes (TNT) to prepare composite membranes based on quaternary ammonium functionalized polysulfone (QAPSU) for AFC application. It was found that the addition of [MTIM][Cl] and TNT led to enhancing the water content, ion exchange capacity (IEC), and hydroxyl conductivity of composite membranes. The composite membrane with 5 wt.% of [MTIM][Cl]-TNT showed the maximum value of water uptake and IEC (15.97 % and 1.93 $meq \cdot g^{-1}$, respectively). Furthermore, this composite membrane demonstrated the highest power density and conductivity (302 $mW \cdot cm^{-2}$ and 20.8 $mS \cdot cm^{-1}$, respectively). In another research [MTIM][Cl]-Santa Barbara amorphous-15 (SBA-15) was used to prepare composite membranes based on quaternary polysulfone (QPSU) [107]. The composite membrane containing 3 wt.% of [MTIM][Cl]-SBA-15 showed the maximum value of water absorption and IEC (15.87 % and 1.86 $meq \cdot g^{-1}$, respectively). Additionally, this composite membrane demonstrated the highest open circuit potential (OCP), power density and conductivity – 0.87 V, 278 $mW \cdot cm^{-2}$ and 18.9 $mS \cdot cm^{-1}$, respectively [107].

ILs are also widely used in microbial fuel cell (MFC) [108,109]. Hernández-Fernández et al. [108] used two ILs (methyltrioctil ammonium chloride [MTOA][Cl] and 1-octyl-3-methylimidazolium hexafluorophosphate [OMIM][PF_6]) to fabricate supported ionic liquid membrane (SILM) based on the polyvinylchloride (PVC). It was observed that the proton conductivity of membrane increased considerably by adding ILs. The highest power value (450 $mW \cdot cm^{-2}$) was observed for SILM with [MTOA][Cl]. Moreover, the chemical organic demand removal (COD_R) of the composite membrane containing [MTOA][Cl] was 80%. In another study, Hernández-Fernández et al. [109] used different cations and anions (1-octyl-3-methylimidazolium [OMIM], 1-butyl-3-methylimidazolium [BMIM], methyl trioctyl ammonium [MTOA], tetrafluoroborate [BF_4], hexafluorophosphate [PF_6], bis((trifluoromethyl)sulfonyl)imide [NTF_2], and chloride [Cl]) for preparing SILM based on the Nylon® membrane. The SILM with [MTOA][Cl] showed the highest COD_R of 89.1%. Besides, the SILM with [OMIM][PF_6] demonstrated the maximum power value (215 $mW \cdot cm^{-2}$).

ILs are also utilized in PEMFC application in a wide temperature range (from 25 to 170 °C) owing to their great thermal stability, low volatility as well as excellent ionic conductivity [110-112]. The

composite membrane based on ILs are able to conduct hydrogen ions (protons) from anodic section to cathodic one at elevated temperature without presence of humidity by Grotthuss mechanism. However, the way of the IL introduction into the polymer film is very important as it has a strong influence on the physical and chemical properties of the resultant composite membrane [113]. Generally, there are some techniques to introduce ILs into the polymer film such as spin-coating (SC), layer by layer self-assembly (LbLSA), freeze drying (FD), and vacuum-assisted flocculation (VAF), IL incorporation into the polymer solution, swelling the polymer film (dense or porous) into the IL solution, and crosslinking but the last three are the most commonly used methods (Table 1.3).

Table 1.3. Common methods of IL introduction for the fabrication of composite membranes.

Method	Membrane composition	Operation temperature (°C)	Highest proton conductivity ($S \cdot cm^{-1}$)	Observations	Ref.
Incorporation of IL in polymer solution	[BMI][HSO_4]/SPEEK [IM][HSO_4]/SPEEK [MI][HSO_4]/SPEEK	25 and 80	$150 \cdot 10^{-3}$	Different amount of ILs was added to polymer solution (0, 5, 10, and 15 wt.%). The surface roughness of membranes decreased by adding ILs. The composite polymer film with 5 wt.% of [MI][HSO_4] demonstrated the highest ionic conductivity.	[114]
	Phosphonated IL-SBA-15/SPEEK	60 to 140	$10.2 \cdot 10^{-3}$	Various concentration of IL-SBA was added to polymer solution (0, 2, 4, 6, and 8 wt.%). The WU of membranes increased by adding IL-SBA. The composite polymer film with 6 wt.% of IL-SBA demonstrated the highest proton conductivity.	[115]
	[BAIM][TFSI]/PI	25 to 160	$1.0 \cdot 10^{-2}$	Composite polymer films containing 30, 40, 50, and 60 wt.% of [BAIM][TFSI] were fabricated. The composite membranes showed excellent thermal stability up to ~ 350 °C IL revealed great ionic conductivity of $5.6 \cdot 10^{-2}$ $S \cdot cm^{-1}$ at 140 °C. The membrane with 30 wt.% of [BAIM][TFSI] demonstrated the good tensile strength of 72.5 MPa.	[116]
Impregnation of the polymer with IL	[MIM][TFSI]/Matrimid® [EIM][TFSI]/Matrimid® [PIM][TFSI]/Matrimid® [BIM][TFSI]/Matrimid®	25 to 150	$1 \cdot 10^{-3}$	It was found that there was a linear correlation between temperature and ionic conductivity. The modified membrane containing [MIM][TFSI] showed the highest conductivity at 150 °C. The modified membranes demonstrated excellent thermal stability from 260 to 290 °C.	[117]

				The mechanical stability of modified polymer films was better than that of unmodified Matrimid® membrane.	
	[VIM][TFS]/PI [AIM][TFS]/PI [MIM][TFS]/PI [PVIM][TFS]/PI [VIM][TFS]/[PVIM][TFS]/PI	30 to 150	$1.0 \cdot 10^{-4}$	The composite polymer film with [VIM][TFS]/[PVIM][TFS] exhibited the maximum values of Young's modulus and elongation at break (1371 MPa and 271%, respectively). The greatest loading content was obtained for [VIM][TFS]/[PVIM][TFS]/PI polymer film (276 ± 16 wt.%). The composite membranes showed remarkable thermal stability up to 300 °C.	[118]
	[MIM][TFS]/Polyoxadiazole/PVP	40 to 120	$1.3 \cdot 10^{-3}$	Increasing temperature from 40 to 120 °C led to the enhancement of the conductivity of composite film. The polyoxadiazole-based membrane showed a great degree of impregnation of 297%. The polymer films exhibited tunable thermal stability of ~ 350 °C. The resultant membranes were also mechanically stable.	[119]
Crosslinking	P[VBIM]Cl/NbPBI P[MPIM]Br/NbPBI P[TPAM]Br/NbPBI	110 to 170	$7.4 \cdot 10^{-2}$	*In-situ* free radical polymerization technique was used for PIL synthesis. FTIR spectra showed that PILs were chemically cross-linked to the polymer backbone. It was found that there was a linear correlation between temperature and ionic conductivity. The composite membrane containing P[MPIM]Br has the best ionic conductivity at 170 °C. The composite polymer membranes demonstrated tunable thermal stability (~ 220 and 250 °C).	[120]

[APMIM][Br]-GO/[MIM][TFS]/PSAN	100 to 160	$1.48 \cdot 10^{-2}$	Composite polymer films containing 0.3, 0.7, 1, and 1.2 wt.% of [APMIM][Br]-GO and 40 wt.% of [MIM][TFS] were fabricated. The polymer film with 1 wt.% of [APMIM][Br]-GO showed the highest ionic conductivity at 160 °C. It was observed that the mechanical features of membranes decreased by adding [APMIM][Br]-GO. It was found that the addition of [APMIM][Br]-GO resulted in reducing the PIL leakage from the PEM.	[23]
PIL(PBI-BF_4)/PBI PIL(PBI-BF_4)/PA/PBI	110 to 170	0.117	Composite polymer films with 0, 10, 20, 30, and 40 wt.% of IL were fabricated. To rise the ionic conductivity, some membranes were submerged into the PA solution. The polymer film with 40 wt.% of IL showed the highest value of ionic conductivity at 170 °C. The rise of PIL amount caused reducing the mechanical properties of composite membranes.	[121]

1.3.3. Incorporation of IL in Polymer Matrix

1.3.3.1. Dissolving of IL in Polymer Solution

IL incorporation in the polymer solution is the most common way to prepare composite IL-based polymer membrane. In this case, IL is dissolved or dispersed in the polymer solution containing solvent and polymer (Fig. 1.10). The IL addition into the polymer solution before the membrane casting leads to forming an ion gel solution and the physical and chemical features of this ion gel solution are dependent on the ratio of IL and polymer in the solution. Another important factor is the compatibility between IL and polymer. Despite the fact that the ionic conductivity and thermal stability of composite membrane prepared by this method are improved, the reduction of mechanical stability is the main limitation of this technique. Therefore, there is a trade-off between the membrane conductivity improvement and mechanical stability. This means that by increasing the IL amount, the proton conductivity increases while the mechanical properties of the resultant membrane are reduced at the same time [113].

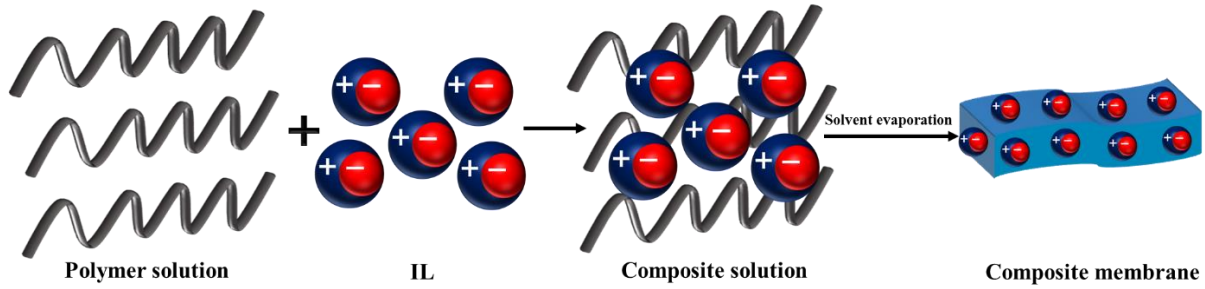

Figure 1.10. Scheme of membrane preparation by IL incorporation into polymer solution (From "Different Approaches for the Preparation of Composite Ionic Liquid-Based Membranes for Proton Exchange Membrane Fuel Cell Applications–Recent Advancements" by Ebrahimi, M.; Fatyeyeva, K.; Kujawski, W., 2023, Membranes, 13, 593, under the license CC BY 4.0) [113].

da Trindade et al. [114] fabricated composite membranes by incorporating ILs (5, 10, 15 wt.%) in the SPEEK polymer solution. They used imidazolium-based ILs with different cations (imidazolium [IM], 1-methylimidazolium [MI], 1-butyl-3-methylimidazolium [BMI]) and hydrogen sulfate as the anion ([HSO_4]). To prepare the composite membranes, the polymer and ILs were initially dissolved in *N*, *N*-methylpyrrolidone (NMP). The composite solution was stirred at 80 °C until obtaining the homogeneous solution. After casting of the resultant composite solution on the glass plate the membranes were dried at 80 °C under vacuum. The ionic conductivity of pristine and composite membranes was measured at low and moderate temperatures (25 and 80 °C). It was observed that the proton conductivity at 80 °C was higher than that at 25 °C. The composite membrane with 5 wt.% of [MI][HSO_4] showed the maximum conductivity

of 150 $mS \cdot cm^{-1}$ at 80 °C. The polymer and ILs demonstrated good compatibility as the IL addition led to obtaining membranes with smoother surface as compared with pristine membrane. However, the composite membranes were not thermally stable. Elumalai et al. [115] introduced phosphonated IL containing SBA-15 into SPEEK polymer solution in NMP. The influence of the IL content (2, 4, 6, and 8 wt.%) on the membrane properties was studied. The composite solution was stirred 48 h and sonicated during 30 min till obtaining homogeneous solution before casting and drying. It was found that the WU of composite membrane was enhanced by addition of modified phosphonated IL thanks to increasing the number of gaps and voids in the membrane structure. The mechanical stability of composite membranes was higher than that of pure SPEEK membrane. Indeed, by increasing the IL concentration from 2 to 6 wt.%, the tensile strength increased, while further IL addition up to 8 wt.% caused the reduction of tensile strength. The highest value of tensile strength (23 MPa) was noted for composite membrane with 6 wt.% of modified IL. Besides, the proton conductivity of resultant membranes was investigated in the operating temperature range from 60 to 140 °C and the maximum value (10.2 $S \cdot cm^{-1}$) was obtained for composite membrane containing 6 wt.% of modified phosphonated IL at 140 °C. Rogalsky et al. [116] fabricated composite membranes by incorporating 2-butylaminoimidazolinium bis(trifluoromethylsulfonyl)imide ([BAIM][TFSI]) (30, 40, 50, and 60 wt.%) in the Matrimid® polymer solution in methylene chloride. During the membrane preparation, the polymer was initially dissolved in methylene chloride by stirring. Then, various contents of [BAIM][TFSI] were introduced to the polymer solution. Finally, the membrane was cast on the glass plate and dried at RT and 60 °C for 24 and 12 h, respectively, in order to remove residual solvent. The ionic conductivity test performed for pure IL demonstrated acceptable conductivity (~ 10^{-2} $S \cdot cm^{-1}$ at 140 °C). Moreover, TGA analysis showed that IL and composite membranes are thermally stable up to 350 °C. The mechanical stability of composite membrane (72.5 MPa) containing 30 wt.% of IL was better than that of the pure membrane (37 MPa). However, by adding further amount of IL (from 30 to 60 wt.%), the mechanical stability of composite membrane was considerably reduced (16 MPa). The ionic conductivity of composite membranes was found between ~ 10^{-6} to 10^{-3} $S \cdot cm^{-1}$ at the temperature range from 25 to 160 °C.

1.3.3.2. Polymer Impregnation with IL

In this case, IL is introduced into the polymer by the membrane swelling in the IL-based solution (Fig. 1.11). The polymer film can have both porous (micro- and nanoporous) and dense morphology and can be prepared by ordinary phase inversion technique or other methods (i.e. sintering, stretching, or track-etching). Furthermore, different polymers (both homopolymers and copolymers) can be used [113]. IL is trapped in the polymer structure by weak electrostatic interactions. The IL amount is rather limited as it is influenced by the number of available gaps, cavities, and free volume (pore) of the pure polymer membrane.

The physical and chemical affinity between polymer chain and IL also have a crucial role. Although this method is usual for preparing PEM on the lab scale, it is not a common way for preparing membranes on the commercial scale owing to the IL leakage during the process [113].

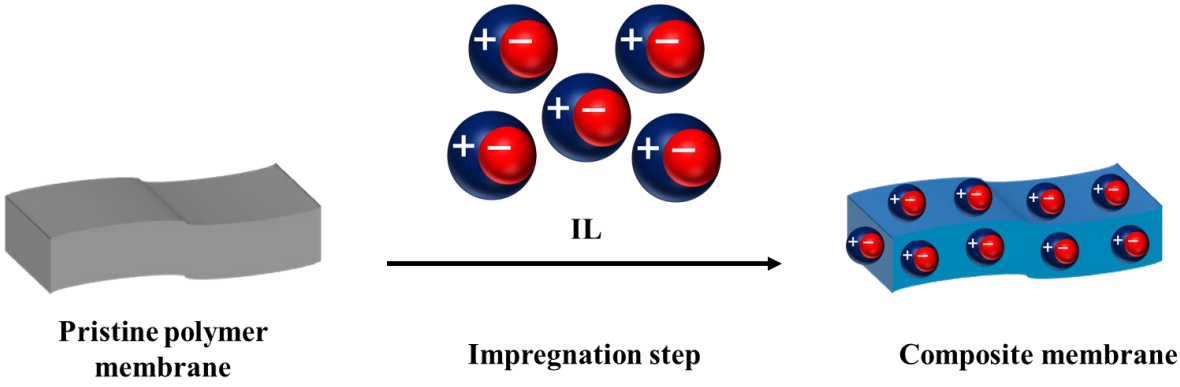

Figure 1.11. Scheme of membrane preparation by polymer impregnation with IL (From "Different Approaches for the Preparation of Composite Ionic Liquid-Based Membranes for Proton Exchange Membrane Fuel Cell Applications–Recent Advancements" by Ebrahimi, M.; Fatyeyeva, K.; Kujawski, W., 2023, Membranes, 13, 593, under the license CC BY 4.0) [113].

Fatyeyeva et al. [117] prepared composite membranes based on Matrimid® and different ILs (1-methylimidazolium bis(trifluoromethylsulfonyl)imide [MIM][TFSI], 1-ethylimidazolium bis(trifluoromethylsulfonyl)imide [EIM][TFSI], 1-propylimidazolium bis(trifluoromethylsulfonyl)imide [PIM][TFSI], and 1-butylimidazolium bis(trifluoromethylsulfonyl)imide [BIM][TFSI]). The pure porous Matrimid® membrane was immersed into the IL-based solution for 24 h at 60 °C for the IL impregnation. Then, the temperature of the solution was reduced till RT and membranes were dried. The ionic conductivity of composite membranes was measured in the temperature range between 25 and 150 °C and a linear correlation between temperature and ionic conductivity was observed. The composite membranes demonstrated high proton conductivity at elevated temperature (~ 1.0 $mS \cdot cm^{-1}$ at 150 °C). Moreover, the composite membranes were thermally stable up to 280 °C. It was found that the mechanical stability of modified membranes are better than that of pure Matrimid® membrane. Kobzar et al. [118] fabricated composite membranes based on the polyimide membrane modified by various ILs with the same anion (trifluoromethane sulfonate [TFS]) and different cations (vinyl imidazolium [VIM], allyl imidazolium [AIM], methacrylate imidazolium [MIM], and polymerized vinyl imidazolium [PVIM]). The pure membrane was swelled in the solution containing IL and water. The content of IL loading into the membrane structure was different (between 146 and 276 wt.%) owing to the physical and chemical affinity between polymer chains and ILs. Also, the composite membranes demonstrated excellent mechanical

properties, such as Young's modulus (1371 MPa) and elongation at break (271%). Besides, the composite membranes were thermally stable up to 300 °C. The composite membranes showed great ionic conductivity of ~ 10^{-1} mS·cm^{-1} at 150 °C. In another research, Kobzar et al. [119] fabricated a novel supported ionic liquid membrane based on polyoxadiazole modified by 1-methyl imidazolium trifluoromethane sulfonate ([MIM][TFS]). To prepare a membrane with high capacity of IL retention, a composite polymer solution containing polyoxadiazole and PVP (50/50, v/v) was prepared. Then, the cast composite membrane was immersed into the aqueous solution containing water and methanol to remove PVP, thus, creating numerous gaps and cavities. The dried resultant membrane was finally swelled in an aqueous solution of [MIM][TFS], followed by drying (this step was repeated several times). Owing to the PVP removal, a large amount of [MIM][TFS] was loaded into the membrane (up to 297%). The ionic conductivity test performed from 40 to 120 °C revealed the highest value of $1.3 \cdot 10^{-3}$ S·cm^{-1} at 120 °C. Moreover, the membrane was thermally stable up to 350 °C. Furthermore, the composite membrane showed great Young's modulus and elongation at break of 21.4 MPa and 174%, respectively [119].

1.3.3.3. Crosslinking of IL

Because of the absence of chemical bonds between IL and polymer chain during the IL incorporation in the polymer solution and polymer impregnation with IL, the IL leaching from polymer is observed. Therefore, such membranes are not stable and their ionic conductivity reduces with time. This problem can be solved by the chemical crosslinking of IL and polymer chain which leads to membrane strengthening and IL retention. However, as IL is fixed, its mobility is reduced that influences the IL proton conductivity. The general scheme of IL-based membrane preparation by crosslinking is shown in Fig. 1.12.

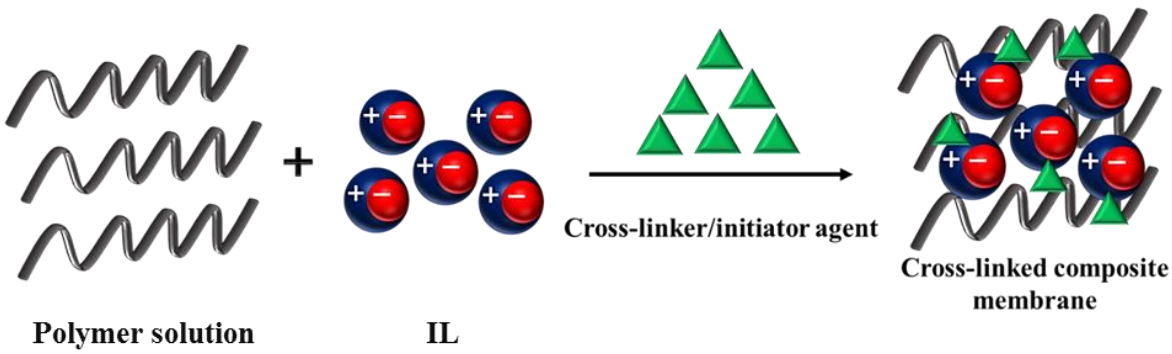

Figure 1.12. Scheme of membrane preparation by crosslinking (From "Different Approaches for the Preparation of Composite Ionic Liquid-Based Membranes for Proton Exchange Membrane Fuel Cell Applications–Recent Advancements" by Ebrahimi, M.; Fatyeyeva, K.; Kujawski, W., 2023, Membranes, 13, 593, under the license CC BY 4.0) [113].

Liu et al. [120] prepared composite membranes containing PIL/norbornene (Nb)-type PBI with cross-linked PILs. PILs with different cations ([VBIM], [MPIM], and [TPAM]) and anions ([Br] and [Cl]) were used. To fabricate membrane, PILs, polymer, and azobis-(isobutyronitrile) were dissolved in the dimethylacetamide (DMAc). The composite polymer solution was cast on the hot plate at 60 °C and then placed in the oven (110 °C) to remove the solvent. FTIR analysis showed that PILs were chemically cross-linked into the membrane. Besides, the membrane resistance evaluated in DMAc revealed that cross-linked membranes demonstrated excellent resistance against solvent and composite membrane with P[TPAM]Br showed the best performance (58.2%). The composite membrane containing P[MPIM]Br showed the highest proton conductivity of 0.74 $S \cdot cm^{-1}$ at 170 °C. Moreover, the composite membranes showed a great thermal stability between 220 and 250 °C. P[TPAM]Br/Nb-PBI composite membrane demonstrated the greatest power density of 385 $mW \cdot cm^{-2}$ at 160 °C. Lin and coworkers [23] fabricated composite membrane based on poly(styrene/acrylonitrile) (PSAN). Two ILs were used: 1-methylimidazolium trifluoromethanesulfonate [MIM][TFS] and 1-(3-aminopropyl)-3-methylimidazolium bromide functionalized graphene oxide [APMIM][Br]-GO. PSAN and IL were dissolved and stirred in the presence of photo initiator (benzoin isobutyl ether). The homogenous composite solution was cast on the glass plate to form the membrane. The cast polymer was exposed to UV during 1.5 h to form new bonds between IL and polymer chain (cross linking step). It was found that the addition of [APMIM][Br]-GO allows significant improvement of the proton conductivity – 14.8 $mS \cdot cm^{-1}$ at 160 °C, while the proton conductivity of membrane without [APMIM][Br]-GO is 1.4 $mS \cdot cm^{-1}$ at the same operating condition. The results of mechanical test showed that the addition of [APMIM][Br]-GO (from 0 to 1.2 wt.%) to the composite membrane resulted in improving tensile strength and tensile modulus, whereas elongation at break decreased. Additionally, the resultant membranes (modified and unmodified membranes) showed excellent thermal stability (up to 300 °C). The leaching test revealed that the leaching of [MIM][TFS] decreased considerably by introducing [APMIM][Br]-GO owing to possible interactions between ILs together and polymer chain (cross linking step). In another research, Chen et al. [121] prepared composite membrane based on PBI and IL. At the beginning, polymer and IL (10, 20, 30, and 40 wt.%) were dissolved in DMAc and stirred to obtain homogenous solution. Then, 3 wt.% of γ-(2, 3-epoxypropoxy)propyltrimethoxysilane (as the cross linker agent) were added to the composite solution and it was stirred again. The obtained composite solution was cast and dried at 80 °C for 24 h. After this, the composite membrane was swelled in an acidic solution of 1M H_2SO_4 at 80 °C for 24 h and heated at 120 °C overnight. The resultant composite membranes showed good proton conductivity at high temperature and composite containing 40 wt.% of IL demonstrated the highest conductivity of 117 $mS \cdot cm^{-1}$ at 170 °C. However, by further addition of IL (from 10 to 40 wt.%) the mechanical stability of membranes decreased. The composite membrane were also thermally stable up to 300 °C.

1.4. Research Motivation

Nowadays, PEMFC attracts a lot of attention since it is considered as the green source of energy generation. Nafion® is the most commonly used polymer owing to its unique physical-chemical properties namely high proton conductivity, excellent thermal, mechanical, and chemical stabilities. However, proper performance of Nafion® in PEMFC is observed up to moderate temperature (~ 80 °C) and humid condition. Indeed, the presence of water molecules is necessary for the proton transfer in Nafion® membrane as water plays the role of proton carrier agent. The rise of temperature (higher than 80 °C) causes proton conductivity reduction because of the water evaporation. As a result, Nafion® cannot be a suitable polymer for HT-PEMFC application. There are some methods to prepare PEM for HT-PEMFC application such as modification of Nafion® membranes with NPs, the use of PA-based membranes, introduction of inorganic compounds in non-fluorinated membrane, and using IL-based membrane. The use of composite IL-based membranes can be a promising way to overcome proton conductivity reduction at the temperature higher than 80 °C in anhydrous condition, since in this case ILs can transport the protons.

The main goal of this PhD thesis is the synthesis of new Pr-ILs and the preparation of conductive PEM for HT-PEMFC application. Therefore, eighteen new imidazolium- and hydroxylammonium-based Pr-ILs containing various anions were synthesized *via* acid-base neutralization reaction. The chemical structure of synthesized Pr-IL was confirmed and their thermal stability and ionic conductivity at the wide temperature range (25 to 150 °C) under dry condition were evaluated. Then, composite membranes based on cellulose acetate butyrate (CAB) and synthesized Pr-ILs were obtained. Composite membranes containing cellulose acetate propionate (CAP) and commercial ILs were also fabricated. The morphological, mechanical, chemical, and thermal stabilities of CAB/Pr-ILs and CAP/A-ILs composite membranes were investigated. In addition, ionic conductivity of CAB/Pr-ILs composite membranes was investigated by the electrochemical impedance spectroscopy (EIS) in a wide range of temperature (25 to 130 °C) under non-humid condition. The obtained membrane performance was correlated with the membrane composition. Porous polyamide-6 (PA6) membranes were prepared and their physical, morphological, and transport properties were evaluated. The results demonstrated that PA6 membranes may be considered as the promising SILM candidate.

This PhD study possesses the following novelties:

- synthesis of new Pr-ILs containing excellent thermal stability and ionic conductivity;
- a deep discussion about the correlation between IL nature and its thermochemical properties;

- a research work about the use of CAB polymer in PEMFC application at elevated temperature;
- elaboration of a new conductive PEM based on a non-conductive polymer (CAB) by utilization of only ILs.

Chapter 2. Materials and Methods

This chapter provides information about the utilized chemical compounds (both commercial and synthesized). The experimental protocols for synthesis and preparation of ILs and membranes are also given. Furthermore, details regarding the characterization techniques are presented.

2.1. Materials

2.1.1. Polymers

In this work, three types of polymers were utilized to prepare polymer membranes: polyamide-6 (PA6) (Fig. 2.1a), cellulose acetate propionate (CAP) (Fig. 2.1.b), and cellulose acetate butyrate (CAB) (Fig. 2.1c).

PA6 (also known as polycaprolactam) was purchased from ZWCH STILON S.A. (Gorzów Wielkopolski, Poland). Some of its properties are presented below: chemical formula: $(C_6H_{11}NO)_n$, appearance: pellet, color: white, molecular weight (Mw): 26800 g·mol^{-1}, specific weight: 1.4 g·cm $^{-3}$, density (d): 1.084 g·mL^{-1}, melting point: 230 °C, autoignition temperature: 434 °C, and stability: stable (incompatible with strong acids).

CAP was provided by Eastman (Kingsport, Tennessee, USA). Here, some features of CAP are given: chemical formula: $(C_{76}H_{114}O_{49})_n$, appearance: powder, color: white, Mw: 75000 g·mol^{-1}, specific gravity: 1.22, d: 1.23 g·mL^{-1}, melting point: 188–210 °C, autoignition temperature: 432 °C, moisture content: 3.0 max%, and acetyl, propionyl, and hydroxyl (group) contents: 1.3, 48.0, and 1.7 wt.%, respectively.

CAB was also received from Eastman (Kingsport, Tennessee, USA). Some of its properties are presented below: chemical formula: $(C_{84}H_{130}O_{49})_n$, appearance: powder, color: white, Mw: 30000 g·mol^{-1}, melting point: 130 °C.

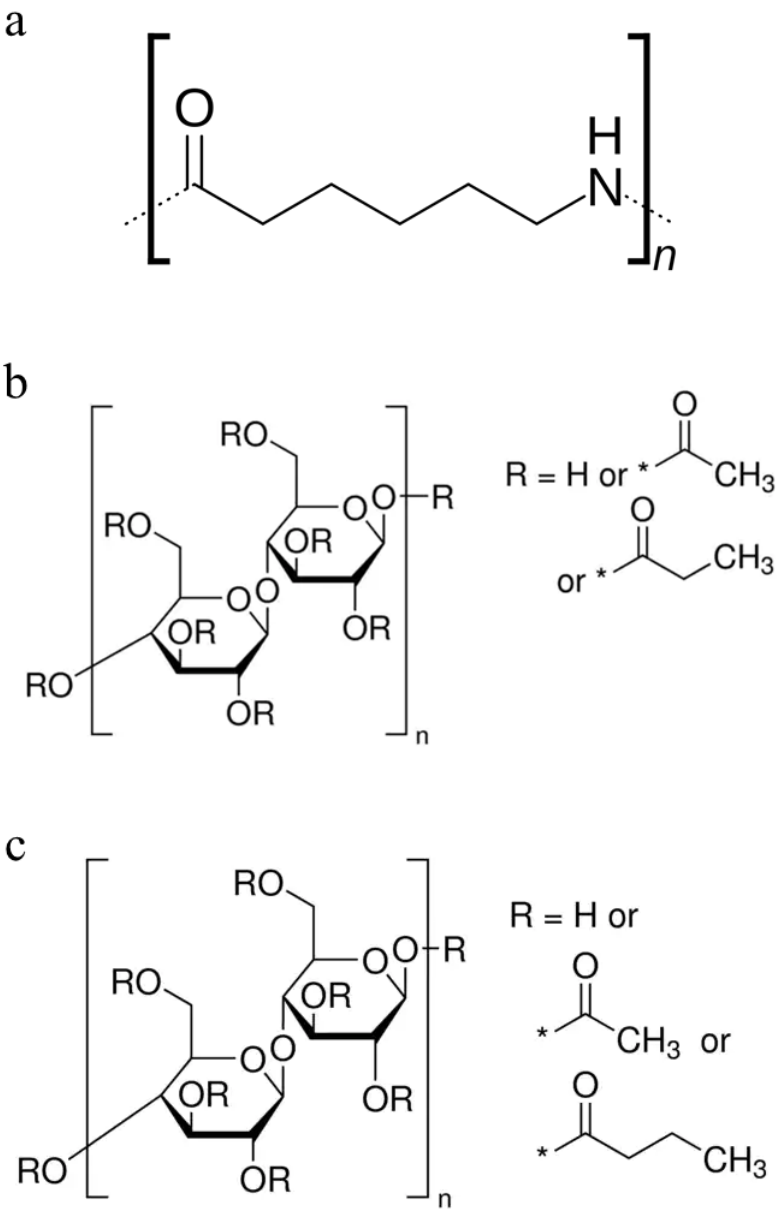

Figure 2.1. Chemical structure of a) polyamide-6, b) cellulose acetate propionate, and c) cellulose acetate butyrate.

2.1.2. Solvents and Chemical Reagents

Following solvents were used:

- formic acid, chemical formula: CH_2O_2, purity: 99%, Mw: 46.03 g·mol^{-1}, d: 1.22 g·mL^{-1}, melting point: 8.3 °C, boiling point: 100–107 °C, company: Chempur, Piekary Śląskie, Poland;

- acetic acid, chemical formula: CH_4O_2, purity: 99%, Mw: 60.052 g·mol^{-1}, d: 1.05 g·mL^{-1}, melting point: 16.6 °C, boiling point: 118 °C, company: Chempur, Piekary Śląskie, Poland;
- chloroform, chemical formula: $CHCl_3$, purity: 99.8%, Mw: 119.38 g·mol^{-1}, d: 1.49 g·mL^{-1}, melting point: -63.5 °C, boiling point: 61.2 °C, company: Fisher Scientific, Hampton, New Hampshire, United States;
- acetone, chemical formula: C_3H_6O, purity: 99%, Mw: 58.08 g·mol^{-1}, d: 0.784 g·mL^{-1}, melting point: -95 °C, boiling point: 56 °C, company: Fisher Scientific, Hampton, New Hampshire, United States;
- diethyl ether, chemical formula: $C_4H_{10}O$, purity: 99.5%, Mw: 74.12 g·mol^{-1}, d: 0.713 g·mL^{-1}, melting point: -116.3 °C, boiling point: 34.6 °C, company: Fisher Scientific, Hampton, New Hampshire, United States;
- dimethylformamide, chemical formula: C_3H_7NO, purity: 99.5%, Mw: 73.09 g·mol^{-1}, d: 0.944 g·mL^{-1}, boiling point: 153 °C, company: Fisher Scientific company, Hampton, New Hampshire, United States.

Other chemical reagents were utilized:

- 1-methylimidazole, chemical formula: $C_4H_6N_2$, purity: 99%, Mw: 82.1 g·mol^{-1}, d: 1.69 g·mL^{-1}, melting point: -6 °C, boiling point: 195–197 °C, flash point: 97°, company: Alfa Aesar, Haverhill, Massachusetts, United States;
- 1-(*n*-butyl)imidazole, chemical formula: $C_7H_{12}N_2$, purity: 99%, Mw: 124.19 g·mol^{-1}, d: 0.948 g·mL^{-1}, boiling point: 257 °C, flash point: 145°, company: Thermo Scientific corporation, Waltham, Massachusetts, United States;
- trifluoromethanesulfonic acid, chemical formula: CF_3SO_3H, purity: +99%, Mw: 150.07 g·mol^{-1}, d: 1.031 g·mL^{-1}, company: Thermo Scientific corporation, Waltham, Massachusetts, United States;
- trifluoroacetic acid, chemical formula: CF_3CO_2H, purity: +99%, Mw: 114.02 g·mol^{-1}, d: 1.535 g·mL^{-1}, boiling point: 72.0 °C, company: Acros Organics BVBA, Thermo Fisher Scientific, New Jersey, United States;
- sulfuric acid, chemical formula: H_2SO_4, purity: 95%, Mw: 98.07 g·mol^{-1}, d: 1.83 g·mL^{-1}, melting point: 10 °C, boiling point: 337 °C, company: Thermo Scientific corporation, Waltham, Massachusetts, United States;

- di-*n*-butyl phosphate, chemical formula: $(CH_3CH_2CH_2CH_2O)_2P(O)OH$, purity: 96%, Mw: 210.21 g·mol^{-1}, d: 1.058 g·mL^{-1}, melting point: -13 °C, boiling point: 250 °C, flash point (FP): 157°, company: Alfa Aesar company, Haverhill, Massachusetts, United States;
- bis(2-ethylhexyl)phosphate, chemical formula: $(CH_3(CH_2)_3CH(C_2H_5)CH_2O)_2P(O)(OH)$, purity: 95%, Mw: 322.42 g·mol^{-1}, d: 0.965 g·mL^{-1}, melting point: -50 °C, boiling point: 48 °C (at 2mm^{-1}), FP: 171°, company: Alfa Aesar company, Haverhill, Massachusetts, United States;
- 2-(dimethylamino)ethanol, chemical formula: $(CH_3)_2NCH_2CH_2OH$, purity: 99%, Mw: 89.14 g·mol^{-1}, d: 0.886 g·mL^{-1}, melting point: -60 °C, boiling point: 134–136 °C, FP: 40°, company: Alfa Aesar company, Haverhill, Massachusetts, United States;
- 3-dimethylamino-1-propanol, chemical formula: $(CH_3)_2N(CH_2)_3OH$, purity: +99%, Mw: 103.16 g·mol^{-1}, d: 0.88 g·mL^{-1}, melting point: -35 °C, boiling point: 162–164 °C, FP: 54°, company: Alfa Aesar company, Haverhill, Massachusetts, United States;
- chlorotrimethylsilane, chemical formula: $(CH_3)_3SiCl$, purity: 98%, Mw: 108.64 g·mol^{-1}, d: 0.85 g·mL^{-1}, boiling point: 57 °C, FP: 18°, company: Acros Organics BVBA, Thermo Fisher Scientific, New Jersey, United States;
- calcium chloride, chemical formula: $CaCl_2$, Mw: 110.98 g·mol^{-1}, d: 0.944 g·mL^{-1}, melting point: 775 °C, boiling point: 1935 °C, density: 2.15 g·mL^{-1}, company: Sigma-Aldrich, Poznań, Poland;
- ethanol, chemical formula: C_2H_6O, purity: 96%, Mw: 46.07 g·mol^{-1}, d: 0.789 g·mL^{-1}, melting point: -114.1 °C, boiling point: 78.37 °C, company: VWR International, Radnor, Pennsylvania, United States;
- methanol, chemical formula: CH_3OH, purity: 99.9%, Mw: 32.04 g·mol^{-1}, d: 0.792 g·mL^{-1}, melting point: -97.6 °C, boiling point: 64.7 °C, company: Fisher Scientific company, Hampton, New Hampshire, United States.

Deionized water was obtained by Milli-Q system (18.2 MΩ·cm, Millipore®, Fontenay-sous-Bois, France). For cooling the chemical reactors, liquid nitrogen was used.

2.1.3. Hydrophobization of Petri dish Glass

In general, the hydrophilic polymer membranes sticking to the glass is a common problem. In fact, since numerous hydroxyl groups (−OH) are present in the CAP and CAB structures (Figs. 2.1b and 2.1c), hydrogen bonds may be formed between the polymer membrane and Petri dish, thus making difficult membrane peeling. One of the effective way to overcome this problem is to hydrophobize the glass plate (Fig. 2.2). In this study, chlorotrimethylsilane (TMSCl) was utilized for hydrophobization. In the first step,

the adequate amount of concentrated sulfuric acid was poured in the Petri dish for 30 min. Subsequently, acid was removed and Petri dish was washed with deionized water and then placed in the oven for 1 h at 80 °C. The dried Petri dish was submerged in the solution containing dimethylformamide (DMF) and TMSCl (320 mL and 38 g, respectively) for 24 h. Finally, the hydrophobized Petri dish was washed with deionized water and placed in the oven for 1 h at 80 °C. It was observed that after hydrophobization, the polymer membranes were peeled off without any difficulty.

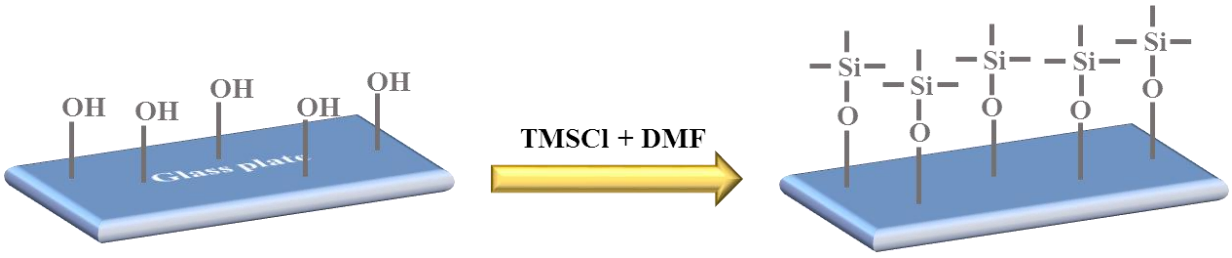

Figure 2.2. Hydrophobization of the Petri dish.

2.2. Ionic Liquids

Three commercial A-ILs were purchased whereas eighteen Pr-ILs were synthesized.

2.2.1. Commercial ILs

All commercial ILs were purchased from SOLVIONIC (Chemin des Silos, Toulouse, France):

- 1-(4-sulfobutyl)-3-methylimidazolium trifluoromethanesulfonate ([SMIM][TFS]) (Fig. 2.3a), chemical formula: $C_9H_{15}F_3O_6S_2N_2$, purity: 98%, appearance: liquid, color: colorless, Mw: 368.35 g·mol^{-1}, $H_2O \leq 0.2\%$;
- 1-(4-sulfobutyl)-3-methylimidazolium hydrogen sulfate ([SMIM][HS]) (Fig. 2.3b), chemical formula: $C_8H_{16}O_7S_2N_2$, purity: 98%, appearance: liquid, color: colorless, Mw: 316.35 g·mol^{-1}, $H_2O \leq 1\%$;
- 1-(4-sulfobutyl)-3-methylimidazolium bis(trifluoromethanesulfonyl)imide ([SMIM][TFSI]) (Fig. 2.3c), chemical formula: $C_{10}H_{15}F_6O_7S_3N_3$, purity: 98%, appearance: liquid, color: colorless, Mw: 499.43 g·mol^{-1}, $H_2O \leq 0.2\%$.

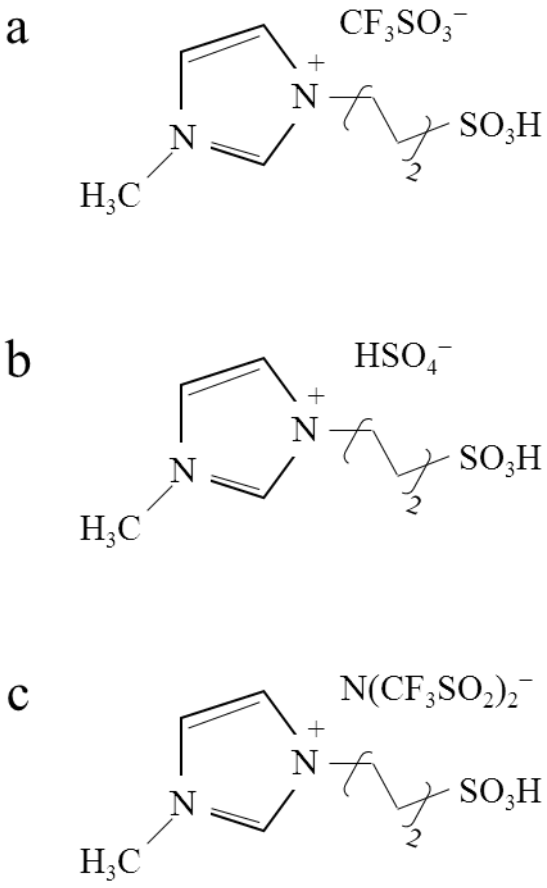

Figure 2.3. Chemical structure of a) [SMIM][TFS], b) [SMIM][HS], and c) [SMIM][TFSI].

2.2.2. Synthesized ILs

Several imidazolium- (Fig. 2.4) and hydroxylammonium- (Fig. 2.5) based Pr-ILs were synthesized by an acid-base neutralization method. For this purpose, acid and base were used in equimolar amounts. The details about synthesis of Pr-ILs are gathered in Chapter 4.

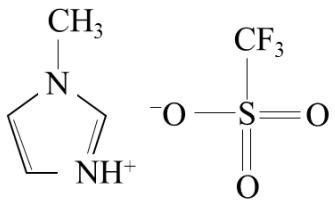

1-methylimidazolium trifluoromethanesulfonate [MIM][TFS]

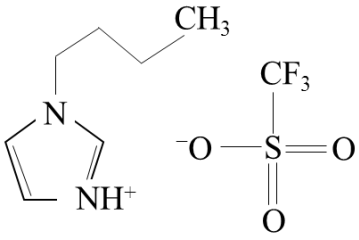

1-(n-butyl)imidazolium trifluoromethanesulfonate [BIM][TFS]

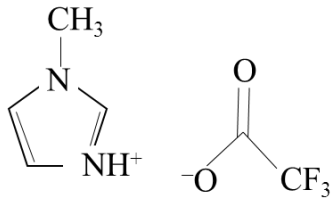

1-methylimidazolium trifluoroacetate [MIM][TFA]

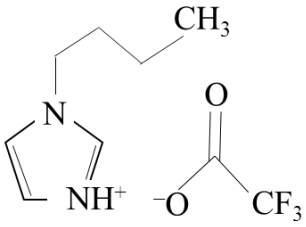

1-(n-butyl)imidazolium trifluoroacetate [BIM][TFA]

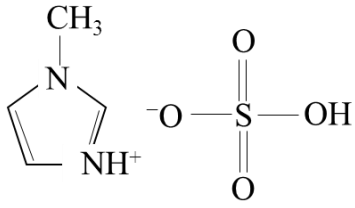

1-methylimidazolium hydrogen sulfate [MIM][HS]

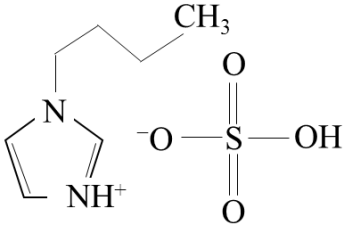

1-(n-butyl)imidazolium hydrogen sulfate [BIM][HS]

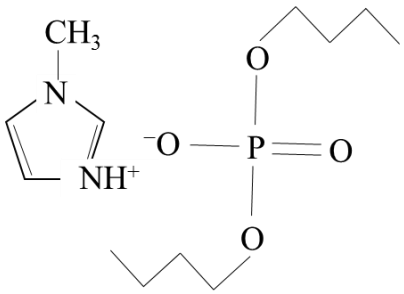

1-methylimidazolium di-n-butyl phosphate [MIM][BUPH]

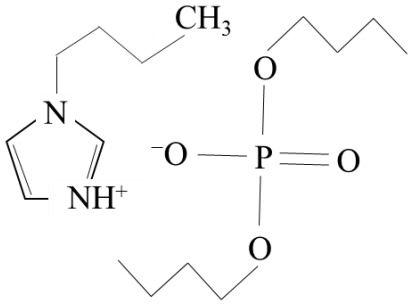

1-(n-butyl)imidazolium di-n-butyl phosphate [MIM][BUPH]

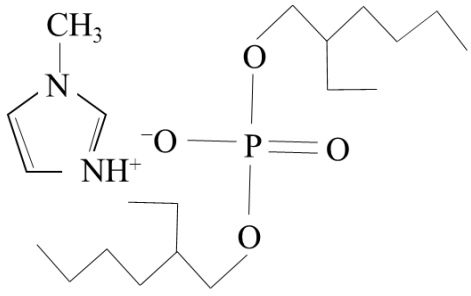

1-methylimidazolium bis(2-ethylhexyl) phosphate [MIM][EHPH]

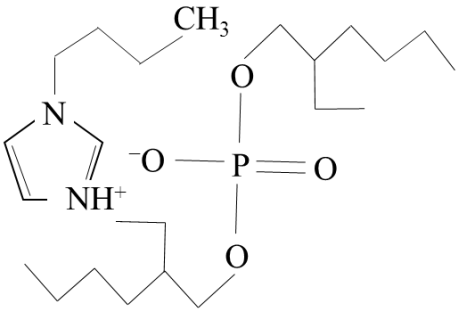

1-(n-butyl)imidazolium bis(2-ethylhexyl) phosphate [BIM][EHPH]

Figure 2.4. Chemical structure of imidazolium-based Pr-ILs.

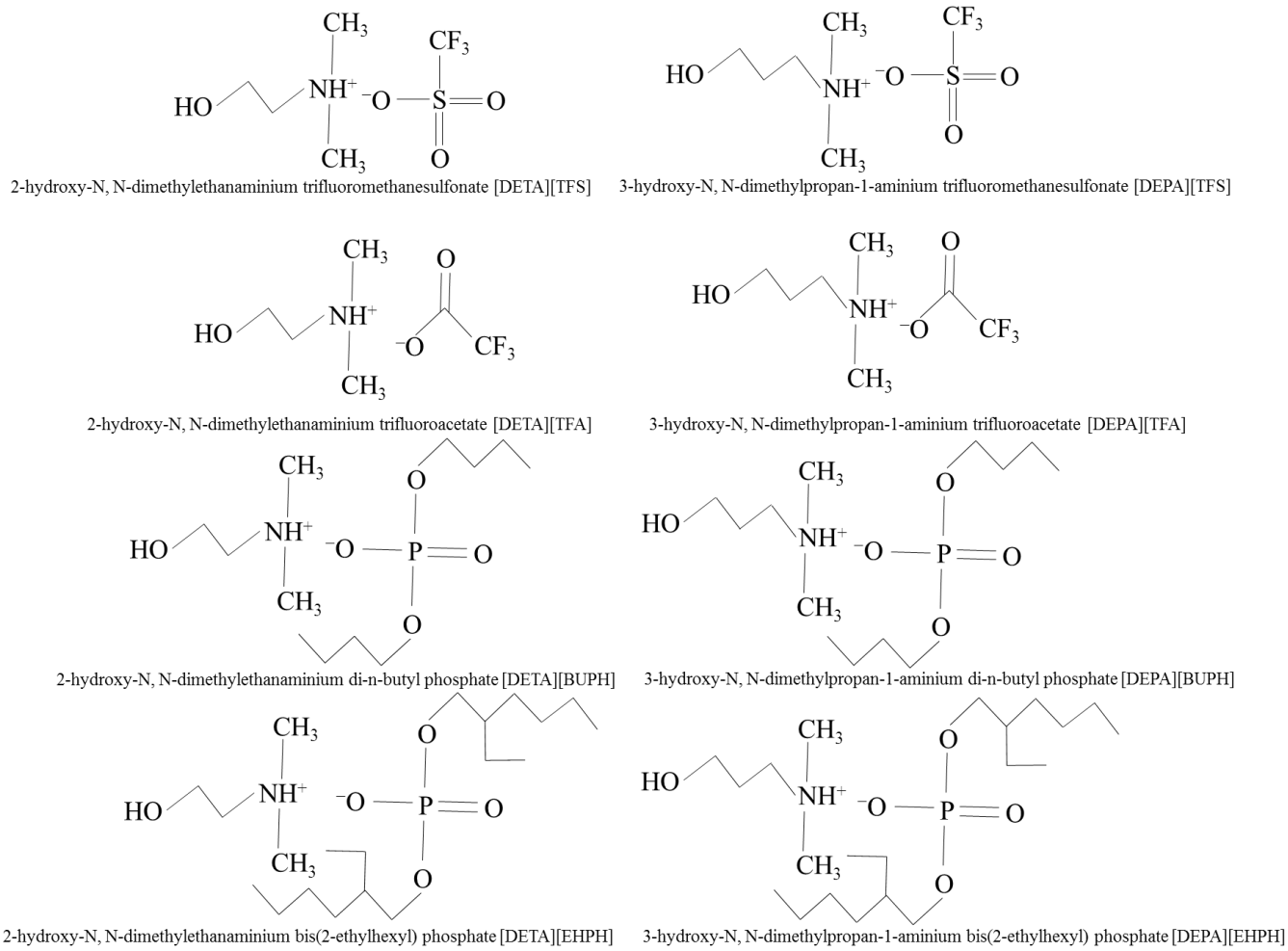

Figure 2.5. Chemical structure of hydroxylammonium-based Pr-ILs.

2.3. Membrane Fabrication

2.3.1. PA6 Membrane

The original protocol for preparation of PA6 membrane was proposed by Ceynowa and Adamczak [122]. Initially, PA6 pellets were dissolved in the solution containing formic acid (43 mL) and acetic acid (8 mL) to obtain a 13.5 wt.% solution. The solution was stirred vigorously for 24 h at 25 ± 3 °C to obtain homogenous polymer solution. In the next step, 8.3 g of calcium chloride was dissolved in 17.5 mL of water (to improve PA6 mechanical properties) [122]. Subsequently, the aqueous solution of $CaCl_2$ was slowly added to the polymer solution. The obtained solution was stirred for another 24 h at 25 ± 3 °C and then filtered to remove impurities. The PA6 membrane was prepared *via* phase inversion method induced by non-solvent in which the resultant polymer solution was cast on the hydrophobic glass by automatic film applicator (Erichsen Gmbh Co., Hemer, Germany). The slit of casting knife and casting rate were 0.2 mm

and 10 mm·sec^{-1}, respectively. During next crucial step (Fig. 2.6) glass plate with the cast polymer solution was exposed to air for a certain time. This time is known as gelation time and membranes with different gelation times (0 (M_0), 2 (M_2), 4 (M_4), and 10 (M_{10}) min) were prepared. After the delay stage, the membrane with the glass plate was submerged into the coagulation bath (containing deionized water) till the polymer film formation (Fig. 2.6). The resultant PA6 membrane was washed in the deionized water for 24 h for removing the solvent traces and then dried at 100 °C for 24 h. The fabricated PA6 membrane was opaque, flexible, and white in color.

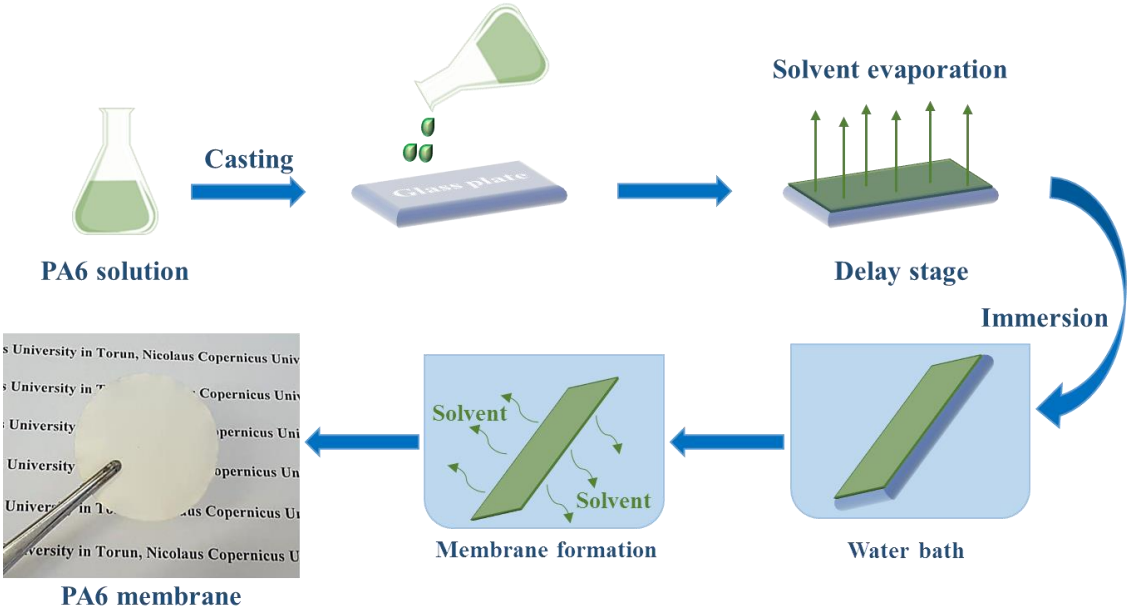

Figure 2.6. PA6 membrane preparation by phase inversion technique.

2.3.2. Composite CAP/IL- and CAB/IL-based Membranes

The composite CAP/IL- and CAB/IL-based membranes were fabricated by a phase inversion method induced by the solvent evaporation. For this purpose, CAP (or CAB) powder was added to the vessel containing acetone/chloroform (50/50, w/w) to obtain 10 wt.% polymer solution and the solution was stirred for 12 h at 25 ± 3 °C (Fig. 2.7). Then, IL was added to obtained solution and stirred for 16 h at 25 ± 3 °C until obtaining homogenous composite solution. Subsequently, the composite solution was sonicated for 30 min and left without movement for another 24 h to remove air bubbles from solution. The solution was cast on the hydrophobized Petri dish and covered with the lid till complete solvent evaporation. In order to remove the solvent traces, the membrane was placed in an oven for 24 h at 80 °C. The scheme of the composite CAP/IL- and CAB/IL-based membranes fabrication is depicted in Fig. 2.7. The thickness of membrane samples was measured by a micrometer device (Sylvac, Switzerland). Prior to perform the

thickness measurement, the membranes should be dried at appropriate temperature (~ 80 °C). To evaluate the quality of membrane formation, the measurement was repeated on 30 different places of polymer film.

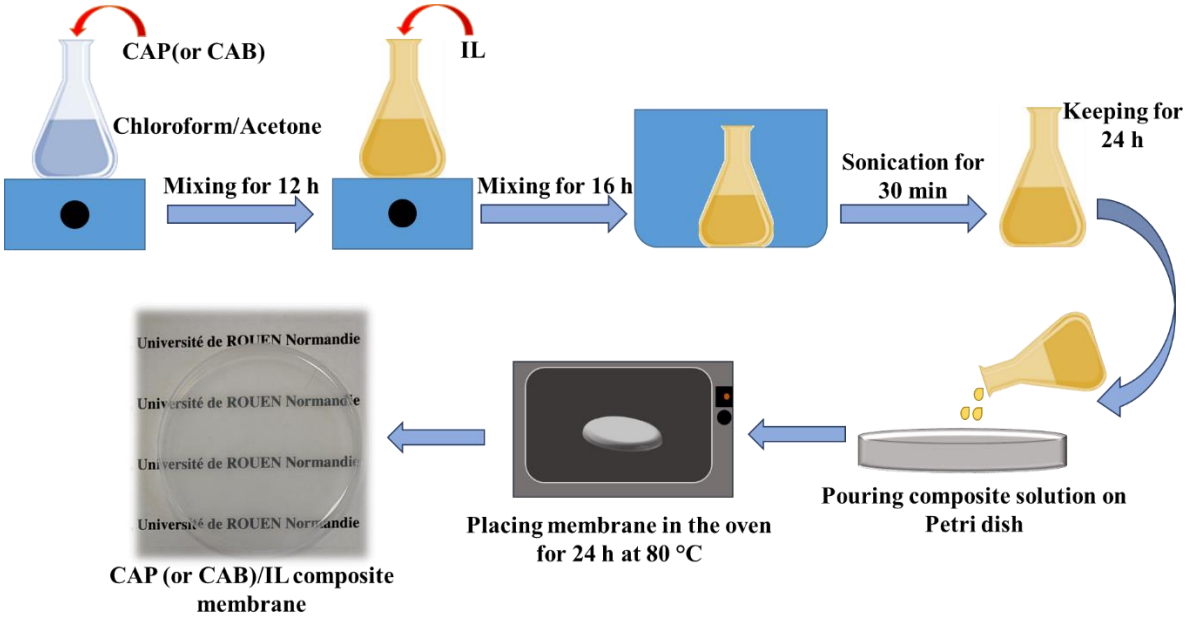

Figure 2.7. Fabrication of CAP (or CAB)/IL-based membrane.

2.4. Physical-Chemical Characterization Methods

2.4.1. Nuclear Magnetic Resonance (NMR) Spectroscopy

The ^{1}H NMR and ^{19}F NMR spectra were recorded by Bruker Avance DRX 300 MHz spectrometer (Bruker, Wissembourg, France) with gradient amplifier at the operating temperature of 25 °C. This spectrometer takes advantage of a 5 mm triple-resonance TXI (^{1}H and ^{19}F) probe containing shielded z-gradient. Dimethyl sulfoxide (DMSO–d_6) was used as the solvent for performing the NMR experiments. The peak at the chemical shift of 2.50 ppm is for DMSO-d_6 in ^{1}H NMR spectra.

The utilized internal standards for ^{19}F NMR were fluorotrichloromethane or hexafluorobenzene. Different operation conditions of experiments were defined for ^{1}H NMR and ^{19}F NMR experiments: scan: 64, recycle delay time: 2.5 s, domain points: 65536 for ^{1}H NMR spectra and scan: 32, recycle delay time: 10 s, domain points: 65536 for ^{19}F NMR spectra. The sample concentration was in the range of 3.33 to 20 mg·mL^{-1}. MestReNova sofware (version 5.3.0-4399) was used for the analysis.

2.4.2. Fourier Transform Infrared (FTIR) Spectroscopy

The FTIR analysis was performed in attenuated total reflection (ATR) mode. Nicolet Avatar iS50 spectrometer (Thermo Fischer, Waltham, Massachusetts, United States) was used with a germanium crystal. The FTIR-ATR spectra were recorded in the range from 4000 to 500 cm^{-1}. The spectra were measured using 128 scans with the resolution of 2 cm^{-1}. Omnic® software (version 5.2a) was used for the analysis.

2.4.3. Thermogravimetric Analysis (TGA)

TGA 209 F1 apparatus (Netzsch, Germany) was used and the analysis was performed in both dynamic and static (isothermal) modes. TGA test was carried out under nitrogen atmosphere with the N_2 flow rate of 20 $mL \cdot min^{-1}$. The dynamic TGA measurements were performed at the temperature range from 25 to 800 °C and heating rate of 10 $°C \cdot min^{-1}$. The static measurements were conducted at a specified temperature (80, 100, and 120 °C) for 24 h. Degradation temperature (T_{deg}) (T_{deg} corresponds to the most intensive weight loss) as well as temperatures of 5 and 10% of weight loss (T_5 and T_{10}%) were determined using Proteus® software (version 8.0.0 19107.3).

2.4.4. Differential Scanning Calorimetry (DSC)

DSC analysis was carried out by the DSC 200 F_3 apparatus (Netzsch, Germany). The indium standard was used for temperature and energy calibration. All tests were carried out under N_2 atmosphere for preventing oxidative degradation. The certain amount (between 5 and 10 mg) of sample (IL or membrane) was placed in an aluminum pan and sealed. An empty sealed aluminum pan was used as the reference. The DSC analysis of membranes was conducted by heating/cooling cycle performed twice with the rate of 10 $°C \cdot min^{-1}$ from of -70 to 200 °C and for Pr-ILs – the analysis was carried out by heating/cooling/heating cycle at 10 $°C \cdot min^{-1}$ from -150 to 250 °C. Proteus® software (version 6.1.0) was used for the data analysis.

2.4.5. Scanning Electron Microscopy (SEM) Coupled with Energy-Dispersive X-Ray (EDX) Spectroscopy

SEM microscope (LEO 1430 VP, LEO Electron Microscopy Ltd. Cambrigde, England) equipped by EDX spectrometer (Quantax 200, Bruker AXS Microanalysis GmBH, Germany) and EDX detector (XFlash 4010, Bruker AXS Microanalysis GmBH, Germany) was used at 10 kV. SEM images of the membrane surface and cross-section were analyzed. The liquid nitrogen was utilized for membrane fracturing prior to measurements.

2.4.6. Atomic Force Microscopy (AFM)

A microscope equipped by scanning probe microscopy (SPM) probe of the NanoScope MultiModetype (Veeco Metrology, Inc., Santa Barbara, CA, USA) in tapping mode was used for determining the surface roughness of membrane samples. In order to analyze the AFM results, Nanoscope software (version 6.11) (Bruker Optoc GmbH, Ettlingen, Germany) was used. Average roughness (R_a) and root mean square (R_q) values were determined. Average roughness is typically used to detect general variations in the whole profile height specifications and is calculated as follows [123]:

$$R_a = \frac{1}{L_x L_y} \int_0^{Lx} \int_0^{Ly} \left| f(x,y) \right| dxdy, \tag{2.1}$$

where f(x,y) is surface relative to the center plane and L is surface dimension.

To represent the standard deviation of profile height, root mean square is used [123]:

$$R_q = \sqrt{\frac{\sum (Z_i - Z_{ave})^2}{N_p}}, \tag{2.2}$$

where Z_i, Z_{ave}, and N_p are the current height value, average height, and number of points in a given area, respectively.

2.4.7. Swelling Degree

The membrane swelling degree was measured taking into account the membrane dimension. The circle-like membrane sample was initially immersed in the water for 24 h and its dimension (i.e. wet dimension) was measured. Then, the membrane was placed in the oven for another 24 h at 80 °C and the membrane dimension was measured once again. Swelling degree (single-dimensional, area, and volume) is calculated as follows [111,114]:

$$Single\text{-}dimensional\ \% = \left(\frac{t - t_0}{t_0} \right) \cdot 100, \tag{2.3}$$

$$Swelling\ Area\ (\%) = \left(\frac{A_w - A_0}{A_0} \right) \cdot 100, \tag{2.4}$$

$$Swelling\ Volume\ (\%) = \left(\frac{V - V_0}{V_0} \right) \cdot 100, \tag{2.5}$$

where t, A_w, and V are thickness, surface area, and volume of membrane in wet state, respectively, and t_0, A_0, V_0 are the membrane thickness, surface area, and volume in dry state. The measurements were repeated three times for each membrane sample for the measurement accuracy.

2.4.8. Water Uptake (WU)

The standard protocol for measuring WU consists of several steps. Firstly, the membrane was dried at the temperature of 80 °C during 6 h. Subsequently, the dried membrane was weighed (W_{dry}). In the next step, the membrane was swelled in the water for 24 h and the sample was again weighed (W_{wet}) after removing extra water from the membrane surface by a tissue. The measurements were repeated three times for the accuracy. The WU is calculated using the following equation [124,125]:

$$WU\ (\%) = \left(\frac{W_{wet} - W_{dry}}{W_{dry}} \right) \cdot 100 \qquad 2.6$$

2.4.9. Contact Angle (CA) Measurements

CA measurements were carried out by two techniques (sessile drop; and captive bubble) using contact angle meter (Goniometer, Optical Tensiometer, Theta Flex, Biolin Scientific, Gothenburge, Sweden).

The sessile drop method is the most used technique to evaluate the wettability of solid materials and it can be carried out in both dynamic and static modes [126]. For this purpose, a liquid drop (i.e. water, glycerol, and diiodomethane) is deposited on the solid surface. An angle is formed between a liquid and solid phases (Fig. 2.8a). There exist different theories to determine and explain the CA and among them Young's, Wenzel's, and Cassie–Baxter's theories are the most common [127].

In our case, Young's equation can be applied but this equation can be only used for smooth surfaces [127,128]:

$$\cos\theta_Y = \frac{\gamma^{sg} - \gamma^{sl}}{\gamma^{lg}}, \qquad 2.7$$

where θ_Y is contact angle, γ^{sg}, γ^{sl}, and γ^{lg} are interface tension of solid/gas, solid/liquid, and liquid/gas phases, respectively. For hydrophilic surfaces, the θ_Y value is lower than 90° and the liquid is spread on the solid surface, thus making it whereas for hydrophobic surfaces, the value of θ_Y is higher than 90° and the liquid is not able to wet the solid surface:

The Wenzel's theory is another important theory to calculate the CA considering surface roughness. Indeed, the Wenzel's equation (Eq. 2.8) is similar to Young's equation (Eq. 2.7). The only difference between them is the presence of roughness factor (r) in Wenzel's equation. The roughness factor is described as the actual area of the membrane surface divided by the apparent geometry area. This factor always is higher than one owing to the fact that the apparent geometry area is lower than the actual area of the membrane surface [127,129].

$$\cos\theta_w = \frac{r\left(\gamma^{sg} - \gamma^{sl}\right)}{\gamma^{sl}} = r\cos\theta_Y, \qquad 2.8$$

As a result, the roughness factor will reduce hydrophilicity when the value of θ_Y is higher than 90°, while when the value of θ_Y is lower 90°, the roughness factor will enhance hydrophilicity.

Cassie and Baxter modified the Wenzel's theory for hydrophobic surfaces by introducing the horizontal projection area fraction of the solid-liquid interface (φ) to the Wenzel's equation [127]:

$$\cos\theta_{CB} = r\cos\theta_Y + \varphi + 1, \qquad 2.9$$

Another technique to measure the CA value is the captive bubble method (Fig. 2.8b). This method is used in the case of super hydrophilic and porous membranes when measurement by the sessile drop method is not possible as the water drop is immediately absorbed by the surface [126,130]. The air bubble is formed on the immersed sample by using J-type needle (Fig. 2.8b). The CA determination is based on the Young's equation (Eq. 2.7).

In order to evaluate the CA values of membrane samples, One Attention software (version 4.02) was used. The measurements (both by sessile drop and captive bubble methods) were carried out at 24 ± 3 °C. Measurements were repeated 5–6 times to estimate the measurement accuracy.

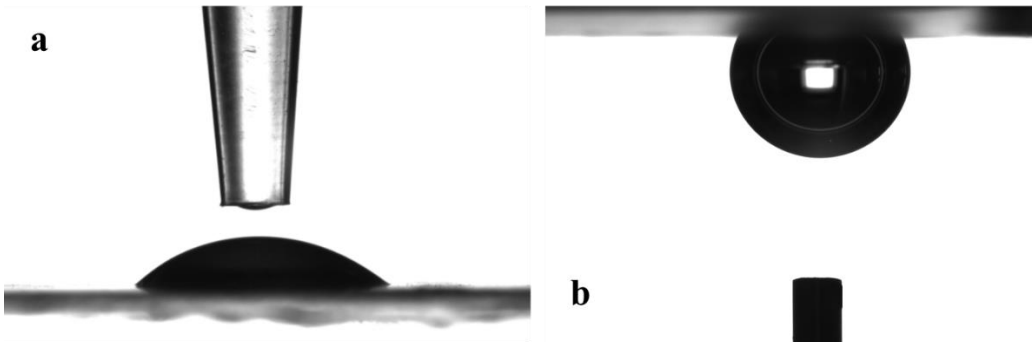

Figure 2.8. Illustration of CA measurements with sessile drop (a) and the captive bubble (b) techniques.

2.4.10. Average Pore Size and Porosity Measurements

The pore size (average, maximum, and minimum pore size) was determined by Porometer 3G Micro (Quantachrome Instruments, Boynton Beach, FL, USA). The average, maximum, and minimum pore size was obtained by applying modified bubble point method [131-133]. The principle of this technique is based on the measurement of the necessary pressure for passing an inert gas (such as nitrogen) through the wet porous film [134]. Before starting the test, the membrane should be immersed in a liquid with a very low surface tension (in our case Porefil was used with the surface tension of 16.6 $mN \cdot m^{-1}$) in order to fill all membrane pores with liquid [131,133,135]. The experiment is divided into two runs: 1. wet run; 2. dry run. During the wet run, nitrogen gas removes the liquid from the pores by applying the increasing pressure to the membrane which opens the pores from the biggest to the smallest ones (Fig. 2.9a). During dry run, the inert gas passes continuously through the membrane in order to measure the gas flow as a function of pressure. Moreover, the pore size distribution of the membrane can be estimated by plotting the pore size curve as a function of the differential flow (Fig. 2.9b).

The measurement of pore size is performed by increasing the pressure. For measurement accuracy, the test was repeated twice for each porous membrane. In order to calculate the pore radius, Laplace equation is used [131,133]:

$$r_p = \frac{2\sigma}{\Delta p}\cos\theta, \qquad 2.10$$

where r_p is the pore radius, σ is the surface tension of air-liquid interface, Δp is the applied pressure, and θ is the wetting angle with membrane solid matrix. When liquid wets completely the polymer membrane, $\cos\theta = 1$. It can be seen that there exists an opposite correlation between the pore radius (pore size) and applied pressure (Eq. 2.10).

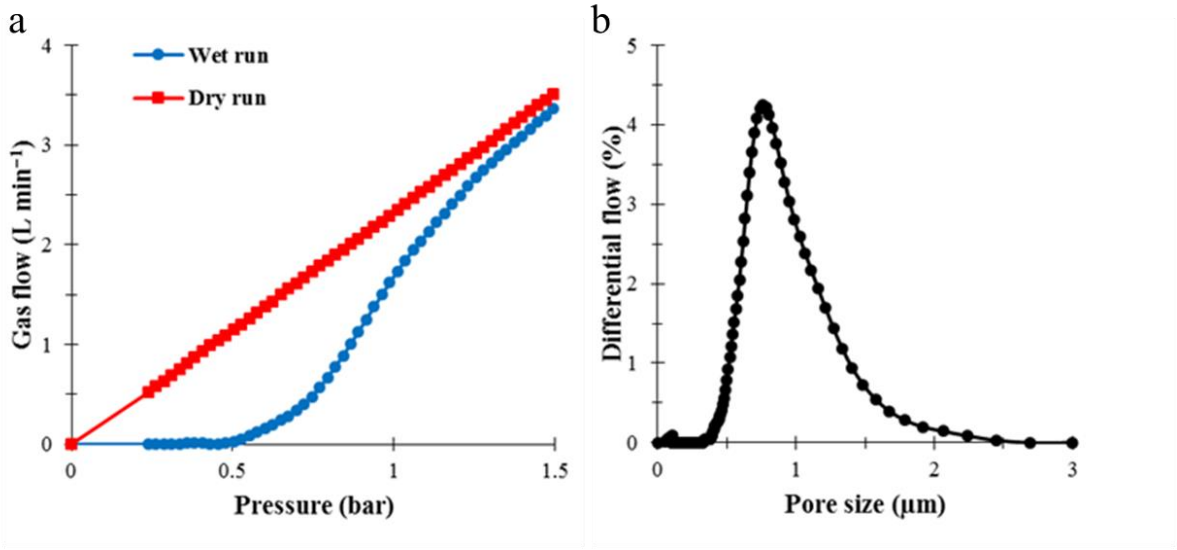

Figure 2.9. Bubble point method: a) gas flux measured during wet and dry runs; b) pore size distribution.

To measure the membrane porosity, the membrane sample was firstly placed in the oven at 80 °C for 6 h. Then it was weighted (W_{dry}) and its dimension (diameter and thickness) was determined. After this step, membrane was immersed in the deionized water for 24 h at 24 ± 3 °C. The extra water from the membrane surface was removed by tissue and the membrane was weighted again (W_{wet}). The porosity (ε) value was determined as follows [124,136]:

$$\varepsilon\ (\%) = \left(\frac{W_{wet} - W_{dry}}{\rho_{water} \cdot A \cdot L} \right) \cdot 100, \qquad 2.11$$

where W_{wet}, W_{dry}, ρ_{water}, A, and L are the membrane weight in wet state, the membrane weight in dry state, water density, membrane surface area, and membrane thickness, respectively. The measurements for each membrane was repeated three times.

2.4.11. Mechanical Tensile Tests

The mechanical properties of fabricated membranes were measured by the Shimadzo EZ-X machine (SHIMADZU, Kyoto, Japan) based on the PN-C-89034:1981 standard. The membrane samples with certain profile (length: 30 mm, width: 5 mm) were prepared. The prepared sample was fixed between two clamps. The measurement started by stretching the sample between two clamps with a strain rate of 1 $cm \cdot min^{-1}$ till the sample breaking. The mechanical test was performed at 25 ± 2 °C, and 40 ± 2% of relative humidity. Tensile strength, Young's modulus, maximum force, elongation at break, stress at break, and force at the break were determined by Trapeziumx software (version 1.5.4). For each membrane at least five samples were tested [137,138].

2.4.12. Filtration Test

To measure the hydrodynamic water flux through a porous membrane, a dead-end filtration setup was used (Fig. 2.10). The experimental setup includes cell, air tank, mixer, rubber gasket (O-ring), membrane, and water tank. The cylindrical cell with volume of 200 mL and the active surface area of 25.2 cm^2 was used. The membrane was fixed on the cell bottom. An O-ring gasket was utilized to seal the cell. A volume of 5 L was used to have continuous filtration for a long-duration process. The membrane hydrodynamic water flux was evaluated at three different operating pressures − 0.5, 1.0, and 2.0 bar by the following equation [139]:

$$J_v = \frac{\Delta V}{A \cdot \Delta t}, \quad 2.12$$

where J_v, ΔV, A, and Δt are hydrodynamic water flux, volume of permeate, area of the used membrane, and duration of filtration, respectively.

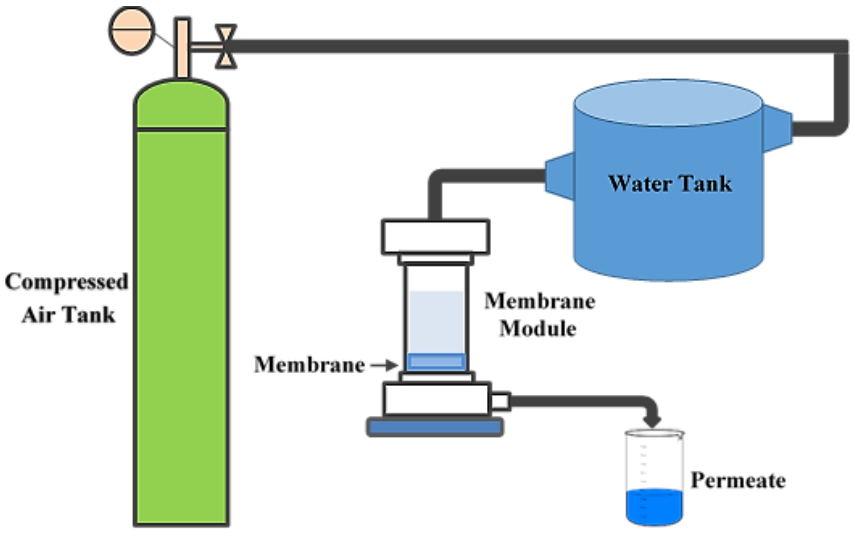

Figure 2.10. Experimental filtration setup (From "Fabrication of Polyamide-6 membranes—The effect of gelation time towards their morphological, physical and transport properties" by Ebrahimi, M.; Kujawski, W.; Fatyeyeva, K., 2022, Membranes, 12, 315, under the license CC BY 4.0) [139].

The membrane hydrodynamic permeability (L_p) was calculated by Hagen Poiseuille equation (Eq. 2.13). A high L_p value is characterized for the membrane with large pores, while a low L_p value reveals the small membrane pores [131].

$$J_v = \frac{\rho \varepsilon \pi r^2}{8 \eta \tau} \cdot \frac{\Delta p}{l}, \quad 2.13$$

and

$$L_p = \frac{\rho \varepsilon \pi r^2}{8 \eta l \tau} \qquad 2.14$$

By merging Eq. 2.13 and 2.14, the L_p value may be expressed as:

$$L_p = \frac{J_v}{\Delta p}, \qquad 2.15$$

where L_p is the membrane hydrodynamic permeability, Δp is the operating pressure, ρ is the fluid density, ε is the membrane porosity, r is the radius of pore, η is the viscosity of the medium, l is the membrane thickness, and τ is the tortuosity factor,.

The rejection rate of porous membranes was also determined. For this purpose, an aqueous solution of polyethylene glycol (PEG) with the molecular weight of 20000 $g \cdot mol^{-1}$ was prepared. The porous membranes were compressed at 3 bar for 2 h prior to start each measurement. The cell was filled with the PEG solution and the filtration was performed under determined operating pressure (2 bar). The filtration was carried out under vigorous stirring (1000 rpm) in order to decrease the concentration polarization influence. The rejection rate (R) is calculated by following equation [139]:

$$R\ (\%) = \left(1 - \frac{C_p}{C_f}\right) \cdot 100, \qquad 2.16$$

where C_p and C_f are the PEG concentration in the downstream and upstream compartments, respectively. An UV−VIS Spectrometer Lambda 25 apparatus was utilized to measure the PEG concentration in solution.

2.4.13. Ionic Conductivity Measurement

The electrochemical impedance spectroscopy (EIS) was used to evaluation of ionic conductivity of Pr-ILs and composite membranes. For this purpose M_2 Materials Mates 7620 impedance analyzer (Italy) was used. The measurements were carried out at the temperature range between 25 and 150 °C and frequency range from 0.1 Hz to 5 MHz. Impedance results were represented by Nyquist plot (Fig. 2.11). The resistance of the each sample was measured from the intersection of circle with the horizontal axis (Fig. 2.11). In the case of liquid (i.e. IL), the liquid (between 2 and 3 mL) was poured in a cylindrical glass cell which is connected to the thermostat (Lauda, Königshofen, Germany). Two Pt parallel electrodes were placed in the cell in order to measure the liquid resistance. In case of the polymer films, four Pt electrodes were placed on the sample surface. Two internal electrodes are used for measuring the applied current and

two external electrodes – to measure the potential. The conductivity was determined for each sample during two heating/cooling cycles and after the isothermal step during 24 h at the highest possible temperature. Scope® (version 4.1.0.4) and Zview® (version 2.9c) softwares were used for the analysis. The ionic conductivity was calculated by following equation [140,141]:

$$\sigma = \frac{1}{R} \cdot \frac{d}{e \cdot l}, \qquad 2.17$$

where σ, R, d, e, and l are ionic conductivity, the sample resistance, distance between electrodes, membrane width, and membrane thickness, respectively.

Also, the apparent activation energy of transport was measured by Arrhenius equation [117-119,142]:

$$\sigma = \sigma_0 \exp\left(\frac{-E_a}{RT}\right), \qquad 2.18$$

where σ, σ_0, E_a, R, and T are ionic conductivity, pre-exponential factor, activation energy, universal gas constant, and absolute temperature, respectively.

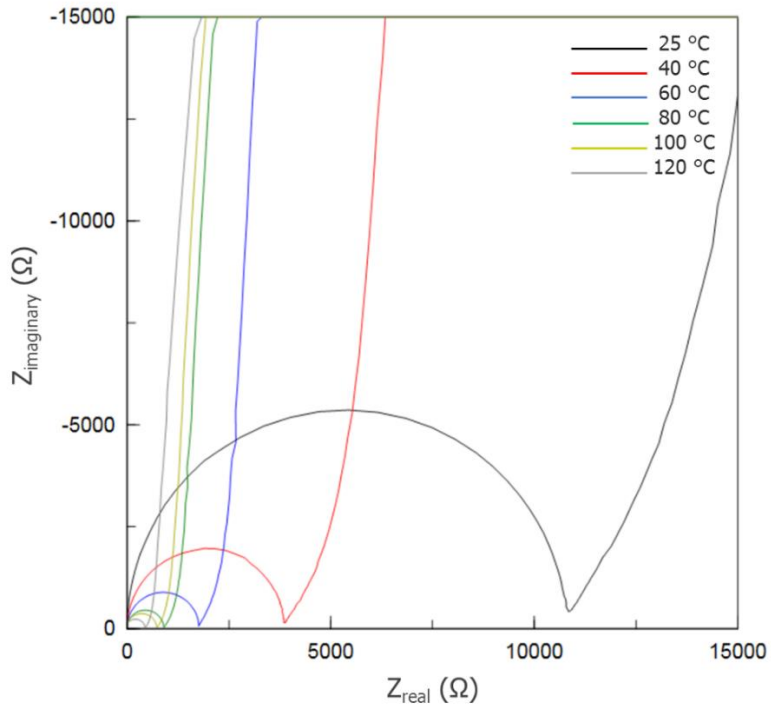

Figure 2.11. The Nyquist plot of the [BIM][BUPH] at various operating temperatures.

2.4.14. Leaching Test

In order to evaluate the stability of ILs in the composite membranes, leaching test was carried out for composite membranes. For this purpose, the membrane was initially dried at 80 °C for 24 h and weighted (W_0). Then, the membrane was immersed into the deionized water for 24 h and then dried for another 24 h at 80 °C. The dried membrane was again weighted (W_i). The leaching test was performed for composite membranes at 25 and 80 °C. Following equation was used to calculate the IL quantity leached from the composite membrane [143-146]:

$$Weight\ Loss\ (\%) = \frac{W_0 - W_i}{W_i} \cdot 100 \qquad 2.19$$

Chapter 3. Ionic Liquids: Synthesis and Characterization

This chapter is devoted to the description of synthesis of several Pr-ILs containing various cations and anions by acid-base neutralization reaction. The influence of anion and cation nature on the thermal property and ionic conductivity of ILs is evaluated. In fact, owing to the huge diversity of the number of available anions and cations, numerous types of ILs can be synthesized with various chemical structures and different thermal, chemical, and physical properties [147,148]. Up to now, a number of researches have been carried out [117,147,149,150]. However, there is still a debate regarding the main factors influencing the ILs properties (i.e. anion and cation type, chain length, substituent number, pK_a and pK_b values, and functionalization). In order to have a better vision and understanding of the correlation between these factors and IL thermochemical properties, deeper investigations are needed.

Eighteen Pr-ILs containing different imidazolium- (i.e. 1-methylimidazolium ([MIM]) and 1-(*n*-butyl)imidazolium ([BIM]) and hydroxylammonium- (2-hydroxy-N,N-dimethylethanaminium ([DETA]) and 3-hydroxy-N,N-dimethylpropan-1-aminium ([DEPA])) based cations and various anions (such as [TFS], [TFA], [BUPH], [EHPH], and [HS]) have been synthesized. The chemical structure of obtained Pr-ILs was confirmed by performing FTIR and NMR (^{1}H and ^{19}F) analyses. TGA (in both dynamic and static modes) and DSC analyses were carried out to evaluate thermal properties of synthesized Pr-ILs. In addition, ionic conductivity of Pr-ILs was measured (in dynamic and isothermal modes) in the wide temperature range by using EIS.

3.1. ILs synthesis

Acid-base neutralization reaction for Pr-ILs synthesis was used in this study [117-119,149,150]. The neutralization reaction was carried out in one step. To investigate an influence of the chemical structure of the synthesized Pr-ILs on their thermochemical properties, two different types of cations (i.e. imidazolium- (Fig. 3.1) and hydroxylammonium-based (Fig. 3.2) cations) with different length of alkyl and hydroxyl chains were used. Moreover, various anions (i.e. perfluorinated-, phosphate-, and sulfate-based anions) were utilized. Diethyl ether was used as the solvent. After the neutralization reaction, the solvent was removed and resultant Pr-ILs was washed three times (with diethyl ether) to remove the unreacted products. The acid-base neutralization reaction is an exothermic reaction. For this reason, the synthesis was done in bath (i.e. methanol or water) for controlling the temperature at 5–10 °C. In the final step, each Pr-IL was dried at the certain temperature and under vacuum condition. Some physical characteristics of synthesized Pr-ILs are gathered in Table 3.1. All synthesized Pr-ILs (except [MIM][TFS], [MIM][TFA], [BIM][TFA], and [DETA][TFA]) are liquid at room temperature.

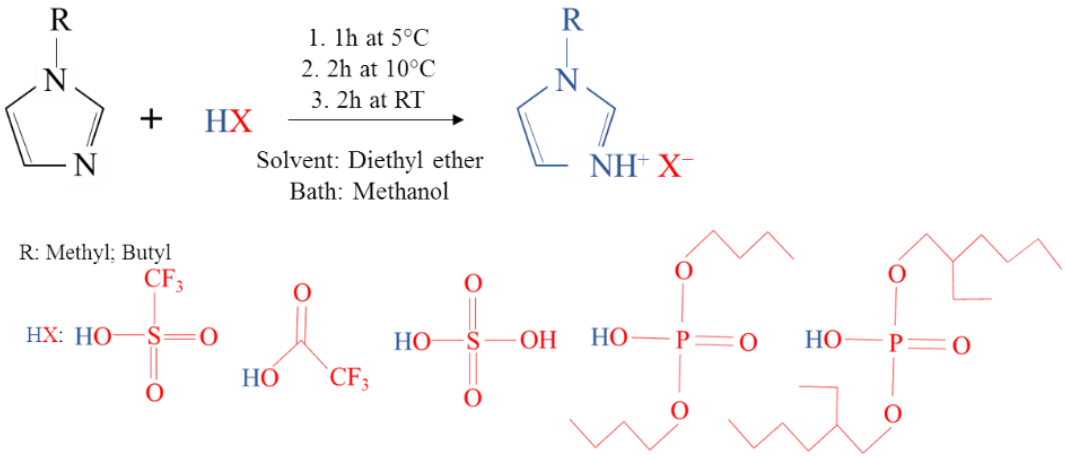

Figure 3.1. Reaction scheme of the synthesis of imidazolium-based Pr-ILs.

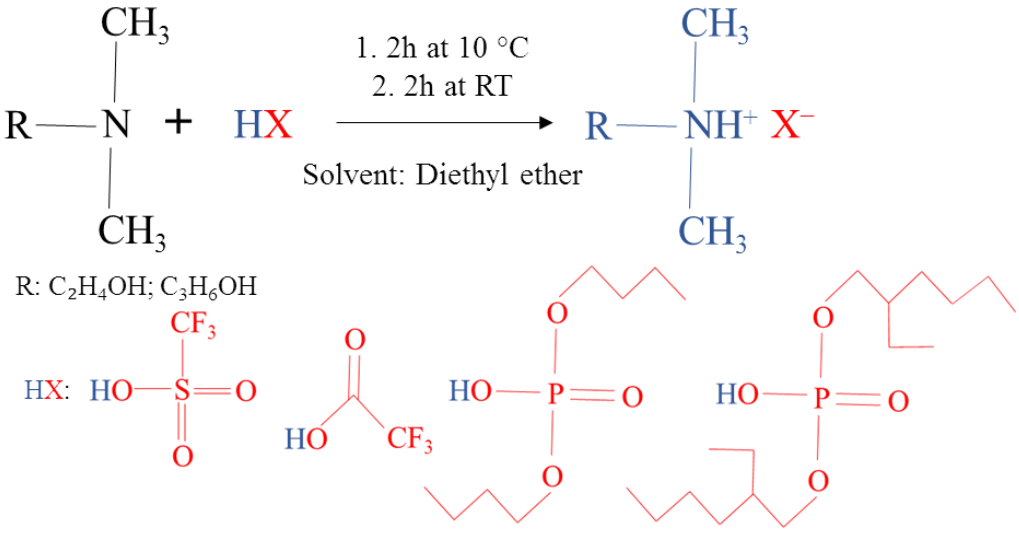

Figure 3.2. Reaction scheme of the synthesis of hydroxylammonium-based Pr-ILs.

Table 3.1. General specification of the synthesized Pr-ILs.

Pr-IL	Base	Acid	Abbreviation	State at RT	Color
1-methylimidazolium triflouromethanesulfonate	1-methylimidazole	trifluoromethanesulfonic acid	[MIM][TFS]	solid	white
1-methylimidazolium triflouroacetate		trifluoroacetic acid	[MIM][TFA]	solid	white
1-methylimidazolium hydrogen sulfate		sulfuric acid	[MIM][HS]	liquid	yellow
1-methylimidazolium di-*n*-butyl phosphate		di-*n*-butyl phosphate	[MIM][BUPH]	liquid	colorless
1-methylimidazolium bis(2-ethylhexyl)phosphate		bis(2-ethylhexyl)phosphate	[MIM][EHPH]	liquid	colorless
1-(*n*-butyl)imidazolium triflouromethanesulfonate	1-(*n*-butyl)imidazole	trifluoromethanesulfonic acid	[BIM][TFS]	liquid	brown
1-(*n*-butyl)imidazolium triflouroacetate		trifluoroacetic acid	[BIM][TFA]	solid	white
1-(*n*-butyl)imidazolium hydrogen sulfate		sulfuric acid	[BIM][HS]	liquid	orange
1-(*n*-butyl)imidazolium di-*n*-butyl phosphate		di-*n*-butyl phosphate	[BIM][BUPH]	liquid	colorless
1-(*n*-butyl)imidazolium bis(2-ethylhexyl)phosphate		bis(2-ethylhexyl)phosphate	[BIM][EHPH]	liquid	colorless

2-hydroxy-*n*, *n*-dimethylethanaminium triflouromethanesulfonate	2-(dimethylamino) ethanol	trifluoromethanesulfonic acid	[DETA][TFS]	liquid	brown
2-hydroxy-*n*, *n*-dimethylethanaminium triflouroacetate		trifluoroacetic acid	[DETA][TFA]	solid	brown
2-hydroxy-*n*, *n*-dimethylethanaminium di-*n*-butyl phosphate		di-*n*-butyl phosphate	[DETA][BUPH]	liquid	orange
2-hydroxy-*n*, *n*-dimethylethanaminium bis(2-ethylhexyl)phosphate		bis(2-ethylhexyl)phosphate	[DETA][EHPH]	liquid	orange
3-hydroxy-*n*, *n*-dimethylpropan-1-aminium triflouromethanesulfonate	3-dimethylamino-1-propanol	trifluoromethanesulfonic acid	[DEPA][TFS]	liquid	orange
3-hydroxy-*n*, *n*-dimethylpropan-1-aminium triflouroacetate		trifluoroacetic acid	[DEPA][TFA]	Liquid	brown
3-hydroxy-*n*, *n*-dimethylpropan-1-aminium di-*n*-butyl phosphate		di-*n*-butyl phosphate	[DEPA][BUPH]	liquid	brown
3-hydroxy-*n*, *n*-dimethylpropan-1-aminium bis(2-ethylhexyl)phosphate		bis(2-ethylhexyl)phosphate	[DEPA][EHPH]	liquid	orange

3.2. Spectral Behavior

To verify the chemical structure of synthesized Pr-ILs the NMR analysis (^{1}H and ^{19}F) was carried out. ^{1}H NMR spectrum of [MIM][TFS] is shown in Fig. 3.3a. Five peaks can be seen. The peak observed at the chemical shift of 2.50 ppm corresponds to the solvent (DMSO-d_6) used as the reference. The second peak at 3.86 ppm is a singlet peak corresponding to 3 hydrogens (a) of methyl group attached to the imidazole ring. Two other peaks are observed (triplet peaks) at the chemical shift of 7.64 and 7.66 ppm, respectively. These peaks correspond to two hydrogens (b and c) on the imidazole ring. The last peak is located at 9.01 ppm is a singlet peak correlated with a hydrogen (d) on the imidazole ring. Indeed, this peak is the most electronegative peak since the hydrogen is located between two nitrogen atoms. The ^{19}F NMR spectrum of [MIM][TFS] (Fig. 3.3b) reveals only one singlet peak at the chemical shift of -77.86 ppm, assigned to 3 fluorine atoms (e) in trifluoromethanesulfonate anion.

[MIM][TFA] ^{1}H NMR (DMSO-d_6, 300 MHz, δ, ppm): 9.06 (s, 1H), 7.65 (t, 1H), 7.69 (t, 1H), and 3.87 (s, 3H) (Fig. S1a). ^{19}F NMR (DMSO-d_6, 300 MHz, δ, ppm): -73.71 (s, 3F, –CF_3) (Fig. S1b).

[MIM][HS] ^{1}H NMR (DMSO-d_6, 300 MHz, δ, ppm):11.24 (s, 2H), 9.01 (s, 1H), 7.68 (t, 1H), 7.61 (t, 1H), and 3.87 (s, 3H) (Fig. S2).

[MIM][BUPH] ^{1}H NMR (DMSO-d_6, 300 MHz, δ, ppm): 13.26 (s, 1H), 8.99 (s, 1H), 7.67 (t, 1H), 7.56 (t, 1H), 3.87 (s, 3H), 3.81 (m, 4H), 1.52 (m, 4H), 1.29 (m, 4H), and 0.85 (t, 6H) (Fig. S3).

[MIM][EHPH] ^{1}H NMR (DMSO-d_6, 300 MHz, δ, ppm): 9.64 (s, 1H), 8.93 (s, 1H), 7.60 (t, 1H), 7.51 (t, 1H), 3.80 (s, 3H), 3.65 (m, 4H), 1.39 (m, 2H), 1.27 (m, 4H), 1.25 (m, 4H), 1.22 (m, 4H), 1.17 (m, 4H), 0.79 (m, 6H), and 0.77 (m, 6H) (Fig. S4).

[BIM][TFS] ^{1}H NMR (DMSO-d_6, 300 MHz, δ, ppm): 9.07 (s, 1H), 7.74 (t, 1H), 7.65 (t, 1H), 4.18 (t, 2H), 1.76 (m, 2H), 1.22 (m, 2H), and 0.87 (m, 3H) (Fig. S5a). ^{19}F NMR (DMSO-d_6, 300 MHz, δ, ppm): -73.91 (s, 3F, –CF_3) (Fig. S5b).

[BIM][TFA] ^{1}H NMR (DMSO-d_6, 300 MHz, δ, ppm): 9.13 (s, 1H), 7.79 (t, 1H), 7.68 (t, 1H), 4.19 (t, 2H), 1.79 (m, 2H), 1.24 (m, 2H), and 0.90 (t, 3H) (Fig. S6a). ^{19}F NMR (DMSO-d_6, 300 MHz, δ, ppm): -73.68 (s, 3F, –CF_3) (Fig. S6b).

[BIM][HS] ^{1}H NMR (DMSO-d_6, 300 MHz, δ, ppm): 12.18 (s, 2H), 9.11 (s, 1H), 7.78 (t, 1H), 7.63 (t, 1H), 4.21 (t, 2H), 1.74 (m, 2H), 1.18 (m, 2H), and 0.84 (t, 3H) (Fig. S7).

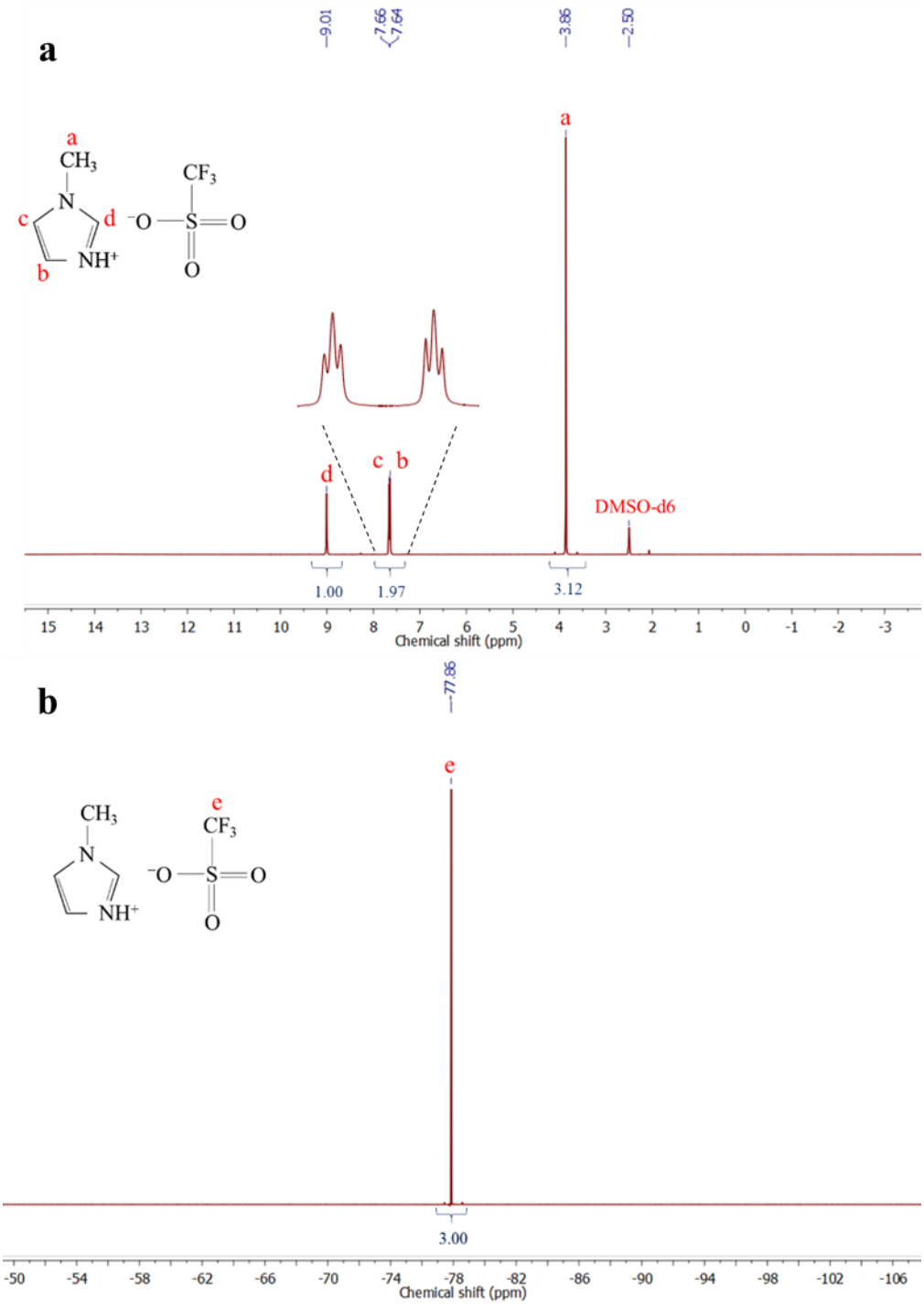

Figure 3.3. (a) ^{1}H NMR and (b) ^{19}F NMR spectra of [MIM][TFS].

[BIM][BUPH] ^{1}H NMR (DMSO-d_6, 300 MHz, δ, ppm): 13.38 (s, 1H), 8.54 (s, 1H), 7.54 (t, 1H), 7.30 (t, 1H), 4.10 (t, 4H), 3.69 (m, 2H), 1.75 (m, 4H), 1.49 (m, 4H), 1.31 (m, 2H), 1.20 (m, 2H), 0.85 (t, 3H), and 0.83 (s, 6H) (Fig. S8).

[BIM][EHPH] ^{1}H NMR (DMSO-d_6, 300 MHz, δ, ppm): 8.85 (s, 1H), 7.68 (t, 1H), 7.48 (t, 1H), 4.15 (m, 2H), 3.68 (m, 4H), 1.76 (m, 2H), 1.44 (m, 4H), 1.38 (m, 2H), 1.36 (m, 2H), 1.33 (m, 4H), 1.31 (m, 4H), 1.28 (m, 4H), 1.24 (m, 6H), 0.86 (m, 3H), and 0.83 (m, 6H) (Fig. S9).

[DETA][TFS] ^{1}H NMR (DMSO-d_6, 300 MHz, δ, ppm): 9.18 (s, 1H), 5.23 (s, 1H), 3.68 (t, 2H), 3.12 (t, 2H), 2.76 (s, 6H) (Fig. S10a). ^{19}F NMR (DMSO-d_6, 300 MHz, δ, ppm): -73.70 (s, 3F, $–CF_3$) (Fig. S10b).

[DETA][TFA] ^{1}H NMR (DMSO-d_6, 300 MHz, δ, ppm): 9.92 (s, 1H), 5.07 (s, 1H), 3.68 (t, 2H), 3.15 (t, 2H), 2.78 (s, 6H) (Fig. S11a). ^{19}F NMR (DMSO-d_6, 300 MHz, δ, ppm): -73.84 (s, 3F, $–CF_3$) (Fig. S11b).

[DETA][BUPH] ^{1}H NMR (DMSO-d_6, 300 MHz, δ, ppm): 10.53 (s, 1H), 8.29 (s, 1H), 3.71 (m, 4H), 3.63 (t, 2H), 3.03 (t, 2H), 2.68 (s, 6H), 1.44 (m, 4H), 1.26 (m, 4H), and 0.80 (t, 6H) (Fig. S12).

[DETA][EHPH] ^{1}H NMR (DMSO-d_6, 300 MHz, δ, ppm): 10.80 (s, 1H), 5.65 (s, 1H), 3.66 (t, 2H), 3.60 (m, 4H), 3.05 (t, 2H), 2.70 (s, 6H), 1.37 (m, 2H), 1.28 (m, 4H), 1.26 (m, 4H), 1.24 (m, 4H), 1.18 (m, 4H), 0.80 (m, 6H), and 0.78 (t, 6H) (Fig. S13).

[DEPA][TFS] ^{1}H NMR (DMSO-d_6, 300 MHz, δ, ppm): 10.31 (s, 1H), 4.88 (s, 1H), 3.47 (t, 2H), 3.10 (t, 2H), 2.77 (s, 6H), 1.78 (s, 2H) (Fig. S14a). ^{19}F NMR (DMSO-d_6, 300 MHz, δ, ppm): -78.03 (s, 3F, $–CF_3$) (Fig. S14b).

[DEPA][TFA] ^{1}H NMR (DMSO-d_6, 300 MHz, δ, ppm): 9.09 (s, 1H), 4.61 (s, 1H), 3.48 (t, 2H), 3.10 (m, 2H), 2.77 (s, 6H), 1.75 (s, 2H) (Fig. S15a). ^{19}F NMR (DMSO-d_6, 300 MHz, δ, ppm): -73.91 (s, 3F, $–CF_3$) (Fig. S15b).

[DEPA][BUPH] ^{1}H NMR (DMSO-d_6, 300 MHz, δ, ppm): 11.61 (s, 1H), 7.00 (s, 1H), 3.79 (m, 4H), 3.53 (t, 2H), 3.09 (t, 2H), 2.76 (s, 6H), 1.85 (m, 2H), 1.57 (m, 4H), 1.40 (m, 4H), and 0.94 (t, 6H) (Fig. S16).

[DEPA][EHPH] ^{1}H NMR (DMSO-d_6, 300 MHz, δ, ppm): 11.44 (s, 1H), 6.19 (s, 1H), 3.70 (m, 2H), 3.53 (t, 4H), 3.10 (t, 2H), 2.76 (s, 6H), 1.85 (m, 2H), 1.47 (m, 2H), 1.43 (m, 4H), 1.40 (m, 4H), 1.36 (m, 4H), 1.30 (m,4H), 0.92 (t, 6H), and 0.90 (t, 6H) (Fig. S17).

The FTIR spectra of imidazolium- and hydroxylammonium-based Pr-ILs are shown in Figs. 3.4 and 3.5, respectively. The assignments of characteristic bands of these synthesized Pr-ILs are gathered in Tables 3.2 and 3.3. The band at ~ 3265–3460 cm^{-1} which is observed for all Pr-ILs is assigned to N–H vibration bands (NH^{+}), confirming the salt formation and proton transferring in acid-base neutralization

reaction (Figs. 3.4, 3.5) [151]. Bands at the region between ~ 2900 and 3150 cm^{-1} are assigned to C−H stretching vibration band of –CH groups [119]. The C=O stretching vibration band of ester group presented in acetate based Pr-ILs is observed at ~ 1670 cm^{-1} (Figs. 3.4c,d and 3.5c,d) [149]. In addition, two bands at ~ 1585 and ~ 1550 cm^{-1} are, respectively, ascribed to C=N and C=C (skeletal) bonds of the imidazole ring of imidazolium-based Pr-ILs (Fig. 3.4a-j) [151]. Peak at ~ 1460 cm^{-1} belongs to $–CH_2$ bending (Figs. 3.4 and 3.5) [151]. Bands between ~ 1240 and 1100 cm^{-1} are assigned to S=O stretching vibration bands (Figs. 3.4a,b,e,f and 3.5a,b) [119]. Moreover, bands between ~ 1200 and 1150 cm^{-1} are assigned to P=O stretching vibration bands of phosphate-based Pr-ILs (Figs. 3.4g-j and 3.5e-h) [150,151]. The peak observed at the wavenumber of ~ 1170 cm^{-1} is attributed to C−O symmetric stretching vibration band of −COO− ester group in acetate based Pr-ILs (Figs. 3.4c,d and 3.5c,d) [151]. A peak at the wavenumber of ~ 1030 cm^{-1} is ascribed with C–F stretching vibration band in the structure of perfluorinated Pr-ILs (Figs. 3.4a-d and 3.5a-d) [149]. Moreover, a band at ~ 1020 cm^{-1} is attributed to P−O−C bond in phosphoric ester group for phosphate-based Pr-ILs (Figs. 3.4g-j and 3.5e-h) [150]. Besides, the peak of C−S stretching vibration band can be seen at ~ 750-650 cm^{-1} (Figs. 3.4a,b and 3.5a,b) [151].

The NMR (both ^{1}H and ^{19}F) and FTIR spectra confirmed the purity and chemical structure of synthesized Pr-ILs.

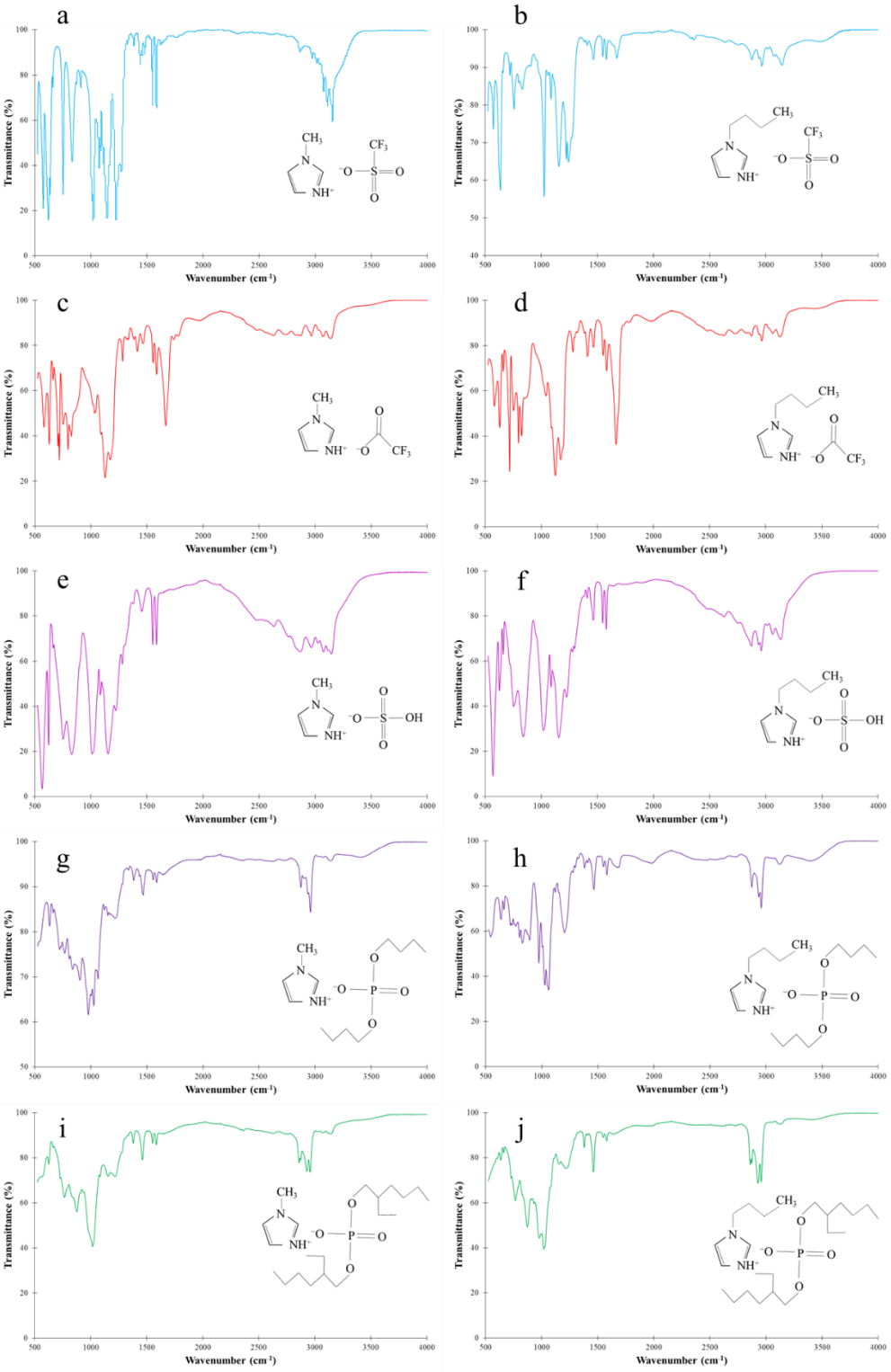

Figure 3.4. FTIR spectra of imidazolium-based Pr-ILs: a) [MIM][TFS]; b) [BIM][TFS]; c) [MIM][TFA]; d) [BIM][TFA]; e) [MIM][HS]; f) [BIM][HS]; g) [MIM][BUPH]; h) [BIM][BUPH]; i) [MIM][EHPH]; j) [BIM][EHPH].

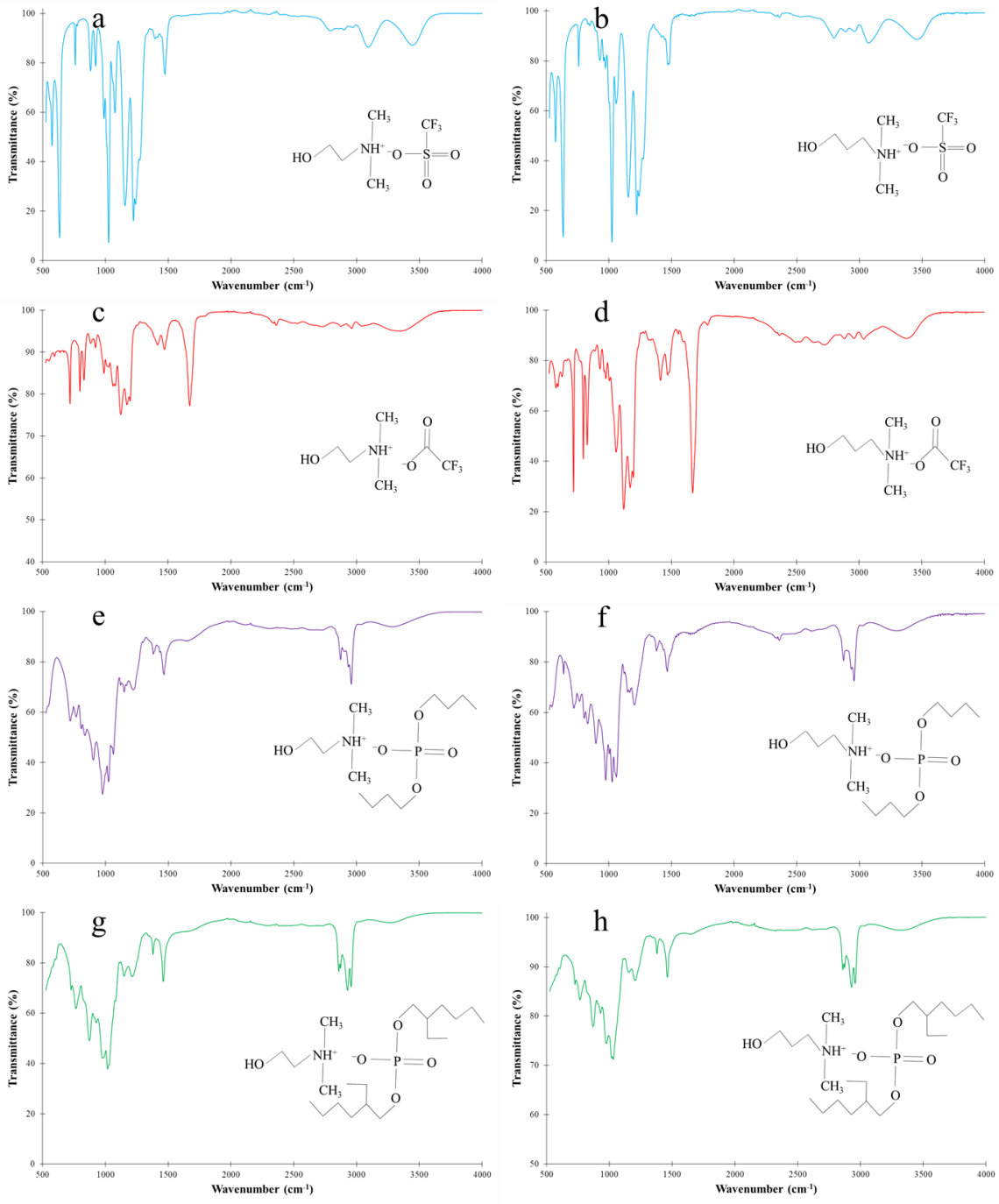

Figure 3.5. FTIR spectra of hydroxylammonium-based Pr-ILs: a) [DETA][TFS]; b) [DEPA][TFS]; c) [DETA][TFA]; d) [DEPA][TFA]; e) [DETA][BUPH]; f) [DEPA][BUPH]; g) [DETA][EHPH]; h) [DEPA][EHPH].

Table 3.2. Assignments of vibrational modes for imidazolium-based Pr-ILs.

Band assignments	Wavenumber (cm^{-1})									
	[MIM][TFS]	**[MIM][TFA]**	**[MIM][HS]**	**[MIM][BUPH]**	**[MIM][EHPH]**	**[BIM][TFS]**	**[BIM][TFA]**	**[BIM][HS]**	**[BIM][BUPH]**	**[BIM][EHPH]**
$^{+}$N–H stretching	3300	3519	3302	3435	3468	3503	3488	3299	3417	3451
C−H stretching	3110, 3155	3072, 3138	3063, 3135	2874, 2956	2930, 2959	2965, 3145	2964, 3132	3076, 3147	2873, 2957	2860, 2959
O−H stretching (acid)	–	–	2631	–	–	–	–	2632	–	–
C=O stretching vibration (ester group)	–	1667	–	–	–	–	1668	–	–	–
C=N imidazole ring	1585	1585	1580	1586	1587	1579	1582	1585	1582	1580
C=C skeletal (imidazole ring)	1550	1552	1545	1553	1552	1550	1550	1551	1547	1548
CH_2 bending	1440	1413	1464	1464	1460	1463	1413	1445	1464	1460
S=O stretching	1145, 1224	–	1086, 1154	–	–	1160, 1242	–	1086, 1153	–	–
P=O stretching	–	–	–	1148, 1220	1150, 1217	–	–	–	1202	1157, 1224
C−O symmetric stretching (ester group)	–	1125	–	–	–	–	1173	–	–	–
C−F stretching	1023	1031	–	–	–	1027	1040	–	–	–
P−O−C (phosphoric ester)	–	–	–	1025	1019	–	–	–	1026	1018
C−S stretching	755	–	–	–	–	759	–	–	–	–

Table 3.3. Assignments of vibrational modes for hydroxylammonium-based Pr-ILs.

Band assignments	**Wavenumber (cm^{-1})**							
	[DETA][TFS]	**[DETA][TFA]**	**[DETA][BUPH]**	**[DETA][EHPH]**	**[DEPA][TFS]**	**[DEPA][TFA]**	**[DEPA][BUPH]**	**[DEPA][EHPH]**
$^{+}$N–H stretching	3450	3356	3286	3266	3462	3380	3306	3339
C−H stretching	2990, 3094	2963	2934, 2961	2928, 2959	2963, 3075	2963, 3039	2937, 2959	2930, 2957
C=O stretching vibration (ester group)	−	1673	_	_	_	1671	_	_
CH_2 bending	1475	1475	1465	1463	1471	1469	1465	1463
S=O stretching	1154, 1225	_	_	_	1156, 1223	_	_	_
P=O stretching	_	_	1148, 1217	1146, 1215	_	_	1146, 1205	1146, 1201
C−O symmetric stretching (ester group)	−	1171	_	_	_	1170	_	_
C−F stretching	1023	1060	_	_	1025	1058	_	_
P−O−C (phosphoric ester)	_	_	978	1021	_	_	1027	1031
C−S stretching	635	_	_	_	633	_	_	_

3.3. Thermal Properties

As the synthesized Pr-ILs are intended to be used in fuel cell application, therefore, their thermal stability is rather important. To study the influence of chemical structure on the thermal properties of Pr-ILs, the TGA analysis was carried out in dynamic and isothermal modes (Figs. 3.6 and 3.7). The isothermal mode was chosen to evaluate the performance of Pr-ILs during the long-term process. For this purpose, the TGA analysis at different temperatures (i.e. 150, 120, 100, and 80 °C) during 24 h was carried out. The main thermal parameters of synthesized Pr-ILs are gathered in Table 3.4. The TGA and DTG curves (Figs. 3.6a,b and 3.7a,b) demonstrate that the thermal stability of synthesized Pr-ILs has a stronger dependence on the anion nature than on the cation nature. It can be seen that Pr-ILs containing trifluoromethanesulfonate anion (i.e. [MIM][TFS], [BIM][TFS], [DETA][TFS], and [DEPA][TFS]) are more thermally stable (T_{deg} ~ 415−435 °C) than other Pr-ILs (i.e. trifluoroacetate-, phosphate-, and sulfate-based ILs). Such observation can be explained by super acidity property of trifluoromethansulfonic acid (pKa ~ -14). This value is much lower than the pKa value of sulfuric acid, trifluoroacetic acid, bis(2-ethylhexyl)phosphate, and di-*n*-butyl phosphate (~ -3, 0.23, 1.47, and 1.53, respectively) [152-154]. In fact, there is a direct correlation between thermal stability of ILs and the acidity of utilized Brønsted acid [147,149]. Sulfate-based Pr-ILs also showed a great thermal stability of ~ 370−375 °C owing to high acidity of sulfuric acid (pKa ~ -3) [155]. It can be seen that acetate-based Pr-ILs showed the lowest thermal stability of ~ 200−215 °C as compared with phosphate-based Pr-ILs in spite of the fact that trifluoroacetic acid is a stronger acid than di-*n*-butyl phosphate and bis(2-ethylhexyl)phosphate. Similar results were also reported in literature [147]. The low thermal stability of acetate-based ILs may be explained by the high hydrophilicity of the acetate group [147]. The presence of two symmetrical alkyl chains in the anion structure of phosphate-based Pr-ILs increases the fluidity of these Pr-ILs, thus leading to improvement of the thermal stability as compared with the stability of trifluoroacetate-based Pr-ILs [150]. Pr-ILs containing di-*n*-butyl phosphate and bis(2-ethylhexyl)phosphate anions reveal practically similar thermal stability (~ 250−280 °C) notwithstanding the fact that bis(2-ethylhexyl)phosphate is a stronger acid than di-*n*-butyl phosphate. However, it was revealed that Pr-ILs with bis(2-ethylhexyl)phosphate are more thermally stable in static mode than those with di-*n*-butyl phosphate. For instance, the weight loss of [DETA][EHPH] and [DEPA][EHPH] at 120 °C for 24 h was ~ 9 and 13%, respectively, while it was ~ 16 and 23% for [DETA][BUPH] and [DEPA][BUPH], respectively, confirming the better thermal behavior of bis(2-ethylhexyl)phosphate in comparison with phosphate during long-term operation. Similar results were obtained by Rogalsky et al. showing that [EHPH]-based Pr-IL showed higher thermal stability than the stability of [BUPH]-based ILs [150]. So, the order of anion thermal stability is the following: [TFS] > [HS] > [EHPH] > [BUPH] > [TFA].

The nature of cation can also influence the thermal behavior of ILs (Fi. 3.6 and 3.7) [117,149]. Prykhodko and coworkers [149] synthesized different types of imidazolium-based Pr-ILs containing various anions and cations. It was shown that for the same cation, increasing the alkyl chain length leads to a slight rise in the Pr-ILs thermal stability. However, it was confirmed that the influence of anion is much stronger than that of cation [149]. On the contrary, Fatyeyeva et al. [117] studied four Pr-ILs containing the same anion (i.e. bis(trifluoromethylsulfonyl)imide) and imidazolium-based cations with different alkyl chain lengths (i.e. methyl, ethyl, propyl, and butyl). The TGA results revealed that the rise of alkyl chain leads to decreasing the thermal stability of synthesized Pr-ILs. [MIM][TFSI] showed the highest thermal stability in comparison with Pr-ILs containing ethylimidazolium, propylimidazolium, and butylimidazolium cations [117]. Thus, one can conclude that in order to find a clear correlation between the cation nature and IL thermal stability, further research is required. In our case, two different types of cation were used: imidazolium-based cations ([MIM] and [BIM]) and hydroxylammonium-based cations ([DETA] and [DEPA]). It can be seen that cations with different alkyl or hydroxyl chain length were utilized. The obtained results showed that despite the fact that imidazolium-based Pr-ILs are known as thermally stable Pr-ILs, there is no significant difference in thermal stability of imidazolium- and hydroxylammonium-based cations with the same anion (Fig. 3.6 and 3.7 and Table 3.4) (~ 415-434 °C, ~ 369-375 °C, ~ 257-277 °C, ~ 242-267 °C, and ~ 202-216 °C for [TFS]-, [HS]-, [EHPH]-, [BUPH]-, and [TFA]-based Pr-ILs). However, from environmental point of view, hydroxylammonium-based Pr-ILs are more interesting as they can be biodegradable and recyclable owing to their aliphatic nature and linear structure.

The obtained results showed that there is no clear correlation between alkyl (or hydroxyl) chain length and thermal stability. In some cases the rise of alkyl (or hydroxyl) chain length provokes an increase of the thermal stability, while opposite behavior is observed for some other Pr-ILs. The isothermal tests demonstrate that [TFS]-based Pr-ILs (i.e. [MIM][TFS], [BIM][TFS], [DETA][TFS], and [DEPA][TFS]) have the highest thermal stability among all Pr-ILs. The weight loss after 24 h at 150 °C for [TFS]-based Pr-ILs is ~ 0−3% and this loss can be due to the humidity evaporation. These results prove the great potential of [TFS]-based Pr-ILs for high temperature industrial applications and long-term process (e.g. HT-PEMFC) [147,149]. Even though sulfate-based Pr-ILs ([MIM][HS] and [BIM][HS]) showed a good isotherm performance at 120 °C for 24 h (only ~ 1% of weight loss), they were not thermally stable at 150 °C for 24 h (~ 9−11% of weight loss). Also, phosphate-based Pr-ILs showed a good performance at 100 °C during 24 h (between 5−10% of weight loss). The weakest isothermal behavior was noted for [TFA]-based Pr-ILs (i.e. [MIM][TFA], [BIM][TFA], [DETA][TFA], and [DEPA][TFA]) as they were not thermally stable at 120, 100, and even 80 °C during continuous test of 24 h owing to the presence of hydrophilic acetate group [147].

The evaluation of thermal stability as a function of Pr-ILs structure is plotted on Fig. 3.8. The Pr-ILs can be divided into four groups: super thermally stable (i.e. [TFS]-based Pr-ILs), high thermally stable (i.e. [HS]-based Pr-ILs), moderate thermally stable (i.e. [BUPH] and [EHPH]-based Pr-ILs), and low thermally stable (i.e. [TFA]-based Pr-ILs). The most promising Pr-ILs for fuel cell application are [TFS]-based Pr-ILs.

The DSC measurements were performed in order to study possible thermal transition of synthesized Pr-ILs. The measurements were performed in the temperature region based on the Pr-ILs thermal stability. An example of measurements is presented in Fig. 3.9 for [DETA][TFS] and obtained results are gathered in Table 3.4. As one can see, some of the Pr-ILs (i.e. [MIM][TFS], [BIM][TFS], [DETA][TFS], and [MIM][TFA]) have two or more melting T_m and crystallization T_c, confirming their polymorphic character (Table 3.4). Presence of cations and anions of different size and different spatial shape (orientation) may explain such results. For several Pr-ILs, T_m and T_c were not detected in the studied temperature region, i.e. from -150 to 80 °C for [TFA]-based Pr-ILs, from -150 to 100 °C for phosphate-based Pr-ILs, from -150 to 120 °C for sulfate-based Pr-ILs, and from -150 to 200 °C for [TFS]-based Pr-ILs. It can be seen that the nature of Pr-ILs has only an influence on the T_g value – [TFS]-based Pr-ILs are characterized by higher T_g than the T_g value of sulfate-, phosphate-, and acetate-based Pr-ILs owing to the strong acidity feature of trifluoromethansulfonic acid [147,149]. Besides, the effect of cation structure on the T_g value can be observed as the rise of alkyl chain length of cation causes the slight increase of the T_g value owing to the fluidity rising (Table 3.4) [149].

Table 3.4. Thermal parameters of synthesized Pr-ILs.

Pr-IL structure	T_5% (°C)	T_{10}% (°C)	T_{deg} (°C)	T_g (°C)	T_m (°C)	T_c (°C)	Weight loss (%) after 24 h at			
							150 °C	120 °C	100 °C	80 °C
[MIM][TFS]	359	376	420	–	86; 111	77; 101	0	–	–	–
[MIM][TFA]	168	178	202	–	-10; 71	-48; 28	–	100	100	28
[MIM][HS]	281	321	375	-75	–	–	9	1	–	–
[MIM][BUPH]	194	217	242	-93	–	–	–	22	12	–
[MIM][EHPH]	227	242	257	-99	–	–	–	5	1	–
[BIM][TFS]	374	390	434	–	-16; 17	-41; -16	1	–	–	–
[BIM][TFA]	156	169	205	–	53	30	–	100	64	9
[BIM][HS]	276	321	369	-60	–	–	11	1	–	–
[BIM][BUPH]	162	184	245	-68	–	–	–	24	19	–
[BIM][EHPH]	194	222	257	-94	–	–	–	16	8	–
[DETA][TFS]	323	355	419	–	-23; 23	-46; -19	2	–	–	–

[DETA][TFA]	170	185	214	-106	-56	-40	_	97	72	18
[DETA][BUPH]	215	228	267	-95	_	_	_	16	6	–
[DETA][EHPH]	190	224	265	-91	_	_	_	9	5	–
[DEPA][TFS]	319	344	415	-86	_	_	1	–	–	–
[DEPA][TFA]	177	187	216	-94	_	_	_	96	57	11
[DEPA][BUPH]	174	199	247	-87	_	_	_	23	10	–
[DEPA][EHPH]	204	233	277	-89	_	_	_	13	7	–
[MIM][TFS]/[BIM][TFS]	383	397	430	_	_	_	2	–	_	_
[DETA][TFS]/[DEPA][TFS]	315	342	413	_	_	_	4	–	_	_

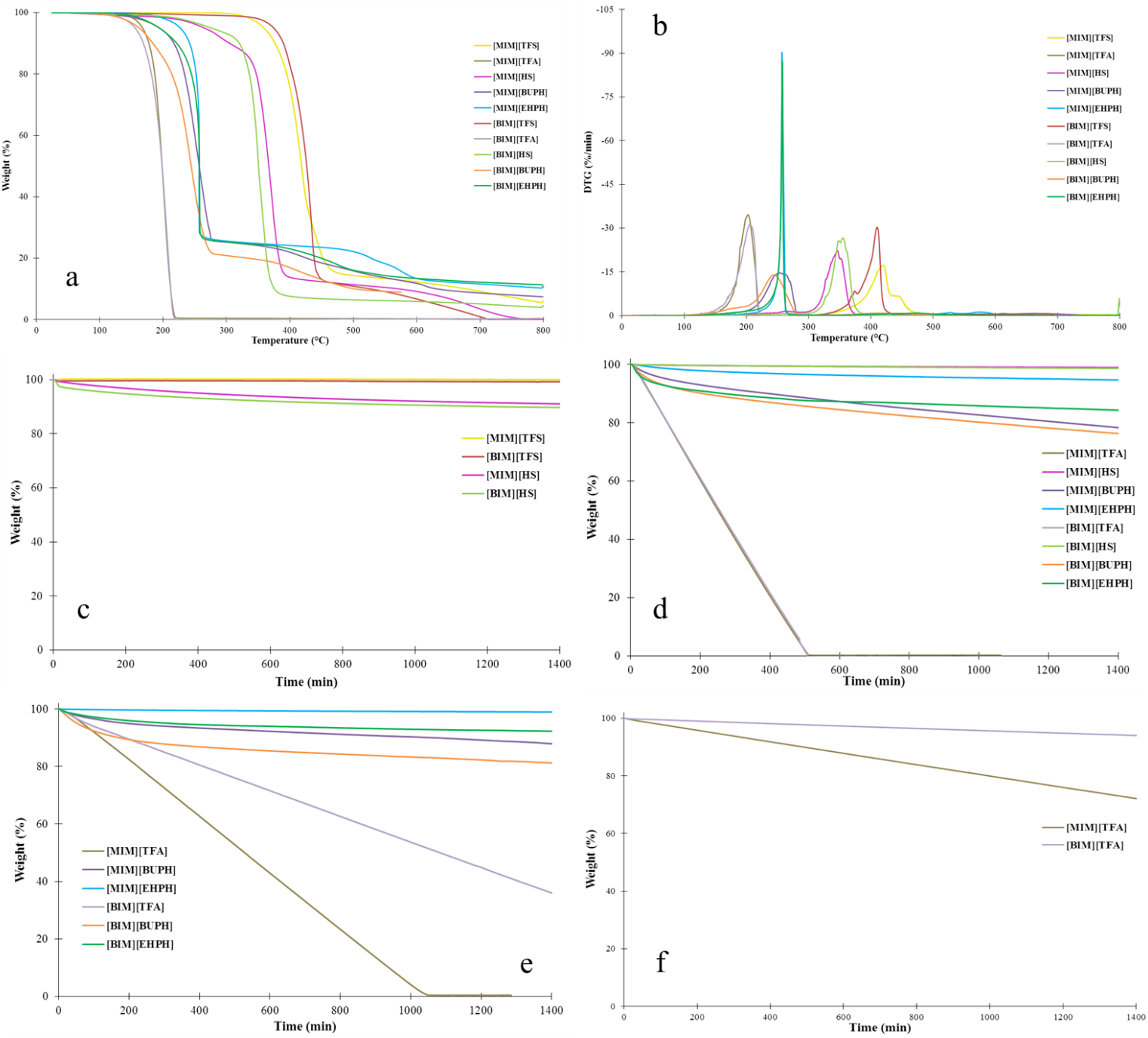

Figure 3.6. Thermal behavior of synthesized imidazolium-based Pr-ILs: a) dynamic TGA; b) DTG; c) isothermal at 150 °C; d) isothermal at 120 °C; e) isothermal at 100 °C; f) isothermal at 80 °C.

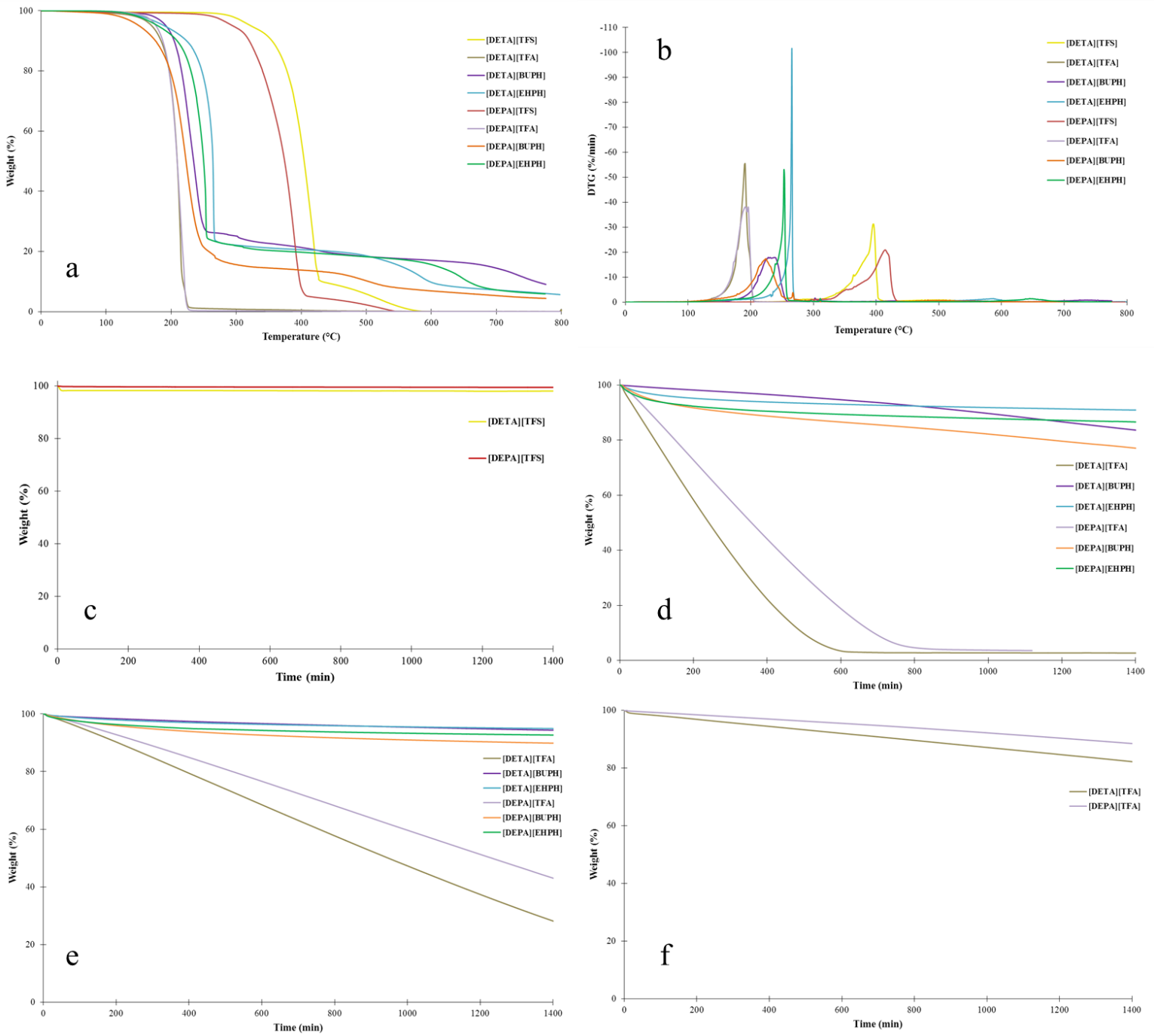

Figure 3.7. Thermal behavior of synthesized hydroxylammonium-based Pr-ILs: a) dynamic TGA; b) DTG; c) isothermal at 150 °C; d) isothermal at 120 °C; e) isothermal at 100 °C; f) isothermal at 80 °C.

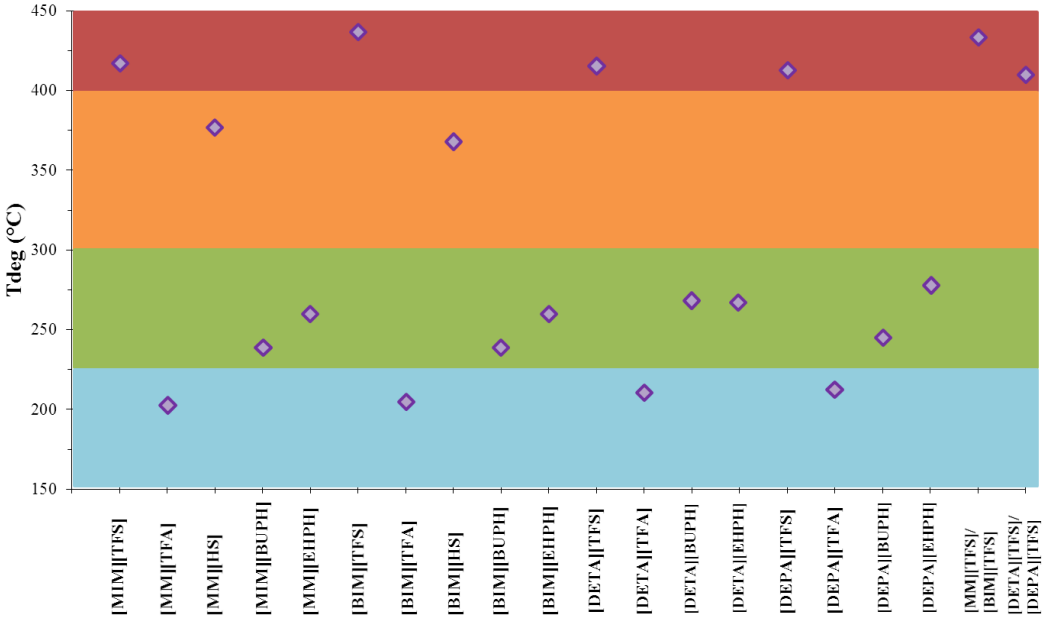

Figure 3.8. Evaluation of thermal stability as a function of Pr-ILs structure.

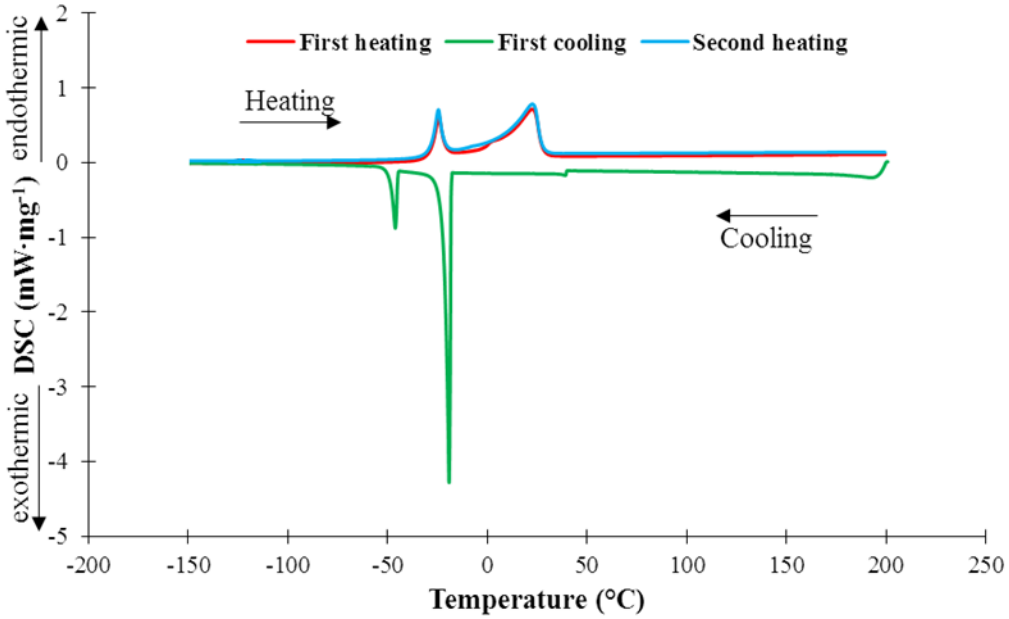

Figure 3.9. DSC heating/cooling/heating thermograms of [DETA][TFS].

3.4. Ionic Conductivity

The ionic conductivity is an important parameter for fuel cell application [150]. The ionic conductivity of ILs is strongly dependent on the degree of ion (i.e. cations and anions) mobility [117,150]. Therefore, the ionic conductivity of all synthesized Pr-ILs was investigated in a wide temperature range

based on the Pr-ILs thermal stability − for trifluoromethanesulfonate- and sulfate-based Pr-ILs from 25 to 150 °C, for phosphate-based Pr-ILs from 25 to 120 °C, and for trifluoroacetate-based Pr-ILs from 25 to 80 °C (Table 3.5). To investigate the ionic conductivity stability, the measurements were performed during two cycles of heating/cooling (Fig. 3.10a). Also, the static measurements were performed at the highest operating temperature during 24 h (Fig. 3.11).

The results showed that the temperature increase leads to the increase of the ionic conductivity owing to the rising of the ionic mobility of cations and anions (Fig. 3.10 and Table 3.5). This result is in accordance with the literature data [7,116-119,150]. The ionic conductivity values of Pr-ILs during different heating/cooling cycles are rather close revealing the conductivity stability (Fig. 3.10a). However, it can be seen that the nature of Pr-IL plays a crucial role on the ionic conductivity (Table 3.5) [118]. In any case, the anion nature has a dominant influence on the Pr-IL ionic conductivity. The highest ionic conductivity values were measured for trifluoromethanesulfonate-based Pr-ILs (~ 34.5−63.7 $mS \cdot cm^{-1}$ at 150 °C). Indeed, the IL conductivity strongly depends on the acidity of utilized Brønsted acid. Trifluoromethanesulfonic acid is considered as a super acid with a very low pKa value (~ -14), thus Pr-ILs synthesized using this acid reveal the highest ionic conductivity at high temperature [152]. Sulfate-based Pr-ILs (i.e. [MIM][HS] and [BIM][HS]) show a good ionic conductivity of ~ 17.3−41.0 $mS \cdot cm^{-1}$ at 150 °C as sulfuric acid is the second strongest acid (pKa ~ -3) among all used acids for Pr-ILs synthesis [155]. Acetate-based Pr-ILs reveal a good ionic conductivity (~ 2.4−28.6 $mS \cdot cm^{-1}$) in the temperature range of 25 to 80 °C, showing that their performance is rather close to the conductivity level of trifluoromethanesulfonate- and sulfate-based Pr-ILs in this temperature range (Table 3.5). However, owing to the low thermal stability of acetate-based Pr-ILs, they are not able to be used at temperatures higher than 80 °C [147]. Therefore, rising temperature at more than 80 °C leads to the thermal decomposition of acetate-based Pr-ILs and, thus, the ionic conductivity reduction (Table 3.5). Phosphate-based Pr-ILs are characterized by the lowest ionic conductivity in comparison with other Pr-ILs – 0.13−2.5 $mS \cdot cm^{-1}$ at 120 °C (Table 3.5). The presence of long alkyl chains in the anion structure (i.e. [BUPH] and [EHPH]) increases the viscosity for these Pr-ILs and, thus, reduces the ionic mobility [150]. Indeed, the ionic mobility increases by rising the temperature [117,150]. Besides, it is found that the ionic conductivity of [BUPH]-based Pr-ILs is higher than that of [EHPH]-based Pr-ILs at the same temperature. The similar observation was reported by Rogalsky et al. in case of imidazolium-based Pr-ILs [150]. In fact, [EHPH] anion has longer alkyl chain (i.e. lower ionic mobility) as compared with [BUPH] anion [150]. Based on the obtained results, the following ionic conductivity order of studied anions can be proposed: [TFS] > [HS] > [TFA] > [BUPH] > [EHPH].

Despite the fact that anion nature has the dominant influence on the ionic conductivity, the cation nature also influences the ionic conductivity of Pr-ILs. The alkyl chain length has a crucial influence on the

IL ionic conductivity as the shorter alkyl chain length results in ionic conductivity increasing owing to the ionic mobility rising [117]. The ionic conductivity results revealed that for both types of cation (imidazolium- and hydroxyammonium-based Pr-ILs), the ionic conductivity is slightly enhanced by increasing the alkyl chain length from [TFS]-, to [TFA]-, and to [HS]-based Pr-ILs. However, such correlation was not observed for phosphate-based Pr-ILs (i.e. [BUPH]- and [EHPH]-based Pr-ILs), for which the measured values are rather close (Table 3.5). In case of hydroxylammonium-based Pr-ILs, [DEPA] cation has only one carbon atom more than [DETA] cation and in case of imidazolium-based Pr-ILs, [BIM] has three carbon atoms more than [MIM] cation. Therefore, a significant difference of the ionic mobility is not observed. Following order of cation ionic conductivity can be proposed based on the obtained results: [MIM] > [BIM] and [DETA] > [DEPA].

To evaluate the performance of synthesized Pr-ILs, isothermal measurements were performed (Fig. 3.11). Among all tested Pr-ILs, [TFS]- (Fig. 3.11a) and [HS]-based (Fig. 3.11b) Pr-ILs demonstrated a stable ionic conductivity at 150 and 120 °C during 24 h, respectively, showing their great potential for high temperature-based application.

Arrhenius equation (Eq. 2.18) was used to determine the activation energy of transport during both heating ($E_{a\ heating}$) and cooling ($E_{a\ cooling}$) cycles [117]. The obtained E_a values are between ~ 21 kJ·mol^{-1} and ~ 31 kJ·mol^{-1} (Table 3.5). In general, the proton conduction is explained by two mechanisms: Einstein transport (vehicle mechanism) and proton hopping (Grotthuss mechanism) [7,142]. Based on the literature, the Grotthuss mechanism is the dominant proton conduction mechanism when E_a > 14 kJ·mol^{-1} [118,142]. Thus, taking into account E_a values for all synthesized Pr-ILs (Table 3.5), the Grotthuss mechanism can be considered to be a dominant mechanism for ion conductivity of all synthesized Pr-ILs.

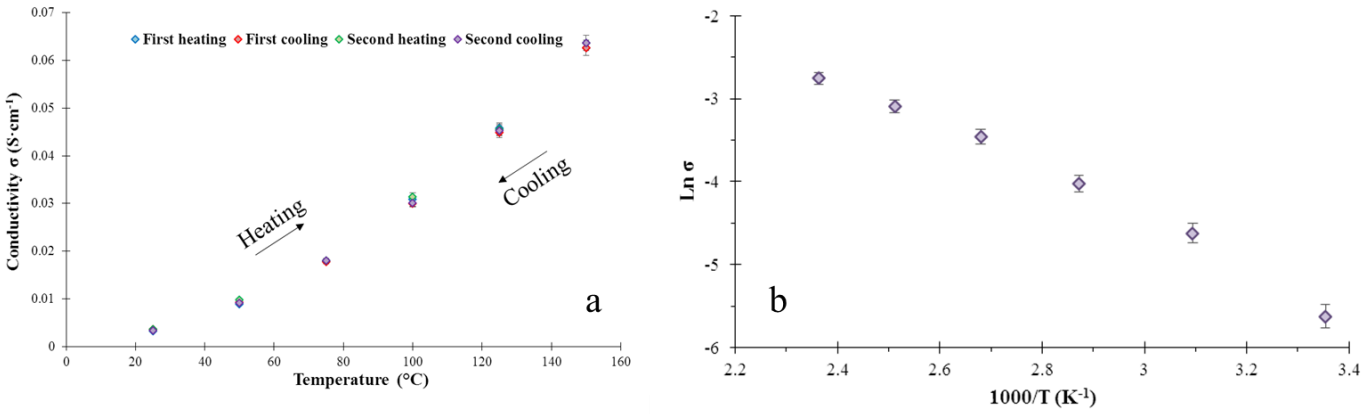

Figure 3.10. Ionic conductivity of [DETA][TFS] as a function of temperature: a) influence of heating/cooling cycles; b) Arrhenius plot.

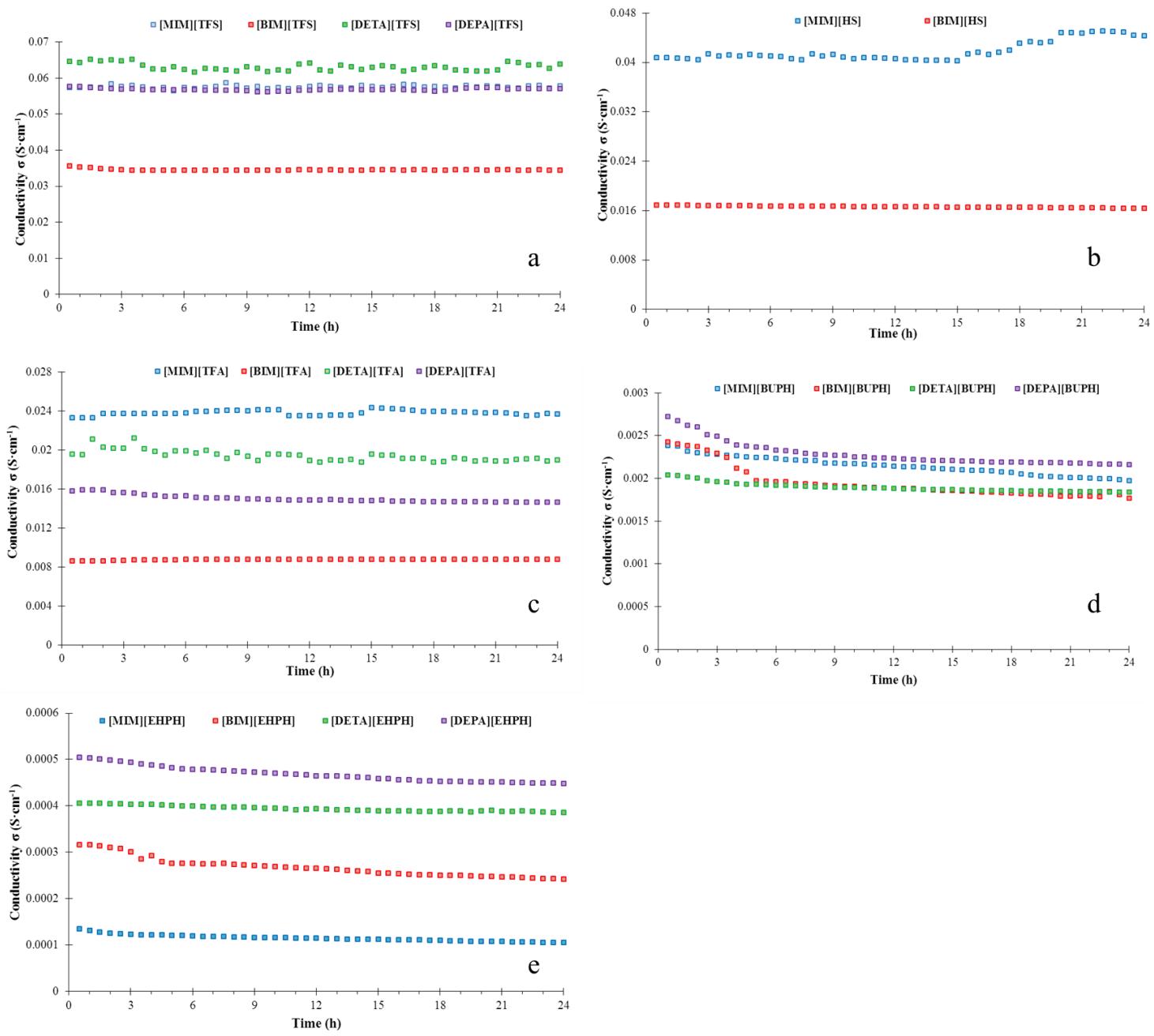

Figure 3.11. Ionic conductivity as a function of time: a) [TFS]-based Pr-ILs at 150 °C; b) [HS]-based Pr-ILs at 150 °C; c) [TFA]-based Pr-ILs at 80 °C; d) [BUPH]-based Pr-ILs at 120 °C; e) [EHPH]-based Pr-ILs at 120 °C.

Table 3.5. Ionic conductivity (σ) and activation energy (E_a) of synthesized Pr-ILs.

Pr-IL	Operating temperature range (°C)	σ (mS·cm^{-1})		E_a (kJ·mol^{-1})	
		at minimum temperature	at maximum temperature	heating	cooling
[DETA][TFS]	25 − 150	3.6	63.7	23.8	24.3
[DEPA][TFS]		2.8	57.8	25.2	25.1
[MIM][TFS]	110 − 150	34.2	57.8	17.8	17.8
[BIM][TFS]	25 − 150	1.6	34.5	25.8	25.5
[MIM][HS]		0.75	41.0	33.3	33.5
[BIM][HS]		0.09	17.30	44.0	43.9
[DETA][TFA]	25 − 80	3.20	19.30	28.7	28.0
[DEPA][TFA]		2.40	15.50	30.8	29.5
[MIM][TFA]	60 − 90	15.30	28.60	21.6	21.0
[BIM][TFA]	50 − 90	4.00	11.90	28.2	27.5
[DETA][BUPH]	25 − 120	0.16	2.00	20.6	21.3
[DETA][EHPH]		0.02	0.42	27.4	27.6
[DEPA][BUPH]		0.16	2.50	23.4	22.5
[DEPA][EHPH]		0.03	0.52	28.3	28.3
[MIM][BUPH]		0.17	2.46	22.3	22.6
[MIM][EHPH]		0.006	0.13	26.7	27.7
[BIM][BUPH]		0.09	2.22	27.6	27.0
[BIM][EHPH]		0.008	0.30	30.5	30.1
[DETA][TFS]/ [DEPA][TFS]	25 −150	3.30	59.60	24.7	24.0
[MIM][TFS]/ [BIM][TFS]	50 −150	7.60	47.90	20.9	21.0

3.5. ILs Mixture

As it was noted, [TFS]-based Pr-ILs were characterized by the highest ionic conductivity (~ 34.5−63.7 $mS \cdot cm^{-1}$ at 150 °C) and thermal stability (~ 419−434 °C). Hence, in order to increase more conductivity, the mixture of ILs was prepared. For imidazolium-based ILs, [MIM][TFS] and [BIM][TFS] were chosen. In case of hydroxylammonium-based ILs, [DETA][TFS] and [DEPA][TFS] were studied. In each case a 50/50 (w/w) mixture was prepared at 120 °C during 24 h. The dynamic TGA curves (Fig. 3.12a,b and Fig. 3.8 and Table 3.4) showed that obtained mixtures are thermally stable in the temperature range of 413−430 °C. Also, the isothermal curves (Fig. 3.12c and Table 3.4) reveal only a negligible weight loss (~ 2−4%) at 150 °C during 24 h. This result confirms the interest of using ILs for high temperature-based process (e.g. PEMFC). It can be seen that the thermal stability of imidazolium-based mixture is slightly higher than that of hydroxylammonium-based ILs (Table 3.4). In fact, imidazolium-based Pr-ILs are known to be more stable due to the presence of imidazole ring in their structure. The ionic conductivity measurements (Fig. 3.12d,e) confirm high ionic conductivity values (~ 47.9−59.6 $mS \cdot cm^{-1}$ at 150 °C) obtained for two mixed ILs. Moreover, the conductivity measurements in static mode (Fig. 3.12f) reveal a stable ionic conductivity at 150 °C during 24 h, confirming the possibility of using these IL mixture in long-term applications. However, it was found that the mixed Pr-ILs showed the same thermal stability and ionic conductivity as pure Pr-ILs (Table 3.4 and Table 3.5). These results testify the absence of new physical (electrostatic) or chemical bonds in the mixed Pr-ILs. Performed FTIR analysis (Fig. 3.13) did not demonstrate any considerable shift in the bands, thus confirming the absence of new electrostatic interactions.

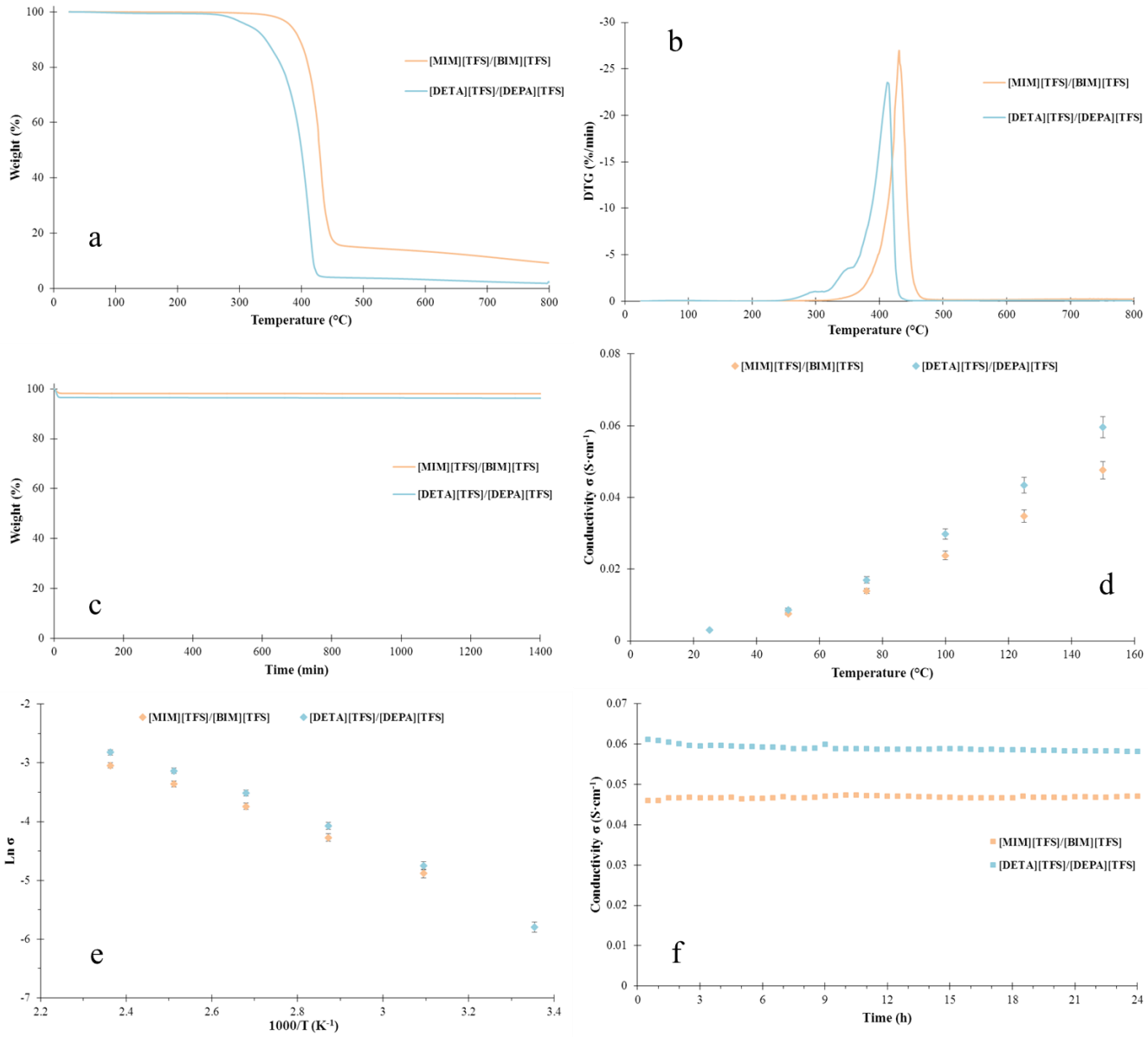

Figure 3.12. The ionic conductivity and thermal behavior of [MIM][TFS]/[BIM][TFS] and [DETA][TFS]/[DEPA][TFS] mixtures: a) TGA curves; b) DTG curves; c) isotherm at 150 °C; d) ionic conductivity as a function of temperature; e) Arrhenius plot; f) ionic conductivity in isothermal mode at 150 °C.

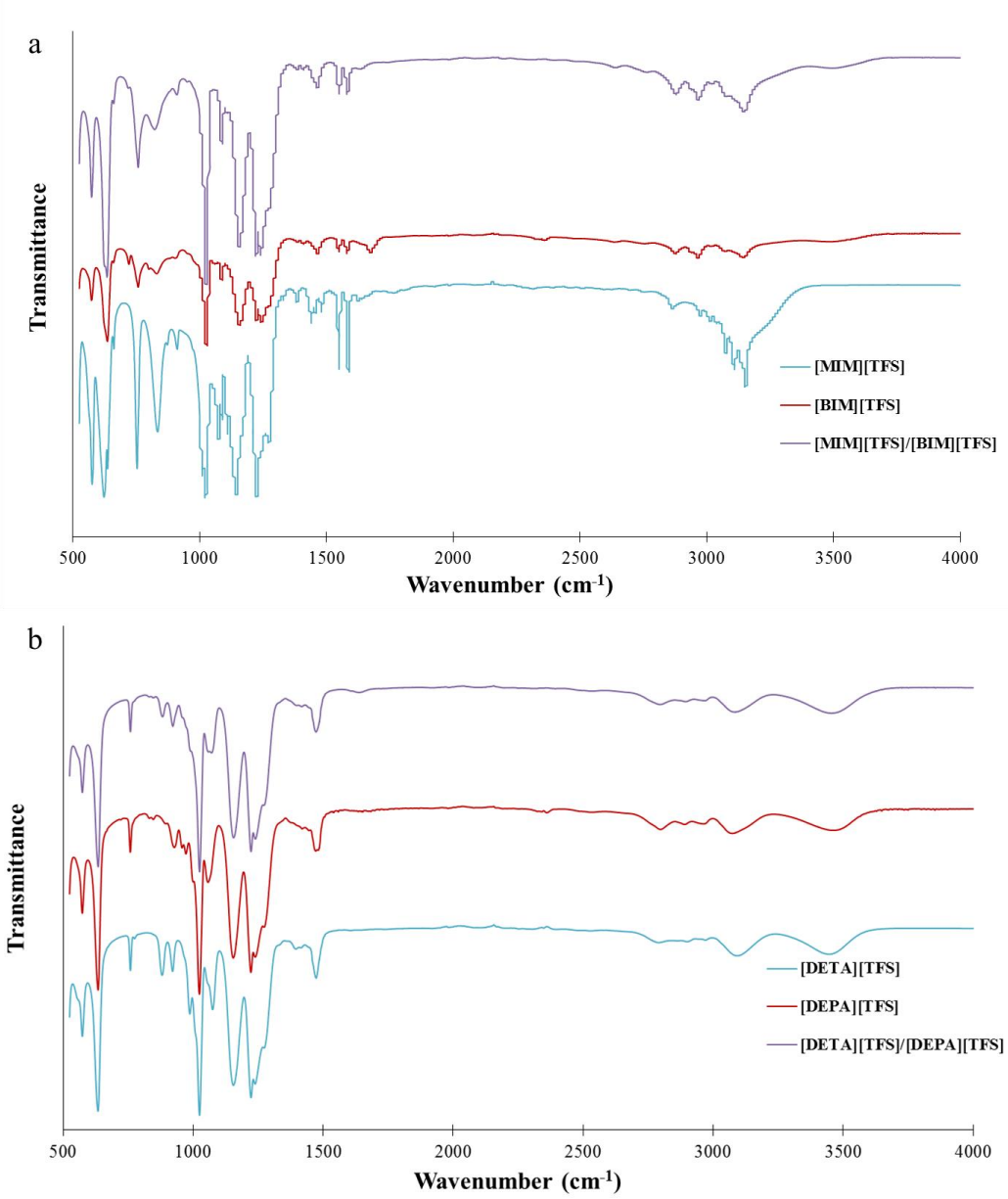

Figure 3.13. FTIR spectra of Pr-ILs mixture: a) imidazolium-based Pr-ILs; b) hydroxylammonium-based Pr-ILs.

3.6. Conclusion

Several new Pr-ILs with different nature (i.e. imidazolium- and hydroxylammonium-based Pr-ILs) were synthesized *via* acid-base neutralization reaction. In order to confirm the chemical structure of obtained Pr-ILs, NMR (^{1}H and ^{19}F) and FTIR analyses were performed. TGA (static and dynamic modes) and DSC analyses were carried out to evaluate the thermal behavior of synthesized Pr-ILs. Moreover, the ionic conductivity (isothermal and dynamic modes) of Pr-ILs was measured by EIS.

It was found that the chemical nature of anion and cation can influence the thermal stability of Pr-ILs, however, the influence of anion nature is more pronounced. Among different types of anions ([TFA], [HS], [BUPH], and [EHPH]), [TFS]-based Pr-ILs showed the highest thermal stability (T_{deg} ~ 415–435 °C) owing to the strong acid property of trifluoromethansulfonic acid. Also, [TFS]-based Pr-ILs showed the best thermal stability in static TGA tests by only ~ 0−3% of weight loss at 150 °C during 24 h. Indeed, there is a direct link between acidity of acid and thermal stability of IL (i.e. stronger acid, higher thermal stability). Therefore, the order of IL thermal stability based on the anion nature is as follows: [TFS] > [HS] > [EHPH] > [BUPH] > [TFA]. Acetate-based Pr-ILs showed the lowest thermal stability (T_{deg} ~ 200–215 °C) due to the hydrophilic property of acetate group in their structure. Sulfate-based Pr-ILs showed good thermal stability up to ~ 370–375 °C while phosphate-based Pr-ILs demonstrated lower thermal stability (T_{deg} ~ 250–280 °C). Two cations of different nature (i.e. imidazolium- and hydroxylammonium-based cations) were used for IL synthesis. Although, imidazolium-based ILs are well-known to be thermally stable ILs, hydroxylammonium-based ILs showed almost the same thermal stability as compared with imidazolium-based ones.

The ionic conductivity of obtained Pr-ILs was measured in dynamic and isothermal modes and it was observed that the anion type has the dominant effect on the ionic conductivity value. [TFS]-based Pr-ILs showed the highest values between ~ 34.5 and 63.7 $mS \cdot cm^{-1}$ at 150 °C without presence of humidity owing to the low pK_a value of trifluoromethansulfonic acid (~ -14). The isothermal analysis showed the ionic conductivity stability of [TFS]-based Pr-ILs at 150 °C during 24 h. Also, [HS]-based Pr-ILs revealed good ionic conductivity, especially at 150 °C (~ 17.3–41.0 $mS \cdot cm^{-1}$) due to the viscosity reduction (ion mobility increase). The presence of long alkyl chains in the anion structure (i.e. [BUPH] and [EHPH]) increases the viscosity for these Pr-ILs and, thus, reduces the ionic mobility – ~ 0.13−2.5 $mS \cdot cm^{-1}$ at 120 °C. Moreover, [EHPH]-based Pr-ILs demonstrated lower ionic conductivity than the conductivity of [BUPH]-based ILs owing to the lower ionic mobility because of the presence of longer alkyl chain in their structure. [TFA]-based Pr-ILs showed a good ionic conductivity of ~ 28.6 $mS \cdot cm^{-1}$ up to moderate temperature (~ 80−90 °C) that is almost comparable with the conductivity of [TFS]-based Pr-ILs at the same temperature. However, acetate-based Pr-ILs are not thermally stable owing to the presence of hydrophilic acetate group. So, the order of ionic conductivity according to the anion nature is as follows: [TFS] > [HS] > [TFA] > [BUPH] > [EHPH]. It was found that by increasing the alkyl and hydroxyl chain in cation structure, the ionic conductivity reduces due to the ionic mobility reduction. Following order of cation ionic conductivity can be proposed: [MIM] > [BIM] and [DETA] > [DEPA]. The dominant transport mechanism for all synthesized Pr-ILs is proton hopping since E_a > 14 $kJ \cdot mol^{-1}$.

The obtained results prove that the [TFS]-based Pr-ILs are the ideal choice for high temperature industrial applications and long-term processes (e.g. HT-PEMFC) owing to their excellent thermal stability and ionic conductivity.

Chapter 4. Polyamide 6-based Membrane

In the present chapter, the fabrication and characterization of the porous membranes based on the PA6 are presented. The influence of the membrane elaboration parameters (namely, gelation time) on the morphological and transport properties (i.e. hydrodynamic water flux, hydrodynamic permeability, and retention test) of resultant membranes is studied. The obtained results of this chapter were published in the Membranes journal (https://doi.org/10.3390/membranes12030315).

4.1. PA6 Membrane Elaboration

Nowadays, in order to improve the chemical, physical, thermal, and transport properties of membranes, several modifications can be performed, such as the addition of nano materials (i.e. nanoparticles, nanotubes, and nanofibers), surface modification by polymer immobilization, the use of inorganic and organic materials, plasma treatment, and graft polymerization [139]. However, to have a desirable membrane for selected application, several parameters that influenced the morphological and transport properties should be taken in to account, namely the polymer nature, nature of solvent and non-solvent, gelation time, coagulation medium composition, coagulation medium temperature, casting solution composition, casting solution temperature, membrane casting rate, casting knife thickness, relative humidity, and temperature of the atmosphere [139]. Up to now, several studies have been carried out to investigate the influence of gelation time on the membrane properties [156-159]. Vandezande et al. [159] investigated the influence of different phase inversion parameters (i.e. casting solution composition, evaporation time, and coagulation medium composition) on the polyimide-based membrane properties for nanofiltration application. 145 membranes with different phase inversion parameters were prepared. It was found that by increasing the polyimide concentration from 15 to 25 wt.%, the complete rejection was obtained (~ 100 %) although the permeation flux was reduced at the same time. The same trend was observed for the evaporation time – by rising the evaporation time from 0 to 120 s, the rejection reached ~ 100%, however, permeation rate reduces significantly. In fact, cross-section SEM images showed that the rise of evaporation time led to decreasing the size and number of pores in the membrane structure. It was also found that the membrane elaboration in the coagulation bath containing methanol caused the highest flux as compared to the membrane obtained using other non-solvents, namely water, methanol, ethanol, propanol, and isopropyl alcohol. In another research, Li and coworkers [157] studied the influence of membrane thickness on the morphology of polyethersulfone and polyimide membranes. The SEM images demonstrated that the membrane morphology was strongly influenced by membrane thickness as the membrane morphology changed from the sponglike structure to fingerlike one by rising the membrane thickness. Fan et al. [156] evaluated the effect of coagulation media on the physical property and permeation performance of polyamide membranes. Different coagulation media (i.e. water, methanol, ethanol, *n*-propanol, *iso*-propanol, *n*-butanol, and *iso*-butanol) were used. Membrane prepared in water bath showed

the highest porosity (~ 86%) while membranes prepared in *iso*-propanol, and *iso*-butanol revealed the highest Yonug's modulus of 420 MPa. Furthermore, the optimum permeation rate (657 $g \cdot m^{-2} \cdot h^{-1}$) was observed for polyamide membrane prepared in ethanol bath. See-Toh et al. [158] investigated the influence of evaporation time and casting solution composition on the transport properties of polyimide membranes. It was found that at the same evaporation time (i.e. 10 s), the flux reduced from 170 to 30 $L \cdot m^{-2} \cdot h^{-1}$ by increasing the polymer concentration from 20 to 26 wt.%. Also, the rise of gelation time from 10 to 70 s at the same polyimide concentration (22 wt.%) led to the flux reduction from 110 to 50 $L \cdot m^{-2} \cdot h^{-1}$.

In this section, porous PA6 membranes were prepared by a phase inversion method by varying gelation time (i.e. 0, 2, 4, 10 min). The protocol of PA6 membrane preparation have been already presented in the chapter 2 (Fig. 2.6 and Table 2.1). Several analysis were performed in order to discuss the morphological and transport properties of resultant PA6 membranes.

4.2. Morphological Properties

In order to study the influence of the gelation times (0, 2, 4, and 10 min) on the membrane structure both surface and cross-sectional images were taken (Figs. 4.1 and 4.2). Besides, the membrane porosity was evaluated by the porosity, average pore size, and bubble point pressure (Table 4.1). The SEM images of the membrane surface reveal a strong effect of the gelation time on the apparent morphology of PA6 membranes (Fig. 4.1). It can be observed that the apparent morphology of PA6 membrane was not changed significantly from 0 to 2 min of gelation time – the pore size of M_2 sample is a little bit smaller than that of M_0 one. However, the M_4 and M_{10} membranes are characterized by much smaller pore size – 0.468 ± 0.023 μm and 0.234 ± 0.019 μm for M_4 and M_{10}, respectively (Table 4.1). The cross-section SEM images allow us to evaluate the inner structure of PA6 membranes (Fig. 4.2). It can be observed that both M_0 and M_2 membranes have rather symmetric porous structure. However, the rise of gelation time for more than 2 min (i.e. M_4 and M_{10}) provokes the change of the inner structure to asymmetric membrane (Figs. 4.2C and 4.2D). In addition, a skin top layer on the membrane surface (in contact with air) (which is present even for the M_0 membrane) becomes denser (i.e. smaller pores) with the gelation time increasing. Such observation can be explained by the fact that with the rise of gelation time, larger amount of solvent (i.e. formic and acetic acid) is evaporated during the delay stage [139]. As a result, changes in both skin layer and inner structure (i.e. sub layer) of M_{10} membrane are more significant than those for the M_0 membrane.

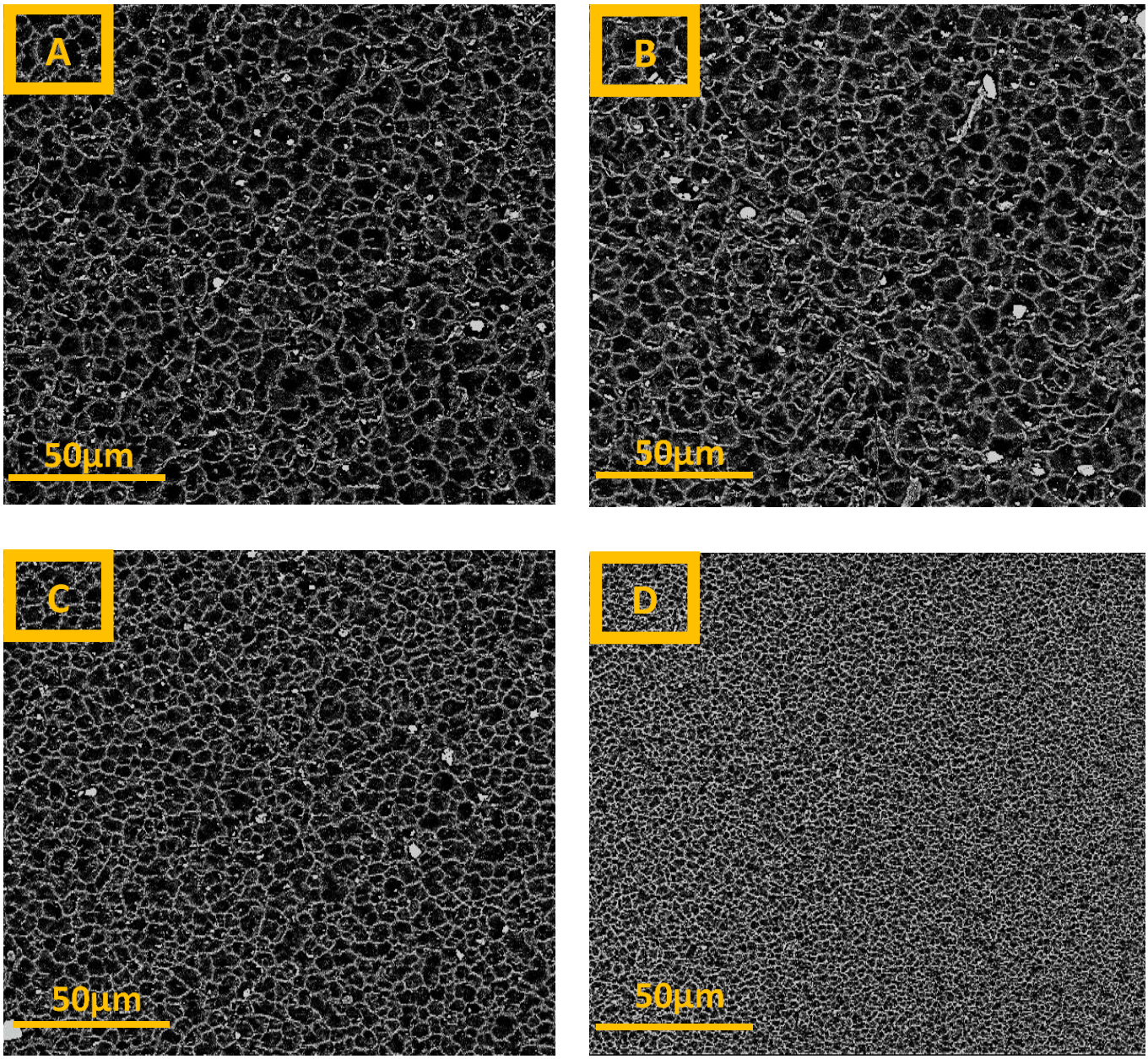

Figure 4.1. SEM images with magnification of 1500X of PA6 membranes with various gelation time: A) 0 min; B) 2 min; C) 4 min; and D) 10 min.

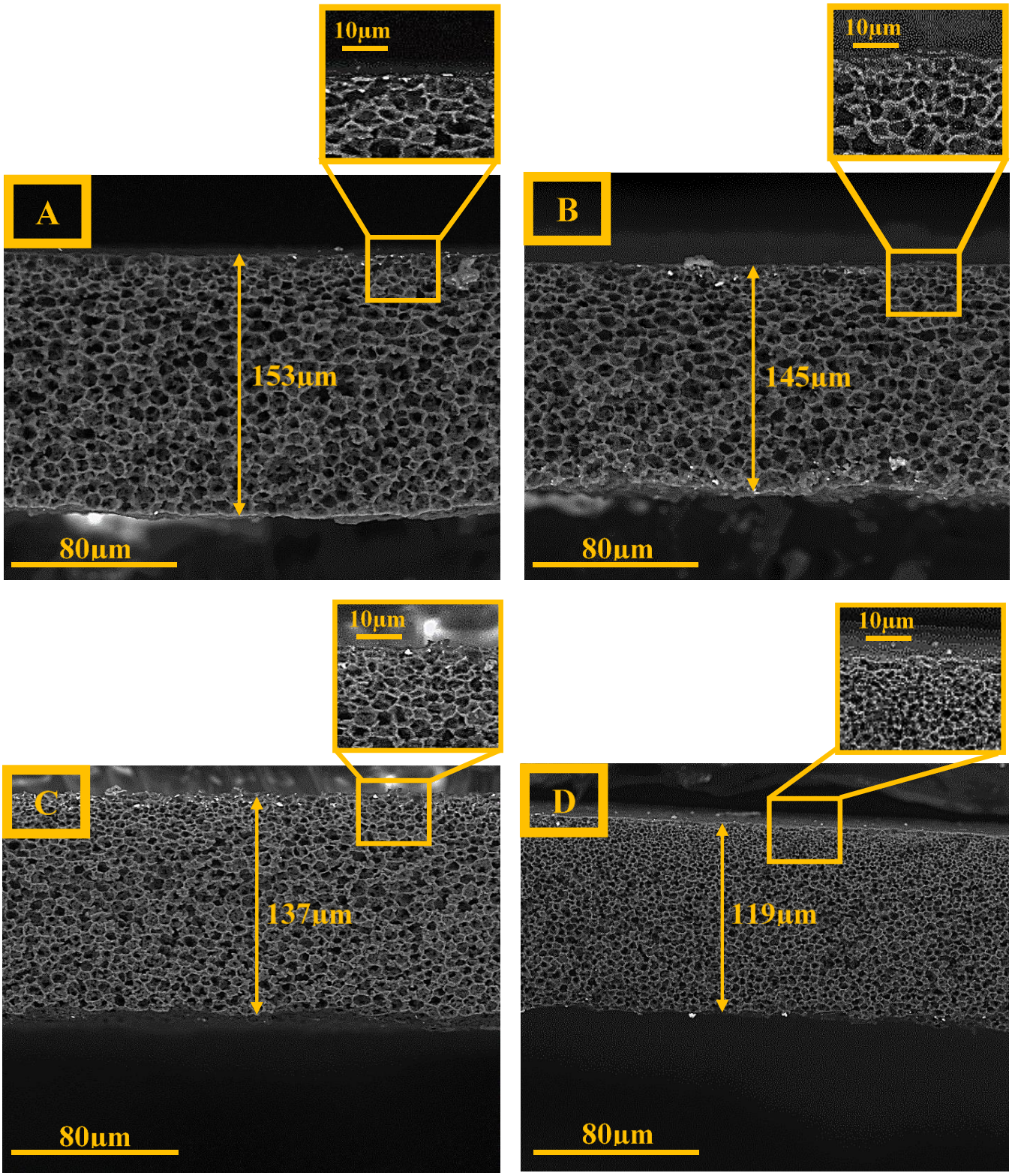

Figure 4.2. Cross-section SEM images (1000X) for PA6 membranes with different gelation time: A) 0 min; B) 2 min; C) 4 min; and D) 10 min.

Table 4.1. The effect of gelation time on porosity and average pore size of PA6-based membranes.

Membrane	Gelation time (min)	Porosity (%)	Average pore size (μm)*	Bubble point pressure (bar)*
M_0	0	72 ± 2	0.710 ± 0.060	0.226
M_2	2	59 ± 1	0.563 ± 0.036	0.442
M_4	4	54 ± 2	0.468 ± 0.023	0.618
M_{10}	10	39 ± 4	0.234 ± 0.019	0.667

* The applied liquid was Porefil with a surface tension of 16 $mN \cdot m^{-1}$.

The results of the surface topography and roughness of PA6 porous membranes are gathered in Fig. 4.3 and Table 4.2. A direct correlation between membrane surface roughness and gelation time can be seen as the increase of gelation time from 0 to 10 min leads to the membrane surface roughness increasing (R_a and R_q values) (Table 4.2). The surface roughness parameters (R_a and R_q) are quite similar for M_0 and M_2 samples meaning no considerable changes in membrane roughness with the gelation time increasing from 0 to 2 min (Table 4.2). This result is in good agreement with the membrane morphology results (Figs. 4.1-4.3) testifying to the fact that 2 min are not sufficient for the evaporation of high solvent quantity. However, by further gelation time rising, the membrane morphology and surface roughness changed significantly (Figs. 4.1 and 4.2 and Table 4.2). The PA6 membrane with the highest gelation time (i.e. M_{10}) showed the highest R_a and R_q values (189 ± 53 nm and 240 ± 59 nm, respectively). Indeed, longer time of exposure of the cast polymer solution to the air for this sample provokes changing the gel structure owing to solvent evaporation during the delay stage [139].

Table 4.2. Surface roughness of PA6 membranes for 5×5 μm^2 scanned area.

Membrane	R_a (nm)	R_q (nm)
M_0	154 ± 22	200 ± 34
M_2	155 ± 32	195 ± 42
M_4	166 ± 28	203 ± 31
M_{10}	189 ± 53	240 ± 59

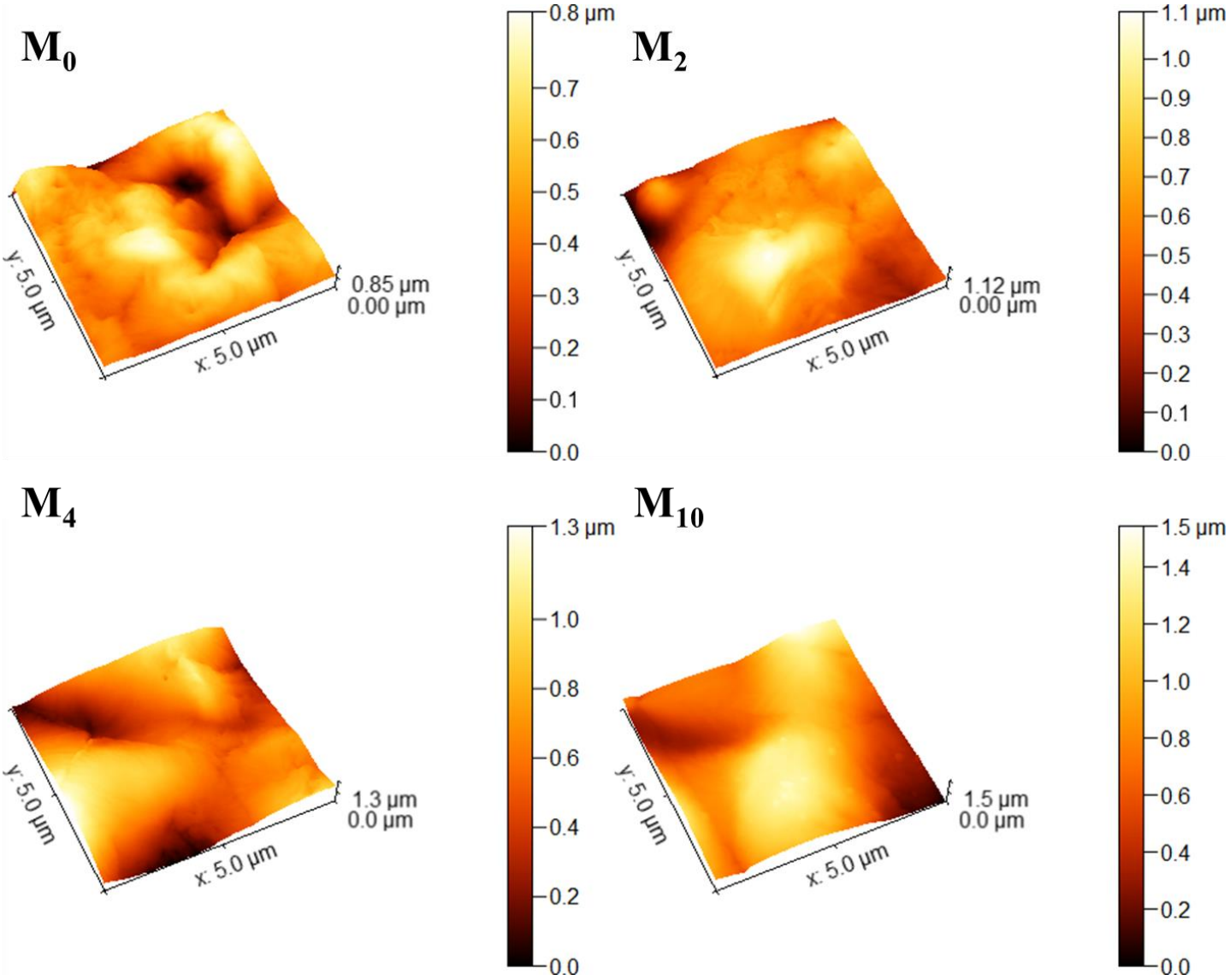

Figure 4.3. Surface morphology of PA6 membranes with different gelation time for 5×5 μm^2 scanned area.

In order to see the influence of the gelation time on the membrane thickness, the thickness of PA6 porous membranes was measured in both wet and dry states (Fig. 4.4). For this purpose, membranes were initially immersed in the deionized water for 24 h and the thickness was measured (T_w) after removing the excess water from the membrane surface. Then, membranes were placed in an oven at 80 °C for 24 h and their thickness was measured again (T_d). The obtained values of membrane thickness in both dry and wet states are plotted in Fig. 4.4. The membrane thickness measured by the SEM analysis (Fig. 4.2) was added for comparison. It can be seen that the membrane thickness values in both states (i.e. T_w and T_d) showed a downward tendency with rising the gelation time. The rise of gelation time leads to reduction of apparent pore size owing to the solvent evaporation during the delay stage. Thus, by increasing the gelation time,

higher amount of solvent was evaporated. It is observed that T_w values for each sample are higher than T_d ones as the membrane swelling takes place by the water molecules [139]. The membrane thickness measured by SEM is close to the values measured in dry state proving the measurement accuracy. In order to have a deeper insight into the membrane morphology, bubble point method was used to measure the membrane pore size and pore size distribution. The bubble point pressure values are gathered in Table 4.1. This pressure corresponds to the pressure, at which the first air bubble passes through a wet membrane. The high pressure value indicates a membrane with small pore size while the low pressure value is characterized to a membrane with large pore size [131,133,139]. Therefore, membranes possessing compact porous structure will require higher pressure in comparison with porous membrane containing large pores. One can see that by increasing the gelation time, the average pore size of PA6 membranes decreases – 0.710 and 0.234 μm are obtained for M_0 and M_{10} membranes, respectively. These results confirm well the results of the SEM analysis (Figs. 4.1 and 4.2) indicating that gelation time increasing provokes membrane denser morphology. On the contrary, an opposite correlation between gelation time and membrane porosity can be seen – the maximum and minimum values are reported for M_0 and M_{10} membrane (72 and 39%, respectively) (Table 4.1). This result confirms that less porous membrane is obtained by the gelation time increase owing to a longer solvent evaporation during the delay stage.

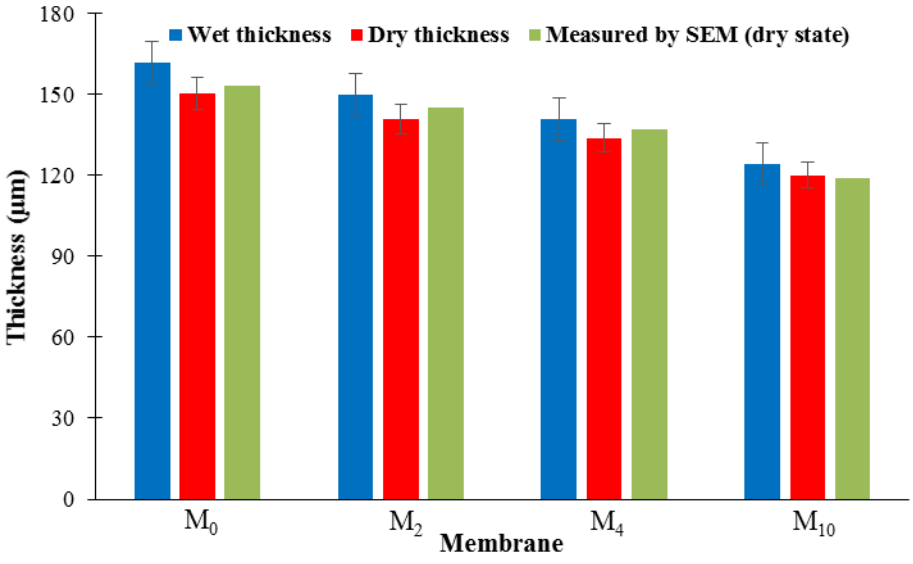

Figure 4.4. Wet and dry thickness of PA6 porous membranes.

4.3. Hydrophilic/Hydrophobic Balance

The membrane swelling degree was calculated as a function of gelation time (Table 4.3). It can be seen that the increase of gelation time causes the decrease of swelling degree – the membrane with highest

gelation time (i.e. M_{10} membrane) is characterized by the lowest swelling degree (single-dimensional, area, and volume). Indeed, such result can be explained by changing the membrane morphology as the rising of the gelation time results in the decrease of the apparent pore size of membranes (Figs. 4.1 and 4.2). Therefore, M_0 sample with larger pores reveals the highest swelling degree, while M_{10} sample with the most compact porous structure demonstrates the lowest swelling degree.

Table 4.3. Swelling degree (single-dimensional, area, and volume) of porous PA6 membranes with different gelation time.

Membrane	Gelation time (min)	Swelling degree (%)		
		Single-dimensional (Eq. 2.3)	Area (Eq. 2.4)	Volume (Eq. 2.5)
M_0	0	8 ± 2	20 ± 3	29 ± 4
M_2	2	6 ± 1	14 ± 2	20 ± 4
M_4	4	5 ± 1	11 ± 2	16 ± 3
M_{10}	10	3 ± 1	8 ± 2	11 ± 2

The water uptake of porous PA6 membranes with different gelation times was measured (Fig. 4.5). The results show that the increasing of gelation time results in the water uptake reduction – from ~ 62% for M_0 membrane to 39% for M_{10} membrane. The reason of such water uptake behavior is the reduction of membrane pore size with the gelation time rising, thus, less water molecules can be absorbed by M_{10} sample as compared with the M_0 membrane.

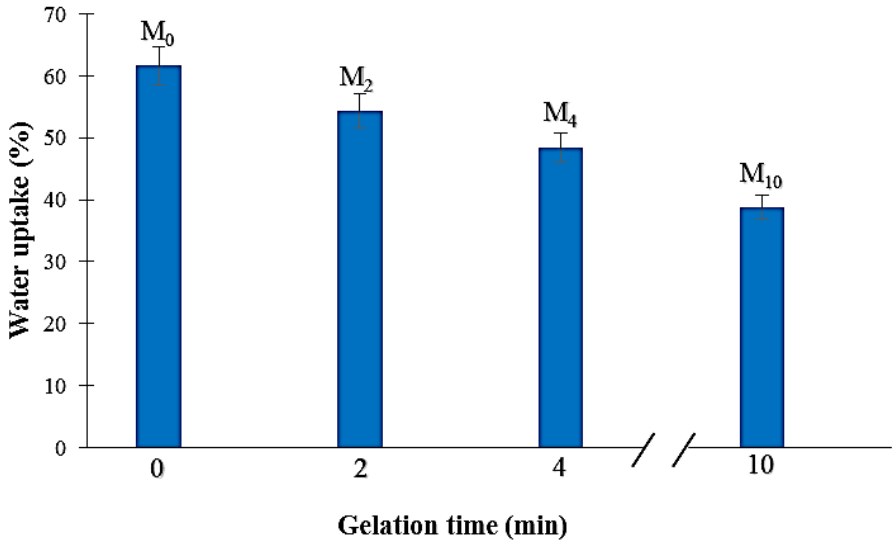

Figure 4.5. Water uptake of obtained PA6 membranes as a function of the gelation time.

The CA value was measured by two different techniques: a sessile drop and a captive bubble. In case of the sessile drop method, the water drop is placed on the surface of the PA6 membrane and the angle between the membrane surface and drop is measured (Fig. 2.8a). However, once the drop is placed on the membrane surface, it disappeared rapidly. The first reason of such result is the hydrophilic nature of PA6 polymer. The second reason is the membrane porous structure (Fig. 4.2). Therefore, the water drops are absorbed by the membrane. In any case it can be revealed that the water CA increases by increasing the gelation time (from M_0 to M_{10}) owing to the pore size decreasing (Fig. 4.6a). It is known that CA is influenced by two parameters: the membrane nature and the surface roughness [139,160-162]. The membrane nature is the same since no additives or fillers were added and the only difference is the membrane morphology and roughness (Figs. 4.1, 4.2 and Table 4.2). The water CA values were also measured for wet membranes. For this purpose, the membrane was initially immersed in water and then the CA value was measured. The water drops are still absorbed by the membrane, however, the absorption rate is slower than that for dry samples. In any case, the increase of gelation time leads to rising the CA values (Fig. 4.6b).

In case of porous and hydrophilic membranes, it is better to measure the CA by captive bubble method (Fig. 2.8b and 4.7). As one can see, the slight increase of the CA value with the gelation time rising is still observed. The CA values were plotted as a function of the membrane roughness (Fig. 4.8). One can see that starting from 2 min of gelation time (i.e. minimum necessary time for the solvent evaporation) the CA increase is observed.

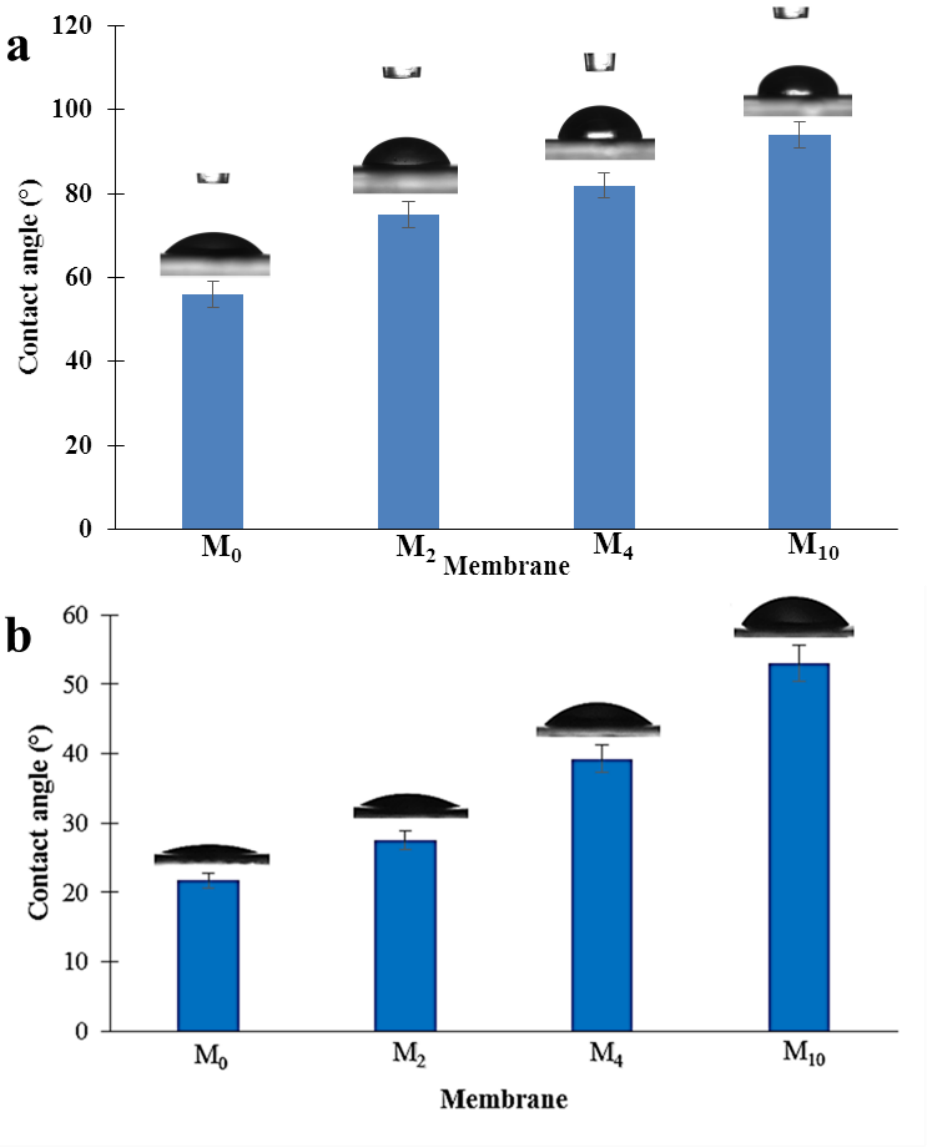

Figure 4.6. CA values of PA6 membranes measured by sessile drop method for dry (a) and wet (b) membranes.

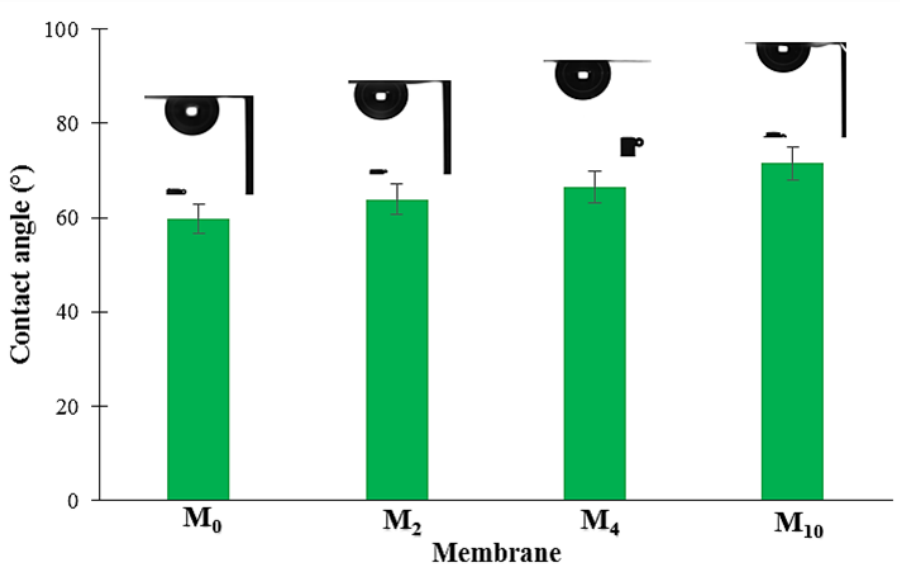

Figure 4.7. CA measurements of PA6 membranes by captive bubble method.

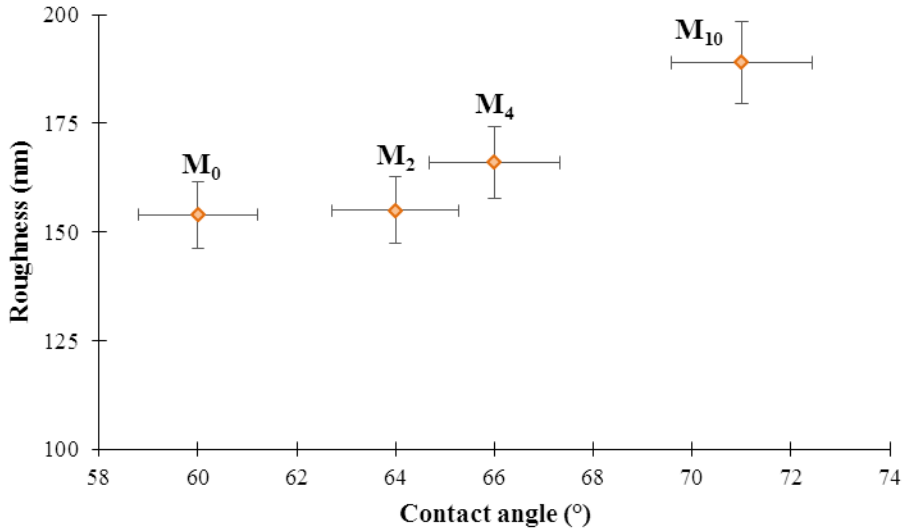

Figure 4.8. Correlation between CA values (measured by captive bubble method) and surface roughness.

4.4. Mechanical Properties

In order to study the influence of the membrane morphology on its mechanical properties, the tensile strength measurements were performed (Fig. 4.9). It is observed that rising the gelation time from 0 to 4 min, does not provoke the change in the membrane mechanical stability. This result may be explained by the fact that the membrane morphology is changed slightly for these membranes (Fig. 4.1 and 4.2). However, further increase of gelation time from 4 to 10 min causes the use of mechanical tensile strength of ~ 28% (Fig. 4.9). In fact, this membrane is characterized by the smallest average pore size among other

samples (Table 4.1) and the compact membrane structure (Fig. 4.2D) leading to increased mechanical stability.

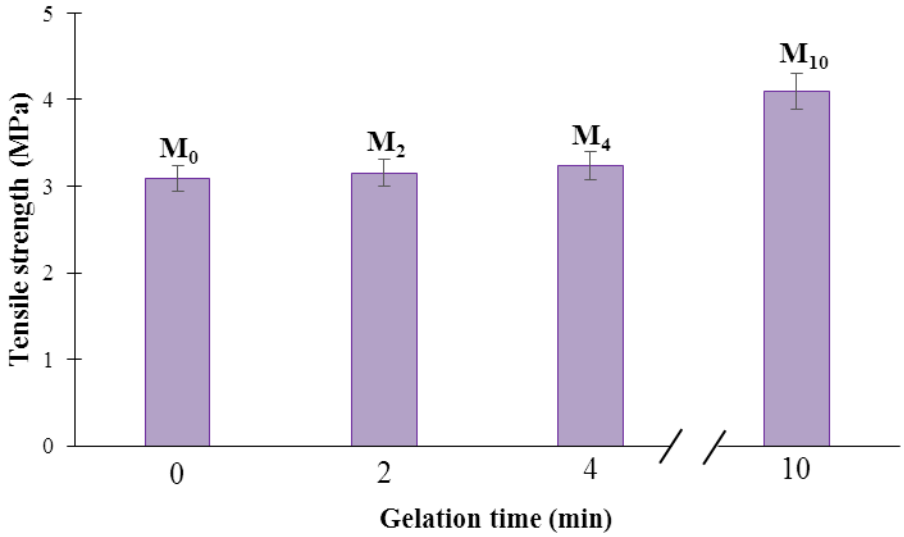

Figure 4.9. Tensile strength of the PA6 membranes as a function of the gelation time.

4.5. Transport Properties

The transport properties (i.e. hydrodynamic water flux, hydrodynamic permeability, and retention) of the obtained PA6 membranes with different gelation times were evaluated. The membrane hydrodynamic water flux was measured using a dead-end experimental filtration setup (Fig. 2.10) and the measurement were carried out at three different operation pressure values (0.5, 1.0, and 2.0 bar). Prior to measurement, the membrane was initially compressed at 3 bar till the water flux through the membrane remained stable. The PA6 membranes are characterized by a high initial hydrodynamic water flux – between 2000 and 3500 $L \cdot m^{-2} \cdot h^{-1}$ at 3 bar. The evaluation of the hydrodynamic water flux of each membrane at different operation pressures versus time is shown in Fig. 4.10. It can be observed that the membrane hydrodynamic water flux initially decreases and then remains stable. Such behavior is explained by the pores compactness owing to the applied pressure. Subsequently, after the pore compression, the hydrodynamic water flux remained stable. It can be seen that the rise of gelation time results in reduction of the membrane hydrodynamic water flux (Fig. 4.10E). In general, the membrane morphology (porosity and average pore size) as well as membrane hydrophilicity influence the membrane hydrodynamic water flux [124,139,163]. As it was shown (Table 4.1) both porosity and average pore size decrease with gelation time increase. The SEM images also showed that the membrane morphology is changed with the gelation time – denser membranes with smaller pores are obtained with increasing the gelation time from 0 to 10 min (Figs. 4.1 and 4.2). Moreover, the CA measurements (Fig. 4.6 and 4.7) revealed the decrease of the surface hydrophilicity of PA6 membranes

with the gelation time increasing. Therefore, the hydrodynamic water flux of the M_0 membrane is the highest in comparison with the flux of other membranes (i.e. M_2, M_4, and M_{10}). In addition, there is a linear correlation between the hydrodynamic water flux and operating pressure – the higher pressure is the higher is the flux (Fig. 4.10E). The maximum and minimum values are obtained for M_0 and M_{10} membranes – 28.6 and 12.9 $L \cdot m^{-2} \cdot h^{-1}$, respectively.

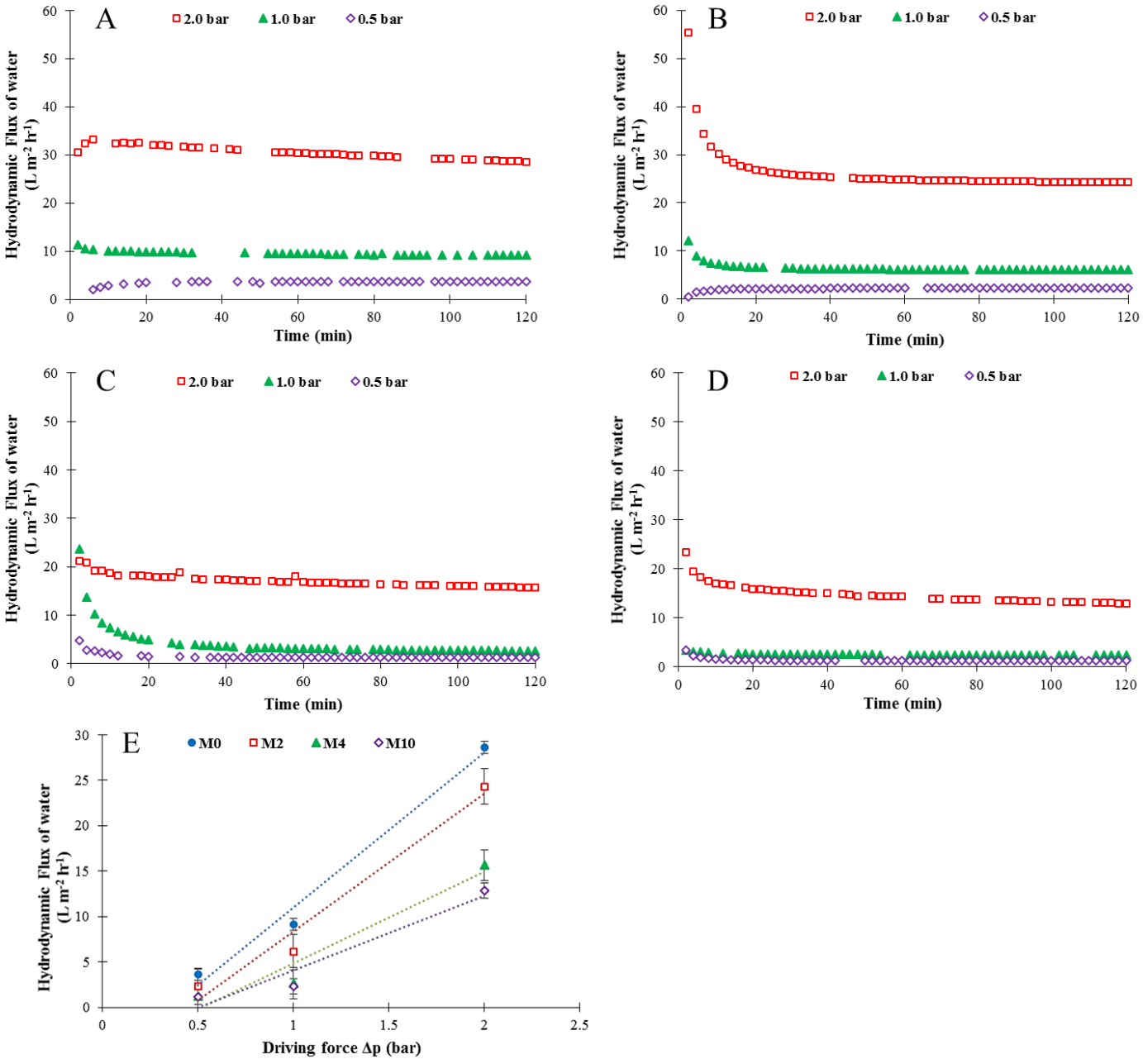

Figure 4.10. Hydrodynamic water flux at different operating pressures of PA6 membranes: A) M_0; B) M_2; C) M_4; D) M_{10}; and E) as a function of driving force.

The membrane hydrodynamic permeability coefficient L_p is an important transport parameter. This value is defined as the slope of the hydrodynamic water flux curve as a function of the applied pressure (Eq. 2.13). As one can see from Fig. 4.11, a correlation between L_p and membrane morphology can be found. The L_p value decreases by increasing the gelation time – the highest L_p value is obtained for M_0 membrane and the lowest value is measured for M_{10} membrane (17.0 and 8.2 $L \cdot m^{-2} \cdot h^{-1} \cdot bar^{-1}$, respectively). The obtained results reveal that both porosity and pore radius of PA6 membranes are reduced, so the L_p reduction is observed by enhancing the gelation time.

The retention measurements were also performed for PA6 membranes. The results are shown in Fig. 4.12. It can be observed that rising the gelation time led to the retention enhancement – the membrane with the highest gelation time (i.e. M_{10}) demonstrated the highest retention value (~ 50%). The main reason of such result is the average pore size decrease with the gelation time rise (Fig. 4.2 and Table 4.1). Therefore, one can confirm that increasing the gelation time results in denser membrane structure (i.e. smaller average pore size), thus, ensuring the higher membrane retention properties.

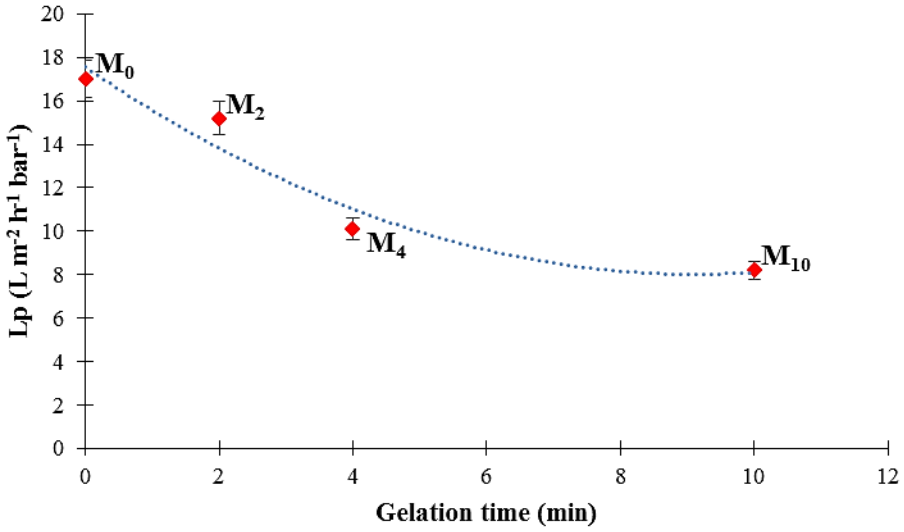

Figure 4.11. Membrane hydrodynamic permeability coefficient L_p as a function of the gelation time.

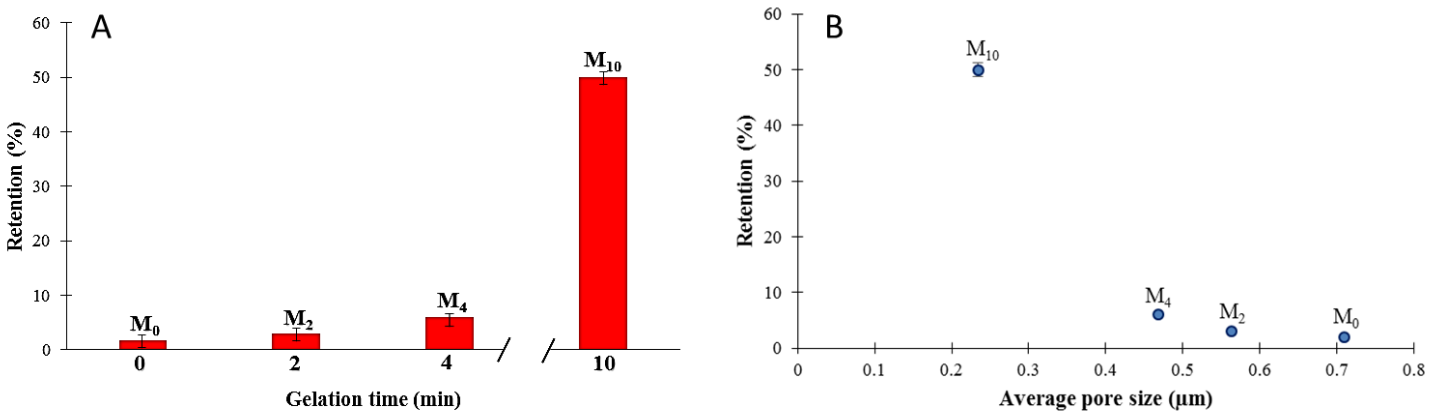

Figure 4.12. Influence of gelation time (A) and average pore size (B) on the membrane retention.

It can be seen that the water flux and L_p values are rather low as compared to the literature data. Zheng and coworkers [164] prepared IL grafted PA6 porous membranes *via* phase inversion method to improve the water flux and heavy metal ion removal. The obtained results showed that by increasing the concentration of IL from 2 to 8 wt.%, the water CA and pore size values decreased while the membrane porosity increased. Also, composite PA6 membrane containing 2 wt.% of IL showed the highest water flux of ~ 3400 $L \cdot m^{-2} \cdot h^{-1}$ which was 2.6 times higher than that of pure PA6 membrane owing to the higher hydrophilicity and porosity of composite membrane. The IL grafted PA6 membranes demonstrated a better heavy metal removal ability than the pure PA6 membrane owing to the great adsorption property of IL. Shin et al. [165] prepared polyethersulfone/N-methyl-2-pyrrolidone microfiltration membranes modified by 2-methoxyethanol as an additive. It was found that the membrane containing 60 and 30 wt.% of 2-methoxyethanol and N-methyl-2-pyrrolidone, respectively, showed the great water flux of 700 $L \cdot m^{-2} \cdot h^{-1}$. Woo and coworkers [166] prepared poly(vinylidene fluoride)-based membrane and evaluate the influence of membrane surface roughness on the permeate flux. It was observed that the membrane surface roughness has an opposite influence on the permeate flux and the smoothest membrane showed the highest value of 146 $L \cdot m^{-2} \cdot h^{-1}$.

Such results confirm that the resultant PA6 membranes are not characterized by satisfactory transport properties (water flux and L_p) and they cannot be considered as a efficient membranes for filtration processes. However, these membranes can be used as the supported ionic liquid membrane (SILM) especially M_{10} membrane with the lowest pure water flux. Indeed, one of the promising ways to fabricate the ion conductive membrane for PEMFC application is to prepare SILM. Fatyeyeva et al. [117] prepared SILMs based on the porous polyimide membrane impregnated by imidazolium-based ILs. The polyimide/IL membranes showed a great ionic conductivity of ~ 10^{-3} $S \cdot cm^{-1}$ at 160 °C. In another work, Dahi et al. [142] prepared SILM based on porous Matrimid® membrane and imidazolium-based ILs. The

composite membranes showed the ionic conductivity of $2.0 \cdot 10^{-2}$ $S \cdot cm^{-1}$ at 115 °C. Kobzar and coworkers [118] impregnated porous polyimide Matrimid® membrane with different polymerized ILs and the ionic conductivity of 0.1 $mS \cdot cm^{-1}$ at 150 °C.

4.6. Conclusion

Different porous PA6 membranes with various gelation times were fabricated by non-solvent induced phase separation technique. SEM analysis showed that the change of the gelation time leads to different membrane morphology – higher gelation time provokes the formation of the porous membranes with smaller pores. M_0 and M_{10} membranes showed the largest and smallest average pore size of 0.71 and 0.23 μm, respectively. AFM analysis revealed that increasing of the gelation time provokes membrane surface roughness increase and the highest surface roughness was observed for M_{10} membrane (R_a and R_q of ~ 189 ± 53 nm and 240 ± 59 nm, respectively). Moreover, water CA increased with the gelation time rising owing to the surface roughness enhancement, while water uptake and membrane porosity was reduced owing to pore size reduction. M_{10} membrane also showed a better tensile strength (around 28%) than that of M_0 membrane due to the change of the structure during the gelation time. The obtained porous PA6 membranes are not characterized by high water flux, L_p, and retention values – ~ 12.9 $L \cdot m^{-2} \cdot h^{-1}$, 8.2 $L \cdot m^{-2} \cdot h^{-1} \cdot bar^{-1}$, and 50%, respectively, for M_{10} membrane. Although, the prepared membranes do not demonstrated sufficient transport properties, they have good potential to be used as a support for the SILM preparation for PEMFC application.

Chapter 5. Ionic Liquid-based Membranes

Composite membranes based on CAP/A-ILs and CAB/Pr-ILs were fabricated. The resultant composite membranes were prepared by phase inversion method (casting followed by the solvent evaporation). CAP and CAB polymers were chosen owing to their applications in various membrane separation processes, such as pervaporation, reverse osmosis, and ultrafiltration. The physical and morphological properties of lab-made composite membranes were evaluated.

This chapter is divided into two parts. The first section is devoted to CAP/A-ILs composite membranes elaborated using commercial A-ILs. CAB/Pr-ILs composite membranes are presented in the second part. The main goal of this research was to investigate the influence of the nature and concentration of A-ILs and Pr-ILs on the physical, chemical, thermal, and transport properties of composite membranes and compare them with pure CAP and CAB membranes.

5.1. CAP/A-ILs Composite Membranes

5.1.1. Membrane Elaboration

As explained in Chapter 2 (Fig. 2.7), the composite CAP/A-IL membranes were prepared by phase inversion method. Three commercial A-ILs containing the same cation (1-(4-sulfobutyl)-3-methylimidazolium [SMIM]) and different anions ([TFS], [HS], and [TFSI]) were used. The membranes with various concentrations of A-ILs (i.e. 0, 9, 17, and 23 wt.%) were fabricated (Table 5.1 and Fig. 5.1) to evaluate the influence of the A-IL content and nature on the properties of composite membranes and compare them with the properties of pure CAP.

Table 5.1. The composition of composite membranes.

Membrane	A-IL content (wt.%)*
M_0	–
M_1	9
M_2	17
M_3	23

*Content of IL in membrane.

The first observations concern CAP/[SMIM][TFS] and CAP/[SMIM][TFSI] composite membranes. The addition of A-ILs (i.e. [SMIM][TFS], [SMIM][HS], and [SMIM][TFSI]) and changing their concentration from 9 to 23 wt.% (i.e. from M_1 to M_3) provokes the membrane transparency (Fig. 5.1) as well as apparent mechanical stability (membrane flexibility) decrease. As to CAP/[SMIM][HS] composite membrane, no significant changes in the membrane transparency and apparent mechanical

stability are noticed. The reason of this result may be a better compatibility between [SMIM][HS] and polymer as compared to two other A-ILs.

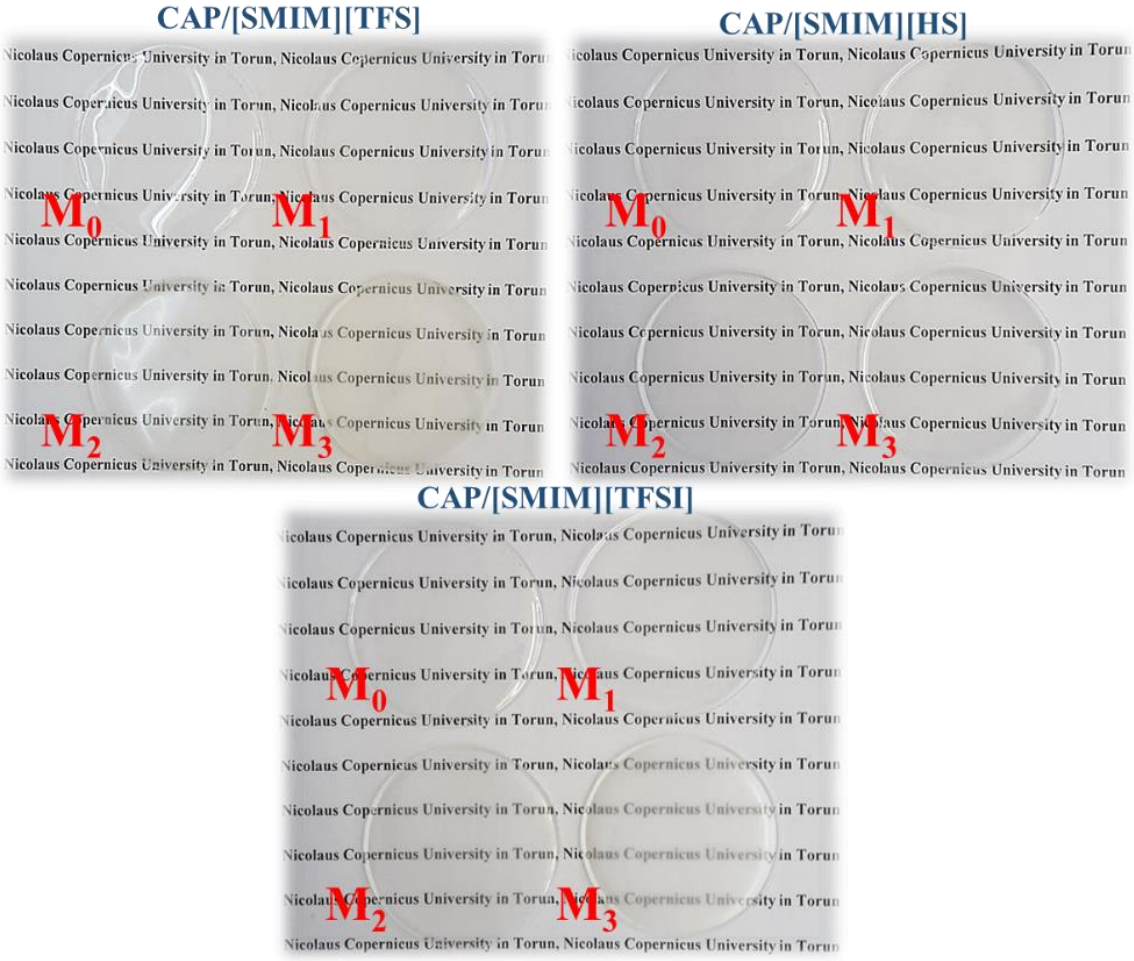

Figure 5.1. Images of obtained pure CAP and CAP/A-IL-based membranes.

5.1.2. Physical-Chemical Characterization

5.1.2.1. Membrane Morphology

To evaluate the morphology of both pure CAP and composite CAP/A-ILs membranes, SEM analysis was carried out (Figs. 5.2 and 5.3). A dense and homogenous structure of the pure CAP membrane (i.e. M_0) can be noted. Such morphology is owing to good polymer dissolution in the solvent (i.e. chloroform and acetone). The A-ILs introduction changes the membrane morphology from homogenous to heterogeneous one. Furthermore, the number of observed gaps and cavities increases with the rise of the A-ILs concentration of A-ILs from 9 to 23 wt.%. The main reason of this result is the incompatibility between the polymer and A-ILs, thus the addition leads to the weakening of the polymer intermolecular and

intramolercular links. The membrane thickness was measured during the SEM analysis and it was found that the A-ILs addition resulted in the thickness increasing of composite membranes as compared with the pure CAP membrane. The rise of A-ILs content provokes further increase of the membranes thickness.

The carried EDX analysis allows to evaluate the presence of A-ILs. As one can see from Fig. 5.4, the presence of characteristic elements of IL (i.e. S, N, and F) in the composite membrane bulk is detected, confirming the dispersion of A-ILs within the membrane.

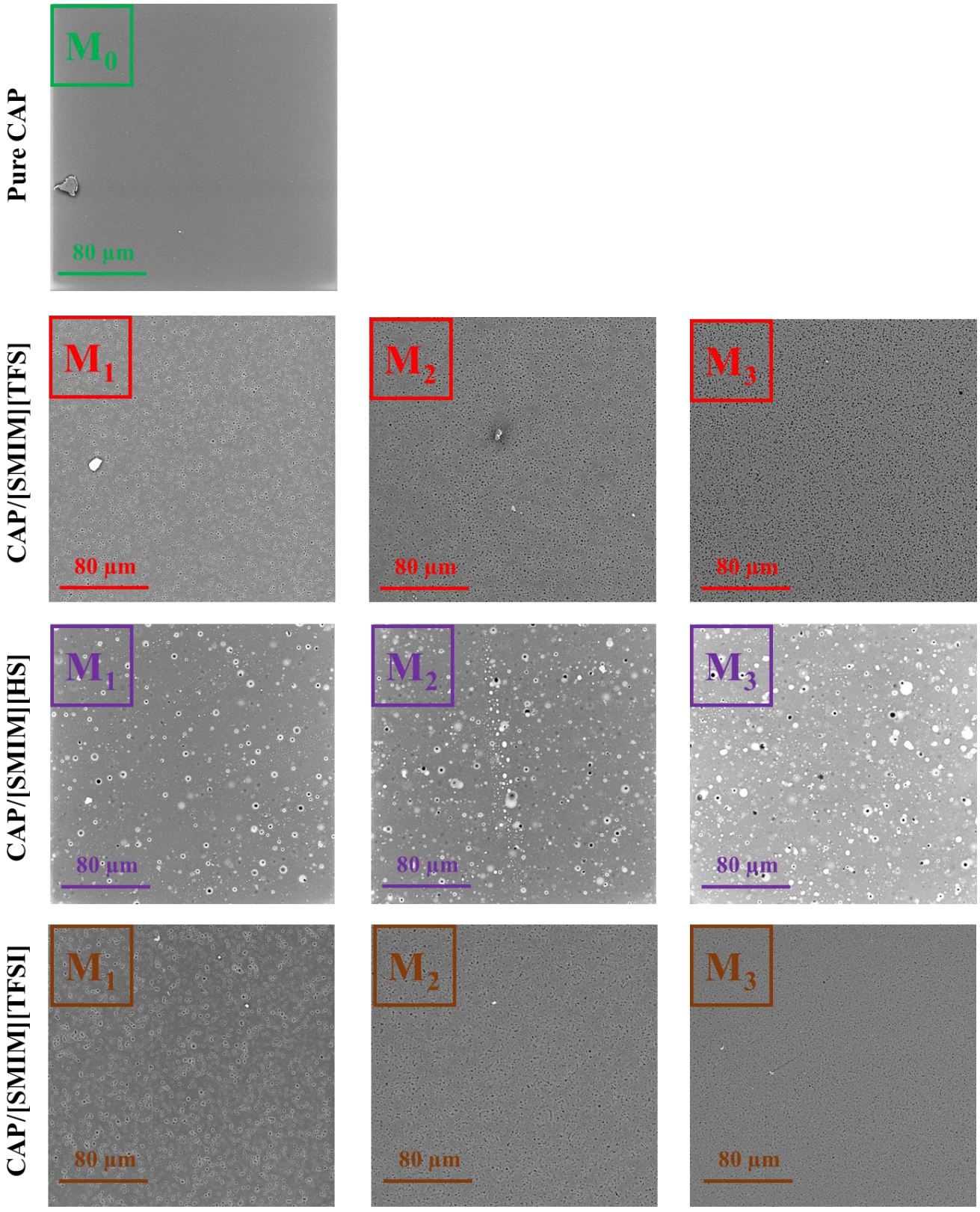

Figure 5.2. SEM images with magnification of 1000X of pure CAP and composite CAP/A-ILs membranes.

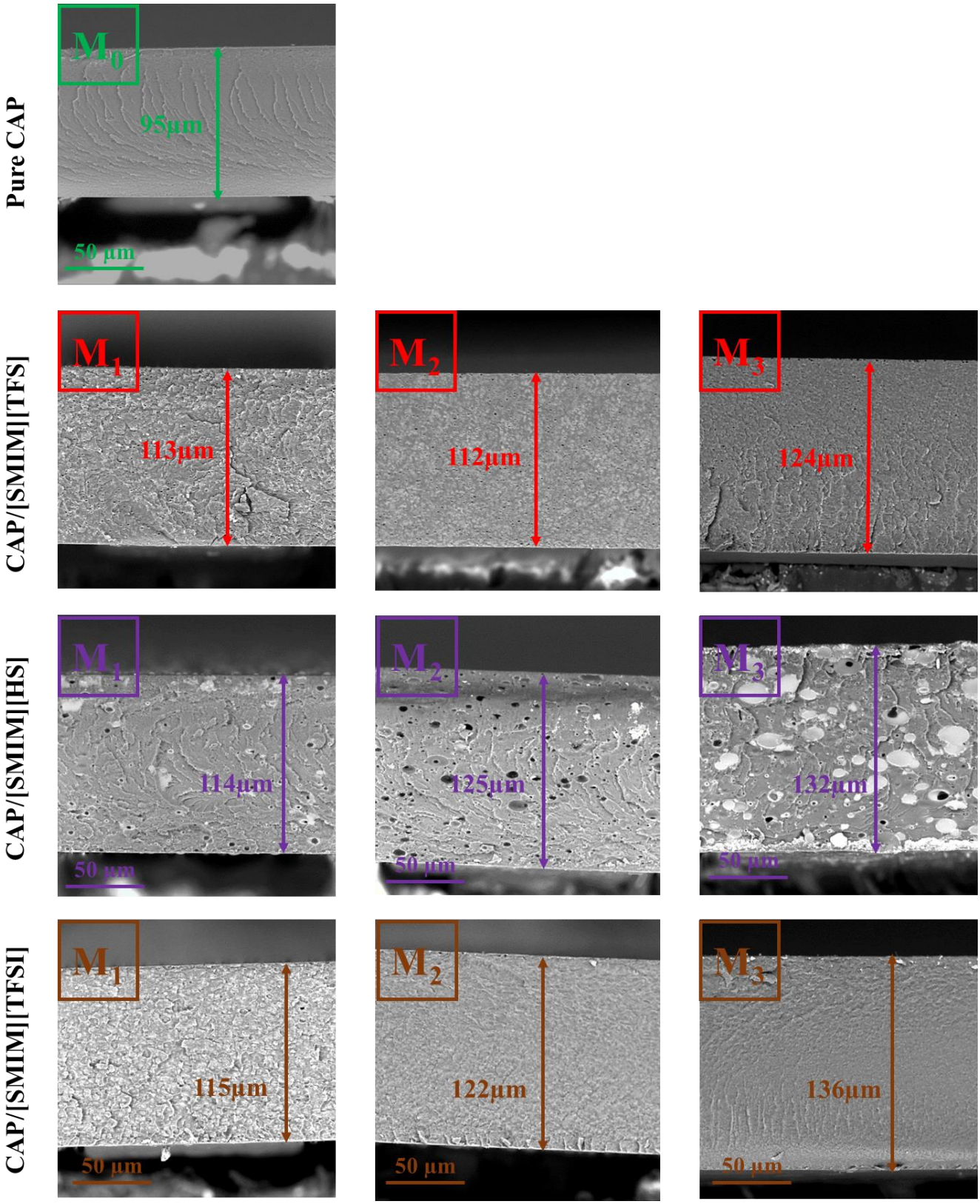

Figure 5.3. Cross-section SEM images with magnification of 1500X of pure CAP and CAP/A-ILs composite membranes.

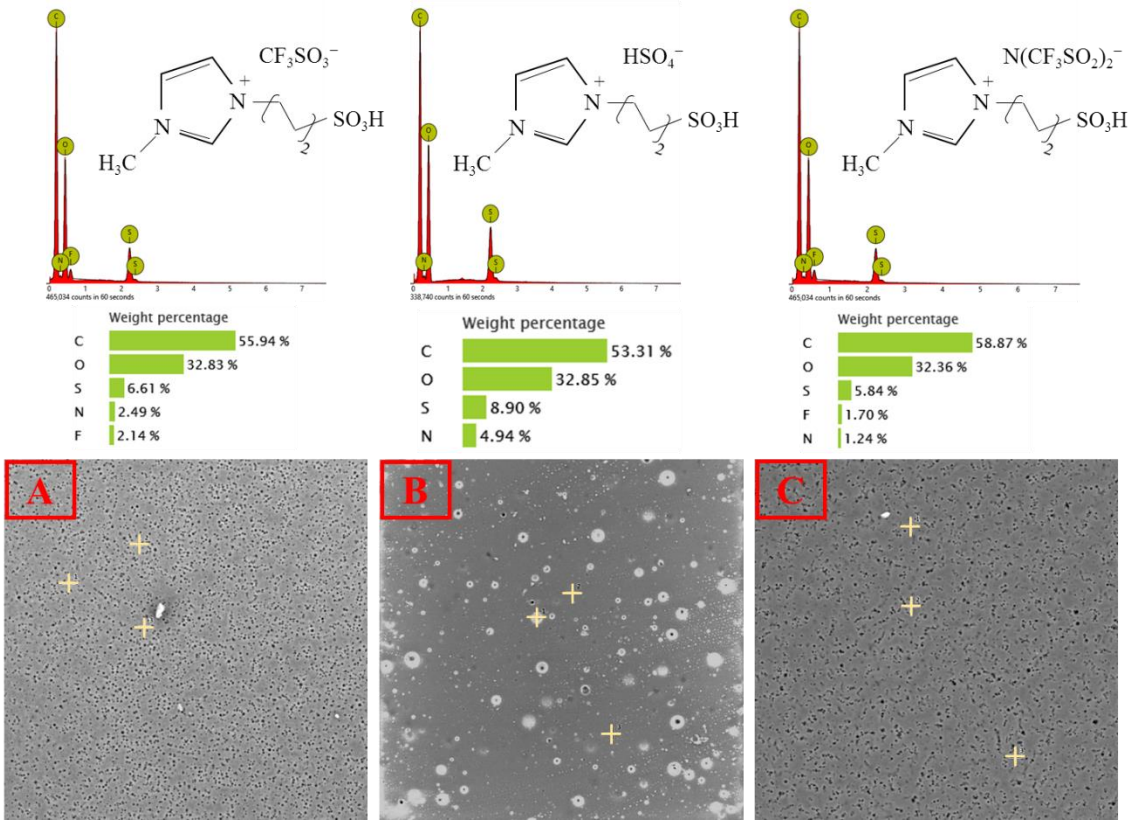

Figure 5.4. EDX spectra of composite membranes containing 17 wt.% of A-ILs: A) CAP/[SMIM][TFS]; B) CAP/[SMIM][HS]; and C) CAP/[SMIM][TFSI].

Surface topography and roughness of pure CAP and composite CAP/A-ILs membranes were measured (Fig. 5.5 and Table 5.2). The results revealed a smooth surface for pure CAP membrane with the surface roughness of ~ 2.8 nm. However, two different tendencies can be observed after the addition of A-ILs. As to composite membranes containing perfluorinated-based A-ILs (i.e. CAP/[SMIM][TFS] and CAP/[SMIM][TFSI]), it can be seen that the surface roughness increases significantly by rising the IL concentration from 9 to 23 wt.% (Table 5.2). Composite membranes with 23 wt.% of [SMIM][TFS] and [SMIM][TFSI] (i.e. M_3) demonstrated the maximum R_a value of ~ 83 and 115 nm, respectively. On the other hand, the surface roughness of CAP/[SMIM][HS] composite membranes is practically the same whatever the [SMIM][HS] concentration (~ 20 nm) (Table 5.2). The reason of such behavior is the different nature of used A-ILs. It should be noted that all studied A-ILs has the same cation ([SMIM]), but various anions ([TFS], [HS], and [TFSI]). Two perfluorinated-based A-ILs (i.e. [SMIM][TFS] and [SMIM][TFSI]) have hydrophobic nature owing to the presence of hydrophobic anions containing the fluorine atoms. Thus, such A-ILs cannot have good compatibility with CAP polymer, which is hydrophilic. Such incompatibility is more pronounced at high concentrations of ILs. [SMIM][HS] has the hydrophilic nature due to a sulfate-

based anion. Thus, [SMIM][HS] has a better compatibility with hydrophilic CAP leading to obtaining a smoother surface as compared to two perfluorinated-based ILs (i.e. [SMIM][TFS] and [SMIM][TFSI]).

Table 5.2. Surface roughness and thickness of pure CAP and CAP/A-ILs membranes.

Parameter	Membrane composition									
	CAP	CAP/[SMIM][TFS]			CAP/[SMIM][HS]			CAP/[SMIM][TFSI]		
	M_0	M_1	M_2	M_3	M_1	M_2	M_3	M_1	M_2	M_3
Roughness R_a (nm)	2.8 ± 1	35.0 ± 4	48.1 ± 11	82.8 ± 25	24.7 ± 11	17.6 ± 3	19.4 ± 6	12.8 ± 5	51.9 ± 6	115.4 ± 31
Thickness (µm)	102 ± 14	113 ± 15	137 ± 35	144 ± 34	116 ± 16	127 ± 16	134 ± 25	110 ± 16	116 ± 13	122 ± 19

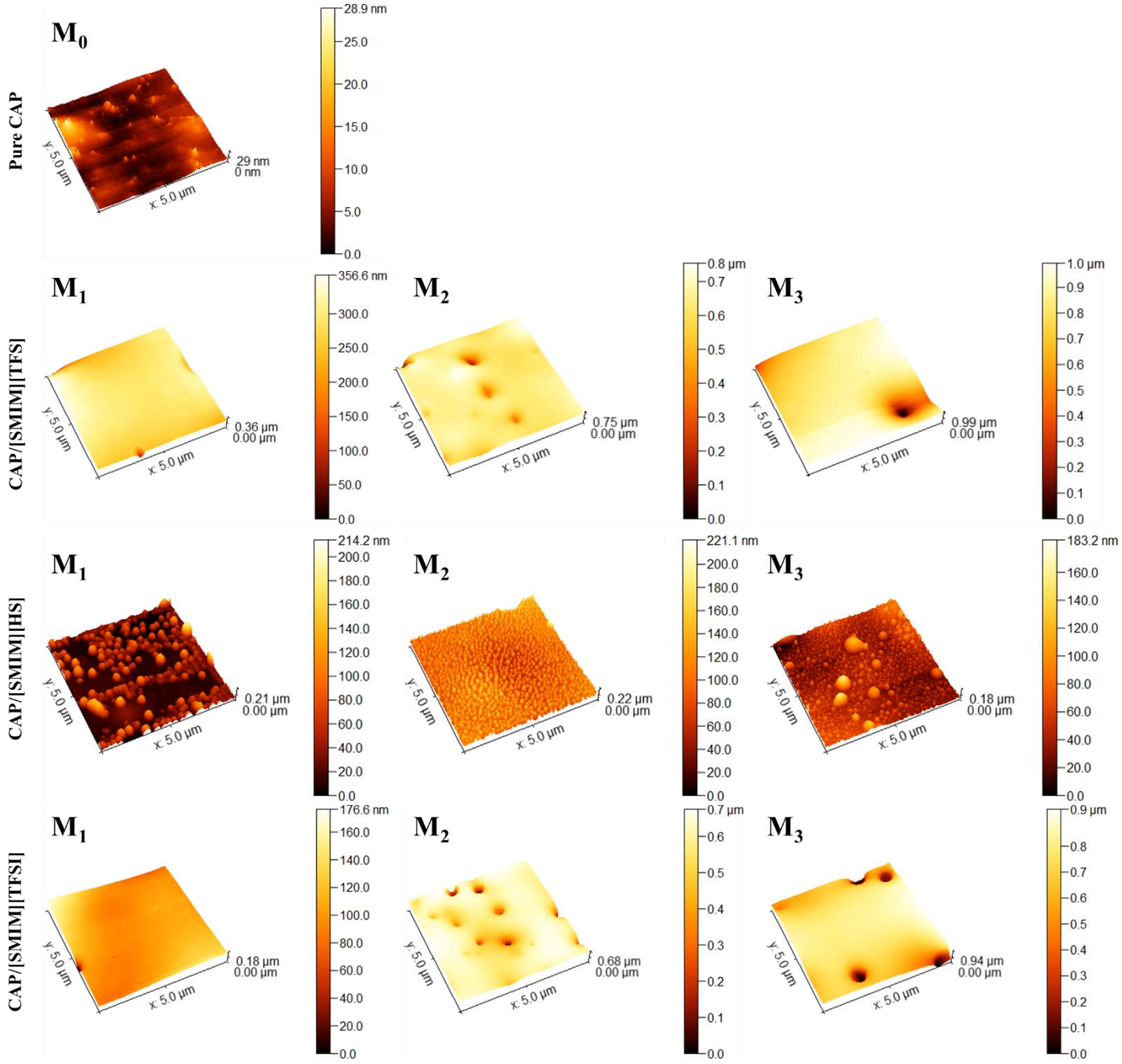

Figure 5.5. Surface morphology of pure CAP and CAP/A-ILs membranes for 5×5 µm^2 scanned area.

The thickness of pure CAP and CAP/A-ILs composite membranes was measured after their drying at 80 °C for 24 h (Table 5.2). Membrane thickness is an important parameter of the PEM efficiency as the proton transport through the thin PEM is facilitated while it is rather long through thick membrane. It can be seen that the thickness of pure CAP membrane is around 102 µm and it increases when introducing A-

ILs (Table 5.2). A direct correlation between the membrane thickness and the A-ILs concentration exists and the rise of ILs concentration leads to the membrane thickness increase [167].

5.1.2.2. Polymer-ILs Interactions

The FTIR spectra of pure CAP, A-ILs, and composite membranes are shown in Fig. 5.6. The assignments of characteristic bands of pure CAP and A-ILs are gathered in Table 5.3. Regarding CAP spectrum, hydroxyl band was observed at ~ 3504 cm^{-1}. Bands at ~ 2946-2985 cm^{-1} are assigned to C−H stretching vibration band of –CH group. The C=O stretching vibration band of ester group of CAP can be seen at ~ 1745 cm^{-1}. Furthermore, two peaks at ~ 1466 and ~ 1353 cm^{-1} are ascribed to CH_2 and C−H bending, respectively. Two other peaks observed at ~ 1166 and ~ 1070 cm^{-1} are attributed to C−O symmetric stretching vibration bands of −COO− ester group [168-170].

In case of A-ILs (i.e. [SMIM][TFS], [SMIM][HS], and [SMIM][TFSI]), bands at ~ 3159-3114 cm^{-1} are characteristic to C−H stretching vibration band of –CH group. Additionally, two bands at ~ 1700 and ~ 1570 cm^{-1} are attributed to C=N and C=C (skeletal) bonds of the imidazole ring, respectively. Two peaks at ~ 1460 and ~ 1350 cm^{-1} belong to CH_2 and C−H bending, respectively. Bands at ~ 1224-1028 cm^{-1} are assigned to S=O stretching vibration bands in the A-ILs structure. A peak at ~ 1050 cm^{-1} is attributed to C–F stretching vibration band of [SMIM][TFS] and [SMIM][TFSI] (Fig. 5.6a). Besides, the peak of C−S stretching vibration band was revealed at ~ 650 cm^{-1} [119,149,151].

Fig. 5.6b-d shows that all characteristic peaks of A-ILs can be found in spectra of composite membranes, i.e C–S vibration at ~ 740-750 cm^{-1}, C–F stretching vibration at ~ 1030-1055 cm^{-1}, and S=O vibration at ~ 1165-1225 cm^{-1}. However, the analysis of C–F and S=O bands in spectra of composite membrane is rather difficult because of band overlapping with C−O band of ester groups of CAP. This result confirms the A-ILs presence in the composite membranes.

Table 5.3. Assignments of vibrational modes for pure CAP membrane and A-ILs.

Band assignments	Wavenumber (cm^{-1})			
	CAP	**[SMIM][TFS]**	**[SMIM][HS]**	**[SMIM][TFSI]**
O−H stretching	3504	–	–	–
C−H stretching	2946, 2985	3118, 3159	3114, 3159	3120, 3159
C=O stretching vibration (ester group)	1745	–	–	–
C=N imidazole ring	–	1704	1694	1702
C=C skeletal (imidazole ring)	–	1572	1575	1572
CH_2 bending	1466	1461	1459	1463
C−H bending	1353	1356	1333	1350
S=O stretching	–	1165, 1224	1028, 1167	1139, 1188
C−O symmetric stretching (ester group)	1070, 1166	–	–	–
C−F stretching	–	1025	–	1056
C−S stretching	–	639	657	606

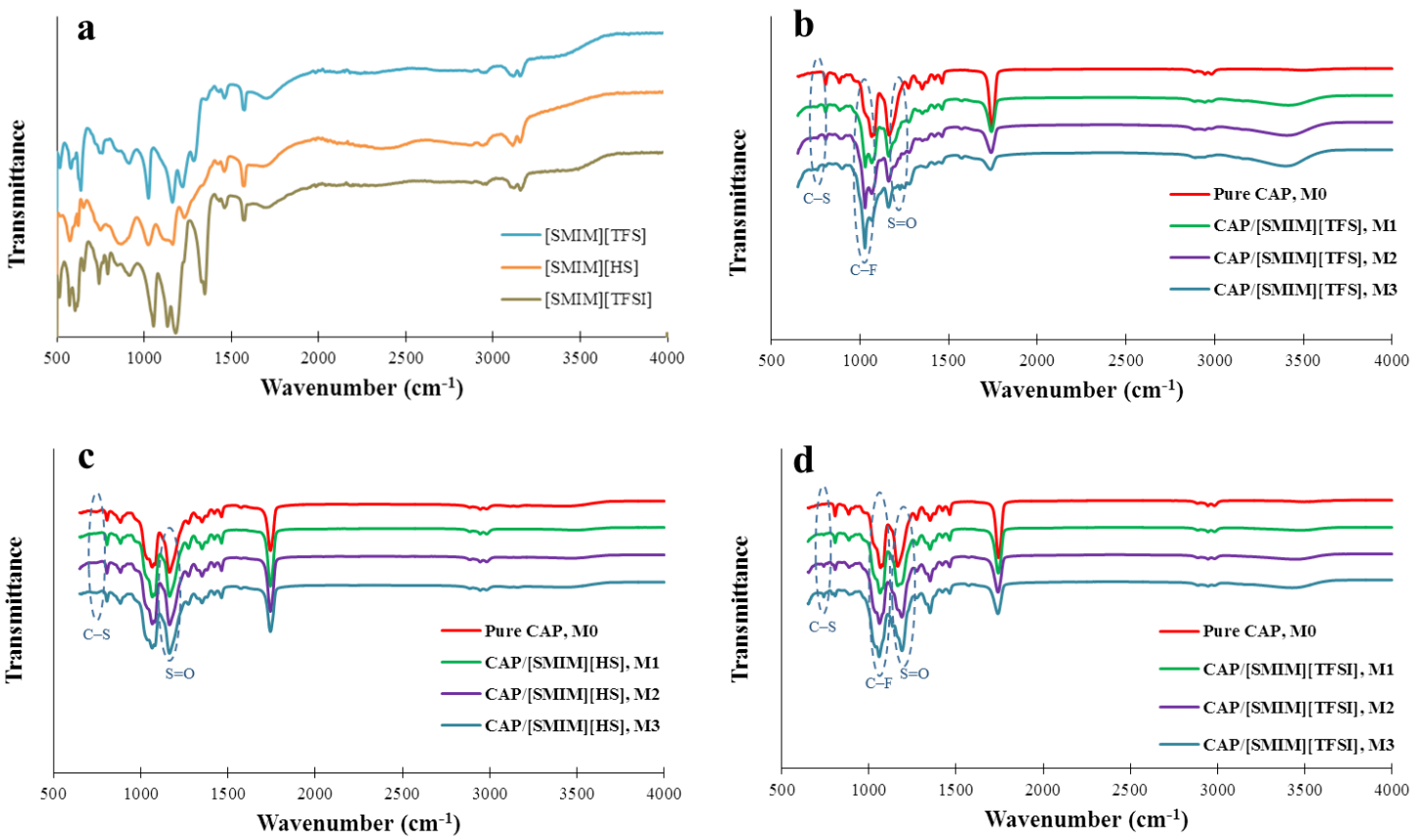

Figure 5.6. FTIR-ATR spectra of: a) A-ILs; b) CAP/[SMIM][TFS]; c) CAP/[SMIM][HS]; and d) CAP/[SMIM][TFSI] membranes.

5.1.2.3. Water Contact Angle

The water CA of CAP and CAP/A-ILs membranes was measured by sessile drop technique and obtained values are gathered in Table 5.4. It can be observed that CA value of pure CAP membrane is 79 ± 1°, thus confirming the CAP hydrophilic nature owing to the presence of a number of hydroxyl groups in its structure. The addition of A-ILs revealed two different water CA behavior. The presence and increasing the concentration of [SMIM][TFS] and [SMIM][TFSI] A-ILs provoke the increase of water CA values (Fig. 5.7a and 5.7c). Indeed, CA value depends on chemistry of material and surface roughness [139,160-162]. As a result, such increase can be caused by the presence of hydrophobic anions (i.e. [TFS] and [TFSI]). Another reason is the continuous increase of the surface roughness of composite membranes (Fig. 5.7). As to CAP/[SMIM][HS] composite membranes, water CA remains practically the same with the [SMIM][HS] concentration increase (Fig. 5.7b). Besides, only the slight increase of the surface roughness is noted with the introduction of [SMIM][HS]. The hydrophilic nature of this IL can reduce the effect of the surface roughness increase on CA. Therefore, CA is not changed significantly (Fig. 5.7b).

Table 5.4. Water contact angle values of pure CAP and composite CAP/A-ILs membranes.

IL content (wt.%)	M_0	M_1	M_2	M_3
	0	9	17	23
		Contact angle (°)		
CAP/[SMIM][TFS]		81 ± 4	84 ± 2	106 ± 5
CAP/[SMIM][HS]	79 ± 1	79 ± 3	82 ± 3	83 ± 3
CAP/[SMIM][TFSI]		87 ± 2	88 ± 1	94 ± 4

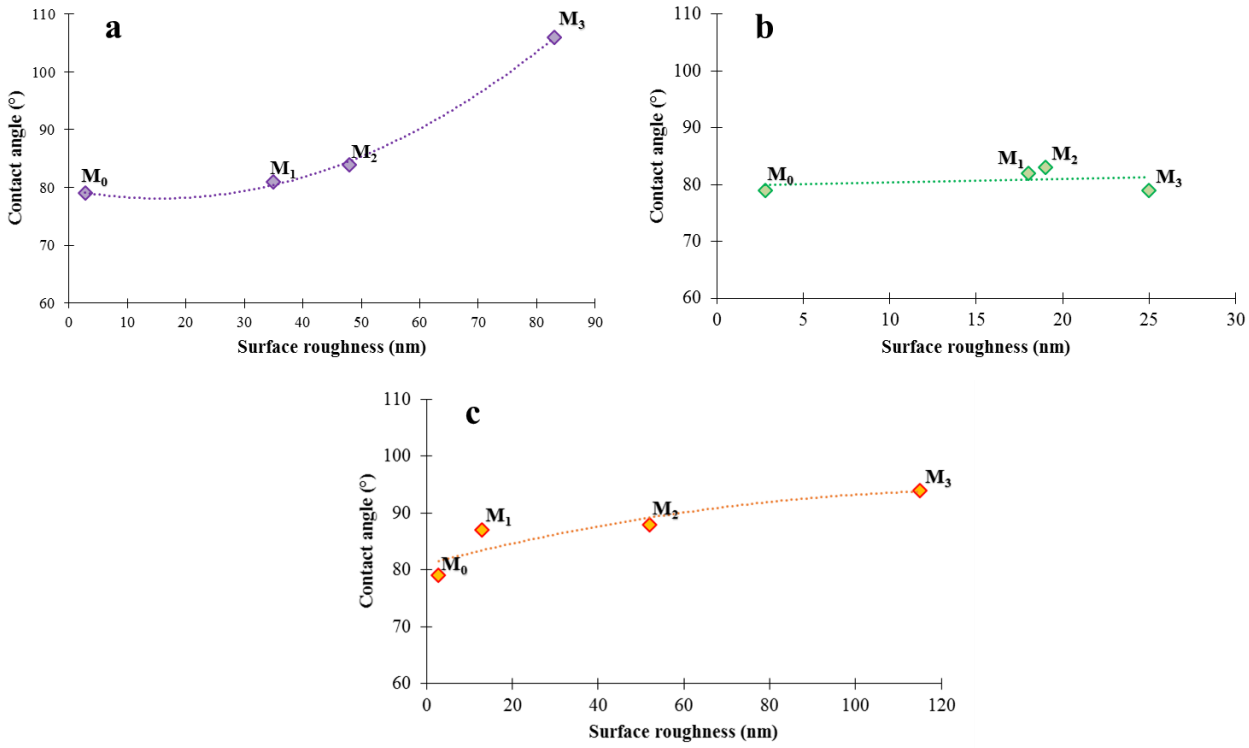

Figure 5.7. Correlation between water contact angle and surface roughness: a) CAP/[SMIM][TFS]; b) CAP/[SMIM][HS]; and c) CAP/[SMIM][TFSI].

5.1.2.4. Thermal Properties

Thermal stability is rather important parameter for PEM, especially for HT-PEMFC. Therefore, TGA analysis in dynamic mode (Fig. 5.8) was performed to investigate the influence of chemical nature of A-ILs on the thermal behavior of composite CAP-based membranes. At the beginning, the thermal stability of pure A-ILs was studied. It can be seen from Fig. 5.8a that [SMIM][HS] is thermally stable up to ~ 363

°C, while [SMIM][TFS] and [SMIM][TFSI] are less thermally stable probably owing to the moisture presence. The main weight loss of [SMIM][TFS] and [SMIM][TFSI] (~ 406 and 421 °C, respectively) is higher than that of [SMIM][HS] (~ 363 °C). In general, the influence of anion on the thermal stability of ILs is more pronounced than that of cation [147,149]. The studied A-ILs have the same cation in their structure but different anions. The sulfonic group is a hydrophilic group with super acidic property which enhances the compatibility with the hydrophilic hydrogen sulfate anion of [SMIM][HS]. However, there is no compatibility between cation hydrophilic sulfonic group and hydrophobic trifluoromethanesulfonate and bis(trifluoromethanesulfonyl)imide anions of [SMIM][TFS] and [SMIM][TFSI]. Therefore, a weight loss (around 20%) observed for these A-ILs is caused by the degradation of sulfonic acid group with temperature increase (Fig. 5.8a). Moreover, the lower weight loss of [SMIM][TFSI] in comparison with [SMIM][TFS] is noted owing to the presence of two hydrophobic trifluoromethanesulfonyl groups with more fluorine atoms.

The TGA curve of pure CAP membrane reveals its thermal stability up to ~ 373 °C (Fig. 5.8b–5.8d). Besides, for all studied composite membranes, three degradation steps can be noted, whatever the A-ILs nature and concentration are (Fig. 5.8b–5.8d). The first step occures at the temperature between ~ 70 and 80 °C owing to the moisture presence. The second degradation step at 150 °C < T < 210 °C is linked to the degradation of ILs. Besides, the polymer also starts to degradate since A-ILs may dissolve the polymer, thus reducing the polymer decomposition temperature. The third degradation step is observed in the temperature range of ~ 335–367 °C owing to the CAP decomposition. It can be seen that that the main degradation temperature of CAP/[SMIM][HS] is ~ 190–210 °C which is higher than the degradation temperature of composite membrane containing [SMIM][TFS] and [SMIM][TFSI] (~ 152–167 °C). Such result may be explained by the incompatibility between sulfonic acid group of cation and [TFS] and [TFSI] anions containing hydrophobic fluorine atoms.

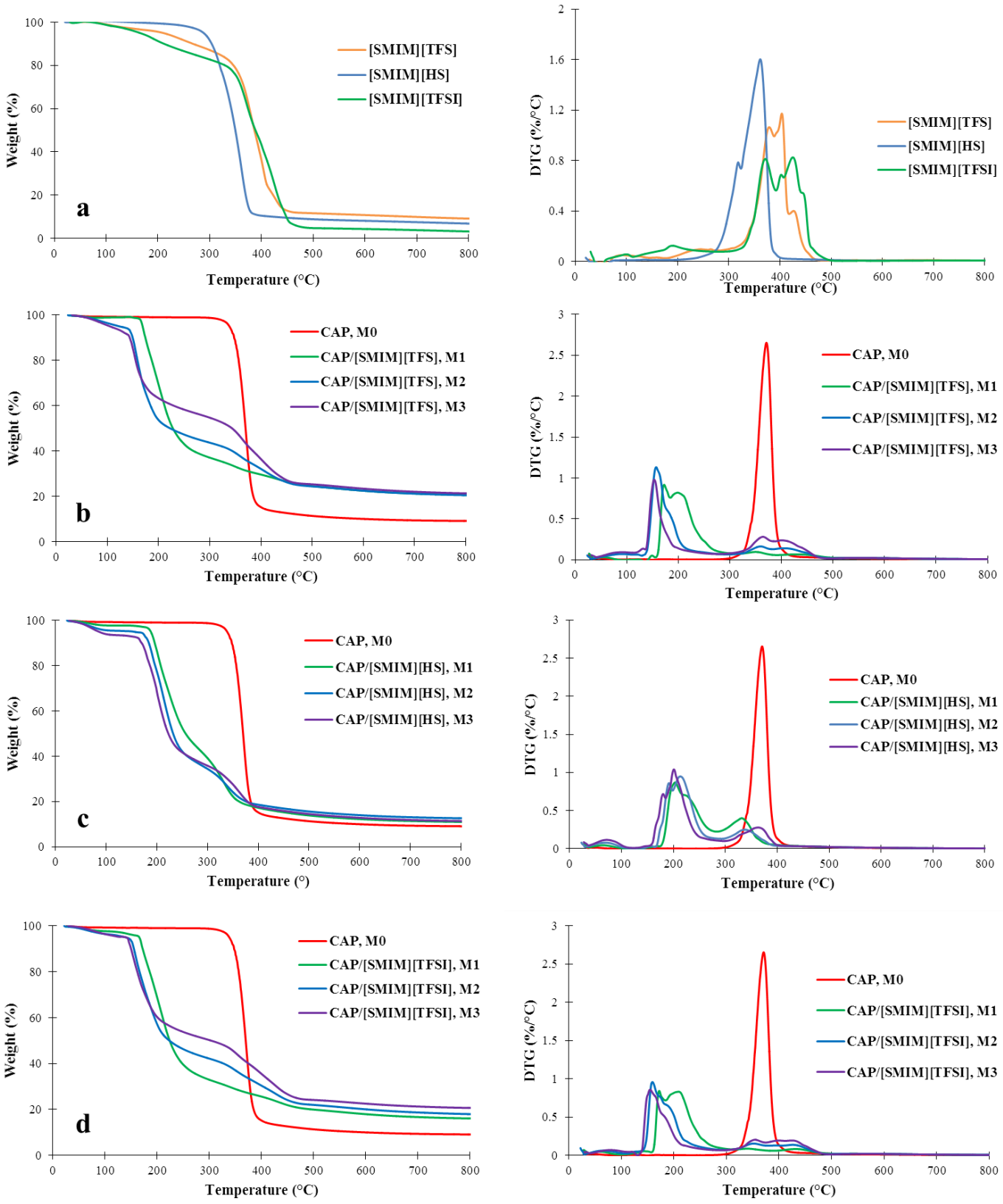

Figure 5.8. TGA (left) and DTG (right) curves of pure A-ILs and CAP-based membranes.

5.1.2.5. Mechanical Properties

The mechanical stability, flexibility, and elasticity of polymer are very important factors that ensure the membrane efficiency in separation processes. Therefore, mechanical behavior (i.e. Young's modulus, elongation at break, force at break, and maximum force) of the CAP-based membranes was investigated by tensile test in order to evaluate the influence of IL concentration on the mechanical properties of composite CAP/A-IL membranes. The values of Young's modulus, elongation at break, force at break, and maximum force of the pure CAP membrane are 977 ± 110 MPa, 24 ± 5 %, 29 ± 1 N, and 30 ± 2 N, respectively (Fig. 5.9). The results showed that the addition and increasing the concentration of [SMIM][TFS] and [SMIM][TFSI] cause the decrease of Young's modulus, elongation at break, force at break, and maximum force values of composite membranes in comparison with pure CAP, while practically the same values are obtained for the CAP/[SMIM][HS] composite membrane. Furthermore, the elongation at break of CAP/[SMIM][HS] composite membranes (i.e. M_1, M_2, and M_3) is higher than that of pure CAP membrane. Indeed, such different behavior may be explained by the nature of A-ILs. CAP polymer owing to the presence of numerous hydroxyl groups has a hydrophilic nature. However, [SMIM][TFS] and [SMIM][TFSI] are rather hydrophobic due to the presence of fluorine atoms. Therefore, the compatibility between polymer and A-ILs is rather low that is why the mechanical stability and flexibility of CAP/[SMIM][TFS] and CAP/[SMIM][TFSI] composite membranes decrease and they are more fragile as compared with the pure CAP membrane. The hydrophilic nature of [SMIM][HS] may be explained by the presence of hydrogen sulfate anion and sulfonic acid group on the cation. As a result, there is an acceptable compatibility between CAP polymer and additive in the membrane matrix, which thus leading to a good mechanical stability of the CAP/[SMIM][HS] composite membranes. Furthermore, the elongation at break values of CAP/[SMIM][HS] composite membranes are higher than that of pure membrane (Fig. 5.9b) confirming that [SMIM][HS] acts as the plasticizer of the CAP membrane.

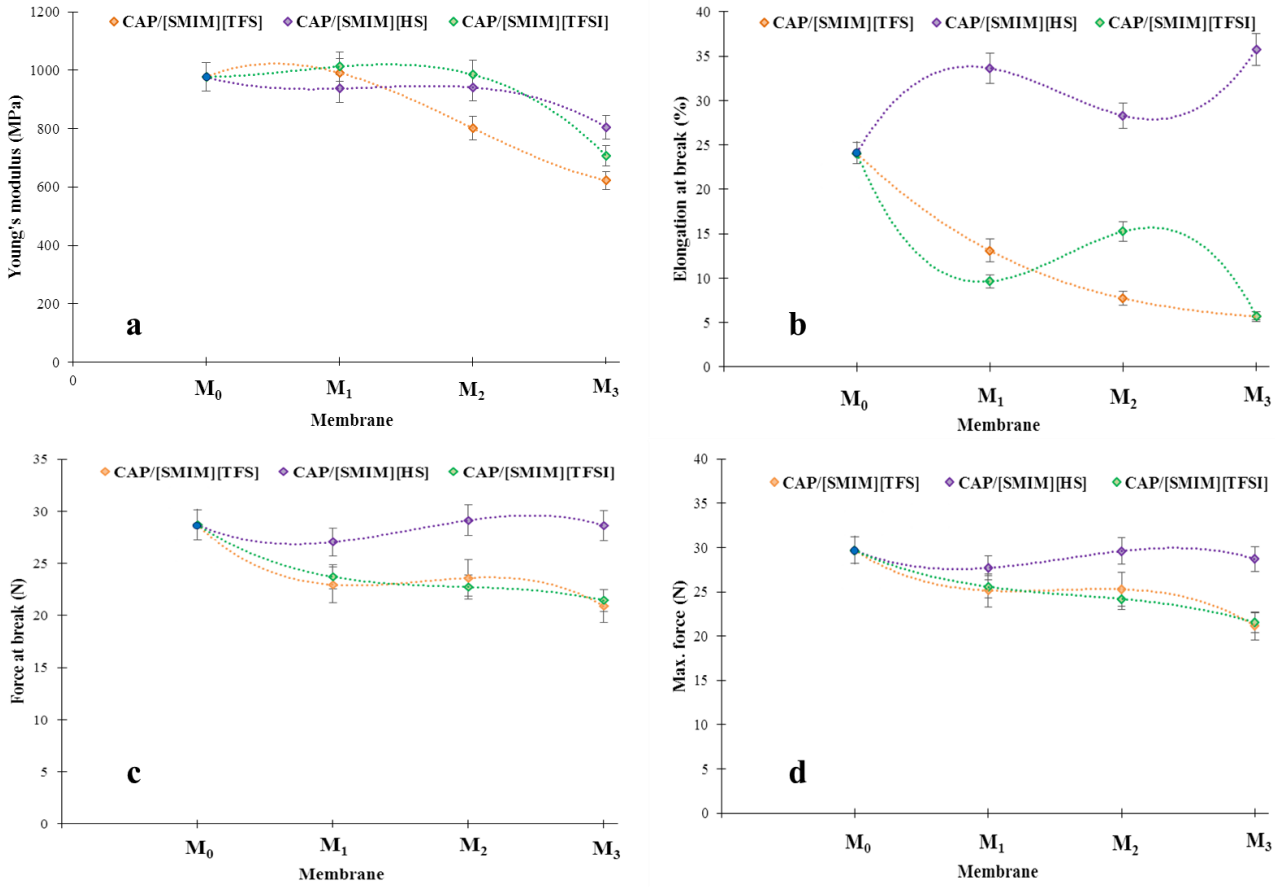

Figure 5.9. Influence of the A-ILs nature and concentration on the mechanical properties of CAP-based membranes: a) Young's modulus; b) elongation at break; c) force at break; and d) maximum force.

5.1.2.6. Leaching Phenomenon

The main drawback of IL-based membranes is the IL leakage from the composite membrane during the membrane application. Such leaching provokes the membrane performance decrease. So, in order to evaluate the stability of A-ILs-based composite membranes, the leaching test was performed at 24 ± 3 °C (section 2.4.14). The results are shown in Fig. 5.10. It can be seen that the weight loss of composite membranes containing 9 wt.% of IL (M_1) is ~ 2–5% and it increases to ~ 13–15% for composite membranes with 23 wt.% of IL (M_3). The leaching phenomenon takes place because of the lack of strong chemical bonds between polymer chains and ILs. Indeed, there are only weak electrostatic interactions. The polymer macromolecular chain movements can also push the excess amount of free ILs from the membrane.

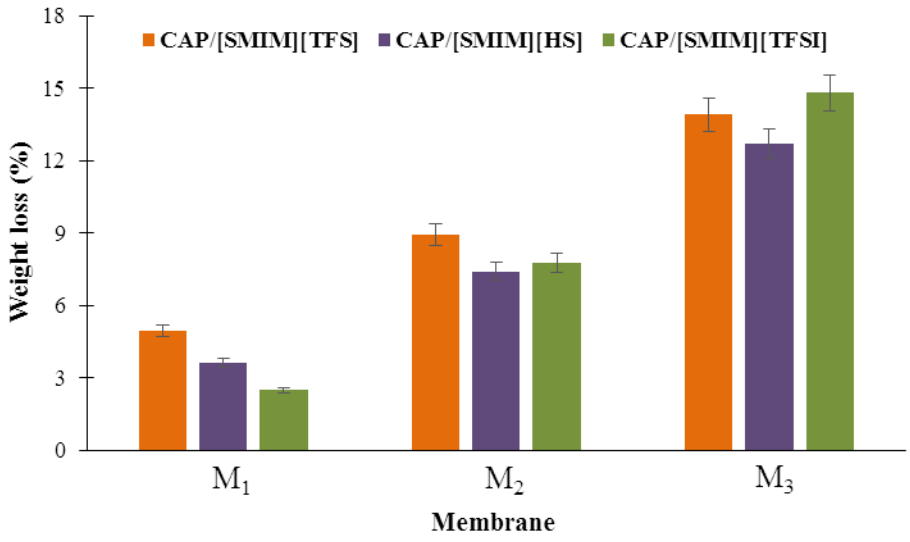

Figure 5.10. Evaluation of CAP-based membranes weight loss during the leaching measurements.

5.1.2.7. Ionic Conductivity

As the composite membranes are intended to the fuel cell application, therefore, their ionic conductivity was measured at 25 ± 3 °C during 24 h under 100% RH (Fig. 5.11). The pure CAP membrane is insulating (0.003 $\mu S \cdot cm^{-1}$ at the same condition)as it does not contain any conductive groups. The addition of ILs results in the significant increase of conductivity. Moreover, it increases with the concentration of A-ILs rising from 9 to 23 wt.% (Fig. 5.11). The increase of IL concentration provokes the increase of the ions number in the membrane, hence, the rise of the ionic conductivity. The similar trend was observed in literature in case of SPEEK/PBI/IL composite membranes containing two different sulfate-based ILs (3-triethylammonium hydrogen sulfate and 1-butylimidazole hydrogen sulfate) [171]. It was found that by increasing the ILs concentration from 2.5 to 5 wt.%, the ionic conductivity of composite membranes increased at 25 and 100% RH. The prepared SPEEK/PBI/IL composite membranes showed good ionic conductivity of 18–74 $mS \cdot cm^{-1}$ at 25 °C and 100% RH. da Trindade et al. [114] prepared SPEEK/IL composite membranes containing different ILs concentrations (5, 10, and 15 wt.%). The prepared SPEEK/IL composite membranes showed great ionic conductivity of 43–120 $mS \cdot cm^{-1}$ at 25 °C and 100% RH. However, the increase of IL concentration (from 5 to 15 wt.%) leads to ionic conductivity reduction owing to the IL agglomeration.

As it was shown in literature [142,150], the influence of anion nature on the membrane ionic conductivity is more pronounced than that of cation. The composite membrane containing 23 wt.% of [SMIM][TFS] reveals the highest ionic conductivity of $1.2 \cdot 10^{-3}$ $mS \cdot cm^{-1}$ at 25 °C and 100% RH. It can be

observed that the ionic conductivity of [SMIM][TFS]- and [SMIM][TFSI]-based composite membranes is higher than that of [SMIM][HS]-based CAP membrane (Fig. 5.11). In general, the acidity of the utilized acid during the IL synthesis has a significant influence on the ionic conductivity of the obtained IL. The pK_a value of trifluoromethanesulfonic acid ($pK_a \sim -14$) is lower than that of sulfuric acid ($pK_a \sim -3$), meaning that trifluoromethanesulfonic acid is stronger than sulfuric acid [152,155]. As a result, the ionic conductivity of CAP/[SMIM][TFS]- and [SMIM][TFSI]-based membranes is higher than that of CAP/[SMIM][HS]-based membranes whatever the IL concentration is, i.e. 9, 17, and 23 wt.%. Moreover, the ionic conductivity of CAP/[SMIM][TFS]-based membranes is higher than that of CAP/[SMIM][TFSI]-based membranes due to the fact that the [TFSI] anion has larger size, so lower ionic mobility, i.e. lower conductivity.

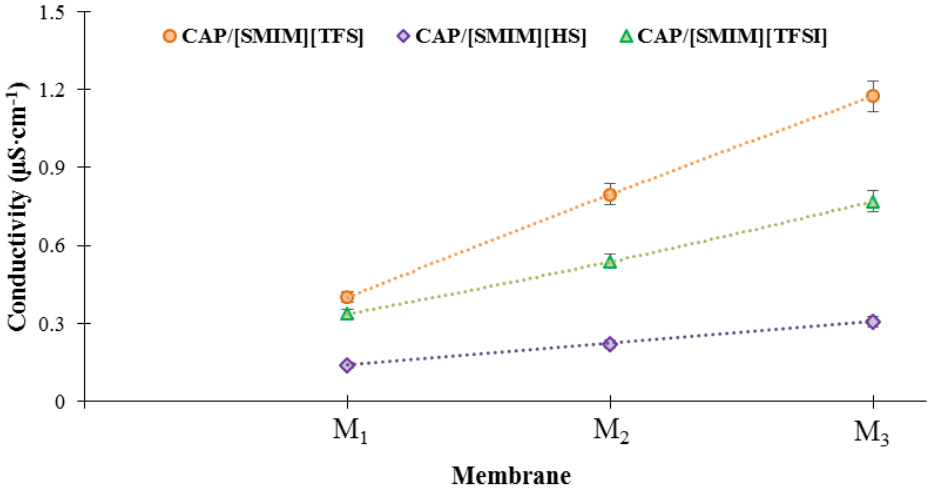

Figure 5.11. Ionic conductivity of CAP/A-ILs composite membranes at 25 ± 3 °C under 100% RH as a function of the IL content and nature.

5.2. Conclusion

In this section, the influence of the A-ILs presence on the ionic conductivity, morphological, physical, thermal, and mechanical properties of CAP-based membranes was evaluated. A-ILs were incorporated in the polymer solution in order to prepare composite membrane. EDX and FTIR analyses confirmed the presence of ILs within the composite membrane. SEM analysis revealed that the addition of A-ILs caused formation of gaps and cavities in the membrane structure. The surface roughness of CAP membranes increased in case of [TFS] and [TFSI]-based ILs, while it did not change in case of [HS]-based IL owing to the good compatibility between polymer and [SMIM][HS]. Besides, the water CA values of CAP/[SMIM][TFS] and CAP/[SMIM][TFSI] membranes are higher than those of the pure CAP membrane, whereas in case of CAP/[SMIM][HS] membrane the water CA value is similar to the value of the pure

membrane. The composite membranes showed less thermal stability as compared with pure CAP membrane. CAP/[SMIM][TFS] and CAP/[SMIM][TFSI] membrane showed lower mechanical stability values as compared with pure membrane while CAP/[SMIM][HS] membrane demonstrated almost the same values as pure CAP membrane. Leaching test revealed that by increasing the IL concentration, the leaching increases considerably owing to the weak electrostatic interactions between IL and polymer. CAP/[SMIM][TFS] composite membrane showed the highest ionic conductivity of $1.2 \cdot 10^{-3}$ mS·cm^{-1} at 25 °C and 100% RH owing to the strong acid property of trifluoromethanesulfonic acid. The obtained results showed that there is a tradeoff between the IL concentration in membranes and the thermochemical properties of composite membranes. It was seen that the ionic conductivity of composite membranes increased by rising the IL concentration while opposite trends were observed regarding thermal and mechanical stability of membranes. Therefore, in order to obtain an ideal IL-based membrane, an optimum concentration of IL should be introduced to the membrane.

5.3. CAB/Pr-ILs Composite Membranes

5.3.1. Membrane Elaboration

In the second part of this chapter CAB polymer is used for membrane fabrication. CAP and CAB have the same chemical nature, and the only difference is the number of carbon atom – 3 for CAP (in propionate) (Fig. 2.1b) and 4 for CAB (in butyrate) (Fig. 2.1c), therefore, CAB can have more electrostatic interactions with ILs (i.e. having better compatibility between polymer and IL). Furthermore, synthesized Pr-ILs with different chemical natures were used (the synthesis procedure was explained in Chapter 3) in order to prepare composite membranes.

CAB/Pr-ILs composite membranes were fabricated *via* phase inversion technique induced by the solvent evaporation (Fig. 2.7). At the beginning, two imidazolium-based Pr-ILs (i.e. [MIM][TFS] and [BIM][TFS]) were used for the preparation of composite membranes (Table 5.5). The choice of these Pr-ILs is based on their stability at elevated temperature owing to the presence of [TFS] anion in their structure. The pure CAB membrane (M_0) is transparent and flexible (Fig. 5.12), however, the addition of 5 wt.% of Pr-IL ([MIM][TFS] or [BIM][TFS]) provokes the reduction of the apparent mechanical stability of obtained membranes as compared with the pure membrane. The further increase of Pr-IL content from 5 to 9 and 17 wt.% leads to the detention of rather fragile membranes. Moreover, the transparency of composite membrane with 5 wt.% of IL is lower than that of the pure CAB membrane (Fig. 5.12) and the increase of the IL concentration, further decreases the membrane transparency. This result may be explained by the incompatibility between polymer and Pr-ILs. CAB polymer (Fig. 2.1c) has a hydrophilic nature due to the presence of many hydroxyl groups in its structure. However, [MIM][TFS] and [BIM][TFS] are hydrophobic

owing to the presence of hydrophobic anion. As a result, such incompatibility between polymer and Pr-ILs provokes the presence of two separate phases and the decrease of the apparent mechanical stability and flexibility of CAB/[MIM][TFS] and CAB/[BIM][TFS] composite membranes. As the membrane mechanical stability and flexibility are very important for their use in PEMFC process, therefore various methods were applined to obtain a mechanically stable composite membrane containing Pr-ILs with a concentration higher than 9 wt.%.

Table 5.5. Composition of CAB/Pr-ILs-based membranes.

Membrane	Pr-IL	Pr-IL content (wt.%)*	Membrane state
M_0	–	–	Flexible
M_1	[MIM][TFS]	5	Flexible
M_2		9	Fragile
M_3		17	Fragile
M_1	[BIM][TFS]	5	Flexible
M_2		9	Fragile
M_3		17	Fragile

*Content of Pr-IL in membrane.

Figure 5.12. Images of obtained composite CAB/Pr-IL membranes.

5.3.1.1. Pr-ILs Mixture

In order to increase the mechanical stability, it was decided to mix both Pr-ILs (50/50, w/w) to have a membrane with 9 wt.% of IL. The membrane preparation technique was the same as previously (Fig. 2.7). It was supposed that some new electrostatic interactions may appeared between both Pr-ILs and polymer

chains, resulting in formation of the flexible composite membrane. However, the resultant membrane was still rather fragile.

5.3.1.2. Porous CAB-based Membranes

In order to increase the content and preserve the mechanical stability of CAB, the SILM approach was used. For this purpose a porous CAB membrane was elaborated. 2 g of CAB was dissolved in solution containing 1,4-dioxane and acetone (3.2 and 3.6 mL, respectively). After certain time, 3.2 mL of formamide was added to the polymer solution and it was stirred until a homogenous polymer solution was obtained. The CAB-based solution was then cast on the glass plate. The polymer solution was cast with different slits of casting knife (0.25 and 0.40 mm) and was exposed to the environment during different gelation time (2 and 5 min) at 24 ± 3 °C. Subsequently, the glass plate with cast polymer solution was immersed in the water coagulation bath (Fig. 5.13). The polymer film was peeled off from the glass plate after some minutes. The obtained polymer films was submerged for 24 h in the deionized water for the solvent removal. The membrane was dried in the oven at 80 °C for 24 h. However, the prepared porous membranes were not enough flexible after drying. Therefore, prepared membranes with this method cannot be used for preparation of composite membrane since a sufficient mechanical stability is a necessary parameter for fuel cell application.

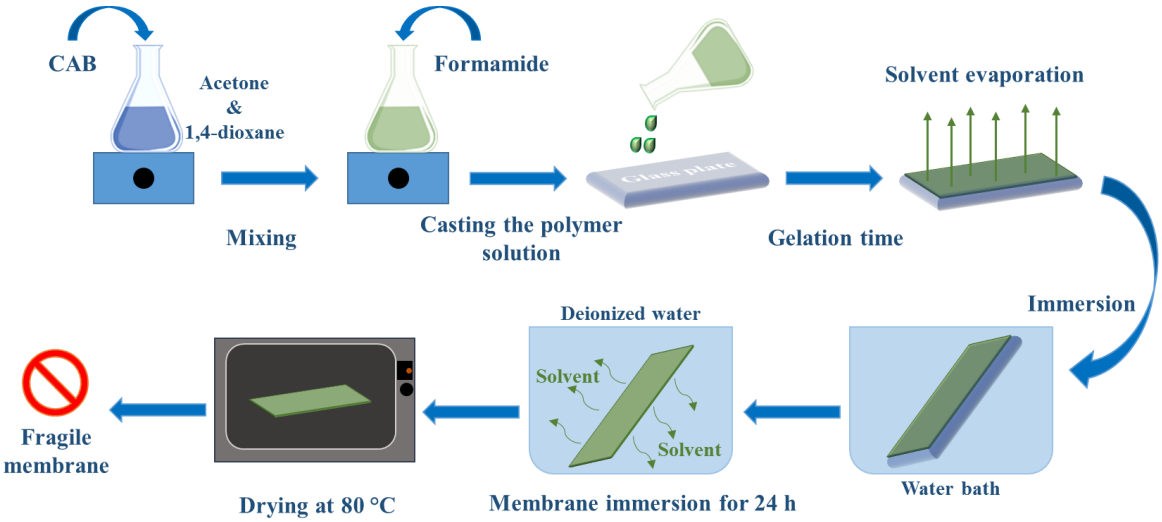

Figure 5.13. Scheme of preparation of porous CAB membrane by phase inversion method.

5.3.1.3. Polymer Blending

In order to obtain conductive membranes, CAB was blended with poly(styrenesulfonic acid) (PSSA). For this purpose, 0.25 g of CAB and 0.83 g of PSSA were dissolved together in DMSO and

vigorously stirred during 12 h (Fig. 5.14). After, 9 wt.% of Pr-IL ([MIM][TFS], or [BIM][TFS], or mixture of both (50/50)) were added to the polymer solution and stirred again for 16 h. The obtained composite solution was cast on the Petri dish, covered and heated at 50 °C till drying and forming the polymer membrane. However, the obtained membranes were also rigid and brittle. Therefore, to prepare a mechanical stable and conductive membrane, other methods should be investigated.

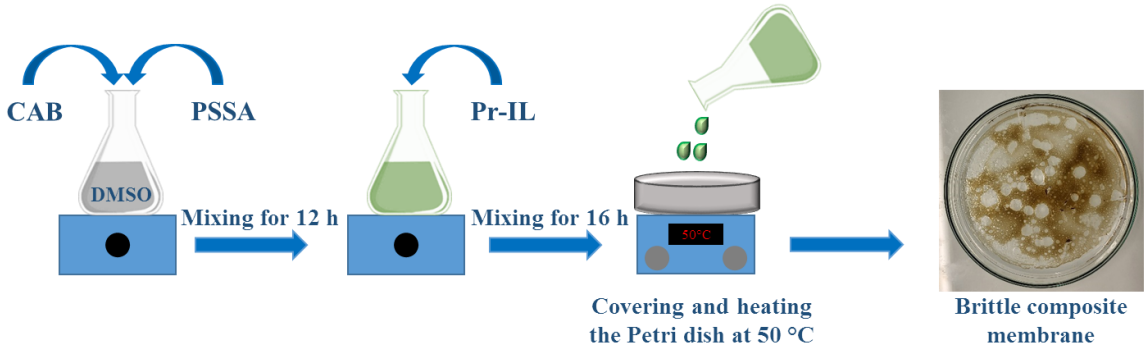

Figure 5.14. Scheme of preparation of composite CAB-PSSA/Pr-ILs membrane.

5.3.1.4. Dense Membranes Using Blending/Washing Method

The fabrication of polymer membrane by blending/washing method was another attempt to prepare mechanically stable composite membrane containing Pr-IL. In this case, CAB and PVP (75/25, w/w) were dissolved in chloroform and acetone used as the solvent (blending stage) (Fig. 5.15). The polymer solution was vigorously stirred during 12 h and then it was cast on the Petri dish. The Petri dish was covered at 24 ± 3 °C till the solvent evaporation. The dried membrane was immersed in the coagulation bath (water/methanol, 50/50, v/v) at 70 °C for two days to remove PVP from the membrane (washing stage). The obtained membrane was rinsed with deionized water and placed in the oven for 24 h at 80 °C. However, the results were not satisfying as the obtained dried CAB membrane was still fragile (Fig. 5.15). The CAB-PVP membrane (50/50, w/w) was also prepared. However, the membrane mechanically decomposed during the washing step. In addition, the CAB composite membranes using CAB-PEG with different molecular weights (Mw: 300, 600, and 20000 $g \cdot mol^{-1}$) and compositions (75/25 and 50/50, w/w) were prepared. However, the obtained membranes were not mechanically stable (fragile). Therefore, this method is not appropriate for the preparation of a mechanically stable and conductive membrane.

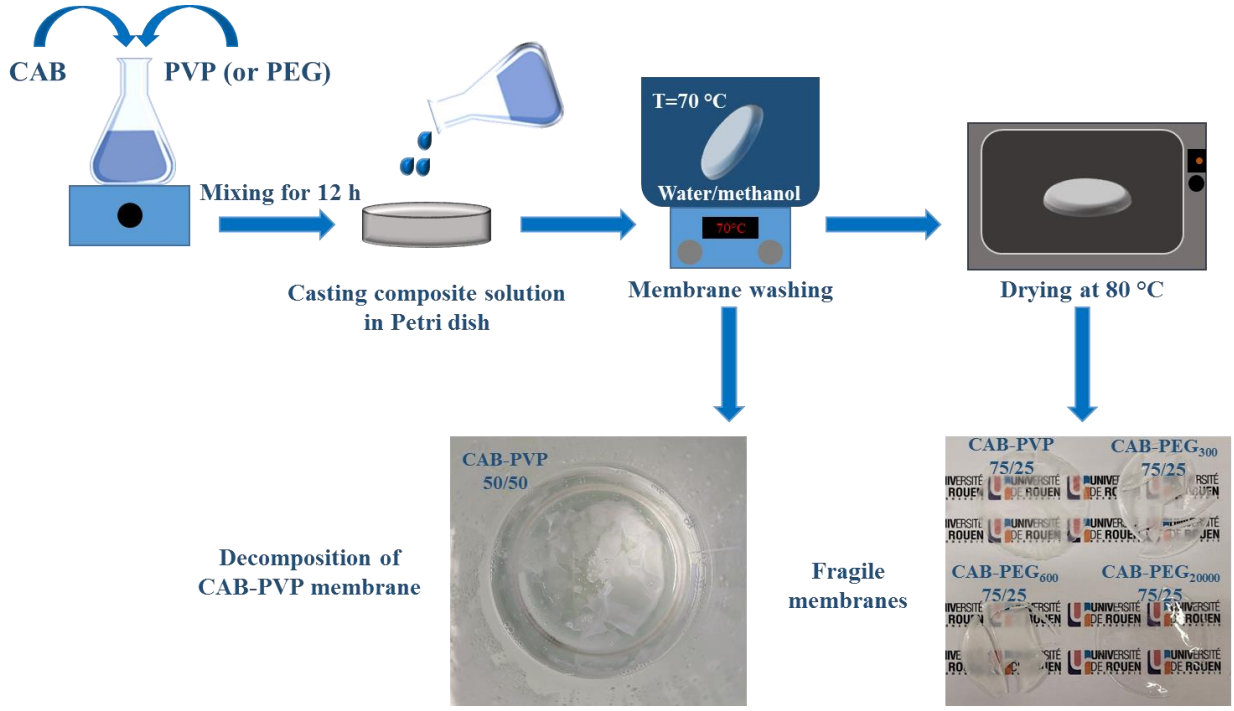

Figure 5.15. Scheme of preparation of composite CAB-PVP and CAB-PEG membranes.

5.3.1.5. New Pr-ILs

In order to improve the compatibility of CAB with Pr-ILs, new Pr-ILs were synthesized (Chapter 3). Pr-ILs with different anions (trifluoromethanesulfonate, trifluoroacetate, hydrogen sulfate, di-*n*-butylphosphate, bis(2-ethylhexyl)phosphate) and cations (1-methylimidazolium, 1-(*n*-butyl)imidazolium, 2-hydroxy-*n*,*n*-dimethylethanaminium, and 3-hydroxy-*n*,*n*-dimethylpropan-1-aminium) were obtained and their properties were discussed in Chapter 3. The procedure of fabrication of CAB/Pr-IL composite membranes is schematically presented in Fig. 2.7. The composite CAB/Pr-IL membrane containing X wt.% of Pr-IL labels as CAB/Pr-IL$_X$. For example, CAB/[DEPA][BUPH]$_{17}$ indicates composite CAB/[DEPA][BUPH] membrane containing 17 wt.% of [DEPA][BUPH]. The physical state of prepared composite CAB-based membranes is presented in Table 5.6.

The composite CAB/Pr-IL membranes with 9 wt.% of trifluoroacetate- and trifluoromethanesulfonate-based Pr-ILs were not enough flexible (Fig. 5.16). This fact may be explained by the incompatibility between polymer and mentioned Pr-ILs owing to the hydrophobic nature of these Pr-ILs. However, fabrication of flexible composite membranes with IL concentration higher than 9 wt.% was possible using phosphate- and sulfate-based Pr-ILs (Figs. 5.16 and 5.17). This result testifies to the good compatibility between phosphate- and sulfate-based Pr-ILs and CAB. Besides, it should be mentioned that it was possible to fabricate flexible composite membranes with the IL concentration up to ~ 44 (with

phosphate-based ILs) and 33 (with sulfate-based ILs) wt.%. However, after some days of storage, Pr-ILs started to leach out from the membrane (Fig. 5.18). This fact may be explained by the polymer macromolecular chain movements that push out the IL excess from the membrane.

In conclusion, different methods used for the membrane preparation are gathered in Table 5.7. It was possible to obtain flexible CAB-based membranes containing more than 9 wt.% of Pr-ILs by using sulfate- and phosphate-based Pr-ILs. Therefore, these membranes where chosen for further characterization.

Figure 5.16. Images of obtained composite [DETA]-based CAB composite membranes.

Figure 5.17. Image of obtained composite CAB/[DETA][BUPH]$_{29}$ membrane.

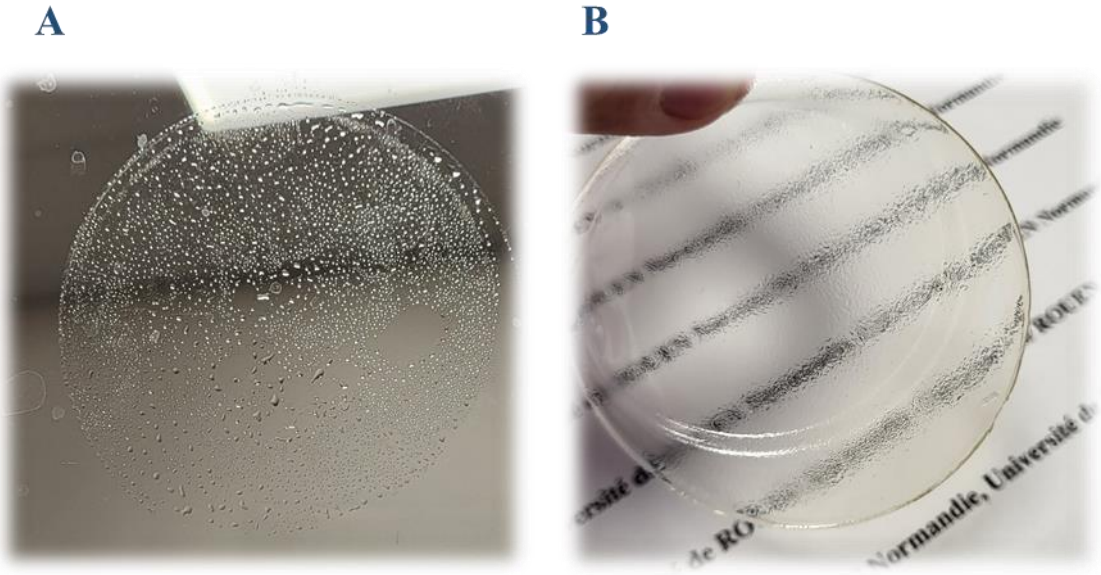

Figure 5.18. ILs leaching phenomenon: A) composite CAB/[MIM][HS]$_{33}$; and B) composite CAB/[DETA][BUPH]$_{44}$ membrane.

Table 5.6. Composition and physical state of composite CAB/Pr-ILs-based membranes.

Pr-ILs	Base	Acid	Pr-ILs concentration (wt.%)*									
			5	9	17	23	29	33	38	41	44	50
[DETA][TFS]	2-(dimethylamino)ethanol	trifluoromethanesulfonic acid	N	F	–	–	–	–	–	–	–	–
[DETA][TFA]		trifluoroacetic acid	N	F	–	–	–	–	–	–	–	–
[DETA][BUPH]		di-*n*-butylphosphate	N	N	N	N	N	L	L	L	L	F
[DETA][EHPH]		bis-(2-ethylhexyl)phosphate	N	N	N	N	N	L	L	L	L	–
[DEPA][TFS]	3-dimethylamino-1-propanol	trifluoromethanesulfonic acid	N	F	–	–	–	–	–	–	–	–
[DEPA][TFA]		trifluoroacetic acid	N	F	–	–	–	–	–	–	–	–
[DEPA][BUPH]		di-*n*-butylphosphate	N	N	N	N	N	L	L	L	L	L
[DEPA][EHPH]		bis-(2-ethylhexyl)phosphate	N	N	N	N	N	L	L	L	L	–
[MIM][TFS]	1-methylimidazole	trifluoromethanesulfonic acid	N	F	–	–	–	–	–	–	–	–
[MIM][TFA]		trifluoroacetic acid	N	F	–	–	–	–	–	–	–	–
[MIM][HS]		sulfuric acid	N	N	L	L	L	L	–	–	–	–
[MIM][BUPH]		di-*n*-butylphosphate	N	N	N	N	L	–	–	–	–	–
[MIM][EHPH]		bis-(2-ethylhexyl)phosphate	N	N	N	N	L	–	–	–	–	–
[BIM][TFS]	1-(*n*-butyl)imidazole	trifluoromethanesulfonic acid	N	F	–	–	–	–	–	–	–	–

[BIM][TFA]	trifluoroacetic acid	N	F	–	–	–	–	–	–	–	–
[BIM][HS]	sulfuric acid	N	N	L	–	–	–	–	–	–	–
[BIM][BUPH]	di-*n*-butylphosphate	N	N	N	N	L	–	–	–	–	–
[BIM][EHPH]	bis-(2-ethylhexyl)phosphate	N	N	N	N	L	–	–	–	–	–

*Content of Pr-IL in membrane.

F: fragile, L: leaching, N: without leaching.

Table 5.7. Summary of methods used for preparing flexible composite membranes.

Method	Remark	Membrane state
Pr-ILs mixing	Mixing of [MIM][TFS] and [BIM][TFS] (5 + 5 wt.%) to prepare composite CAB/$[MIM][TFS]_5$-$[BIM][TFS]_5$ membrane	Fragile
Porous membrane	Fabricating of porous membrane to use as a SILM (gelation time and slit of casting knife): • 2 min and 0.25 mm • 2 min and 0.40 mm • 5 min and 0.25 mm • 5 min and 0.40 mm	 Fragile Fragile Fragile Fragile
Polymer blending	Preparing composite CAB-PSSA/Pr-ILs membrane containing: • 9 wt.% of [MIM][TFS] • 9 wt.% of [BIM][TFS] • 5 wt.% of each IL	 Fragile Fragile Fragile
Blending/washing	Preparing dense CAB-PVP and CAB-PEG (Mw: 300, 600, and 20000 $g \cdot mol^{-1}$) membranes: • CAB/PVP: 50/50 • CAB/PVP: 75/25 • CAB/PEG: 50/50 • CAB/PEG: 75/25	 Decomposed Fragile Fragile Fragile
Synthesis of new Pr-ILs	Synthesis of new Pr-ILs and preparing composite membranes: • acetate-based • trifluoromethanesulfonate-based • sulfate-based • phosphate-based	 Fragile Fragile **Flexible** **Flexible**

5.3.2. Physical-Chemical Characterization

Even if the flexible composite CAB-based membranes containing phosphate- and sulfate-based Pr-ILs were obtained, the IL leakage was observed. In case of sulfate-based composite membranes, it was observed already at 17 wt.% of IL, while leaching was observed for 29-33 wt.% of phosphate-based composite membranes. In addition to the IL leaching, the ionic conductivity of phosphate-based Pr-ILs is rather low (Figs. 3.11 and Table 3.5).

Therefore, a mixture of Pr-ILs was used. For this purpose, two Pr-ILs with the best conductive performance among trifluoromethanesulfonate- and phosphate-based Pr-ILs were chosen: [DETA][TFS] and [DEPA][BUPH]. [DETA][TFS] reveals great thermal stability and ionic conductivity, and good compatibility of [DEPA][BUPH] and polymer makes it possible to have a mechanically stable and flexible composite membrane with the IL concentration higher than 9 wt. %. Furthermore, it was possible to prepare CAB-based composite membranes with the IL content up to 41 wt.% without leaching owing to electrostatic interactions between Pr-ILs and polymer chains. Therefore, membranes with various concentrations of

mixed Pr-ILs (i.e. [DETA][TFS]-[DEPA][BUPH]) were fabricated (Table 5.8 and Fig. 5.19) and their properties were analyzed.

Table 5.8. Composition of CAB/[DETA][TFS]-[DEPA][BUPH] membranes.

Membrane	Total content of Pr-ILs (wt.%)*	[DETA][TFS] content (wt.%)*	[DEPA][BUPH] content (wt.%)*
M_0	–	–	–
M_1	23	8	15
M_2	33	13	20
M_3	41	18	23

*Content of Pr-IL in membrane.

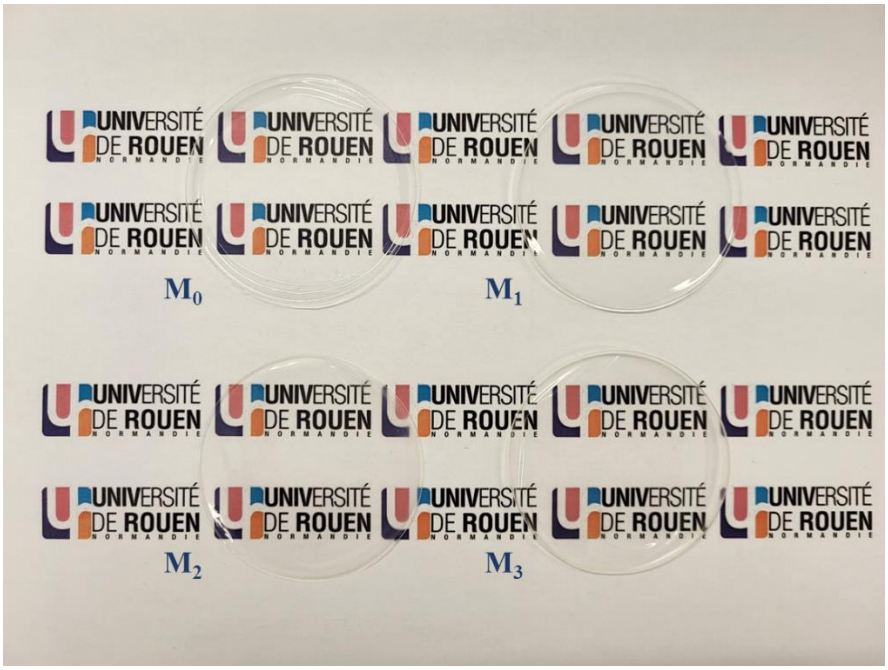

Figure 5.19. Images of obtained composite CAB/[DETA][TFS]-[DEPA][BUPH] membranes.

5.3.2.1. Membrane Morphology

The morphology of pure and composite membranes was characterized by the SEM analysis (Fig. 5.20). The obtained images confirm the dense structure of the pure CAB membrane (i.e. M_0) with a homogenous morphology owing to the appropriate dissolution of CAB in solvent (i.e. chloroform and acetone). It can be seen that the CAB/[DETA][TFS]-[DEPA][BUPH] composite membrane containing 23 wt.% of mixed Pr-ILs (i.e. M_1) also possesses a homogenous morphology due to proper dispersion of Pr-ILs in the polymer solution and the good compatibility between mixed Pr-ILs (especially [DEPA][BUPH])

and CAB polymer. However, further increase of the Pr-ILs concentration to 33 wt.% (M_2 membrane) provokes a change in the membrane morphology as few gaps and cavities may be observed especially in top surface layer (Fig. 5.20). The amount and size of these gaps and cavities increase with the content of the mixed Pr-ILs (41 wt.% in M_3 membrane). Even if the phosphate-based Pr-IL (i.e. [DEPA][BUPH]) has a good compatibility with CAB, high concentration of [DETA][TFS] (18 wt.% in M_3 membrane) increases the formation of gaps and cavities owing to the repulsion interactions with polymer chains. In any case, whatever the Pr-ILs concentration, the EDX analysis reveals good dispersion of Pr-ILs in the polymer membrane (Fig. 5.20).

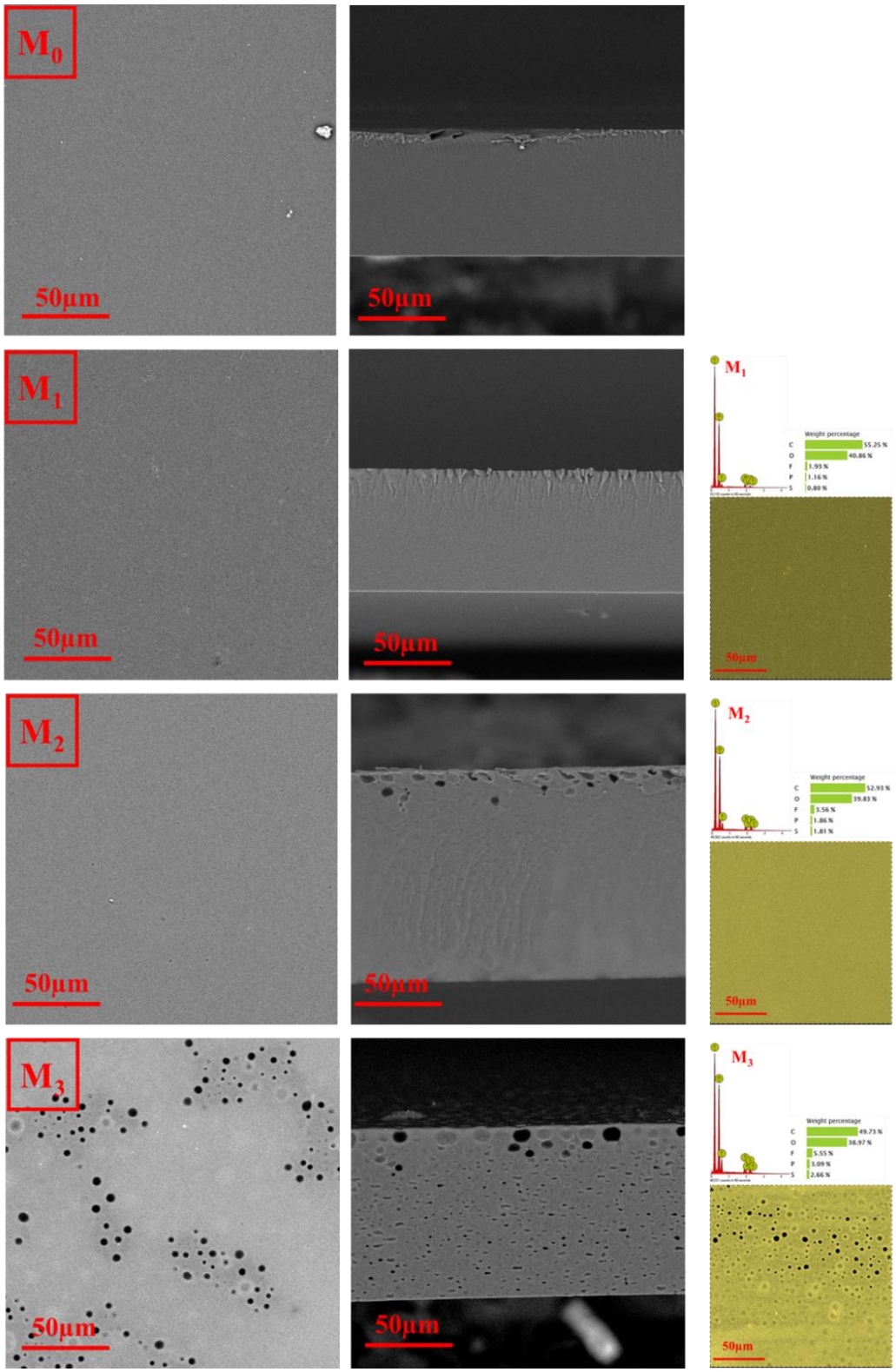

Figure 5.20. The SEM images (surface and cross-section) and surface EDX spectra with magnification of 1500X for pure CAB and composite CAB/[DETA][TFS]-[DEPA][BUPH] membranes.

The surface topography and roughness of both pure and composite CAB-based membranes is shown in Fig. 5.21 and Table 5.9. Two roughness parameters (R_a and R_q) and two scanned areas (5 × 5 and 10 × 10 μm^2) were chosen for surface topography evaluation. It can be seen that the surface roughness values (both R_a and R_q) of 10 × 10 μm^2 scanned area are higher than those of 5 × 5 μm^2 area testifying to the rather heterogeneous surface. A smooth surface can be observed in case of pure CAB membrane (M_0). The introduction of the Pr-ILs up to 33 wt.% slightly increases the membrane roughness. However, the surface roughness of M_3 membrane containing 41 wt.% of Pr-ILs considerably increases as compared to the other membranes (Table 5.9). Such result may be explained by a higher [DETA][TFS] concentration and by its poor compatibility with CAB, thus changing the membrane morphology from homogenous to heterogeneous.

Table 5.9. Surface roughness of pure CAB and CAB/[DETA][TFS]-[DEPA][BUPH] membranes.

Membrane	Scanned area (μm^2)			
	5 × 5		10 × 10	
	R_q (nm)	R_a (nm)	R_q (nm)	R_a (nm)
M_0	4.8 ± 3.0	2.5 ± 1.0	3.9 ± 1.0	2.3 ± 1.0
M_1	3.0 ± 1.0	2.2 ± 1.0	6.9 ± 3.0	4.0 ± 1.0
M_2	6.2 ± 2.0	4.9 ± 1.0	10.4 ± 1.0	7.9 ± 1.0
M_3	28.6 ± 3.0	15.0 ± 7.0	47.9 ± 12.0	25.8 ± 7.0

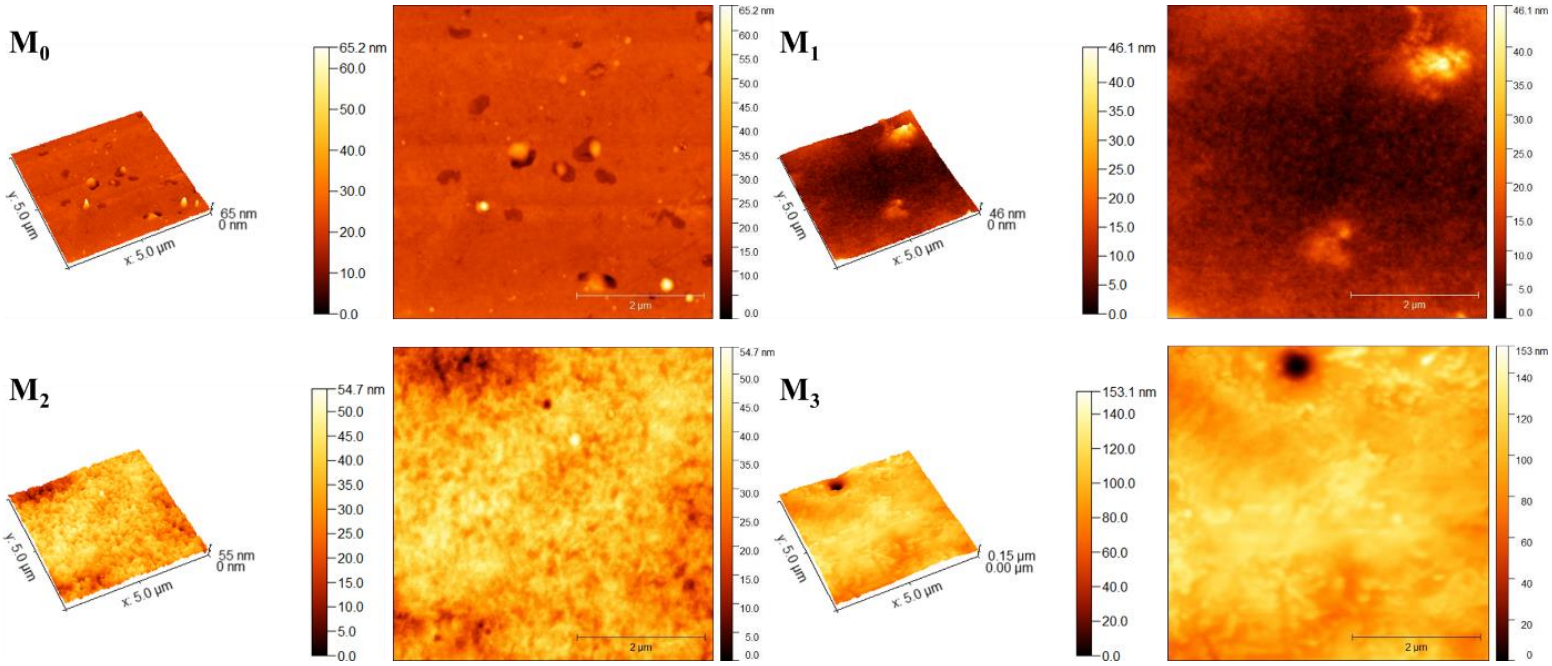

Figure 5.21. Surface morphology of pure CAB and CAB/[DETA][TFS]-[DEPA][BUPH] membranes for 5 × 5 μm^2 scanned area.

5.3.2.2. Swelling Degree and Thickness

Membrane thickness is an important parameter that strongly influences the PEM performance. Besides, the membrane thickness influences differently the ionic conductivity and mechanical stability of PEM as the increase of the membrane thickness improves the membrane mechanical stability of but reduces its ionic conductivity (Eq. 2.17). That is why tradeoff between the membrane mechanical stability and ionic conductivity exists [140,141]. The thickness and swelling degree of pure CAB and CAB/[DETA][TFS]-[DEPA][BUPH] composite membranes were measured and the obtained results are gathered in Table 5.10. The thickness of pure CAB membrane (around 60 µm) increases by introducing Pr-ILs. It was found that there is a direct correlation between the membrane thickness and the IL concentration. In addition, the increase of the IL concentration should increase the ionic conductivity of membrane owing to rising the conductive channels. The higher membrane thickness will increase the proton pathway. The membrane swelling degrees were calculated (Eq. 2.3–2.5) measuring the membrane thickness in wet state (after 1 h and 24 h of the immersion in water at 24 ± 3 °C). It can be seen that for pure CAB membrane the S_{24} value (~ 6%) is slightly higher than the S_1 value (~ 5%). In fact, the slightly higher S_{24} value may be explained by the fact that the immersion time is higher and water molecules have more time to penetrate into the membrane. However, an opposite result is obtained for composite membranes (i.e. M_1, M_2, and M_3), for which the S_{24} value is lower (even negative) than the S_1 value. This fact may be explained by the Pr-ILs

leaching from the membrane. This explanation is also confirmed by the membrane thickness decrease after 24 h of the water immersion (Table 5.10).

Table 5.10. Membrane thickness and swelling degree of CAB-membranes.

Membrane	Thickness (µm)			Swelling degree (%)	
	Dry	Wet			
		W_1*	W_{24}*	S_1*	S_{24}**
M_0	60 ± 2	63 ± 2	64 ± 3	5	6
M_1	78 ± 6	80 ± 7	77 ± 6	2	-2
M_2	90 ± 3	93 ± 4	89 ± 5	3	-1
M_3	112 ± 2	114 ± 5	111 ± 4	2	-1

*1 h immersion, **24 h immersion.

5.3.2.3. Polymer-ILs Interactions

The FTIR spectra of Pr-ILs (i.e. [DETA][TFS] and [DEPA][BUPH]), pure CAB, and composite membranes are shown in Fig. 5.22. Table 5.11 presents the assignments of characteristic bands of Pr-ILs, pure and composite membranes. As to the CAB spectrum, hydroxyl band is observed at ~ 3484 cm^{-1} (Fig. 5.22b). Bands between ~ 2874 and 2957 cm^{-1} are assigned to C−H stretching vibration band of –CH group. The C=O stretching vibration band of ester group of CAB is seen at ~ 1759 cm^{-1}. Furthermore, two peaks at ~ 1416 and ~ 1361 cm^{-1} are ascribed to CH_2 and C−H bending, respectively. The peaks observed at ~ 1156 and 1045 cm^{-1} are related to C−O symmetric stretching vibration bands of −COO− ester group [168-170].

Moreover, bands between ~ 2792 and 3098 cm^{-1} ascribed to C−H stretching vibration band of −CH group can be seen in case of pure Pr-ILs (i.e. [DETA][TFS], and [DEPA][BUPH]) (Fig. 5.22a). Two peaks at ~ 1470 and ~ 1390 cm^{-1} belong to CH_2 and C−H bending, respectively. Bands at ~ 1154–1225 cm^{-1} are assigned to S=O stretching vibration bands of [DETA][TFS]. Additionally, bands at ~ 1146–1205 cm^{-1} are assigned to P=O stretching vibration bands of [DEPA][BUPH]. A peak at ~ 1023 cm^{-1} is characteristic to C–F stretching vibration band of [DETA][TFS]. Besides, in case of [DEPA][BUPH], the peak of P−O−C stretching vibration band is revealed at ~ 1027 cm^{-1}. Two peaks observed at ~ 574 and 635 cm^{-1} are related to C−S stretching vibration band of [DETA][TFS] [119,149-151].

The spectra of composite membranes (Fig. 5.22b) show some characteristic peaks of Pr-ILs – at ~ 1205 cm^{-1} (P=O), ~ 1029 cm^{-1} (C−F), and ~ 572–635 cm^{-1} (C−S). However, the peaks of S=O, and P−O−C bands cannot be detected because of the band overlapping of these peaks with the peaks of CAB polymer. All these results confirm the presence of Pr-ILs in the composite membranes.

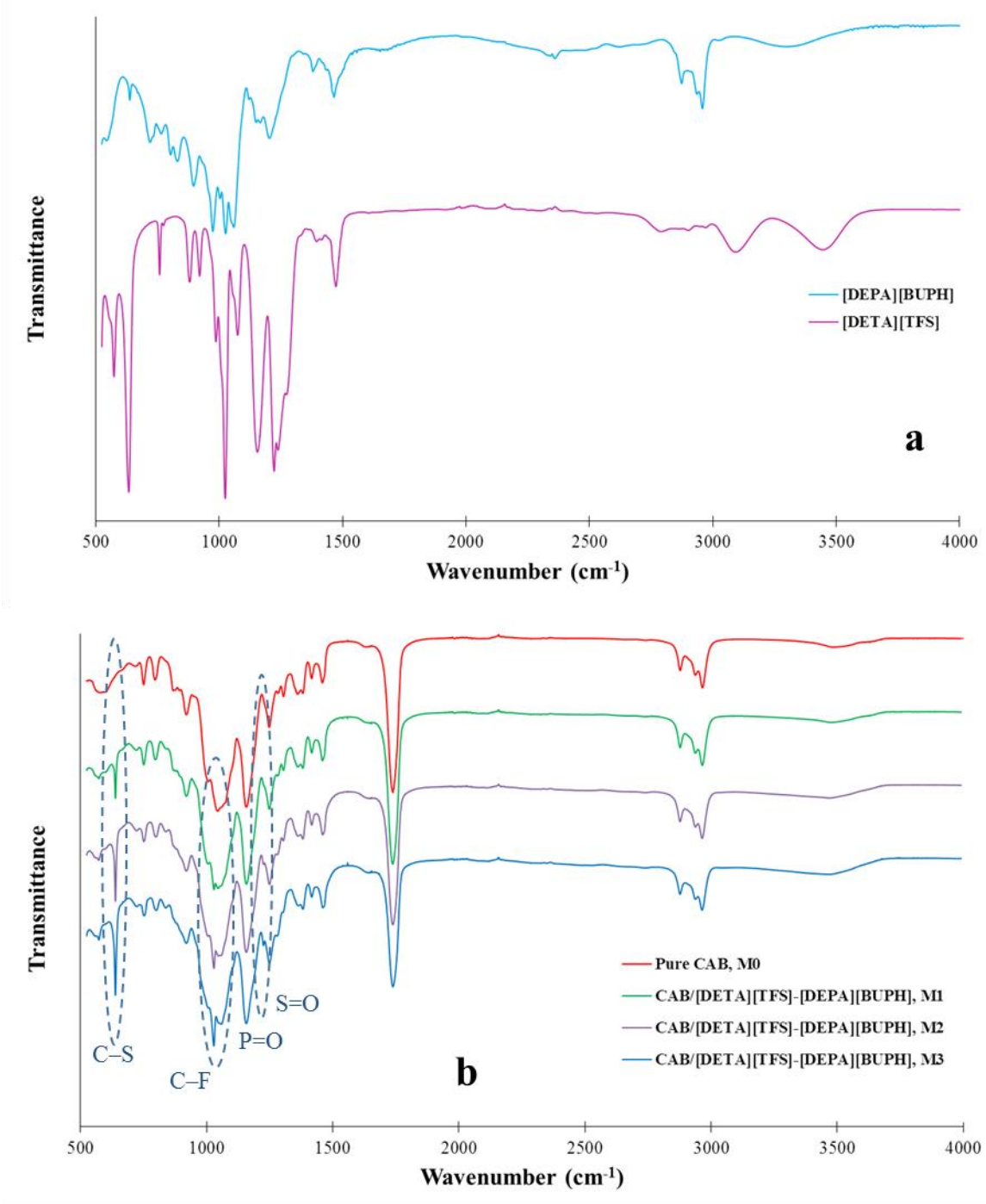

Figure 5.22. FTIR spectra of: a) Pr-ILs; and b) composite membranes.

Table 5.11. Assignments of vibrational modes for [DETA][TFS], [DEPA][BUPH], CAB and composite membranes.

Band assignments	Wavenumber (cm^{-1})					
	[DETA][TFS]	**[DEPA][BUPH]**	**M_0**	**M_1**	**M_2**	**M_3**
O−H stretching	–	–	3484	3474	3476	3488
C−H stretching	2792-3098	2874-2957	2876-2964	2875-2964	2874-2964	2874-2964
C=O stretching vibration (ester group)	–	–	1759	1755	1757	1758
CH_2 bending	1475	1465	1416	1417	1418	1417
C−H bending	1396	1380	1361	1364	1361	1363
S=O stretching	1154, 1225	–	–			
P=O stretching	–	1146,1205	–	1202	1205	1203
C−O symmetric stretching (ester group)	–	–	1045, 1156 –	1043, 1155	1044, 1154	1042, 1156
C−F stretching	1023	–	–			
P−O−C (phosphoric ester)	–	1027	–	1028	1026	1029
C−S stretching	574, 635	–	–	572, 635	574, 636	576, 638

5.3.2.4. Water Contact Angle

The water CA of CAB and CAB/[DETA][TFS]-[DEPA][BUPH] membranes was measured by sessile drop technique (Fig. 5.23). It can be observed that the water CA value of pure CAB membrane (i.e. M_0) is ~ 90 ± 1° (Fig. 5.23a). However, the introduction of the Pr-ILs (i.e. [DETA][TFS] and [DEPA][BUPH]) reduces the water CA value (Fig. 5.23a) confirming the increase of the membrane wettability and hydrophilic character. The water CA values are ~ 87, 85, and 65° for M_1, M_2, and M_3, respectively. This fact may be explained by the hydrophilic nature of [DEPA][BUPH] (owing to the anion phosphate group) which is a dominant IL as its amount is higher than that of [DETA][TFS] (Table 5.8). In fact, CA is strongly dependent on the membrane chemistry and membrane surface roughness [139,160-162]. Even if the membrane surface roughness increases by rising the Pr-ILs concentration (Table 5.9), CA values are reduced since the influence of membrane nature is more pronounced. Rising the amount of Pr-ILs in the composite membrane may also lead to the surface energy increase contributing to reduction of water CA (Fig. 5.23a). Besides, the water CA decreases over the time (Fig. 5.23b). Indeed, the increase of Pr-ILs concentration (especially [DEPA][BUPH]) in the membrane enhances the solubility affinity of water and Pr-ILs. That is why the CA shows a downward trend during the time.

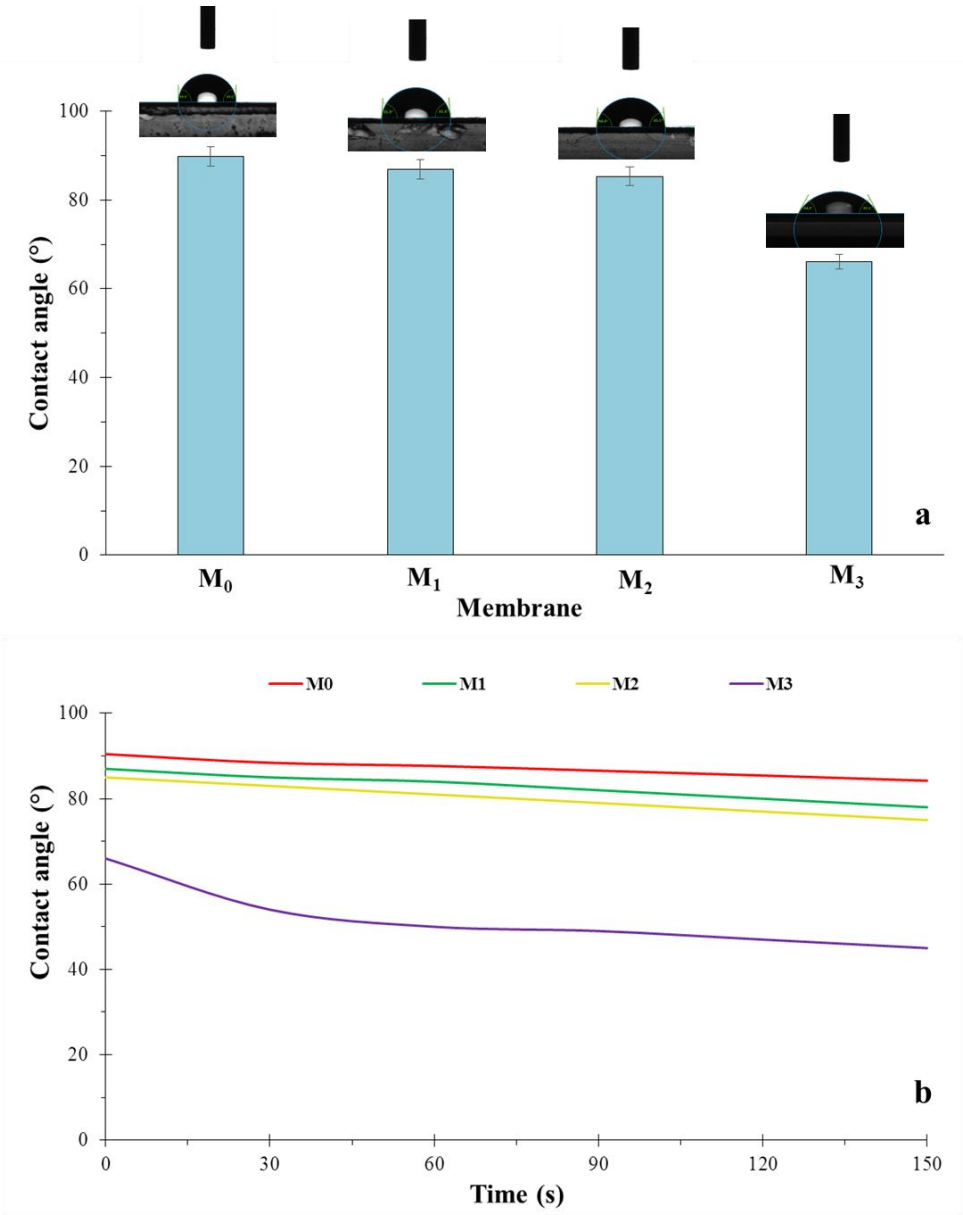

Figure 5.23. Water contact angle of CAB-based membranes: a) apparent CA; and b) CA as a function of time.

5.3.2.5. Thermal Analysis

Thermal stability is another important parameter for fuel cell application, especially for HT-PEMFC [116-118]. The TGA analysis in dynamic mode (Fig. 5.24) was performed (for Pr-ILs, pure CAB, and composite membranes) to study the influence of the presence of mixed Pr-ILs (i.e. [DETA][TFS] and [DEPA][BUPH]) on the thermal behavior of the composite membranes. The TGA curves of pure ILs and CAB membranes are given for comparison. As it was discussed in Chapter 3 (section 3.3), the thermal

stability of ILs depends strongly on the acidity of utilized Bronsted acid. That is why stability of [DETA][TFS] is higher ($T_{5\%}$ = 323 °C) than that of [DEPA][BUPH] ($T_{5\%}$ = 174 °C). Both cations are hydroxylammonium-based and the only difference is the number of carbon atoms in the hydroxyl chain − three carbon atoms for [DEPA] and two – for [DETA].

The TGA curve of the pure CAB membrane reveals the thermal stability up to ~ 360 °C (M_0 Fig. 5.24). However, the thermal stability of composite membranes is reduced by Pr-ILs introducing. Indeed, ILs can dissolve polymer, thus facilitates the membrane thermal degradation. As one can see, the thermal stability of composite membranes (T_{deg} ~ 256–265 °C) is less than that of the pure CAB membrane (T_{deg} ~ 360 °C). Moreover, it can be seen that the increase of the Pr-ILs concentration slightly decreases the thermal stability of composite membranes (T_{deg}: $M_1 > M_2 > M_3$).

The DSC results of Pr-ILs (i.e. [DETA][TFS] and [DEPA][BUPH]), pure and composite membranes are gathered in Table 5.12. The T_g value at ~ 109 °C and no melting or crystallization for pure CAB membrane, confirme the amorphous nature of this polymer. Moreover, no melting and crystallization of Pr-ILs were observed on the DSC curves of composite membranes. Furthermore, the T_g value of CAB decreases with the Pr-ILs concentration increase, revealing the plasticizing behavior of ILs.

Table 5.12. Thermal parameters of Pr-ILs and CAB-based membranes.

Sample	**$T_{5\%}$ (°C)**	**$T_{10\%}$ (°C)**	**T_{deg} (°C)**	**T_g (°C)**	**T_m (°C)**	**T_c (°C)**
[DETA][TFS]	323	355	419	–	-23; 23	-46; 19
[DEPA][BUPH]	174	199	247	-87	–	–
M_0	319	332	360	109	–	–
M_1	235	251	265	77	–	–
M_2	224	242	264	63	–	–
M_3	209	227	256	46	–	–

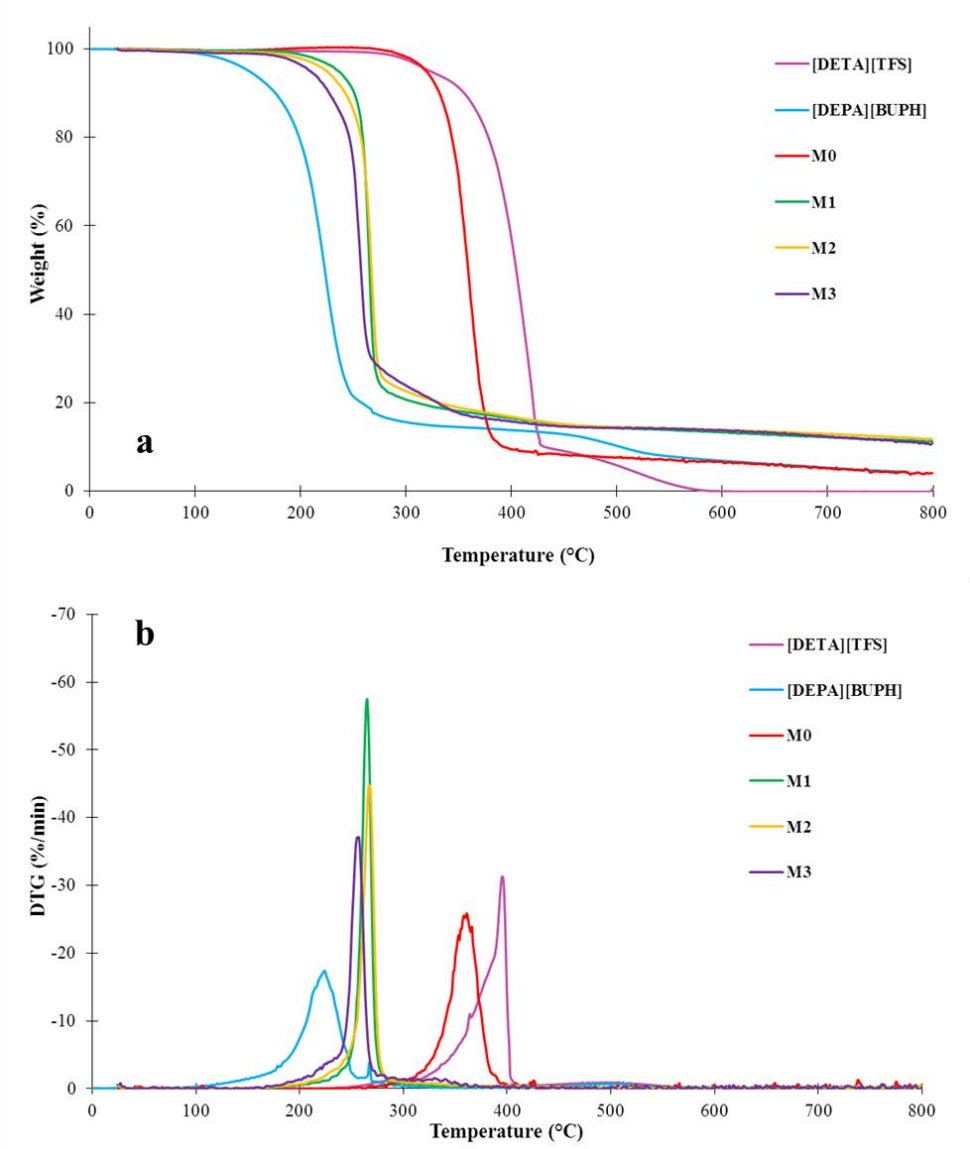

Figure 5.24. Thermal behavior of Pr-ILs and CAB-based membranes: a) TGA curves; b) DTG curves.

5.3.2.6. Mechanical Properties

The mechanical stability of composite CAB/Pr-IL membranes was analyzed (Fig. 5.25). The Young's modulus, force at break, stress at break, and elongation at break values for the pure CAB membrane are 594.0 ± 51.0 MPa, 2.6 ± 0.5 N, 22.0 ± 2.0 MPa, and 10.0 ± 2.0%, respectively. The introduction of Pr-ILs (i.e. [DETA][TFS] and [DEPA][BUPH]) into the composite membranes decreases the Young's modulus, force at break, and stress at break values, while it increases the elongation at break values as compared with the pure CAB membrane. Indeed, the good compatibility of [DEPA][BUPH] (phosphate-based Pr-IL) with CAB polymer and its plasticization enhance the membrane flexibility.

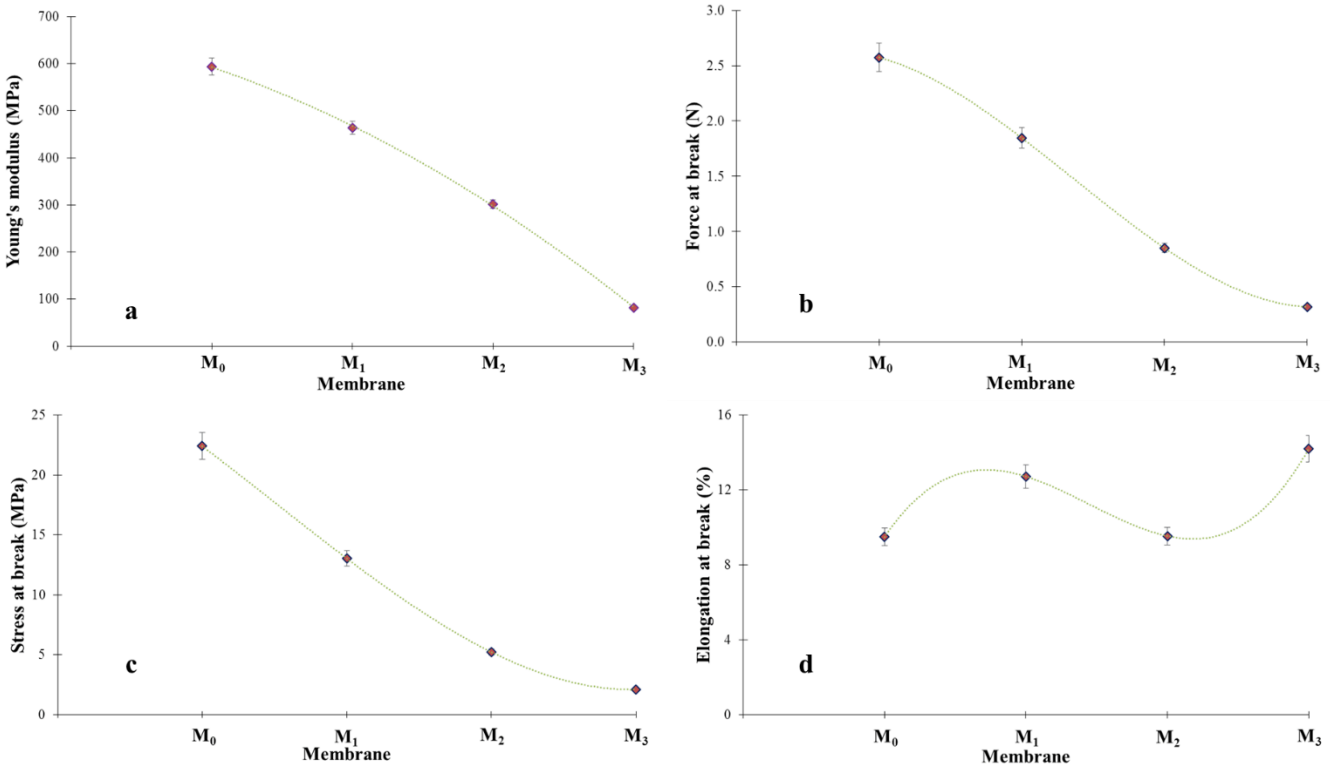

Figure 5.25. Influence of the Pr-ILs concentration on the mechanical properties of CAB-based membranes: a) Young's modulus; b) force at break; c) stress at break; and d) elongation at break.

5.3.2.7. IL Leaching

In order to evaluate the stability of Pr-ILs-based composite membranes, the leaching test was carried out at 25 and 80 °C and fully hydrated condition. The obtained results are shown in Fig. 5.26 for different membranes. It can be seen that the temperature rising from 25 to 80 °C considerably increased the amount of leached IL. Such result can be explained by the increase of the IL mobility and the water molecules diffusion. It is observed that the amount of weight loss of M_1 membrane (containing 8 wt.% of [DETA][TFS] and 15 wt.% of [DEPA][BUPH]) is ~ 4 and 7% (at 25 and 80 °C, respectively) and this value increases to ~ 25 and 31% (at 25 and 80 °C, respectively) for M_3 membrane (containing 18 wt.% of [DETA][TFS] and 23 wt.% of [DEPA][BUPH]). Leaching takes place owing to the lack of strong chemical bonds between polymer chains and ILs as there are only electrostatic (physical) interactions that are not strong enough. Therefore, the IL excess can be released from the polymer matrix.

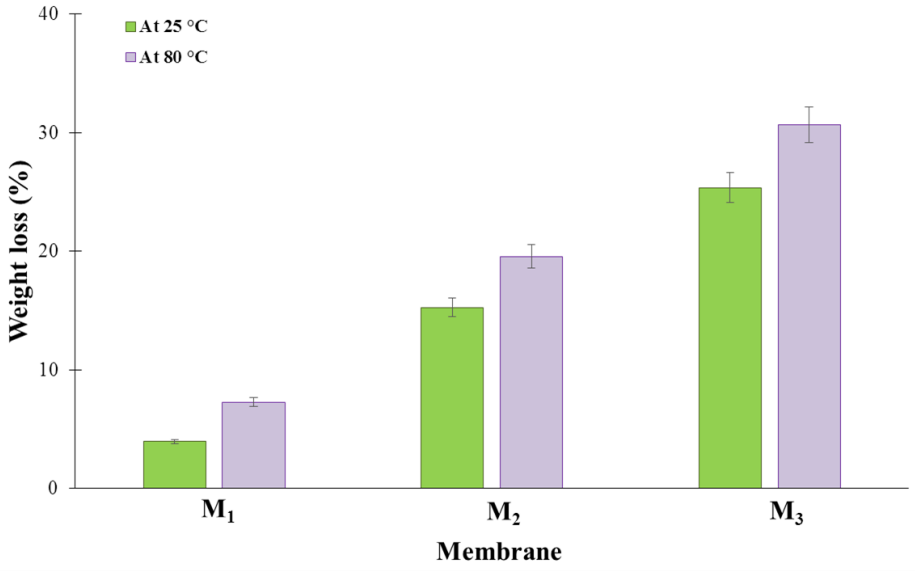

Figure 5.26. IL leaching from the composite membranes at 25 and 80 °C.

5.3.2.8. Conductivity

Ionic conductivity is the most important factor for successful use of PEMs [116,118,119]. Dahi et al. [142] prepared polyimide/IL-based composite membranes with three different phosphate-based ILs ([C_1IM][DBP], [C_4IM][DBP], and [C_4IM][BEHP]) for HT-PEMFC application. The polyimide/[C_1IM][DBP] and polyimide/[C_4IM][DBP] composite membranes showed good ionic conductivity of 0.61 and 4.8 mS·cm^{-1} at 85 °C. The results showed that by increasing the temperature, the ionic conductivity of composite membranes increased and the highest value was observed for [C_4IM][DBP] at 115 °C (20 mS·cm^{-1}). Polyimide/[C_4IM][BEHP] composite membrane showed the lowest ionic conductivity value of ~ 3.16·10^{-3} mS·cm^{-1} at 115 °C. Kobar et al. [118] fabricated different SILMs by impregnation of porous Matrimid® with some ILs ([VIM][TFS], [AIM][TFS], and [VIM][TFS]/[PVIM][TFS]). Matrimid®/[VIM][TFS], Matrimid®/[AIM][TFS], and Matrimid®/[VIM][TFS]/[PVIM][TFS] composite membranes showed ionic conductivity of 2.7·10^{-3}, 7.5·10^{-3}, and 9.9·10^{-4} mS·cm^{-1} at 50 °C, respectively. The temperature rise up to 100 °C increased significantly the ionic conductivity of composite membranes (1.8·10^{-2}, 2.7·10^{-2}, and 4.9·10^{-2} mS·cm^{-1} at 100 °C for Matrimid®/[VIM][TFS], Matrimid®/[AIM][TFS], and Matrimid®/[VIM][TFS]/[PVIM][TFS] membranes, respectively). Fatyeyeva et al. [117] prepared polyimide/IL composite membranes with different imidazolium-based ILs ([MIM][TFSI], [EIM]][TFSI], [PIM][TFSI], and [BIM][TFSI]). The composite membranes showed good ionic conductivity of ~ 10^{-2}–10^{-1} and 1–10 mS·cm^{-1} at 25 and 160 °C, respectively. In general, PEM ionic conductivity depends on the ion mobility and the presence of conductive ions [117].

The pure CAB membrane sample (i.e. M_0) is a non-conductive membrane. Therefore, the sufficient quantity of IL should be introduced into membrane to ensure the ion conductivity. As one can see, introduction of 23 wt.% of [DETA][TFS]-[DEPA][BUPH] allows obtaining a conductive membrane (Fig. 5.27). The ionic conductivity of CAB/[DETA][TFS]-[DEPA][BUPH] composite membranes was measured in a temperature range from 25 to 130 °C during two heating/cooling cycles (Fig. 5.28). As it can be seen from Fig. 5.28, the ionic conductivity of M_2 membrane (as an example) at each temperature in different cycles is almost the same. Such result confirms the ionic conductivity stability of CAB/[DETA][TFS]-[DEPA][BUPH] composite membranes as the function of temperature. In addition, the isothermal measurements of ionic conductivity were carried out at 100 °C for 24 h (Fig. 5.27b). It was found that by rising the temperature from 25 to 120 °C, the ionic conductivity of composite membranes increased considerably. In fact, the rise of temperature leads to the enhancement of the ionic mobility of Pr-ILs. The same tendency was shown by other researchers [7,113,114,116-118,142]. However, it can be seen that by increasing the temperature till 130 °C, the ionic conductivity of composite membranes reduces (Fig. 5.27a). This result cannot be caused by the thermal degradation of composite membrane, since TGA curves showed that composite membranes are thermally stable up to ~ 255–265 °C (Fig. 5.24 and Table 5.12). Indeed, by rising the temperature the viscosity of Pr-ILs in the membrane decreases (i.e. higher mobility) leading to Pr-ILs leaching from membrane. Such release provokes a decrease of the amount of conductive sites and thus, the ionic conductivity. Moreover, it was found that the Pr-ILs concentration increase in the membrane rises the ionic conductivity value and M_3 membrane (containing 41 wt.% of Pr-ILs) showed the highest ionic conductivity of 0.443 $mS \cdot cm^{-1}$ at 120 °C under anhydrous condition, while M_1 membrane (containing 23 wt.% of Pr-ILs) showed the lowest value (0.134 $mS \cdot cm^{-1}$) at the same operating condition (Fig. 5.27a). Indeed, by increasing the concentration of ILs in the membrane, the number of conductive sites and channels (i.e. conductive regions) for transferring the protons enhances. The ionic conductivity of CAB/[DETA][TFS]-[DEPA][BUPH] composite membrane (M_3) is comparable with literature data [117,118,142]. It can be seen that the ionic conductivity of Nafion® membrane at 25 °C (~ 0.1 $S \cdot cm^{-1}$) [172] is much higher than prepared CAB/ILs composite membrane (~ 10^{-5} $S \cdot cm^{-1}$). However, the ionic conductivity of Nafion® membrane decreases at temperature higher than 80 °C (~ 10^{-8} $S \cdot cm^{-1}$) owing to the dehydration phenomenon. This value is much lower as compared to M_3 membrane (~ 10^{-4}–10^{-3} $S \cdot cm^{-1}$ at 120 °C under anhydrous condition).

In order to evaluate the ionic conductivity stability of composite membrane in long-term applications, isothermal test was carried out at 100 °C under non-humid condition for 24 h. The obtained results (Fig. 5.27b) demonstrated that all composite membranes (i.e. M_1, M_2, and M_3) showed stable ionic conductivity for 24 h revealing the excellent potential of CAB/[DETA][TFS]-[DEPA][BUPH] composite membranes for HT-PEMFC application. The activation energy (E_a) calculated by Eq. 2.18 is 62.4, 45.4,

and 38.5 kJ·mol^{-1} for M_1, M_2, and M_3, respectively. As E_a > 14 kJ·mol^{-1}, the proton conduction takes place by Grotthuss mechanism [117-119,142]. Besides, the increase of the concentration of Pr-ILs from 23 to 41 wt.% causes a significant reduction of the E_a value.

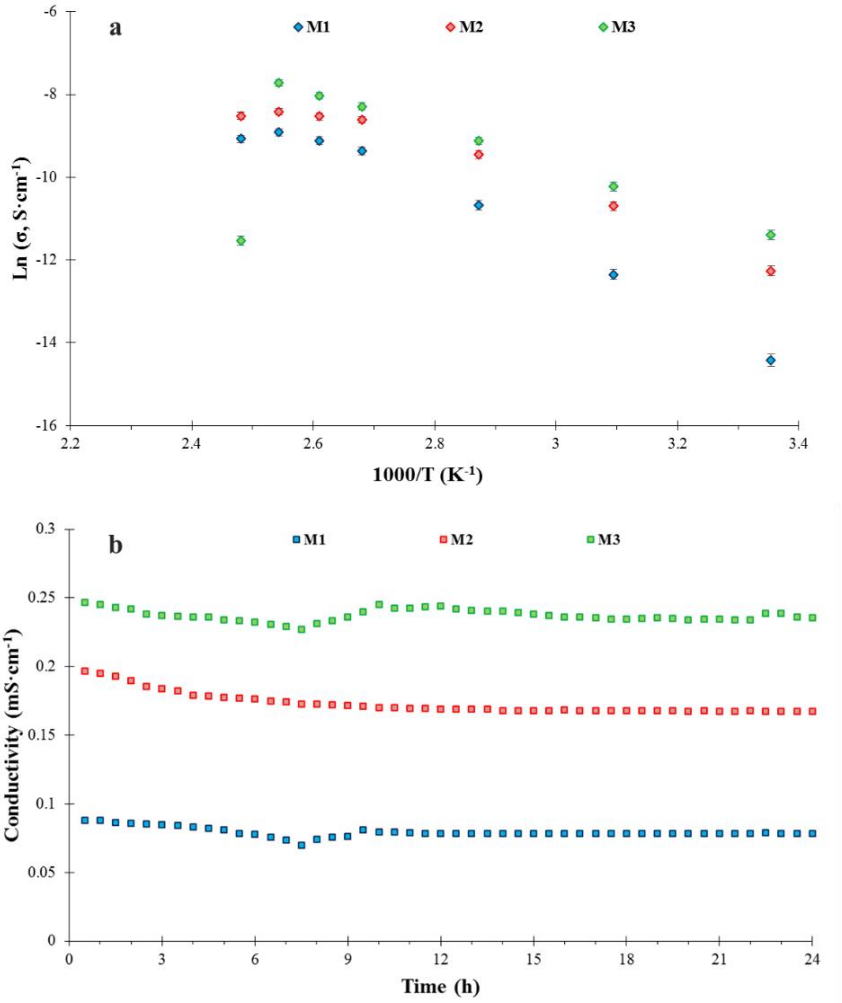

Figure 5.27. Ionic conductivity of CAB/[DETA][TFS]-[DEPA][BUPH] composite membranes: a) dynamic mode; and b) isothermal mode at 100 °C.

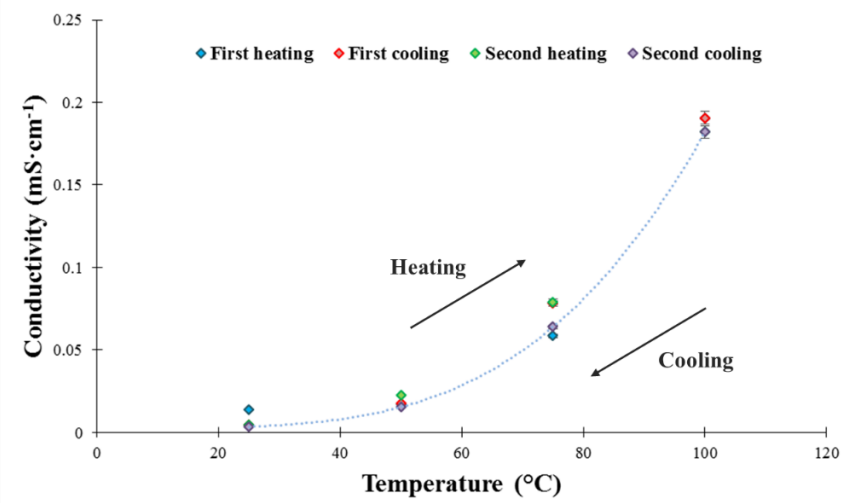

Figure 5.28. Ionic conductivity of M_2 composite membrane during heating/cooling cycles.

5.4. Conclusion

In this study, CAB/[DETA][TFS]-[DEPA][BUPH] composite membranes were prepared by phase inversion method induced by solvent evaporation. The EDX and FTIR analyses proved the presence of ILs in the composite membrane. SEM analysis showed homogenous morphology for M_0 and M_1 (23 wt.%) membranes, but further IL concentration increase in the membrane (33 and 41 wt.%) led to decreasing the membrane homogeneity. The membrane surface roughness firstly remained stable by addition of 23 wt.% of mixed ILs ([DETA][TFS]-[DEPA][BUPH]) while further increase of the IL content provoked surface roughness increase. The water CA of CAB membranes reduced by ILs addition owing to the hydrophilic character of [DEPA][BUPH] as the dominant IL. The CAB/[DETA][TFS]-[DEPA][BUPH] composite membranes showed a great thermal stability (T_{deg} ~ 256–265 °C) even though M_0 membrane showed higher thermal stability (T_{deg} ~ 360 °C). It was found that the increase of the ILs concentration from 23 to 41 wt.% slightly decreases the thermal stability of composite membranes (T_{deg}: $M_1 > M_2 > M_3$). The addition of [DETA][TFS]-[DEPA][BUPH] into the composite membranes reduced the Young's modulus, force at break, and stress at break values, whereas it increased the elongation at break values as compared with the pure CAB membrane. Also, leaching test revealed that the increase of both IL concentration (from 23 to 41 wt.%) and temperature (from 25 to 80 °C) caused enhancing the IL leakage from the composite membrane. The measured ionic conductivity values of composite membranes during heating and cooling cycles revealed the ionic conductivity stability of CAB/[DETA][TFS]-[DEPA][BUPH] composite membranes. M_3 membrane showed the maximum ionic conductivity value of 0.443 $mS \cdot cm^{-1}$ at 120 °C under non-humid condition while further temperature increase up to 130 °C caused ionic conductivity reduction. Besides, the isothermal conductivity test showed the great potential of composite membranes for HT-PEMFC

application for long-term utilization. It was found that the proton conduction takes place by Grotthuss mechanism since the E_a > 14 kJ·mol^{-1} for composite membranes. The obtained results confirm that the prepared CAB/[DETA][TFS]-[DEPA][BUPH] composite membranes are promising candidates for using in electrochemical applications, namely, electrodialysis and fuel cell.

General Conclusion and Prospects

The main aim of the present PhD thesis is to fabricate chemically, thermally, and mechanically stable membrane with high ionic conductivity for HT-PEMFC application as the green source of energy generation. To obtain a conductive membranes with good physical-chemical properties and affordable price, composite membranes should be designed. For this purpose, three polymers (PA6, CAP, and CAB) were used as the basic polymer matrix. The presence of carbonyl, amine, and methylene groups in PA6 and ester and hydroxyl groups in CAP and CAB can be considered as the reactive centers for electrostatic interactions with IL. These polymers were chosen owing to their great physical, chemical, mechanical, and thermal stability. These polymers are commercially available at reasonable price and they have film-forming ability. Moreover, they have been already used in different separation processes – MF, UF, NF, and RO (for PA6) and UF, RO, forward osmosis, and pervaporation (for CAP and CAB). Therefore, they are proposed to be used in the HT-PEMFC application.

However, the chosen polymers are non-conductive, so they cannot be used alone as the ion conductive PEM. Therefore, to ensure the ion conductivity, IL-based composite membranes were prepared and studied. For this purpose, several Pr-ILs containing different cations (imidazolium- and hydroxylammonium-based) and anions (trifluoromethansulfonate-, acetate-, sulfate-, and phosphate-based) were synthesized by acid-base neutralization reaction. The chemical structure of synthesized Pr-ILs was confirmed by NMR (^{1}H and ^{19}F) and FTIR analysis. In order to evaluate the thermal behavior of obtained Pr-ILs, TGA (in static and dynamic modes) and DSC analysis was carried out. In addition, the ionic conductivity (in isothermal and dynamic modes) of Pr-ILs was measured by EIS and the obtained results were correlated with the IL chemical structure.

It is found that the chemical nature of anion and cation influences the thermal stability of Pr-ILs. However, the influence of anion nature is more pronounced. Among different types of anions ([TFA], [HS], [BUPH], and [EHPH]), [TFS]-based Pr-ILs reveal the highest thermal stability (T_{deg} ~ 415–435 °C) owing to the strong acid property of trifluoromethanesulfonic acid. Also, [TFS]-based Pr-ILs are characterized by the highest thermal stability during static TGA tests – only ~ 0–3% of weight loss is noted at 150 °C during 24 h. Indeed, there is a direct link between acidity of acid and thermal stability of IL – the stronger is the acid, the higher is the thermal stability. Therefore, the order of IL thermal stability on the basis of the anion nature is as follows: [TFS] > [HS] > [EHPH] > [BUPH] > [TFA]. Acetate-based Pr-ILs show the lowest thermal stability (T_{deg} ~ 200–215 °C) owing to the hydrophilic property of acetate group. Two different cations (i.e. imidazolium- and hydroxylammonium-based) were used for the IL synthesis. For the same anion, the thermal stability of these two cations is rather similar.

The anion nature has dominant influence on the Pr-IL ionic conductivity measured in dynamic and isothermal modes. [TFS]-based Pr-ILs showed the highest values (between ~ 34.5 and 63.7 $mS \cdot cm^{-1}$ at 150

°C in anhydrous condition) owing to the low pK_a value of trifluoromethanesulfonic acid (~ -14). The presence of long alkyl chains in the anion structure (for [BUPH] and [EHPH]) increases the viscosity for these Pr-ILs and, thus, reduces the ionic mobility – ~ 0.13−2.5 $mS \cdot cm^{-1}$ at 120 °C. Moreover, [EHPH]-based Pr-ILs demonstrated lower ionic conductivity than [BUPH]-based ILs owing to the lower ionic mobility because of the presence of longer alkyl chain. [TFA]-based Pr-ILs showed a good ionic conductivity of ~ 28.6 $mS \cdot cm^{-1}$ up to moderate temperature (~ 80−90 °C), i.e. almost comparable with the conductivity of [TFS]-based Pr-ILs in the same temperature range. However, acetate-based Pr-ILs are not thermally stable owing to the presence of hydrophilic acetate group. So, the order of ionic conductivity according to the anion nature is the following: [TFS] > [HS] > [TFA] > [BUPH] > [EHPH]. It is found that the increase of the cation alkyl and hydroxyl chain reduces the ionic conductivity owing to the ionic mobility reduction. According to the activation energy of conductivity, the main mechanism is the proton hopping. The obtained results prove that the [TFS]-based Pr-ILs are very promising candidates for high temperature industrial applications and long-term processes (e.g. HT-PEMFC) owing to their excellent thermal stability and ionic conductivity. However, ILs cannot be used alone because of their physical state, therefore, they should be added into the polymer matrix.

In the first attempt, porous PA6 membranes with various gelation times were prepared by non-solvent induced phase separation technique. SEM analysis showed that the change of the gelation time leads to changing the membrane morphology – higher gelation time provokes the formation of the porous membranes with smaller pores. AFM analysis revealed that increasing the gelation time causes the membrane surface roughness increase and the highest surface roughness was observed for M_{10} membrane (R_a and R_q are ~ 189 ± 53 nm and 240 ± 59 nm, respectively). Moreover, by increasing the gelation time, water CA increased due to the surface roughness enhancement, while WU and membrane porosity are reduced owing to pore size reduction. M_{10} membrane also showed a higher tensile strength (around 28%) than that of M_0 membrane owing to change the membrane structure during the gelation time. The obtained porous PA6 membranes are characterized by rather low water flux, L_p, and retention capacity – ~ 12.9 $L \cdot m^{-2} \cdot h^{-1}$, 8.2 $L \cdot m^{-2} \cdot h^{-1} \cdot bar^{-1}$, and 50%, respectively, for M_{10} membrane. Although, the prepared membranes do not demonstrated sufficient transport properties for filtration process, they may be used as the support for preparation of SILM for PEMFC application as the pores can be filled by IL and exchange to conductive passages. However, leaching of IL is the main disadvantage of such porous membranes owing to the lack of considerable electrostatic interactions between IL and polymer.

That is why dense IL-based composite membranes (with CAP and CAB polymers) were prepared. In the case of CAP/IL membranes, SEM analysis showed that the addition of A-ILs caused formation of gaps and cavities in the membrane structure. EDX and FTIR analyses confirmed the presence of ILs in the

composite membrane. The surface roughness of CAP membranes increased by addition of [TFS]- and [TFSI]-based ILs, while it remained unchanged in case of [HS]-based IL owing to the good compatibility between polymer and [SMIM][HS]. Besides, the water CA values of CAP/[SMIM][TFS] and CAP/[SMIM][TFSI] membranes were higher than of pure CAP membrane, whereas they stayed constant in case of CAP/[SMIM][HS] membrane. The composite membranes showed lower thermal stability as compared with pure CAP membrane. CAP/[SMIM][TFS] and CAP/[SMIM][TFSI] membranes showed lower mechanical stability as compared with pure membrane, while the mechanical stability of CAP/[SMIM][HS] membrane is close to the stability of pure CAP membrane. Increasing the IL concentration provokes the leaching increase owing to the weak electrostatic interactions between IL and polymer. CAP/[SMIM][TFS] composite membrane showed the highest ionic conductivity of $1.2 \cdot 10^{-3}$ $mS \cdot cm^{-1}$ at 25 °C and 100% RH owing to the strong acid property of trifluoromethanesulfonic acid. However, more promising results were obtained regarding CAB-based composite membranes because of the higher concentration of IL loading in the CAB matrix (up to 41 wt.%).

CAB/[DETA][TFS]-[DEPA][BUPH] composite membranes were prepared by a phase inversion method induced by solvent evaporation. EDX and FTIR analyses proved the presence of ILs in the composite membrane. SEM analysis showed homogenous morphology of M_0 and M_1 (23 wt.%) membranes, but further increase of IL concentration (33 and 41 wt.%) led to the formation of heterogeneity in the membrane bulk. The membrane surface roughness firstly remained stable by addition of 23 wt.% of mixed ILs ([DETA][TFS]-[DEPA][BUPH]) while further increase of IL content provoked the surface roughness increase. The water CA of CAB membranes reduced by ILs addition owing to the hydrophilic property of [DEPA][BUPH] as the dominant IL. The CAB/[DETA][TFS]-[DEPA][BUPH] composite membranes showed a great thermal stability (T_{deg} ~ 256–265 °C) although M_0 membrane showed higher thermal stability (T_{deg} ~ 360 °C). It was found that the increase of the ILs concentration from 23 to 41 wt.% slightly decreases the thermal stability of composite membranes (T_{deg}: $M_1 > M_2 > M_3$). The addition of [DETA][TFS]-[DEPA][BUPH] into the composite membranes reduced the Young's modulus, force at break, and stress at break values, whereas it increased the elongation at break values as compared with the pure CAB membrane. Also, leaching test revealed that the increase of both IL concentration (from 23 to 41 wt.%) and temperature (from 25 to 80 °C) caused higher IL leakage from the composite membrane. The measured ionic conductivity values of composite membranes during heating and cooling cycles revealed the ionic conductivity stability of CAB/[DETA][TFS]-[DEPA][BUPH] composite membranes. M_3 membrane showed the maximum ionic conductivity value of 0.443 $mS \cdot cm^{-1}$ at 120 °C under anhydrous condition, while further temperature increase up to 130 °C caused ionic conductivity reduction. The ionic conductivity of Nafion® membrane at 25 °C (~ 0.1 $S \cdot cm^{-1}$) is much higher than prepared CAB/[DETA][TFS]-[DEPA][BUPH] composite membrane (~ 10^{-5} $S \cdot cm^{-1}$). However, the ionic

conductivity of Nafion® membrane significantly drops at temperature higher than 80 °C (~ 10^{-8} S·cm^{-1}) because of the dehydration phenomenon and the conductivity of M_3 membrane stays high (~ 10^{-4}–10^{-3} S·cm^{-1} at 120 °C under anhydrous condition). Furthermore, the isothermal conductivity test showed the great potential of composite membranes for HT-PEMFC application for long-term utilization. It was found that the proton conduction occurs according to the Grotthuss mechanism since the E_a > 14 kJ·mol^{-1} for composite membranes. The obtained results confirm that the prepared CAB/[DETA][TFS]-[DEPA][BUPH] composite membranes are promising candidates for using in electrochemical applications, namely, electrodialysis and fuel cell.

To conclude, according to the performed investigations, we can summarize the most important results of this PhD thesis:

- the synthesis of new Pr-ILs with different cations and anions as well as the evaluation of the influence of IL nature on its thermal stability and ionic conductivity;
- the preparation of porous PA6 membranes with different gelation time and investigation of their morphological, mechanical, physical, and transport properties to find the best candidate for SILM preparation;
- the fabrication of composite membranes containing CAP/A-ILs and CAB/Pr-ILs and evaluation of their physical-chemical properties;
- the correlation between the IL and polymer nature and the thermal, mechanical, and morphological properties as well as ionic conductivity of obtained composite membranes.

The obtained results, allows deeper understanding about the knowledge of IL-based composite membrane preparation and improvement of their mechanical, thermal, morphological properties as well as ionic conductivity. This knowledge is crucial for tailoring the PEM for HT-PEMFC application. Taking into account these achievements, several prospects can be listed for future studies.

- CAB/[DETA][TFS]-[DEPA][BUPH] composite membranes were prepared at the lab scale. Larger scale will be necessary for industrial implementation. Therefore, the scale up should be performed and membrane performance should be evaluated. However, to obtain a desirable membranes for industrial applications, the thermal and mechanical stability as well as ionic conductivity of membranes should be improved. For this purpose, membrane composition could be changed. For instance, the introduction of third agent (nanoparticles, nanotubes, and/or nanofibers) into the CAB/[DETA][TFS]-[DEPA][BUPH] composite membranes could be proposed. The existence of new electrostatic interactions between third agent, IL, and polymer may improve the physical-chemical properties of composite membranes;

- One of the main disadvantages of the prepared CAB/ILs membrane is the IL leaching from the membrane because of the weak electrostatic interactions between ILs and polymer, thus, reducing the ionic conductivity. Therefore, in order to diminish this problem, synthesis of polymerized IL may be useful;
- several Pr-ILs containing different cations (i.e. [MIM][, [BIM], [DETA], and [DEPA]) and anions (i.e. [TFS], [TFA], [HS], [BUPH], and [EHPH]) were synthesized. However, only CAB-based composite membranes containing [DETA][TFS] and [DEPA][BUPH] were prepared. It could be proposed to prepare CAB-based composite membranes with other synthesized Pr-ILs and evaluate their chemical, physical, and thermal stability as well as ionic conductivity;
- the effective life of synthesized Pr-ILs and CAB/[DETA][TFS]-[DEPA][BUPH] composite membranes should be studied. The ionic conductivity and thermal stability of Pr-ILs and CAB/[DETA][TFS]-[DEPA][BUPH] composite membranes were evaluated in static mode during 24 h. However, the duration of an actual PEM utilization is longer than 24 h (> 1000 h);
- it was observed that the change of gelation time changes the morphological and physical properties of PA6 membranes. It could be useful to prepare SILM based on PA6 membrane and [TFS]-based Pr-ILs (with the highest thermal stability and ionic conductivity) to evaluate the possible influence of gelation time on the thermal stability and ionic conductivity of SILM.

References

References

1. Pacyna, J.M. Monitoring and assessment of metal contaminants in the air. In *Toxicology of Metals, Volume I*; CRC Press: 2023; pp. 9-28.
2. Yang, D.-L.; Zhang, Z.-N.; Liu, H.; Yang, Z.-Y.; Liu, M.-M.; Zheng, Q.-X.; Chen, W.; Xiang, P. Indoor air pollution and human ocular diseases: Associated contaminants and underlying pathological mechanisms. *Chemosphere* **2023**, *311*, 137037.
3. Cho, H.H.; Strezov, V.; Evans, T.J. A review on global warming potential, challenges and opportunities of renewable hydrogen production technologies. *Sustainable Materials and Technologies* **2023**, e00567.
4. Ahmed, A.A.; Nazzal, M.A.; Darras, B.M.; Deiab, I. Global warming potential, water footprint, and energy demand of shared autonomous electric vehicles incorporating circular economy practices. *Sustainable Production and Consumption* **2023**, *36*, 449-462.
5. Zheng, J.; Du, J.; Wang, B.; Klemeš, J.J.; Liao, Q.; Liang, Y. A hybrid framework for forecasting power generation of multiple renewable energy sources. *Renewable and Sustainable Energy Reviews* **2023**, *172*, 113046.
6. Sayed, E.T.; Olabi, A.G.; Alami, A.H.; Radwan, A.; Mdallal, A.; Rezk, A.; Abdelkareem, M.A. Renewable energy and energy storage systems. *Energies* **2023**, *16*, 1415.
7. Ebrahimi, M.; Kujawski, W.; Fatyeyeva, K.; Kujawa, J. A review on ionic liquids-based membranes for middle and high temperature polymer electrolyte membrane fuel cells (PEM FCs). *International journal of molecular sciences* **2021**, *22*, 5430.
8. Ellabban, O.; Abu-Rub, H.; Blaabjerg, F. Renewable energy resources: Current status, future prospects and their enabling technology. *Renewable and sustainable energy reviews* **2014**, *39*, 748-764.
9. Abdelkareem, M.A.; Elsaid, K.; Wilberforce, T.; Kamil, M.; Sayed, E.T.; Olabi, A. Environmental aspects of fuel cells: A review. *Science of The Total Environment* **2021**, *752*, 141803.
10. Jurasz, J.; Canales, F.; Kies, A.; Guezgouz, M.; Beluco, A. A review on the complementarity of renewable energy sources: Concept, metrics, application and future research directions. *Solar Energy* **2020**, *195*, 703-724.
11. Pasupathi, S.; Gomez, J.C.C.; Su, H.; Reddy, H.; Bujlo, P.; Sita, C. Recent advances in high-temperature PEM fuel cells. **2016**.
12. Li, G.; Kujawski, W.; Rynkowska, E. Advancements in proton exchange membranes for high-performance high-temperature proton exchange membrane fuel cells (HT-PEMFC). *Reviews in Chemical Engineering* **2022**, *38*, 327-346.

13. Wee, J.-H. Applications of proton exchange membrane fuel cell systems. *Renewable and sustainable energy reviews* **2007**, *11*, 1720-1738.
14. Valdés-López, V.F.; Mason, T.; Shearing, P.R.; Brett, D.J. Carbon monoxide poisoning and mitigation strategies for polymer electrolyte membrane fuel cells–A review. *Progress in Energy and Combustion Science* **2020**, *79*, 100842.
15. Shahgaldi, S.; Ozden, A.; Li, X.; Hamdullahpur, F. A novel membrane electrode assembly design for proton exchange membrane fuel cells: Characterization and performance evaluation. *Electrochimica Acta* **2019**, *299*, 809-819.
16. Ferreira, R.B.; Falcão, D.; Oliveira, V.; Pinto, A. Experimental study on the membrane electrode assembly of a proton exchange membrane fuel cell: effects of microporous layer, membrane thickness and gas diffusion layer hydrophobic treatment. *Electrochimica Acta* **2017**, *224*, 337-345.
17. Díaz, M.; Ortiz, A.; Vilas, M.; Tojo, E.; Ortiz, I. Performance of PEMFC with new polyvinyl-ionic liquids based membranes as electrolytes. *International Journal of Hydrogen Energy* **2014**, *39*, 3970-3977.
18. Hooshyari, K.; Javanbakht, M.; Naji, L.; Enhessari, M. Nanocomposite proton exchange membranes based on Nafion containing Fe2TiO5 nanoparticles in water and alcohol environments for PEMFC. *Journal of Membrane Science* **2014**, *454*, 74-81.
19. Zhang, Y.; Liu, C.; Wang, J.; Ren, S.; Song, Y.; Quan, P.; Fang, L. Ionic liquids in transdermal drug delivery system: Current applications and future perspectives. *Chinese Chemical Letters* **2023**, *34*, 107631.
20. Alade, O.; Mohammed, I.; Abdel-Azeim, S.; Shakil Hussain, S.M.; Kamal, M.S.; Mahmoud, M.; Shehri, D.A.; Saibi, H.; Adewunmi, A.A.; Murtaza, M. Review on Applications of Ionic Liquids (ILs) for Bitumen Recovery: Mechanisms, Challenges, and Perspectives. *Energy & Fuels* **2023**.
21. Masri, A.N.; Mi, A.M.; Leveque, J.-M. A review on dicationic ionic liquids: Classification and application. *Ind. Eng. Manag* **2016**, *5*, 197-204.
22. Singh, S.K.; Savoy, A.W. Ionic liquids synthesis and applications: An overview. *Journal of Molecular Liquids* **2020**, *297*, 112038.
23. Lin, B.; Yuan, W.; Xu, F.; Chen, Q.; Zhu, H.; Li, X.; Yuan, N.; Chu, F.; Ding, J. Protic ionic liquid/functionalized graphene oxide hybrid membranes for high temperature proton exchange membrane fuel cell applications. *Applied Surface Science* **2018**, *455*, 295-301.
24. Rynkowska, E.; Fatyeyeva, K.; Kujawski, W. Application of polymer-based membranes containing ionic liquids in membrane separation processes: A critical review. *Reviews in Chemical Engineering* **2018**, *34*, 341-363.

25. Jiao, K.; Xuan, J.; Du, Q.; Bao, Z.; Xie, B.; Wang, B.; Zhao, Y.; Fan, L.; Wang, H.; Hou, Z. Designing the next generation of proton-exchange membrane fuel cells. *Nature* **2021**, *595*, 361-369.
26. Field, R.; Derwent, R. Global warming consequences of replacing natural gas with hydrogen in the domestic energy sectors of future low-carbon economies in the United Kingdom and the United States of America. *International Journal of Hydrogen Energy* **2021**, *46*, 30190-30203.
27. Al-Ismail, F.S.; Alam, M.S.; Shafiullah, M.; Hossain, M.I.; Rahman, S.M. Impacts of Renewable Energy Generation on Greenhouse Gas Emissions in Saudi Arabia: A Comprehensive Review. *Sustainability* **2023**, *15*, 5069.
28. Qazi, A.; Hussain, F.; Rahim, N.A.; Hardaker, G.; Alghazzawi, D.; Shaban, K.; Haruna, K. Towards sustainable energy: a systematic review of renewable energy sources, technologies, and public opinions. *IEEE access* **2019**, *7*, 63837-63851.
29. Sinsel, S.R.; Riemke, R.L.; Hoffmann, V.H. Challenges and solution technologies for the integration of variable renewable energy sources—a review. *renewable energy* **2020**, *145*, 2271-2285.
30. Haines, A.; Kovats, R.S.; Campbell-Lendrum, D.; Corvalán, C. Climate change and human health: impacts, vulnerability, and mitigation. *The Lancet* **2006**, *367*, 2101-2109.
31. Pramuanjaroenkij, A.; Kakaç, S. The fuel cell electric vehicles: The highlight review. *International Journal of Hydrogen Energy* **2023**, *48*, 9401-9425.
32. Serov, A.; Zenyuk, I.V.; Arges, C.G.; Chatenet, M. Hot topics in alkaline exchange membrane fuel cells. *Journal of Power Sources* **2018**, *375*, 149-157.
33. Cooper, M.; Hall, V. William Robert Grove and the London Institution, 1841–1845. *Annals of Science* **1982**, *39*, 229-254.
34. St-Pierre, J.; Wilkinson, D.P. Fuel cells: a new, efficient and cleaner power source. *American Institute of Chemical Engineers. AIChE Journal* **2001**, *47*, 1482.
35. Din, M.A.U.; Idrees, M.; Jamil, S.; Irfan, S.; Nazir, G.; Mudassir, M.A.; Saleem, M.S.; Batool, S.; Cheng, N.; Saidur, R. Advances and challenges of methanol-tolerant oxygen reduction reaction electrocatalysts for the direct methanol fuel cell. *Journal of Energy Chemistry* **2023**, *77*, 499-513.
36. Boldrin, P.; Brandon, N.P. Progress and outlook for solid oxide fuel cells for transportation applications. *Nature Catalysis* **2019**, *2*, 571-577.
37. Qu, E.; Hao, X.; Xiao, M.; Han, D.; Huang, S.; Huang, Z.; Wang, S.; Meng, Y. Proton exchange membranes for high temperature proton exchange membrane fuel cells: Challenges and perspectives. *Journal of power sources* **2022**, *533*, 231386.

38. Chandan, A.; Hattenberger, M.; El-Kharouf, A.; Du, S.; Dhir, A.; Self, V.; Pollet, B.G.; Ingram, A.; Bujalski, W. High temperature (HT) polymer electrolyte membrane fuel cells (PEMFC)–A review. *Journal of Power Sources* **2013**, *231*, 264-278.
39. Pollet, B.G.; Kocha, S.S.; Staffell, I. Current status of automotive fuel cells for sustainable transport. *Current opinion in Electrochemistry* **2019**, *16*, 90-95.
40. Randall, C.R.; DeCaluwe, S.C. Predicted Impacts of Graded Catalyst Layer Ionomer and Pt Distributions on PEMFC Performance. In Proceedings of the Electrochemical Society Meeting Abstracts 241, 2022; pp. 1699-1699.
41. Dutczak, J. Issues related to fuel cells application to small drones propulsion. In Proceedings of the IOP Conference Series: Materials Science and Engineering, 2018; p. 042014.
42. Ogungbemi, E.; Wilberforce, T.; Ijaodola, O.; Thompson, J.; Olabi, A. Selection of proton exchange membrane fuel cell for transportation. *International Journal of Hydrogen Energy* **2021**, *46*, 30625-30640.
43. Pollet, B.G.; Staffell, I.; Shang, J.L.; Molkov, V. 22 - Fuel-cell (hydrogen) electric hybrid vehicles. In *Alternative Fuels and Advanced Vehicle Technologies for Improved Environmental Performance*, Folkson, R., Ed.; Woodhead Publishing: 2014; pp. 685-735.
44. Li, H.; Zhao, H.; Jian, S.; Tao, B.; Gu, S.; Xu, G.; Wang, G.; Chang, H. Designing proton exchange membrane fuel cells with high specific power density. *Journal of Materials Chemistry A* **2023**, *11*, 17373-17391.
45. Bhosale, A.C.; Ghosh, P.C.; Assaud, L. Preparation methods of membrane electrode assemblies for proton exchange membrane fuel cells and unitized regenerative fuel cells: A review. *Renewable and Sustainable Energy Reviews* **2020**, *133*, 110286.
46. Chen, M.; Zhao, C.; Sun, F.; Fan, J.; Li, H.; Wang, H. Research progress of catalyst layer and interlayer interface structures in membrane electrode assembly (MEA) for proton exchange membrane fuel cell (PEMFC) system. *ETransportation* **2020**, *5*, 100075.
47. He, Y.; Wang, J.; Zhang, H.; Zhang, T.; Zhang, B.; Cao, S.; Liu, J. Polydopamine-modified graphene oxide nanocomposite membrane for proton exchange membrane fuel cell under anhydrous conditions. *Journal of Materials Chemistry A* **2014**, *2*, 9548-9558.
48. Wang, J.; Bai, H.; Zhang, H.; Zhao, L.; Chen, H.; Li, Y. Anhydrous proton exchange membrane of sulfonated poly (ether ether ketone) enabled by polydopamine-modified silica nanoparticles. *Electrochimica Acta* **2015**, *152*, 443-455.
49. Annapragada, R.; Vandavasi, K.R.; Kanuparthy, P.R. Metal-organic framework membranes for proton exchange membrane fuel cells: A mini-review. *Inorganica Chim. Acta* **2023**, *546*, 121304.

50. Roy, A.; Hickner, M.A.; Yu, X.; Li, Y.; Glass, T.E.; McGrath, J.E. Influence of chemical composition and sequence length on the transport properties of proton exchange membranes. *Journal of Polymer Science Part B: Polymer Physics* **2006**, *44*, 2226-2239.
51. Teixeira, F.C.; de Sá, A.I.; Teixeira, A.P.; Rangel, C.M. Nafion phosphonic acid composite membranes for proton exchange membranes fuel cells. *Applied Surface Science* **2019**, *487*, 889-897.
52. Wu, H.; Wu, X.; Wu, Q.; Yan, W. High performance proton-conducting composite based on vanadium-substituted Dawson-type heteropoly acid for proton exchange membranes. *Composites Science and Technology* **2018**, *162*, 1-6.
53. Oh, K.; Kwon, O.; Son, B.; Lee, D.H.; Shanmugam, S. Nafion-sulfonated silica composite membrane for proton exchange membrane fuel cells under operating low humidity condition. *Journal of Membrane Science* **2019**, *583*, 103-109.
54. Zhang, J.; Xiang, Y.; Lu, S.; Jiang, S.P. High temperature polymer electrolyte membrane fuel cells for integrated fuel cell–methanol reformer power systems: a critical review. *Advanced Sustainable Systems* **2018**, *2*, 1700184.
55. Jung, H.-Y.; Kim, J.W. Role of the glass transition temperature of Nafion 117 membrane in the preparation of the membrane electrode assembly in a direct methanol fuel cell (DMFC). *International Journal of Hydrogen Energy* **2012**, *37*, 12580-12585.
56. Zarrin, H.; Higgins, D.; Jun, Y.; Chen, Z.; Fowler, M. Functionalized graphene oxide nanocomposite membrane for low humidity and high temperature proton exchange membrane fuel cells. *The Journal of Physical Chemistry C* **2011**, *115*, 20774-20781.
57. Jun, Y.; Zarrin, H.; Fowler, M.; Chen, Z. Functionalized titania nanotube composite membranes for high temperature proton exchange membrane fuel cells. *international journal of hydrogen energy* **2011**, *36*, 6073-6081.
58. Boutsika, L.G.; Enotiadis, A.; Nicotera, I.; Simari, C.; Charalambopoulou, G.; Giannelis, E.P.; Steriotis, T. Nafion® nanocomposite membranes with enhanced properties at high temperature and low humidity environments. *International Journal of Hydrogen Energy* **2016**, *41*, 22406-22414.
59. Sacca, A.; Gatto, I.; Carbone, A.; Pedicini, R.; Passalacqua, E. ZrO2–Nafion composite membranes for polymer electrolyte fuel cells (PEFCs) at intermediate temperature. *Journal of power sources* **2006**, *163*, 47-51.
60. Amjadi, M.; Rowshanzamir, S.; Peighambardoust, S.; Hosseini, M.; Eikani, M. Investigation of physical properties and cell performance of Nafion/TiO2 nanocomposite membranes for high temperature PEM fuel cells. *International Journal of Hydrogen Energy* **2010**, *35*, 9252-9260.

61. Amjadi, M.; Rowshanzamir, S.; Peighambardoust, S.; Sedghi, S. Preparation, characterization and cell performance of durable nafion/SiO2 hybrid membrane for high-temperature polymeric fuel cells. *Journal of Power Sources* **2012**, *210*, 350-357.
62. Esmaeilifar, A.; Yazdanpour, M.; Rowshanzamir, S.; Eikani, M.H. Hydrothermal synthesis of Pt/MWCNTs nanocomposite electrocatalysts for proton exchange membrane fuel cell systems. *international journal of hydrogen energy* **2011**, *36*, 5500-5511.
63. Hooshyari, K.; Javanbakht, M.; Shabanikia, A.; Enhessari, M. Fabrication BaZrO3/PBI-based nanocomposite as a new proton conducting membrane for high temperature proton exchange membrane fuel cells. *Journal of Power Sources* **2015**, *276*, 62-72.
64. Mossayebi, Z.; Saririchi, T.; Rowshanzamir, S.; Parnian, M.J. Investigation and optimization of physicochemical properties of sulfated zirconia/sulfonated poly (ether ether ketone) nanocomposite membranes for medium temperature proton exchange membrane fuel cells. *international journal of hydrogen energy* **2016**, *41*, 12293-12306.
65. Guhan, S.; Muruganantham, R.; Sangeetha, D. Development of a solid polymer electrolyte membrane based on sulfonated poly (ether ether) ketone and polysulfone for fuel cell applications. *Canadian Journal of Chemistry* **2012**, *90*, 205-213.
66. Ibrahim, A.; Hossain, O.; Chaggar, J.; Steinberger-Wilckens, R.; El-Kharouf, A. GO-nafion composite membrane development for enabling intermediate temperature operation of polymer electrolyte fuel cell. *International Journal of Hydrogen Energy* **2020**, *45*, 5526-5534.
67. Cozzi, D.; de Bonis, C.; D'Epifanio, A.; Mecheri, B.; Tavares, A.C.; Licoccia, S. Organically functionalized titanium oxide/Nafion composite proton exchange membranes for fuel cells applications. *Journal of power sources* **2014**, *248*, 1127-1132.
68. Haque, M.A.; Sulong, A.; Loh, K.; Majlan, E.H.; Husaini, T.; Rosli, R.E. Acid doped polybenzimidazoles based membrane electrode assembly for high temperature proton exchange membrane fuel cell: A review. *International Journal of Hydrogen Energy* **2017**, *42*, 9156-9179.
69. Yang, Y.; Gao, H.; Zheng, L. Anhydrous proton exchange membranes at elevated temperatures: effect of protic ionic liquids and crosslinker on proton conductivity. *Rsc Advances* **2015**, *5*, 17683-17689.
70. Li, J.; Wang, S.; Liu, F.; Tian, X.; Wang, X.; Chen, H.; Mao, T.; Wang, Z. HT-PEMs based on nitrogen-heterocycle decorated poly (arylene ether ketone) with enhanced proton conductivity and excellent stability. *International Journal of Hydrogen Energy* **2018**, *43*, 16248-16257.
71. Bai, H.; Wang, H.; Zhang, J.; Zhang, J.; Lu, S.; Xiang, Y. High temperature polymer electrolyte membrane achieved by grafting poly (1-vinylimidazole) on polysulfone for fuel cells application. *Journal of Membrane Science* **2019**, *592*, 117395.

72. Che, Q.; Chen, N.; Yu, J.; Cheng, S. Sulfonated poly (ether ether) ketone/polyurethane composites doped with phosphoric acids for proton exchange membranes. *Solid State Ionics* **2016**, *289*, 199-206.
73. Eguizábal, A.; Lemus, J.; Pina, M. On the incorporation of protic ionic liquids imbibed in large pore zeolites to polybenzimidazole membranes for high temperature proton exchange membrane fuel cells. *Journal of power sources* **2013**, *222*, 483-492.
74. Kuo, Y.-J.; Lin, H.-L. Effects of mesoporous fillers on properties of polybenzimidazole composite membranes for high-temperature polymer fuel cells. *International Journal of Hydrogen Energy* **2018**, *43*, 4448-4457.
75. Pan, J.; Wu, B.; Wu, L.; He, Y.; Miao, J.; Ge, L.; Xu, T. Proton exchange membrane from tetrazole-based poly (phthalazinone ether sulfone ketone) for high-temperature fuel cells. *international journal of hydrogen energy* **2016**, *41*, 12337-12346.
76. Moradi, M.; Moheb, A.; Javanbakht, M.; Hooshyari, K. Experimental study and modeling of proton conductivity of phosphoric acid doped PBI-Fe2TiO5 nanocomposite membranes for using in high temperature proton exchange membrane fuel cell (HT-PEMFC). *International Journal of Hydrogen Energy* **2016**, *41*, 2896-2910.
77. Bai, H.; Wang, H.; Zhang, J.; Wu, C.; Zhang, J.; Xiang, Y.; Lu, S. Simultaneously enhancing ionic conduction and mechanical strength of poly (ether sulfones)-poly (vinyl pyrrolidone) membrane by introducing graphitic carbon nitride nanosheets for high temperature proton exchange membrane fuel cell application. *Journal of Membrane Science* **2018**, *558*, 26-33.
78. Ebrahimi, M.; Van der Bruggen, B.; Hosseini, S.; Askari, M.; Nemati, M. Improving electrochemical properties of cation exchange membranes by using activated carbon-co-chitosan composite nanoparticles in water deionization. *Ionics* **2019**, *25*, 1199-1214.
79. Amde, M.; Liu, J.-F.; Pang, L. Environmental application, fate, effects, and concerns of ionic liquids: a review. *Environmental science & technology* **2015**, *49*, 12611-12627.
80. Vekariya, R.L. A review of ionic liquids: Applications towards catalytic organic transformations. *Journal of Molecular Liquids* **2017**, *227*, 44-60.
81. Kaur, G.; Kumar, H.; Singla, M. Diverse applications of ionic liquids: A comprehensive review. *Journal of Molecular Liquids* **2022**, *351*, 118556.
82. Friess, K.; Izák, P.; Kárászová, M.; Pasichnyk, M.; Lanč, M.; Nikolaeva, D.; Luis, P.; Jansen, J.C. A review on ionic liquid gas separation membranes. *Membranes* **2021**, *11*, 97.
83. Zhou, J.; Sui, H.; Jia, Z.; Yang, Z.; He, L.; Li, X. Recovery and purification of ionic liquids from solutions: a review. *Rsc Advances* **2018**, *8*, 32832-32864.

84. Wang, L.; Morales-Collazo, O.; Brennecke, J.F.; Jia, H. Dimeric ionic liquid for improving performance and durability of PEMFCs. *Journal of Power Sources* **2023**, *556*, 232488.
85. de Jesus, S.S.; Maciel Filho, R. Are ionic liquids eco-friendly? *Renewable and Sustainable Energy Reviews* **2022**, *157*, 112039.
86. Mirzaei-Saatlo, M.; Asghari, E.; Shekaari, H.; Pollet, B.; Vinodh, R. Performance of ethanolamine-based ionic liquids as novel green electrolytes for the electrochemical energy storage applications. *Electrochimica Acta* **2023**, 143499.
87. Hagiwara, R.; Lee, J.S. Ionic liquids for electrochemical devices. *Electrochemistry* **2007**, *75*, 23-34.
88. Ghandi, K. A review of ionic liquids, their limits and applications. *Green and sustainable chemistry* **2014**, *2014*.
89. Hajipour, A.; Rafiee, F. Basic ionic liquids. A short review. *Journal of the Iranian Chemical Society* **2009**, *6*, 647-678.
90. Lin, I.J.; Vasam, C.S. Metal-containing ionic liquids and ionic liquid crystals based on imidazolium moiety. *Journal of organometallic chemistry* **2005**, *690*, 3498-3512.
91. Liu, Z.; Hu, P.; Meng, X.; Zhang, R.; Yue, H.; Xu, C.; Hu, Y. Synthesis and properties of switchable polarity ionic liquids based on organic superbases and fluoroalcohols. *Chemical Engineering Science* **2014**, *108*, 176-182.
92. Mehnert, C.P. Supported ionic liquid catalysis. *Chemistry–A European Journal* **2005**, *11*, 50-56.
93. Neto, B.A.; Lapis, A.A.; Souza, R.Y. Task-Specific Ionic Liquids: Design, Properties, and Applications. *Encyclopedia of Ionic Liquids* **2023**, 1273-1283.
94. Pernak, J.; Łęgosz, B.; Klejdysz, T.; Marcinkowska, K.; Rogowski, J.; Kurasiak-Popowska, D.; Stuper-Szablewska, K. Ammonium bio-ionic liquids based on camelina oil as potential novel agrochemicals. *RSC advances* **2018**, *8*, 28676-28683.
95. Ratti, R. Ionic liquids: synthesis and applications in catalysis. *Adv. Chem* **2014**, *2014*, 1-16.
96. Yuan, J.; Mecerreyes, D.; Antonietti, M. Poly (ionic liquid) s: An update. *Progress in Polymer Science* **2013**, *38*, 1009-1036.
97. Zhang, Q.; Shreeve, J.n.M. Energetic ionic liquids as explosives and propellant fuels: a new journey of ionic liquid chemistry. *Chemical reviews* **2014**, *114*, 10527-10574.
98. Kumer, A.; Khan, M.W. Synthesis, characterization, antimicrobial activity and computational exploration of ortho toludinium carboxylate ionic liquids. *Journal of Molecular Structure* **2021**, *1245*, 131087.
99. McIntosh, A.J.; Griffith, J.; Gräsvik, J. Methods of synthesis and purification of ionic liquids. In *Application, Purification, and Recovery of Ionic Liquids*; Elsevier: 2016; pp. 59-99.

100. Ferraz, R.; Prudencio, C.; Vieira, M.; Fernandes, R.; Noronha, J.P.; Petrovski, Z. Ionic liquids synthesis–methodologies. *Organic Chemistry Current Research* **2015**, *4*.
101. Bao, X.; Zhang, F.; Liu, Q. Sulfonated poly (2, 5-benzimidazole)(ABPBI)/MMT/ionic liquids composite membranes for high temperature PEM applications. *international journal of hydrogen energy* **2015**, *40*, 16767-16774.
102. Fang, J.; Lyu, M.; Wang, X.; Wu, Y.; Zhao, J. Synthesis and performance of novel anion exchange membranes based on imidazolium ionic liquids for alkaline fuel cell applications. *Journal of Power Sources* **2015**, *284*, 517-523.
103. Hooshyari, K.; Javanbakht, M.; Adibi, M. Novel composite membranes based on dicationic ionic liquid and polybenzimidazole mixtures as strategy for enhancing thermal and electrochemical properties of proton exchange membrane fuel cells applications at high temperature. *International Journal of Hydrogen Energy* **2016**, *41*, 10870-10883.
104. Lin, B.; Qiao, G.; Chu, F.; Zhang, S.; Yuan, N.; Ding, J. Phosphoric acid doped hydrophobic ionic liquid-based composite membranes for anhydrous proton exchange membrane application. *RSC advances* **2017**, *7*, 1056-1061.
105. Maiti, J.; Kakati, N.; Woo, S.P.; Yoon, Y.S. Nafion® based hybrid composite membrane containing GO and dihydrogen phosphate functionalized ionic liquid for high temperature polymer electrolyte membrane fuel cell. *Composites Science and Technology* **2018**, *155*, 189-196.
106. Elumalai, V.; Sangeetha, D. Synergic effect of ionic liquid grafted titanate nanotubes on the performance of anion exchange membrane fuel cell. *Journal of Power Sources* **2019**, *412*, 586-596.
107. Elumalai, V.; Dharmalingam, S. Synthesis characterization and performance evaluation of ionic liquid immobilized SBA-15/quaternised polysulfone composite membrane for alkaline fuel cell. *Microporous and Mesoporous Materials* **2016**, *236*, 260-268.
108. Hernández-Fernández, F.; de los Ríos, A.P.; Mateo-Ramírez, F.; Juarez, M.; Lozano-Blanco, L.; Godínez, C. New application of polymer inclusion membrane based on ionic liquids as proton exchange membrane in microbial fuel cell. *Separation and Purification Technology* **2016**, *160*, 51-58.
109. Hernández-Fernández, F.; de los Ríos, A.P.; Mateo-Ramírez, F.; Godínez, C.; Lozano-Blanco, L.; Moreno, J.; Tomás-Alonso, F. New application of supported ionic liquids membranes as proton exchange membranes in microbial fuel cell for waste water treatment. *Chemical Engineering Journal* **2015**, *279*, 115-119.
110. Guerreiro da Trindade, L.; Regina Becker, M.; Celso, F.; Petzhold, C.L.; Martini, E.M.; de Souza, R.F. Modification of sulfonated poly (ether ether ketone) membranes by impregnation with the

ionic liquid 1-butyl-3-methylimidazolium tetrafluoroborate for proton exchange membrane fuel cell applications. *Polymer Engineering & Science* **2016**, *56*, 1037-1044.

111. Yang, J.; Che, Q.; Zhou, L.; He, R.; Savinell, R.F. Studies of a high temperature proton exchange membrane based on incorporating an ionic liquid cation 1-butyl-3-methylimidazolium into a Nafion matrix. *Electrochimica Acta* **2011**, *56*, 5940-5946.
112. Wang, S.; Li, Q.; Wang, F. Preparation and properties of sulfonated poly (2, 6-dimethyl-1, 4-phenylene oxide)/ionic liquid/phosphoric acid high temperature proton exchange composite membrane. *Polymer-Plastics Technology and Materials* **2021**, *60*, 650-658.
113. Ebrahimi, M.; Fatyeyeva, K.; Kujawski, W. Different Approaches for the Preparation of Composite Ionic Liquid-Based Membranes for Proton Exchange Membrane Fuel Cell Applications—Recent Advancements. *Membranes* **2023**, *13*, 593.
114. da Trindade, L.G.; Zanchet, L.; Souza, J.C.; Leite, E.R.; Martini, E.M.A.; Pereira, E.C. Enhancement of sulfonated poly (ether ether ketone)-based proton exchange membranes doped with different ionic liquids cations. *Ionics* **2020**, *26*, 5661-5672.
115. Elumalai, V.; Ganesh, T.; Selvakumar, C.; Sangeetha, D. Phosphonate ionic liquid immobilised SBA-15/SPEEK composite membranes for high temperature proton exchange membrane fuel cells. *Materials Science for Energy Technologies* **2018**, *1*, 196-204.
116. Rogalsky, S.; Bardeau, J.-F.; Makhno, S.; Tarasyuk, O.; Babkina, N.; Cherniavska, T.; Filonenko, M.; Fatyeyeva, K. New polymer electrolyte membrane for medium-temperature fuel cell applications based on cross-linked polyimide Matrimid and hydrophobic protic ionic liquid. *Materials Today Chemistry* **2021**, *20*, 100453.
117. Fatyeyeva, K.; Rogalsky, S.; Makhno, S.; Tarasyuk, O.; Soto Puente, J.A.; Marais, S. Polyimide/ionic liquid composite membranes for middle and high temperature fuel cell application: Water sorption behavior and proton conductivity. *Membranes* **2020**, *10*, 82.
118. Kobzar, Y.L.; Azzouz, G.; Albadri, H.; Levillain, J.; Dez, I.; Gaumont, A.-C.; Lecamp, L.; Chappey, C.; Marais, S.; Fatyeyeva, K. Novel Ionic Conducting Composite Membrane Based on Polymerizable Ionic Liquids. *Polymers* **2021**, *13*, 3704.
119. Kobzar, Y.; Fatyeyeva, K.; Lobko, Y.; Yakovlev, Y.; Hrbek, T.; Marais, S. New ionic liquid-based polyoxadiazole electrolytes for hydrogen middle-and high-temperature fuel cells. *Journal of Membrane Science* **2021**, *640*, 119774.
120. Liu, F.; Wang, S.; Wang, D.; Liu, G.; Cui, Y.; Liang, D.; Wang, X.; Yong, Z.; Wang, Z. Multifunctional poly (ionic liquid) s cross-linked polybenzimidazole membrane with excellent long-term stability for high temperature-proton exchange membranes fuel cells. *Journal of Power Sources* **2021**, *494*, 229732.

121. Chen, H.; Wang, S.; Li, J.; Liu, F.; Tian, X.; Wang, X.; Mao, T.; Xu, J.; Wang, Z. Novel cross-linked membranes based on polybenzimidazole and polymeric ionic liquid with improved proton conductivity for HT-PEMFC applications. *Journal of the Taiwan Institute of Chemical Engineers* **2019**, *95*, 185-194.
122. Ceynowa, J.; Adamczak, P. Enzyme membrane based upon polyamide-6 for oil hydrolysis. *Journal of applied polymer science* **1992**, *46*, 749-755.
123. Singh, S.; Khulbe, K.; Matsuura, T.; Ramamurthy, P. Membrane characterization by solute transport and atomic force microscopy. *Journal of Membrane Science* **1998**, *142*, 111-127.
124. Hosseini, S.M.; Moradi, F.; Farahani, S.K.; Bandehali, S.; Parvizian, F.; Ebrahimi, M.; Shen, J. Carbon nanofibers/chitosan nanocomposite thin film for surface modification of poly (ether sulphone) nanofiltration membrane. *Materials Chemistry and Physics* **2021**, *269*, 124720.
125. da Trindade, L.G.; Borba, K.M.; Zanchet, L.; Lima, D.W.; Trench, A.B.; Rey, F.; Diaz, U.; Longo, E.; Bernardo-Gusmão, K.; Martini, E.M. SPEEK-based proton exchange membranes modified with MOF-encapsulated ionic liquid. *Materials Chemistry and Physics* **2019**, *236*, 121792.
126. Baek, Y.; Kang, J.; Theato, P.; Yoon, J. Measuring hydrophilicity of RO membranes by contact angles via sessile drop and captive bubble method: A comparative study. *Desalination* **2012**, *303*, 23-28.
127. Zhao, Y.; Wu, M.; Shen, P.; Uytterhoeven, C.; Mamrol, N.; Shen, J.; Gao, C.; Van der Bruggen, B. Composite anti-scaling membrane made of interpenetrating networks of nanofibers for selective separation of lithium. *Journal of Membrane Science* **2021**, *618*, 118668.
128. Letellier, P.; Mayaffre, A.; Turmine, M. Drop size effect on contact angle explained by nonextensive thermodynamics. Young's equation revisited. *Journal of colloid and interface science* **2007**, *314*, 604-614.
129. Kubiak, K.; Wilson, M.; Mathia, T.; Carval, P. Wettability versus roughness of engineering surfaces. *Wear* **2011**, *271*, 523-528.
130. George, J.E.; Chidangil, S.; George, S.D. Recent progress in fabricating superaerophobic and superaerophilic surfaces. *Advanced Materials Interfaces* **2017**, *4*, 1601088.
131. Mulder, M. *Basic principles of membrane technology*; Springer science & business media: 1996.
132. Kujawski, W.; Adamczak, P.; Narebska, A. A fully automated system for the determination of pore size distribution in microfiltration and ultrafiltration membranes. *Separation Science and Technology* **1989**, *24*, 495-506.
133. Szczerbińska, J.; Kujawski, W.; Arszyńska, J.M.; Kujawa, J. Assessment of air-gap membrane distillation with hydrophobic porous membranes utilized for damaged paintings humidification. *Journal of Membrane Science* **2017**, *538*, 1-8.

134. Hernández, A.; Calvo, J.; Prádanos, P.; Tejerina, F. Pore size distributions in microporous membranes. A critical analysis of the bubble point extended method. *Journal of Membrane Science* **1996**, *112*, 1-12.

135. Kujawa, J.; Chrzanowska, E.; Kujawski, W. Transport properties and fouling issues of membranes utilized for the concentration of dairy products by air-gap membrane distillation and microfiltration. *Chemical Papers* **2019**, *73*, 565-582.

136. Guo, Z.; Xiu, R.; Lu, S.; Xu, X.; Yang, S.; Xiang, Y. Submicro-pore containing poly (ether sulfones)/polyvinylpyrrolidone membranes for high-temperature fuel cell applications. *Journal of Materials Chemistry A* **2015**, *3*, 8847-8854.

137. Jakubowska, E.; Gierszewska, M.; Nowaczyk, J.; Olewnik-Kruszkowska, E. Physicochemical and storage properties of chitosan-based films plasticized with deep eutectic solvent. *Food Hydrocolloids* **2020**, *108*, 106007.

138. Gierszewska, M.; Jakubowska, E.; Olewnik-Kruszkowska, E. Effect of chemical crosslinking on properties of chitosan-montmorillonite composites. *Polymer Testing* **2019**, *77*, 105872.

139. Ebrahimi, M.; Kujawski, W.; Fatyeyeva, K. Fabrication of Polyamide-6 membranes—The effect of gelation time towards their morphological, physical and transport properties. *Membranes* **2022**, *12*, 315.

140. Colpan, C.O.; Nalbant, Y.; Ercelik, M. 4.28 Fundamentals of Fuel Cell Technologies. In *Comprehensive Energy Systems*, Dincer, I., Ed.; Elsevier: Oxford, 2018; pp. 1107-1130.

141. Jain, R.K. Chapter 2 - Development of different types of ionic polymer metal composite-based soft actuators for robotics and biomimetic applications. In *Soft Robotics in Rehabilitation*, Jafari, A., Ebrahimi, N., Eds.; Academic Press: 2021; pp. 39-87.

142. Dahi, A.; Fatyeyeva, K.; Langevin, D.; Chappey, C.; Rogalsky, S.P.; Tarasyuk, O.P.; Marais, S. Polyimide/ionic liquid composite membranes for fuel cells operating at high temperatures. *Electrochimica Acta* **2014**, *130*, 830-840.

143. Li, Y.; Zhang, M.; Wang, X.; Li, Z.; Zhao, L. Anhydrous conducting composite membranes composed of SPEEK/silica/ionic liquids for high-temperature proton exchange. *Electrochimica Acta* **2016**, *222*, 1308-1315.

144. Jothi, P.R.; Dharmalingam, S. An efficient proton conducting electrolyte membrane for high temperature fuel cell in aqueous-free medium. *Journal of membrane science* **2014**, *450*, 389-396.

145. Malik, R.S.; Tripathi, S.N.; Gupta, D.; Choudhary, V. Novel anhydrous composite membranes based on sulfonated poly (ether ketone) and aprotic ionic liquids for high temperature polymer electrolyte membranes for fuel cell applications. *International journal of hydrogen energy* **2014**, *39*, 12826-12834.

146. Fernicola, A.; Panero, S.; Scrosati, B. Proton-conducting membranes based on protic ionic liquids. *Journal of Power Sources* **2008**, *178*, 591-595.

147. Cao, Y.; Mu, T. Comprehensive investigation on the thermal stability of 66 ionic liquids by thermogravimetric analysis. *Industrial & engineering chemistry research* **2014**, *53*, 8651-8664.

148. Flieger, J.; Feder-Kubis, J.; Tatarczak-Michalewska, M. Chiral ionic liquids: Structural diversity, properties and applications in selected separation techniques. *International journal of molecular sciences* **2020**, *21*, 4253.

149. Prykhodko, Y.; Martin, A.; Oulyadi, H.; Kobzar, Y.L.; Marais, S.; Fatyeyeva, K. Imidazolium-based protic ionic liquids with perfluorinated anions: Influence of chemical structure on thermal properties. *Journal of Molecular Liquids* **2022**, *345*, 117782.

150. Rogalsky, S.; Tarasyuk, O.; Vashchuk, A.; Dzhuzha, O.; Cherniavska, T.; Makhno, S. Thermophysical properties and ionic conductivity of new imidazolium-based protic ionic liquids. *Journal of Molecular Liquids* **2023**, *382*, 121942.

151. Parker, F.S. Infrared spectroscopy in biochemistry, biology, and medicine. *Plennum Press, New York, chapters* **1971**, *6*, 8.

152. Gigant, N. Triflic Acid. *Synlett* **2013**, *24*, 399-400.

153. Boutonnet, J.C.; Bingham, P.; Calamari, D.; Rooij, C.d.; Franklin, J.; Kawano, T.; Libre, J.-M.; McCul-Loch, A.; Malinverno, G.; Odom, J.M. Environmental risk assessment of trifluoroacetic acid. *Human and Ecological Risk Assessment: An International Journal* **1999**, *5*, 59-124.

154. Azizi, D.; Larachi, F.; Latifi, M. Ionic-liquid collectors for rare-earth minerals flotation□ Case of tetrabutylammonium bis (2-ethylhexyl)-phosphate for monazite and bastnäsite recovery. *Colloids and Surfaces A: Physicochemical and Engineering Aspects* **2016**, *506*, 74-86.

155. Shin, Y.-R.; Jung, S.-M.; Jeon, I.-Y.; Baek, J.-B. The oxidation mechanism of highly ordered pyrolytic graphite in a nitric acid/sulfuric acid mixture. *Carbon* **2013**, *52*, 493-498.

156. Fan, S.-C.; Wang, Y.-C.; Li, C.-L.; Lee, K.-R.; Liaw, D.-J.; Huang, H.-P.; Lai, J.-Y. Effect of coagulation media on membrane formation and vapor permeation performance of novel aromatic polyamide membrane. *Journal of membrane science* **2002**, *204*, 67-79.

157. Li, D.; Chung, T.-S.; Ren, J.; Wang, R. Thickness dependence of macrovoid evolution in wet phase-inversion asymmetric membranes. *Industrial & engineering chemistry research* **2004**, *43*, 1553-1556.

158. See-Toh, Y.H.; Ferreira, F.C.; Livingston, A.G. The influence of membrane formation parameters on the functional performance of organic solvent nanofiltration membranes. *Journal of Membrane Science* **2007**, *299*, 236-250.

159. Vandezande, P.; Li, X.; Gevers, L.E.; Vankelecom, I.F. High throughput study of phase inversion parameters for polyimide-based SRNF membranes. *Journal of Membrane Science* **2009**, *330*, 307-318.

160. Rosa, M.; De Pinho, M. Membrane surface characterisation by contact angle measurements using the immersed method. *Journal of membrane science* **1997**, *131*, 167-180.

161. Hebbar, R.; Isloor, A.; Ismail, A. Contact angle measurements. In *Membrane characterization*; Elsevier: 2017; pp. 219-255.

162. Chan, M.; Ng, S. Effect of membrane properties on contact angle. In Proceedings of the AIP Conference Proceedings, 2018.

163. Hong, J.; He, Y. Effects of nano sized zinc oxide on the performance of PVDF microfiltration membranes. *Desalination* **2012**, *302*, 71-79.

164. Zheng, X.; Chen, F.; Zhang, X.; Zhang, H.; Li, Y.; Li, J. Ionic liquid grafted polyamide 6 as porous membrane materials: Enhanced water flux and heavy metal adsorption. *Applied Surface Science* **2019**, *481*, 1435-1441.

165. Shin, S.-J.; Kim, J.-P.; Kim, H.-J.; Jeon, J.-H.; Min, B.-R. Preparation and characterization of polyethersulfone microfiltration membranes by a 2-methoxyethanol additive. *Desalination* **2005**, *186*, 1-10.

166. Woo, S.H.; Park, J.; Min, B.R. Relationship between permeate flux and surface roughness of membranes with similar water contact angle values. *Separation and purification technology* **2015**, *146*, 187-191.

167. Luo, X.; Lau, G.; Tesfaye, M.; Arthurs, C.R.; Cordova, I.; Wang, C.; Yandrasits, M.; Kusoglu, A. Thickness dependence of proton-exchange-membrane properties. *Journal of the Electrochemical Society* **2021**, *168*, 104517.

168. Dantas, P.A.; Botaro, V.R. Synthesis and characterization of a new cellulose acetate-propionate gel: Crosslinking density determination. *Open Journal of Polymer Chemistry* **2012**, *2*, 144-151.

169. Manaf, M.E.A.; Tsuji, M.; Nobukawa, S.; Yamaguchi, M. Effect of moisture on the orientation birefringence of cellulose esters. *Polymers* **2011**, *3*, 955-966.

170. Ramesh, S.; Shanti, R.; Morris, E. Plasticizing effect of 1-allyl-3-methylimidazolium chloride in cellulose acetate based polymer electrolytes. *Carbohydrate Polymers* **2012**, *87*, 2624-2629.

171. da Trindade, L.G.; Zanchet, L.; Martins, P.C.; Borba, K.M.; Santos, R.D.; Paiva, R.d.S.; Vermeersch, L.A.; Ticianelli, E.A.; de Souza, M.O.; Martini, E.M. The influence of ionic liquids cation on the properties of sulfonated poly (ether ether ketone)/polybenzimidazole blends applied in PEMFC. *Polymer* **2019**, *179*, 121723.

172. Anantaraman, A.; Gardner, C. Studies on ion-exchange membranes. Part 1. Effect of humidity on the conductivity of Nafion®. *Journal of Electroanalytical Chemistry* **1996**, *414*, 115-120.

Annex

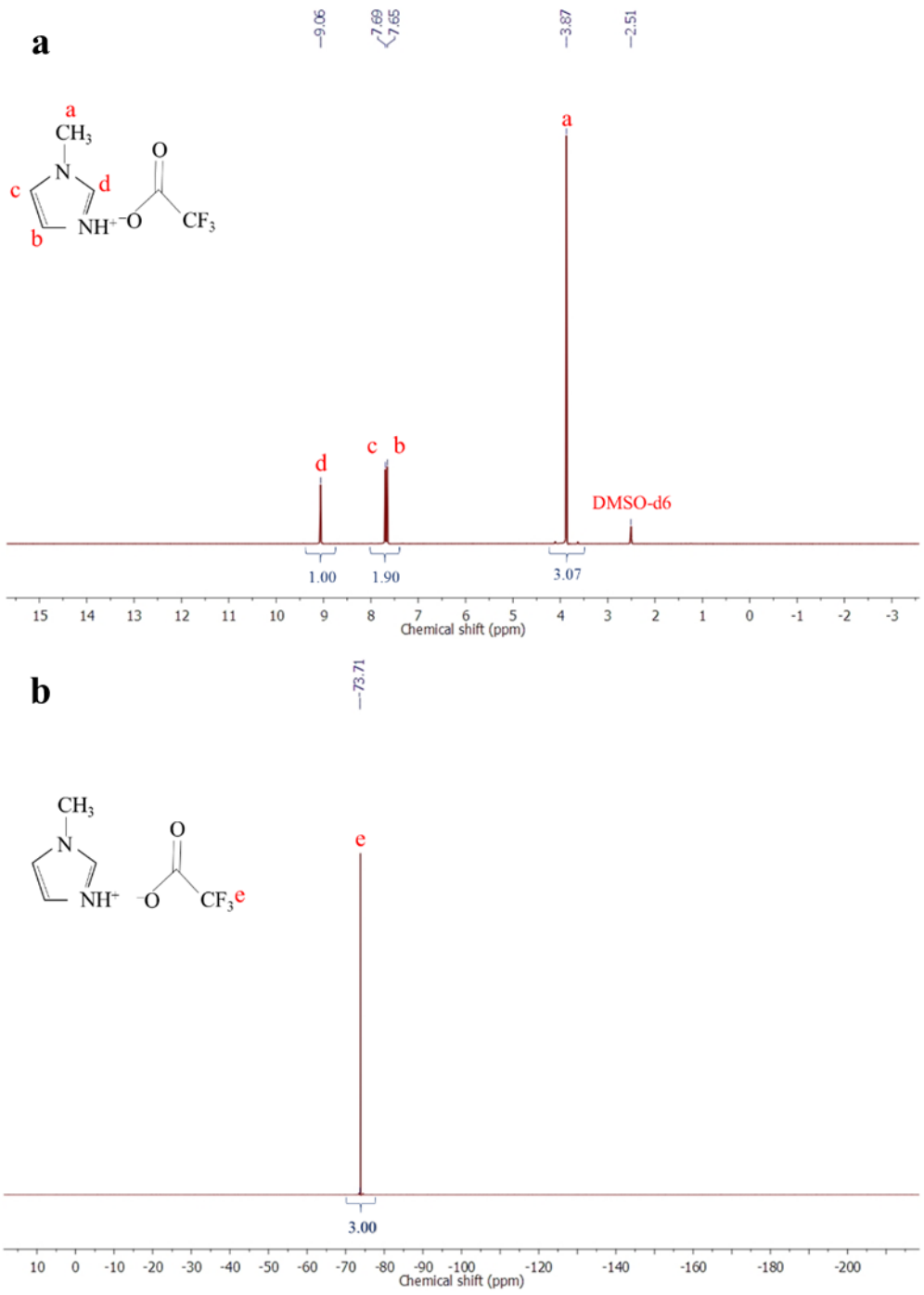

Figure S1. (a) ^{1}H NMR and (b) ^{19}F NMR spectra of [MIM][TFA].

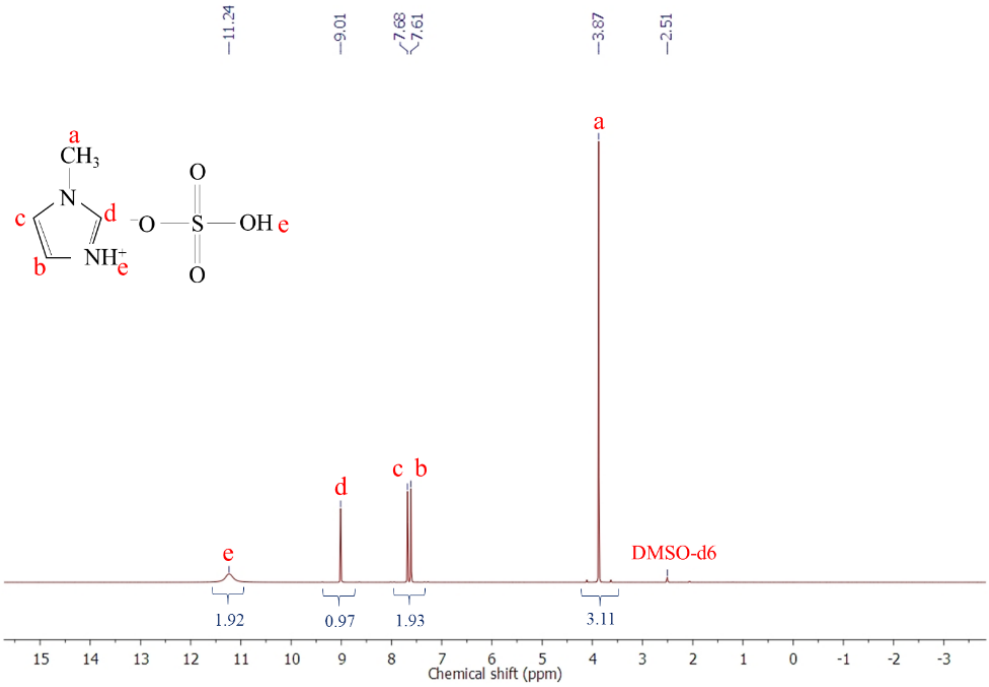

Figure S2. ^{1}H NMR spectrum of [MIM][HS].

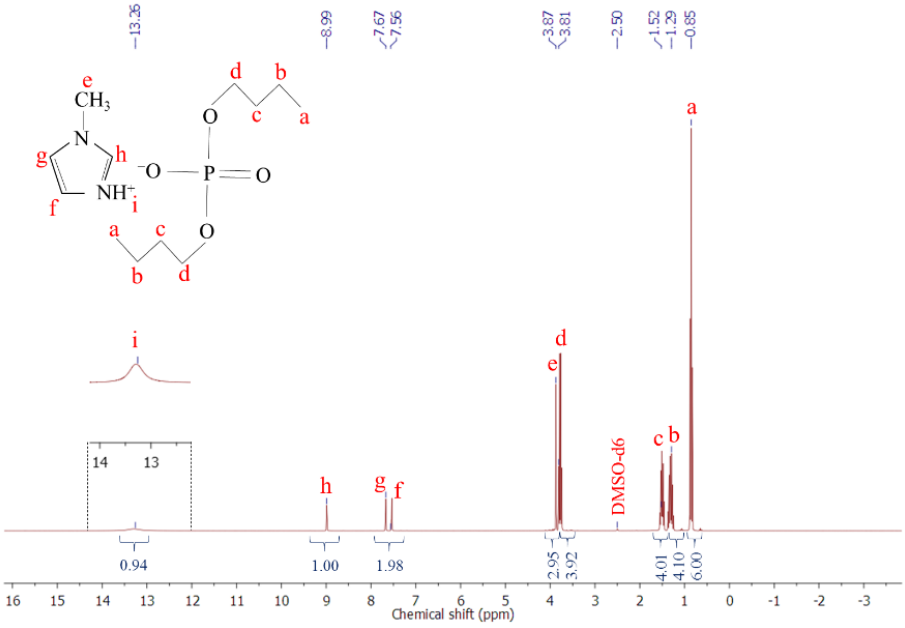

Figure S3. ^{1}H NMR spectrum of [MIM][BUPH].

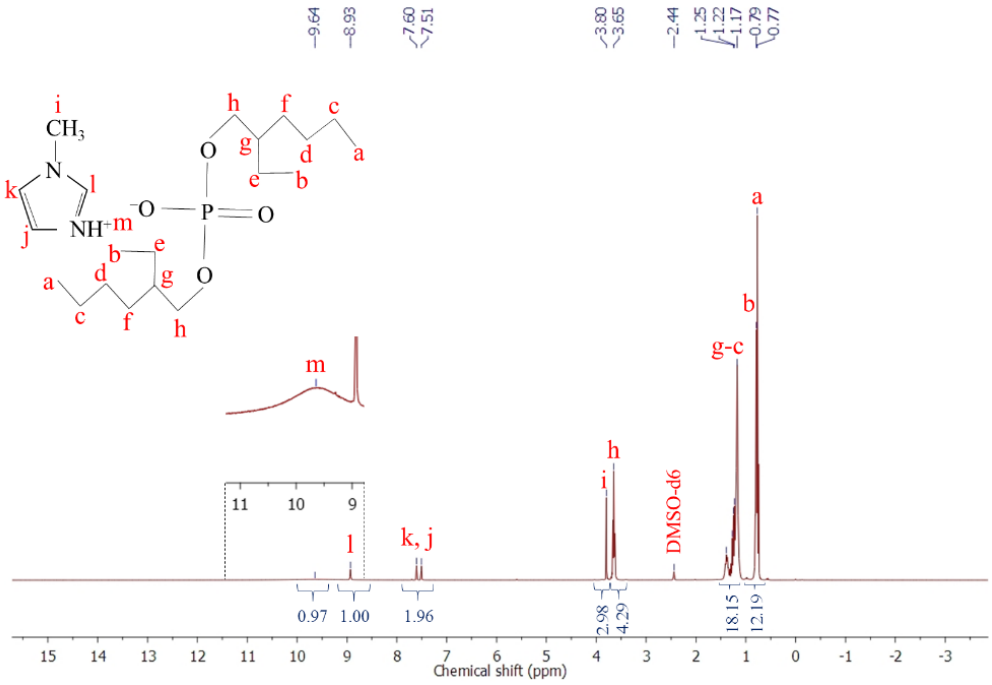

Figure S4. ^{1}H NMR spectrum of [MIM][EHPH].

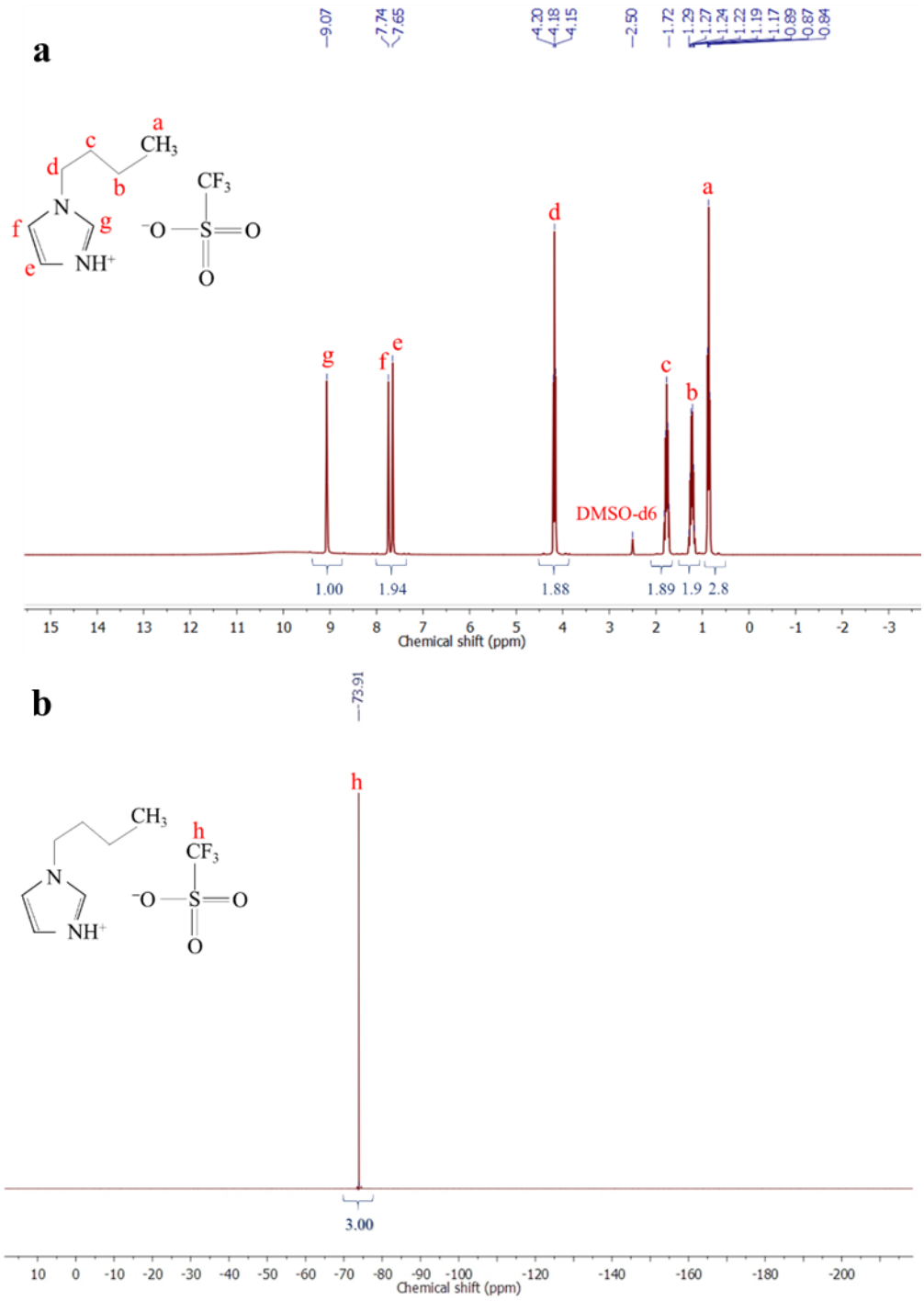

Figure S5. (a) ^{1}H NMR and (b) ^{19}F NMR spectra of [BIM][TFS].

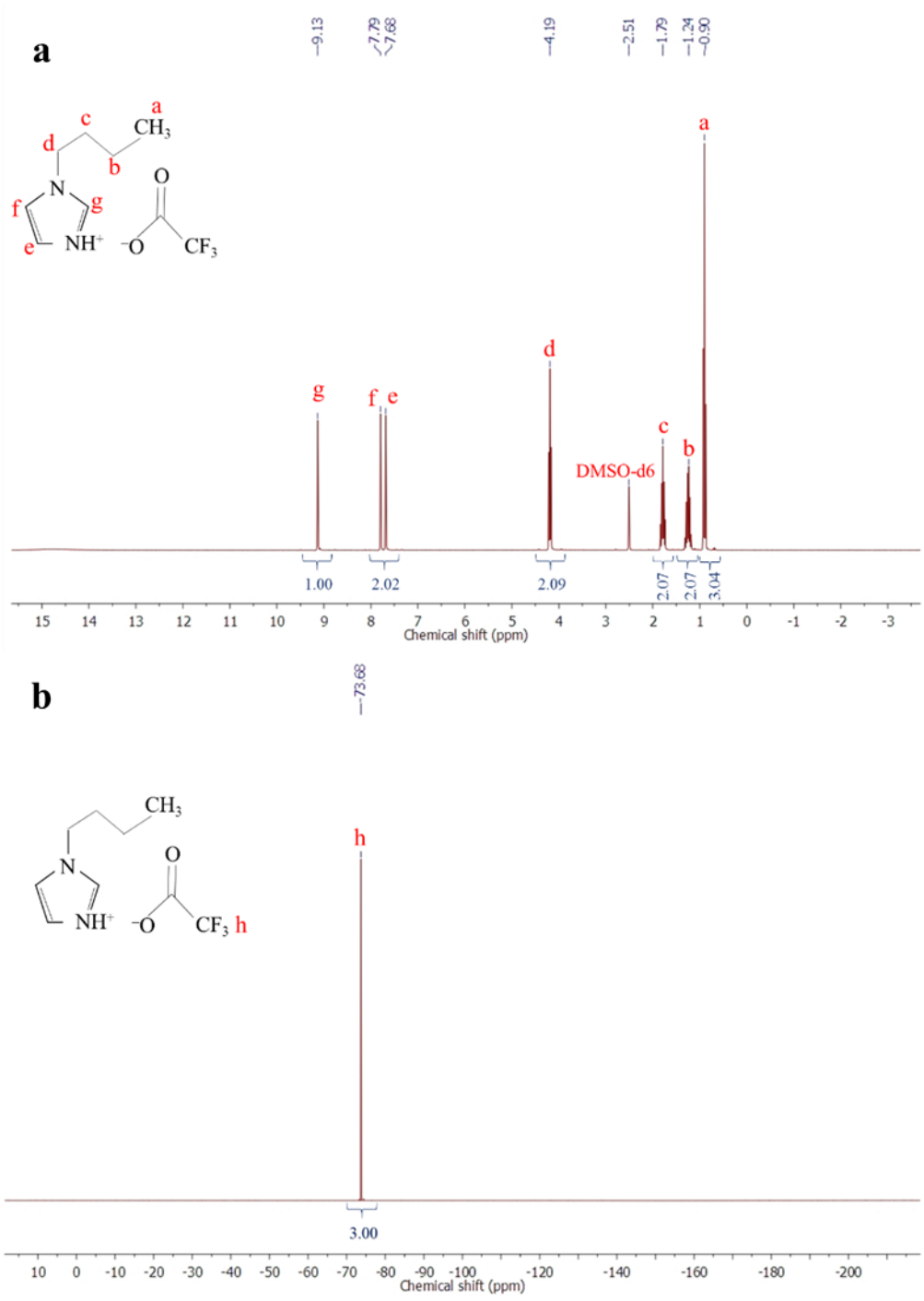

Figure S6. (a) ^{1}H NMR and (b) ^{19}F NMR spectra of [BIM][TFA].

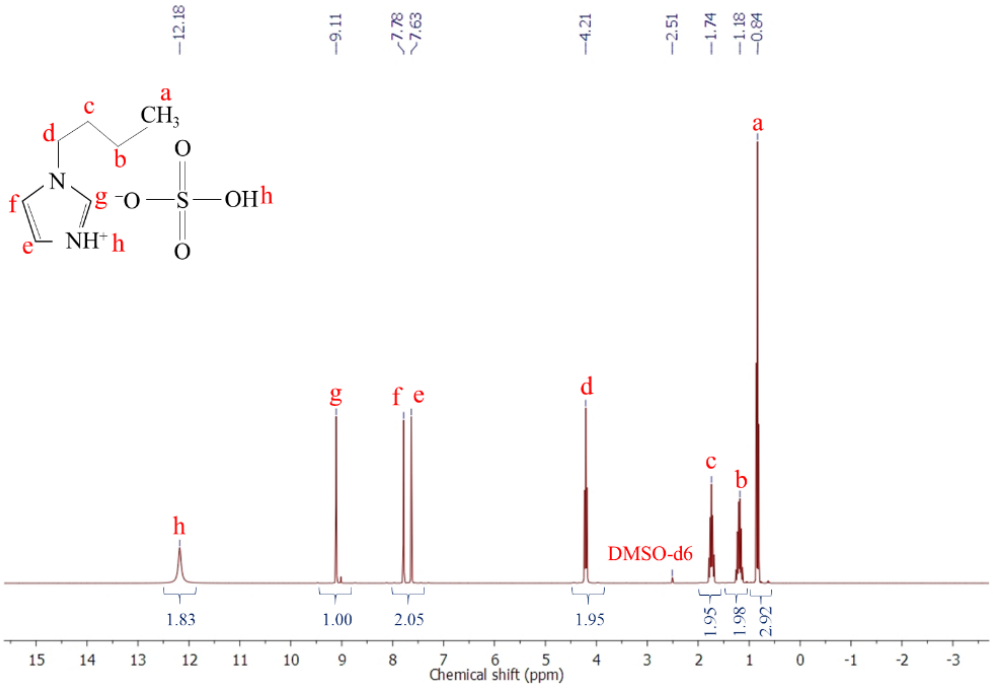

Figure S7. ^{1}H NMR spectrum of [BIM][HS].

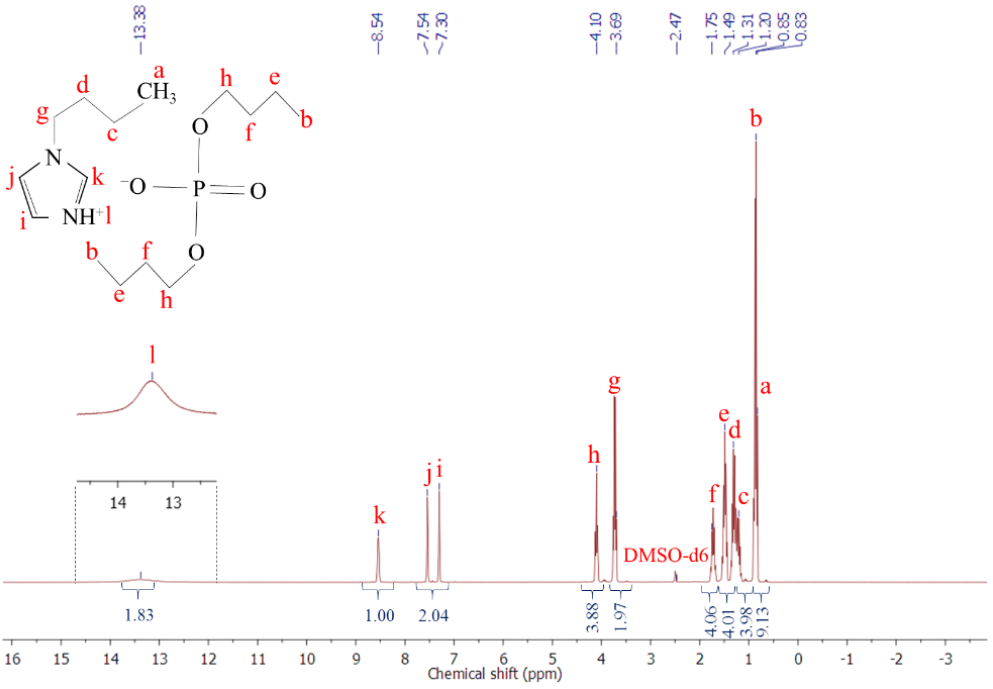

Figure S8. ^{1}H NMR spectrum of [BIM][BUPH].

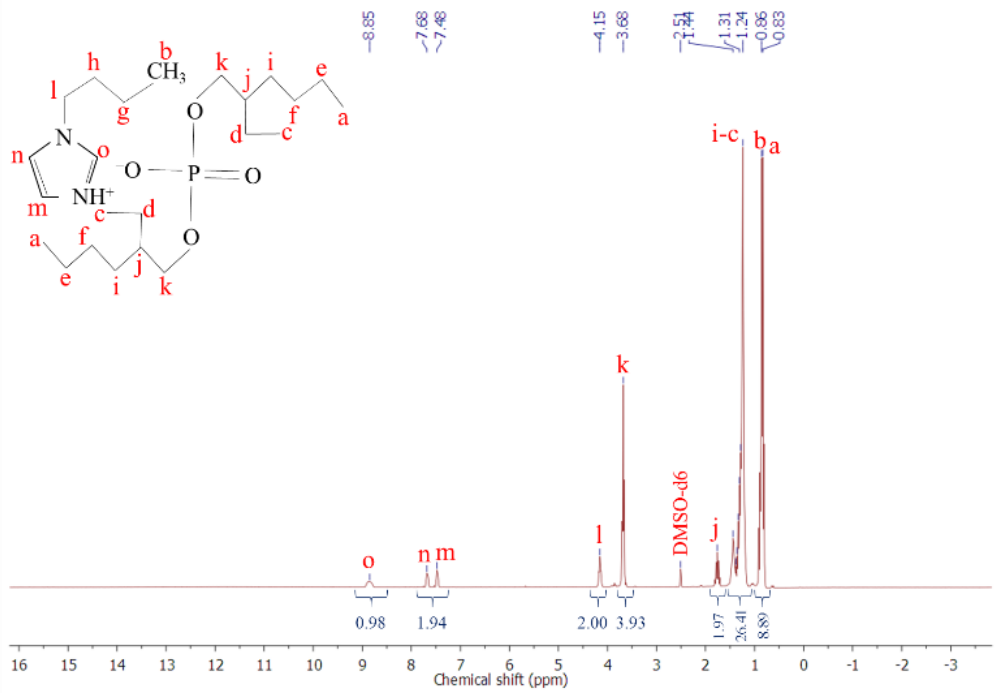

Figure S9. ^{1}H NMR spectrum of [BIM][EHPH].

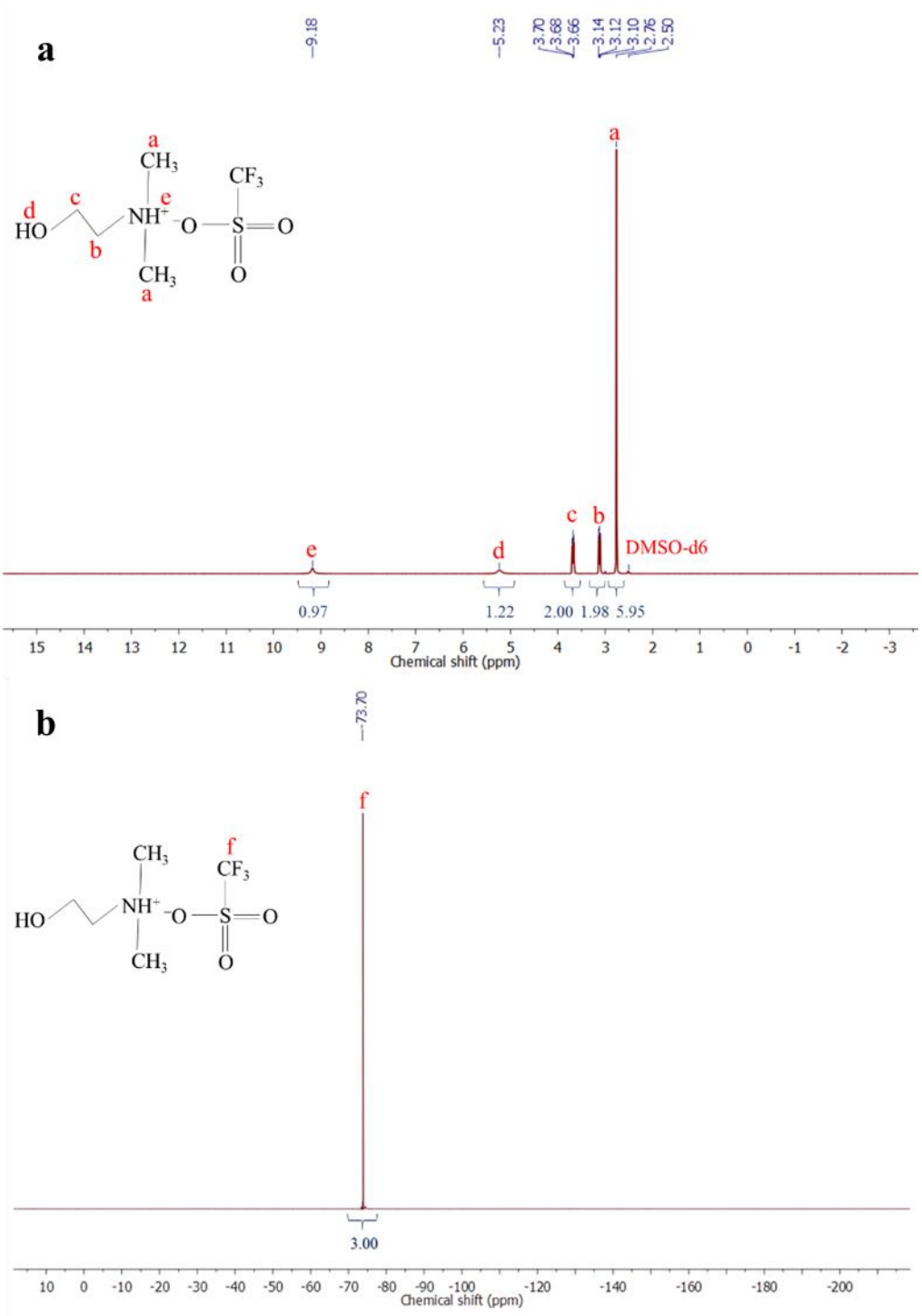

Figure S10. (a) ^{1}H NMR and (b) ^{19}F NMR spectra of [DETA][TFS].

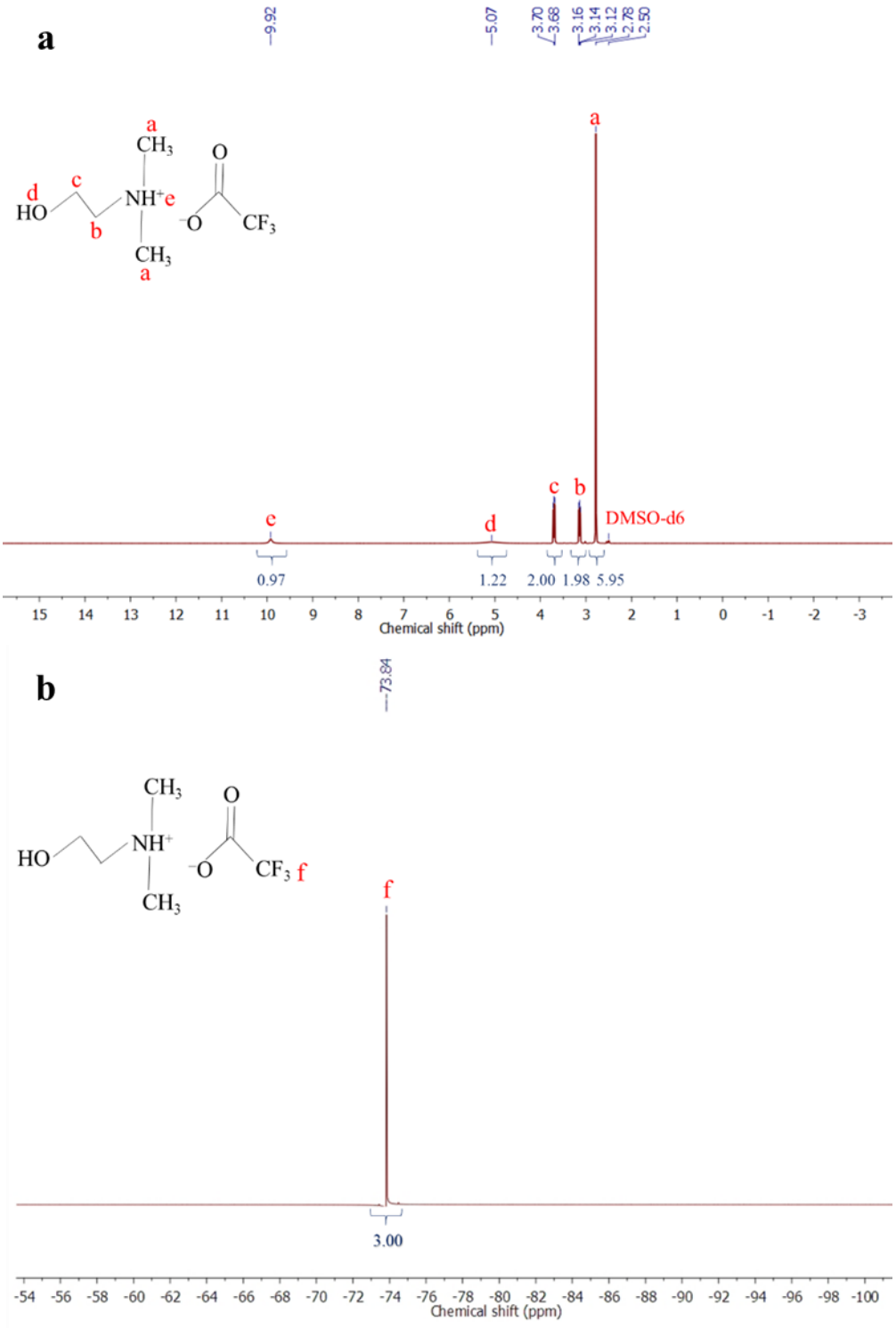

Figure S11. (a) ^{1}H NMR and (b) ^{19}F NMR spectra of [DETA][TFA].

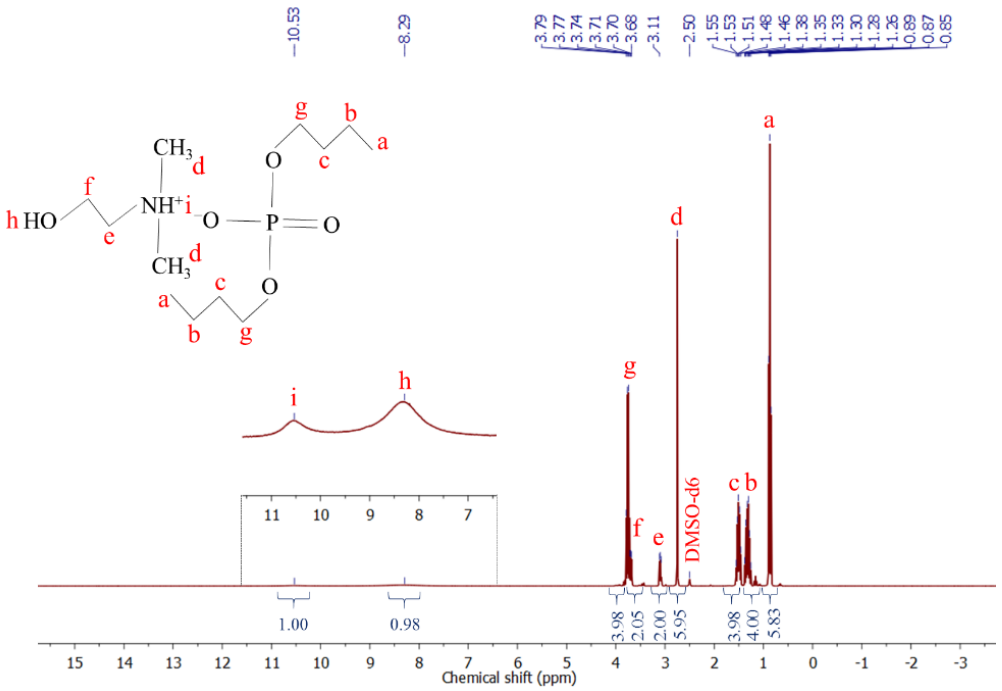

Figure S12. ^{1}H NMR spectrum of [DETA][BUPH].

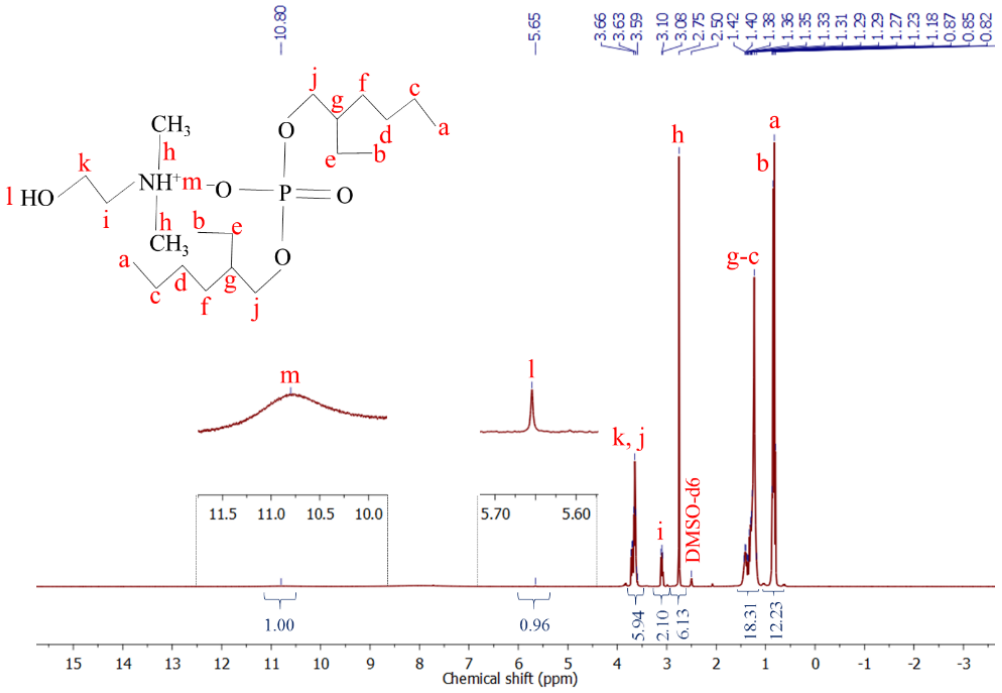

Figure S13. ^{1}H NMR spectrum of [DETA][EHPH].

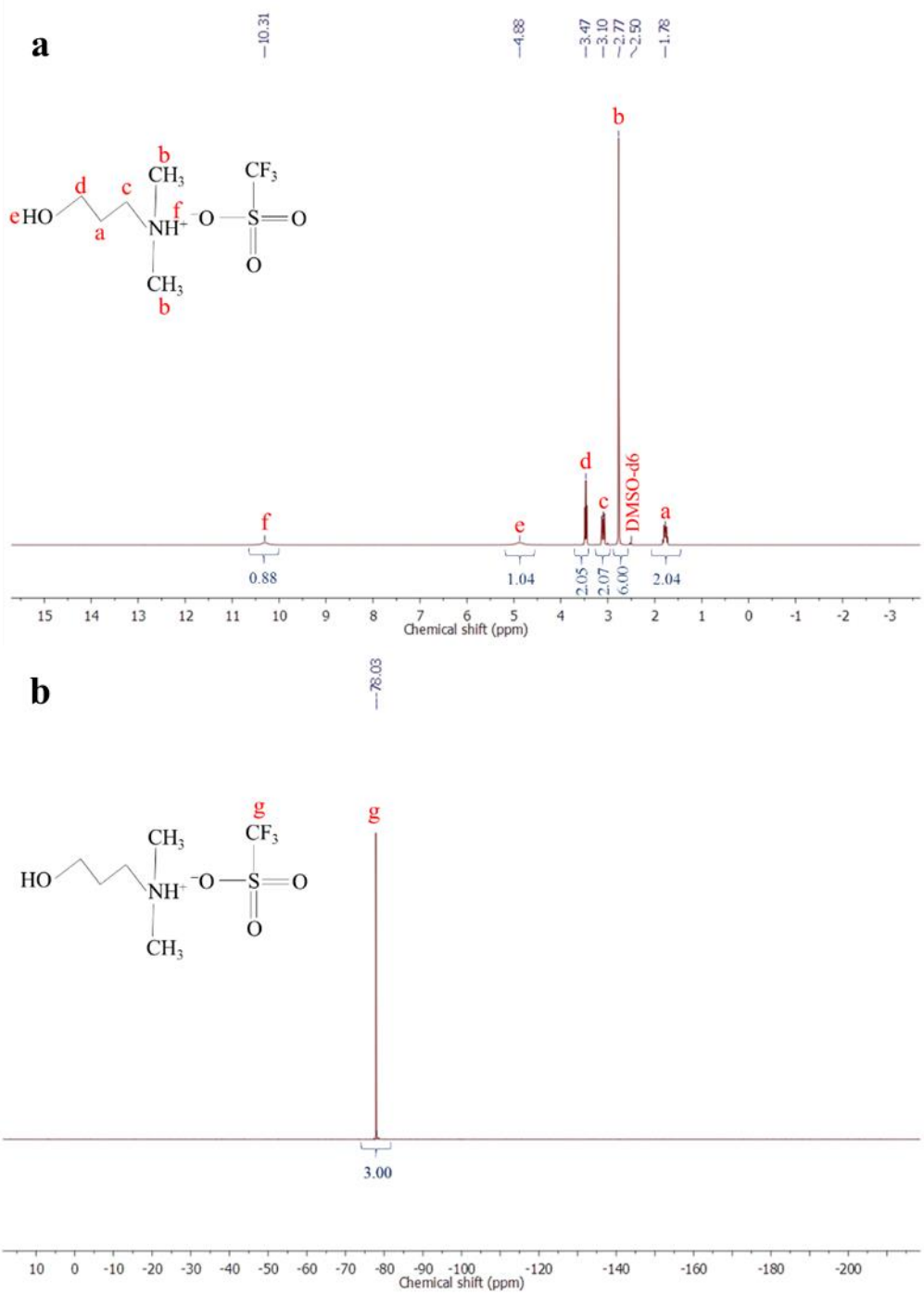

Figure S14. (a) ^{1}H NMR and (b) ^{19}F NMR spectra of [DEPA][TFS].

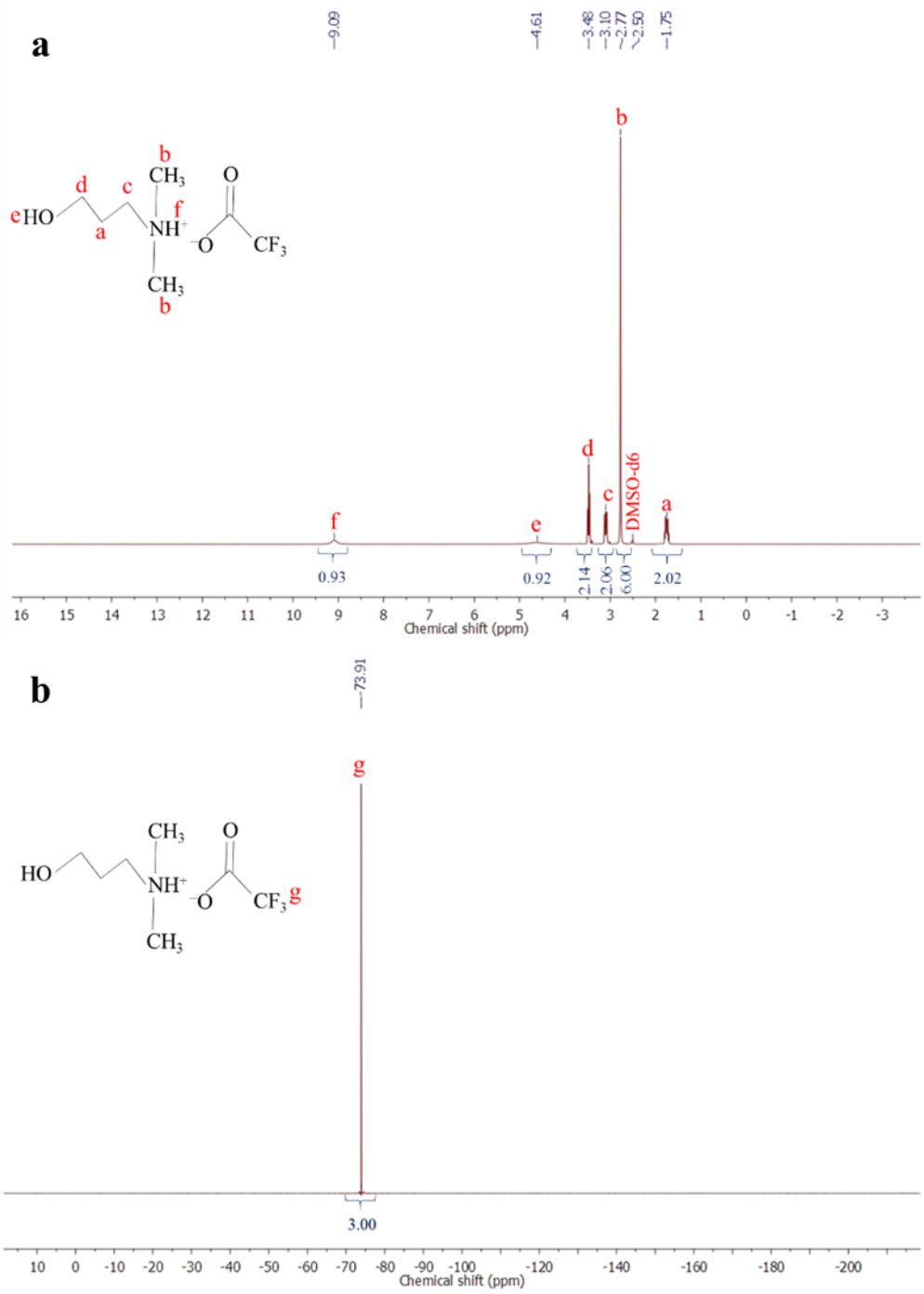

Figure S15. (a) ^{1}H NMR and (b) ^{19}F NMR spectra of [DEPA][TFA].

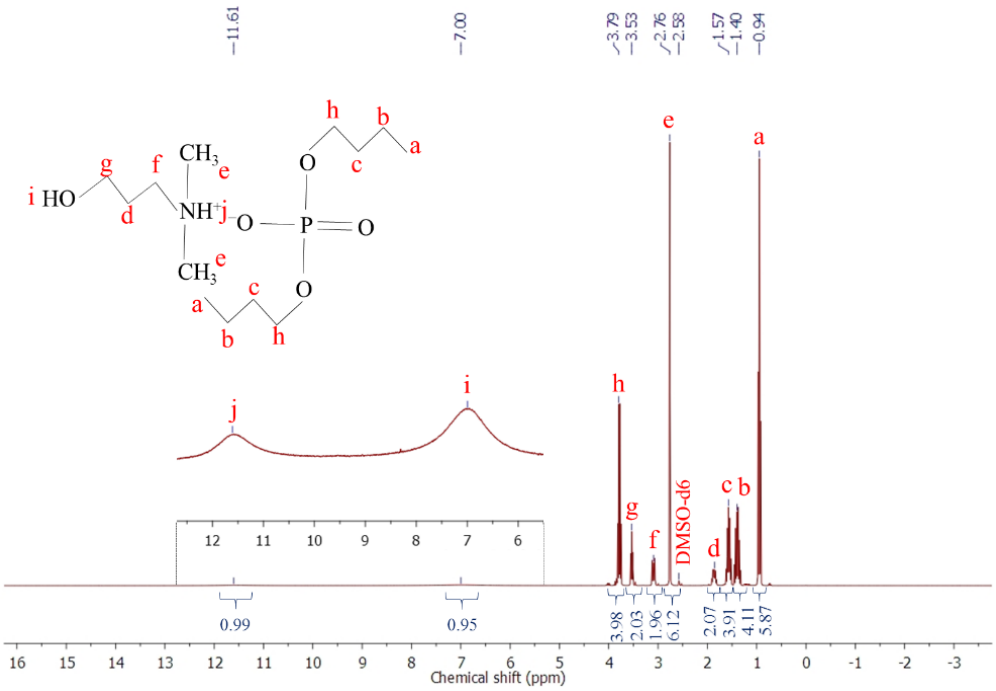

Figure S16. [1]H NMR spectrum of [DEPA][BUPH].

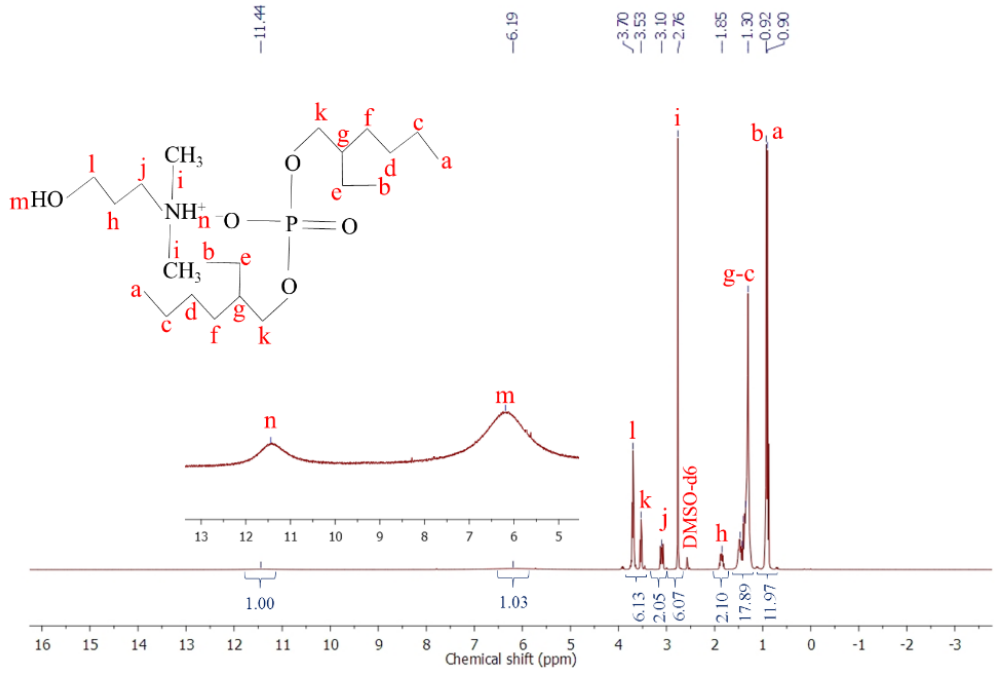

Figure S17. [1]H NMR spectrum of [DEPA][EHPH].

Abstract

Proton exchange membrane fuel cell (PEMC) has attracted a lot of attention in the both, laboratories and industries because PEMFC is considered as the green source of energy. Polymer electrolyte membrane (PEM) is the most important part in PEMFC owing to the fact that it is responsible for carrying protons between electrodes. Nafion® is the most commonly used polymer for PEM preparation because of its good thermal, mechanical, and chemical stability as well as high ionic conductivity. This polymer has excellent performance at low up to moderate temperatures under humidified condition. However, working at elevated temperature (higher than 80 °C) is more desirable and under these conditions the ionic conductivity of Nafion® membrane drops down significantly owing to the water evaporation. To obtain PEMs which can be applied at higher temperatures under anhydrous conditions, ionic liquids (ILs) are used as the proton carrier. The aim of this PhD thesis was to synthesis thermally stable and conductive ILs and use them as the additive to prepare proton conductive membranes for PEMFC application at elevated temperature.

Several Pr-ILs containing different anions ([TFS]-, [TFA]-, [HS]-, [BUPH]-, and [EHPH]-based) and cations ([DETA]-, [DEPA]-, [MIM]-, and [BIM]-based) were prepared by acid-base neutralization reaction. The chemical structure of synthesized Pr-ILs was evaluated by NMR (^{1}H and ^{19}F) and FTIR analysis. It was found that the IL nature has a strong influence on the thermal and electrochemical properties of obtained ILs. In addition, the influence of anion nature on the thermal stability and ionic conductivity of synthesized Pr-ILs is much more pronounced than cation nature. The dynamic TGA results showed that there is a direct link between the acidity of acid and thermal stability of IL and [TFS]-based ILs demonstrated the highest thermal stability (T_{deg} ~ 415−435 °C) owing to the high acidity of trifluoromethanesulfonic acid (pK_a ~ -14). The following thermal stability order was proposed: [TFS] > [HS] > [EHPH] > [BUPH] > [TFA]. The ionic conductivity measurements were carried out in two heating/cooling cycles and no hysteresis was observed. Such results confirm the ionic conductivity of ILs. Furthermore, it was observed that the anion nature has the dominant influence on the ionic conductivity of synthesized Pr-ILs. [TFS]-based ILs showed the highest ionic conductivity values (~ 34.5−63.7 $mS \cdot cm^{-1}$ at 150 °C) because trifluoromethanesulfonic acid is a stronger acid as compared to the other used acids for IL synthesis. According to the results, the following ionic conductivity order of studied anions can be proposed: [TFS] > [HS] > [TFA] > [BUPH] > [EHPH]. The obtained results showed that synthesized Pr-ILs have great potential to be used in PEMFC application. However, owing to the physical state of ILs, it is not possible to use them alone as the electrolyte in PEMFC. In order to have ion conductive PEM, composite membranes (polymer + IL) must be prepared.

CAB/[DETA][TFS]-[DEPA][BUPH] composite membranes were prepared by a phase inversion technique. Composite membranes containing 0, 23, 33, and 41 wt.% of ILs were prepared (M_0, M_1, M_2, and

M_3, respectively) by the phase inversion method. The presence of ILs in the membrane was confirmed by FTIR and EDX analysis. SEM analysis showed a homogenous and dense structure of M_0 and M_1 membranes. However, in case of M_2 and M_3 membranes (containing 33 and 41 wt.% of Pr-ILs), some aps and cavities were observed. AFM analysis revealed that the surface roughness of pure CAB membrane increased by rising the concentration of ILs because of incompatibility between [DETA][TFS] and CAB polymer. Thermal analysis revealed the lower thermal stability of composite membranes (T_{deg} ~ 256–265 °C) in comparison with pure CAB membrane (T_{deg} ~ 360 °C). Composite membrane also showed lower T_g values as compared with the pure CAB membrane, confirming the plasticizing behavior of ILs. The addition of ILs led to reduction of the mechanical stability of composite membrane in comparison with pure CAB membrane, while the membrane flexibility increased. Composite membranes showed good ionic conductivity (0.1–1 $mS \cdot cm^{-1}$ at 120 °C) and it was found that an increase of ILs concentration from 23 to 41 wt.% resulted in rising the membrane ionic conductivity owing to the increase of conductive regions. Furthermore, membrane ionic conductivity increased by rising the operating temperature from 25 to 120 °C owing to the ionic mobility enhancement. M_3 membrane showed the highest ionic conductivity of 0.443 $mS \cdot cm^{-1}$ at 120 °C under anhydrous condition. The stable ionic conductivity of composite membranes (M_1, M_2, and M_3) at 100 °C during 24 h reveals the excellent potential of CAB/[DETA][TFS]-[DEPA][BUPH] composite membranes for HT-PEMFC application for long-term utilization. It was confirmed the proton conduction takes place by Grotthuss mechanism since the calculated E_a > 14 $kJ \cdot mol^{-1}$. The results prove that the fabricated CAB/[DETA][TFS]-[DEPA][BUPH] composite membranes are promising candidates for using in electrochemical applications, namely fuel cell.

Ogniwa paliwowe z membraną protono-wymienną (PEMFC) cieszą się dużym zainteresowaniem zarówno w laboratoriach, jak i przemyśle, ponieważ PEMFC są klasyfikowane jako "zielone źródła energii". Polimerowa membrana jonowymienna (PEM) jest najważniejszą częścią PEMFC, odpowiadającą za przenoszenie protonów pomiędzy elektrodami. Nafion® jest najczęściej stosowanym polimerem do przygotowania PEM ze względu na swoje właściwości, takie jak dobra stabilność termiczna, mechaniczna i chemiczna oraz wysokie przewodnictwo jonowe. Polimer ten charakteryzuje się doskonałą wydajnością w niskich i umiarkowanych temperaturach i w warunkach wysokiego nawilżenia. Bardziej pożądana jest jednak praca w podwyższonej temperaturze (powyżej 80 °C) z uwagi na wyższe przewodnictwo elektryczne membrany. Niestety, w takich warunkach przewodność jonowa membrany Nafion® znacznie spada, głownie z powodu utraty pary wodnej. W celu rozwiązania tego problemu, do wytwarzania membran PEM pracujących w wyższych temperaturach i w warunkach ograniczonej wilgotności, wykorzystuje się ciecze jonowe (IL) jako nośnik protonów. Celem tej pracy doktorskiej była synteza termostabilnych i przewodzących cieczy jonowych i wykorzystanie ich jako dodatku do przygotowania membran przewodzących protony do zastosowań w PEMFC, w podwyższonej temperaturze.

Zsyntezowano protyczne ciecze jonowe (Pr-IL), zawierające różne aniony (na bazie [TFS], [TFA], [HS], [BUPH] i [EHPH]) oraz kationy ([DETA], [DEPA], [MIM] i [BIM]). Pr-IL wytworzono w reakcji neutralizacji kwasowo-zasadowej. Potwierdzenia struktury chemicznej zsyntetyzowanych Pr-IL dokonano za pomocą analizy NMR (^{1}H i ^{19}F) i FTIR. Stwierdzono, że charakter IL ma silny wpływ na właściwości termiczne i elektrochemiczne otrzymanych IL. Ponadto zaobserwowano, że wpływ anionu na stabilność termiczną i przewodność jonową syntetyzowanych Pr-IL jest znacznie większy niż wpływ kationu. Wyniki analizy termograwimetrycznej (TGA) wykazały bezpośredni związek pomiędzy kwasowością kwasu a stabilnością termiczną IL. Stwierdzono, że IL na bazie [TFS] wykazywały najwyższą stabilność termiczną (T_{deg} ~ 415–435 °C) ze względu na wysoką kwasowość TFS (pK_a ~ -14). Stabilność termiczną można uszeregować następująco: [TFS] > [HS] > [EHPH] > [BUPH] > [TFA]. Pomiar przewodności jonowej prowadzono w dwóch cyklach grzania/chłodzenia i zaobserwowano, że uzyskane wartości w cyklach grzania i chłodzenia dla IL są sobie bliskie. Takie wyniki potwierdzają przewodnictwo jonowe zsyntezowanych IL. Ponadto zaobserwowano, że rodzaj anionu ma dominujący wpływ na przewodnictwo jonowe syntetyzowanych Pr-IL. IL na bazie [TFS] wykazały najwyższe wartości przewodności jonowej (~ 34.5–63.7 $mS \cdot cm^{-1}$ w 150 °C), ponieważ kwas trifluorometanosulfonowy jest silniejszym kwasem w porównaniu z innymi kwasami używanymi do syntezy IL. Na podstawie wyników można zaproponować następujący szereg przewodnictwa jonowego badanych anionów: [TFS] > [HS] > [TFA] > [BUPH] > [EHPH]. Uzyskane wyniki wykazały, że zsyntetyzowane Pr-IL mają duży potencjał do zastosowania w PEMFC. Jednakże ze względu na stan fizyczny IL nie jest możliwe zastosowanie ich jako elektrolitu w

PEMFC. Aby uzyskać układ przewodzący jony, należy przygotować membrany kompozytowe (polimer zawierający przewodzącą ciecz jonową IL).

Membrany kompozytowe CAB/[DETA][TFS]-[DEPA][BUPH] przygotowano techniką inwersji faz. Membrany kompozytowe zawierające 0, 23, 33 i 41% wag. zawartości ILs (odpowiednio M_0, M_1, M_2 i M_3) przygotowano metodą inwersji faz. Obecność ILs w strukturze błony potwierdzono analizami FTIR i EDX. Analiza SEM wykazała jednorodną i gęstą strukturę membran M_0 i M_1. Jednakże w przypadku membran M_2 i M_3 (zawierających 33 i 41% mas. Pr-IL) zmniejsza się homogeniczność struktury membrany. Analiza AFM ujawniła, że szorstkość powierzchni czystej membrany CAB wzrosła wraz ze wzrostem zawartości IL, z powodu niskiej kompatybilności pomiędzy [DETA] [TFS] a polimerem CAB. Analiza termiczna wykazała niższą stabilność termiczną membran kompozytowych (T_{deg} ~ 256–265 °C) w porównaniu z czystą membraną CAB (T_{deg} ~ 360 °C). Membrana kompozytowa wykazywała również niższe wartości T_g w porównaniu z czystą membraną CAB, co potwierdza plastyfikujący wpływ IL. Próba rozciągania wykazała, że dodatek ILs spowodował zmniejszenie stabilności mechanicznej membrany kompozytowej w porównaniu z czystą membraną CAB, przy jednoczesnym wzroście elastyczności membrany. Membrany kompozytowe wykazały dobrą przewodność jonową (0.1–1 $mS \cdot cm^{-1}$ w temperaturze 120 °C) i stwierdzono, że wzrost stężenia ILs z 23 do 41% wag. powodował wzrost przewodności jonowej membran kompozytowych dzięki wzrostowi ilości obszarów przewodzących w strukturze membrany. Ponadto, przewodność jonowa membrany wzrosła poprzez podniesienie temperatury roboczej z 25 do 120 °C, dzięki zwiększeniu ruchliwości jonów. Membrana M_3 wykazała najwyższą przewodność jonową wynoszącą 0.443 $mS \cdot cm^{-1}$ w temperaturze 120 °C bez obecności wilgoci. Wykazano stabilną przewodność jonową membran kompozytowych (M_1, M_2 i M_3) w temperaturze 100 °C podczas 24-godzinnego testu, potwierdzając możliwość wykorzystania membrany kompozytowej CAB/[DETA][TFS]-[DEPA][BUPH] do długotrwałego użytkowania w HT-PEMFC. Stwierdzono, że przewodzenie protonów odbywa się według mechanizmu Grotthussa, gdyż obliczone E_a > 14 $kJ \cdot mol^{-1}$. Wyniki potwierdzają, że wytworzone membrany kompozytowe CAB/[DETA][TFS]-[DEPA][BUPH] mogą być praktycznie wykorzystane w elektrodializie i w ogniwach paliwowych.

Resumé

La pile à combustible à membrane échangeuse de protons (PEMFC) suscite beaucoup d'intérêts dans le milieu académique et dans l'industrie, puisqu' elle est considérée comme une source d'énergie verte. La membrane électrolytique polymère (PEM), responsable du transport des protons entres les électrodes, est la partie la plus importante de la PEMFC. Le Nafion® est le polymère le plus couramment utilisé en tant que PEM du fait de ses bonnes stabilités thermique, mécanique et chimique ainsi qu'une conductivité ionique élevée. Ce polymère présente d'excellentes performances à des températures inférieures à 80 °C et dans les conditions humidifiées. Cependant, pour augmenter la vitesse de la réaction et éviter l'empoisonnement du Pt, l'utilisation de la PEMFC à des températures élevées (supérieure à 80 °C) est recommandée. En revanche, dans ces conditions, la conductivité ionique de Nafion® diminue considérablement en raison de sa déshydratation Pour obtenir des PEMs pouvant être utilisées à des températures élevées et dans des conditions anhydres, des liquides ioniques (LIs) jouant le rôle de conducteurs protoniques sont envisagés. L'objectif de cette thèse était de synthétiser des nouveaux LIs thermiquement stables et conducteurs et de les utiliser comme agent de transport pour concevoir des membranes conductrices de protons pour une application PEMFC à température élevée.

Plusieurs LIs protiques (LIs-Pr) contenant différents anions ([TFS]-, [TFA]-, [HS]-, [BUPH]- et [EHPH]) et cations ([DETA]-, [DEPA]-, [MIM]- et [BIM]) ont été synthétisés via une réaction de neutralisation acido-basique. La structure chimique des LIs-Pr synthétisés a été confirmée par les analyses RMN (^{1}H et ^{19}F) et IRTF. Il a été constaté que la nature du LI a une forte influence sur les propriétés thermiques et électrochimiques des LIs obtenus. De plus, l'influence de la nature des anions sur la stabilité thermique et la conductivité ionique des LIs-Pr synthétisés est bien plus importante que celle des cations. Les résultats d'analyse thermogravimétrique ont montré qu'il existe un lien direct entre l'acidité de l'acide utilisé et la stabilité thermique du LI – les LIs à base de [TFS] présentent les plus grandes stabilités thermiques (T_{deg} ~ 415−435 °C) étant donné l'acidité élevée de l'acide trifluorométhanesulfonique (pK_a ~ -14). L'ordre de stabilité thermique obtenu était : [TFS] > [HS] > [EHPH] > [BUPH] > [TFA]. Les mesures de conductivité ionique en fonction de la température ont montré des valeurs similaires lors lu chauffage et du refroidissement confirmant l'absence d'hysteresis. La encore, il a été démontré que la nature de l'anion a une influence majeure sur la conductivité ionique des LIs-Pr synthétisés. Les valeurs de conductivité ionique les plus élevées (~ 34.5 à 63.7 $mS \cdot cm^{-1}$ à 150 °C) ont été obtenues pour les LIs à base de [TFS], du fait du caractère plus acide de du TFS par rapport aux autres acides. D'après les données expérimentales, l'ordre de conductivité ionique est le suivant : [TFS] > [HS] > [TFA] > [BUPH] > [EHPH]. L'ensemble des résultats obtenus confirment que les LIs-Pr synthétisées ont un fort potentiel pour le développement des PEMFC. Cependant, en raison de l'état physique des LIs (solide dans la plupart des cas), il n'est pas possible de les utiliser comme électrolyte directement dans les PEMFC. Ce verrou peut-être levé par la mise au point de PEM à partir de membranes composites (polymère + LI) .

Resumé

Les membranes composites à base de CAB/[DETA][TFS]-[DEPA][BUPH] (0, 23, 33 et 41 % en poids de LI – M_0, M_1, M_2 et M_3, respectivement) ont été préparées par une technique d'inversion de phase. La présence de LI dans la structure membranaire a été confirmée par les analyses IRTF et Rayons-X. L'analyse MEB a révélé une structure homogène et dense pour les membranes M_0 et M_1. Cependant, dans le cas des membranes M_2 et M_3 (contenant respectivement 33 et 41 % en masse de LI), la présence de pores a été observée. Les résultats de microscopie à force atomique ont montré que la rugosité de surface de la membrane CAB pure augmente avec l'augmentation de la concentration de LI en raison de l'incompatibilité entre [DETA][TFS] et le polymère CAB. L'analyse thermogravimétrique a permis de vérifier une stabilité thermique inférieure pour les membranes composites (T_{deg} ~ 256–265 °C) par rapport à la membrane CAB pure (T_{deg} ~ 360 °C). La membrane composite a également été caractérisée par des valeurs de T_g inférieures par rapport aux valeurs obtenues pour la membrane CAB pure confirmant le comportement plastifiant des LI. Par conséquent l'ajout de LI entraînait une réduction de la stabilité mécanique de la membrane composite par rapport à la membrane CAB pure, tandis que la flexibilité de la membrane augmentait. Des mesures d'impédance il résulte que les membranes composites possèdent une bonne conductivité ionique (0.1–1 $mS \cdot cm^{-1}$ à 120 °C). Comme attendu, l'augmentation de la proportion massique de LI de 23 à 41 % dans la membrane a conduit à une augmentation de la conductivité ionique des membranes composites. Aussi une augmentation de la conductivité ionique de la membrane liée à l'augmentation la température de fonctionnement (de 25 à 120 °C) a été vérifiée en raison de l'amélioration de la mobilité ionique. La membrane M_3 a présenté la conductivité ionique la plus élevée – soit 0.443 $mS \cdot cm^{-1}$ à 120 °C dans des conditions anhydres. Les mesures effectuées en mode isotherme ont mis en évidence une conductivité ionique stable des membranes composites (M_1, M_2 et M_3) à 100 °C pendant 24 h ce qui laisse supposer une capacité de ces membranes composites à base de CAB/[DETA][TFS]-[DEPA][BUPH] à pouvoir fonctionner en PEMFC à haute température (≥ 80 °C) et de manière durable. L'étude de conductivité menée en température a permis de déterminer l'énergie d'activation (E_a > 14 $kJ \cdot mol^{-1}$) qui semble indiquer que la conduction protonique s'effectue selon le mécanisme de Grotthuss. Tous les résultats obtenus attestent que les membranes composites à base de CAB/[DETA][TFS]-[DEPA][BUPH] sont des candidats prometteurs pour une utilisation dans des applications électrochimiques, notamment dans les piles à combustible.

Scientific Contribution

Articles (Thesis)

- **M. Ebrahimi**, W. Kujawski, K. Fatyeyeva, "Different Approaches for the Preparation of Composite Ionic Liquid-Based Membranes for Proton Exchange Membrane Fuel Cell Applications—Recent Advancements", Membranes, 2023, 13, 593 (IF: 4.562). DOI: https://doi.org/10.3390/membranes13060593;
- **M. Ebrahimi**, W. Kujawski, K. Fatyeyeva, "Fabrication of Polyamide-6 Membranes—The Effect of Gelation Time towards Their Morphological, Physical, and Transport Properties", Membranes, 2022, 12, 315 (IF: 4.565). DOI: https://doi.org/10.3390/membranes12030315;
- **M. Ebrahimi**, W. Kujawski, K. Fatyeyeva and J. Kujawa, "A Review on Ionic Liquids-Based Membranes for Middle and High Temperature Polymer Electrolyte Membrane Fuel Cells (PEM FCs)", Int. J. Mol. Sci., 2021, 22, 5430 (IF: 5.923). DOI: https://doi.org/10.3390/ijms22115430;
- **M. Ebrahimi**, Y. Kobzar, W. Kujawski, K. Fatyeyeva, "Thermal and electrochemical behavior of synthesized protic ionic liquids: influence of cation and anion structure" (submitted to the Journal of Molecular Liquids, receiving the first review, IF: 6.6).

Articles (Other)

- S.M. Hosseini, P. Golshanikia, M. Habibi, E. Jashni, J. Shen, **M. Ebrahimi**, "Intensifying antibacterial and electrochemical behaviors of CuO induced‐ion exchange membrane for water treatment", Journal of Polymer Research, 2022, 29, 250 (IF: 3.097). DOI: https://doi.org/10.1007/s10965-022-03023-4;
- S.M. Hosseini, F. Moradi, S.K. Farahani, S. Bandehali, F. Parvizian, **M. Ebrahimi** and J. Shen, "Carbon nanofibers/chitosan nanocomposite thin film for surface modification of poly(ether sulphone) nanofiltration membrane", Materials Chemistry and Physics, 2021, 124720 (IF: 4.092). DOI: https://doi.org/10.1016/j.matchemphys.2021.124720;
- S. M. Hosseini, H. Alibakhshi, E. Jashni, F. Parvizian, J. N. Shen, M. Taheri, **M. Ebrahimi**, N. Rafiei. "A novel layer-by-layer heterogeneous cation exchange membrane for heavy metal ions removal from water". Journal of Hazardous Materials, 2020, 381, 120884 (IF: 9.038). DOI: https://doi.org/10.1016/j.jhazmat.2019.120884;
- M. Askari, E. Salehi, **M. Ebrahimi**, A. Barati. "Application of breakthrough curve analysis and response surface methodology for optimization of a hybrid separation system consisting of fixed-bed column adsorption and dead-end depth filtration". Chemical Engineering and Processing, 2019, 143, 107594 (IF: 4.237). DOI: https://doi.org/10.1016/j.cep.2019.107594;

- **M. Ebrahimi**, B. V. d. Bruggen, S. M. Hosseini, M. Asksri, M. Nemati. "Improving electrochemical properties of cation exchange membranes by using activated carbon-co-chitosan composite nanoparticles in water deionization". Ionics, 2019, 25, 1199-1214 (IF: 2.60). DOI: https://doi.org/10.1007/s11581-018-2724-y.

Oral communications

- **M. Ebrahimi,** Y. Kobzar, W. Kujawski, K. Fatyeyeva, "Synthesis of Super Conductive Protic Ionic Liquids: the Influence of Different Cations and Anions on Their Thermal and Electrochemical Properties", Membrane Materials - Modification and Separation (M3-S), Torun, Poland, 2023 – **3rd prize awarded**;
- **M. Ebrahimi**, K. Fatyeyeva, W. Kujawski, " New Ionic Conducting Composite Membrane based on Ionic Liquids for fuel cell application", Membranes and Membrane Processes in Environmental Protection (MEMPEP), Zakopane, Poland, 2023 – **2nd prize awarded**;
- **M. Ebrahimi**, W. Kujawski, K. Fatyeyeva, "How can the gelation time affect membrane morphology?", Membrane Materials - Modification and Separation (M3-S) Conference, Toruń, Poland, 2021;
- **M. Ebrahimi**, W. Kujawski, "Ionic liquids based membranes for High Temperature Proton Exchange Membrane Fuel Cells (HT-PEMFC)", 13th Scientific Conference Membranes and Membrane Processes in Environmental Protection (MEMPEP), Zakopane, Poland, 2021 (online).

Poster

- **M. Ebrahimi**, K. Fatyeyeva, W. Kujawski, "Investigation of physical, chemical, morphological, and thermal properties of polymer membranes for PEMFC application", Journée de l'Ecole Doctorale Normande de Chimie (JEDNC), Caen, France, 2022.

Other achievements

- Part of organization committee in Modification and Separation (M3-S) Conference, Toruń, Poland, 2021;
- Part of organization committee in Modification and Separation (2M3-S) Conference, Toruń, Poland, 2023.